Cristallisation sous contrainte du caoutchouc naturel en fatigue et sous sollicitation multiaxiale

Stéphanie Beurrot-Borgarino

École Centrale de Nantes

École Doctorale

Sciences Pour l'Ingénieur, Géosciences, Architecture

Année 2011-2012

N^o B. U. :

Thèse de Doctorat

Spécialité : GÉNIE MÉCANIQUE

Présentée et soutenue par :

Stéphanie BEURROT

Le 21 Juin 2012
à l'École Centrale de Nantes

TITRE

Cristallisation sous contrainte du caoutchouc naturel en fatigue et sous sollicitation multiaxiale

JURY

Président	Roland Séguéla	Directeur de Recherche CNRS, MATEIS, INSA Lyon
Rapporteurs	Laurent Chazeau	Professeur des Universités, MATEIS, INSA Lyon
	Costantino Creton	Directeur de Recherche CNRS, Laboratoire PPMD, ESPCI ParisTech
Examinateurs	Daniel Berghezan	Docteur, Centre technique Michelin
	Sylvie Castagnet	Chargé de Recherche CNRS, Laboratoire Pprime, ENSMA
	Bertrand Huneau	Maître de Conférences, GeM, Ecole Centrale Nantes
	Erwan Verron	Professeur des Univeristés, GeM, Ecole Centrale Nantes

---

Directeur de thèse	Erwan Verron	Professeur des Universités
Laboratoire	Institut de Recherche en Génie Civil et Mécanique, Ecole Centrale Nantes	
Co-encadrant	Bertrand Huneau	Maître de Conférences
Laboratoire	Institut de Recherche en Génie Civil et Mécanique, Ecole Centrale Nantes	

N^o E. D. : 498-220

Remerciements

Je tiens à remercier tout d'abord les rapporteurs de cette thèse, Messieurs Costantino Creton et Laurent Chazeau, pour leur relecture de ce manuscrit. Je remercie également Madame Sylvie Castagnet et Messieurs Roland Séguéla et Daniel Berghezan pour leur participation à ma soutenance de thèse en tant que membres du jury.

Je remercie sincérement mes directeur et encadrant de thèse, Messieurs Erwan Verron et Bertand Huneau, pour leur encadrement scientifique mais surtout l'amitié que nous avons développée au fil des ans. Leur patience et leurs encouragements ont été décisifs dans les moments de doute et leur amitié a pleinement participé à ma motivation et à mon plaisir au travail.

Je souhaite également exprimer ma gratitude envers les personnes qui m'ont apporté leur aide technique et scientifique. Merci à Pierrick Guégan et Franck Pasco pour le temps passé à mettre en place les essais et pour avoir supporté le bruit des machines pendant de nombreux mois ! Merci aussi à Adrien Leygue et Pierre Rublon pour les débats et les discussions autours du caoutchouc.

Je remercie Steve Jerrams du Dublin Institute of Technology de m'avoir accueilli à Dublin durant un an, et m'avoir ainsi permis de découvrir l'Irlande.

Un grand merci aux membres de l'équipe Matériaux du GeM pour la bonne humeur qui régnait dans les couloirs. Je remercie particulièrement les collègues devenus petit à petit amis : Arthur pour son chaleureux accueil, Marion et toutes nos discussions non scientifiques, Adrien pour son soutien moral et son appui logistique lors de mes visites nantaises, et Coco et sa constante bonne humeur.

Pour finir, je remercie mes proches, famille et amis, pour m'avoir soutenu tout au long de ce projet. Et un très grand merci à Bruno, qui sait me permettre de donner le meilleur de moi-même.

Table des matières

Introduction générale

Le caoutchouc naturel est un matériau élastomère employé pour d'innombrables applications industrielles : joints, systèmes anti-vibratoires, pneumatiques, etc. Dans beaucoup de ces systèmes, le caoutchouc naturel est choisi pour ses très bonnes propriétés mécaniques en grandes déformations et en fatigue car il est soumis à des chargements cycliques, souvent complexes. Pour cette raison, la compréhension et la prédiction du comportement du caoutchouc naturel en fatigue multiaxiale est un enjeu majeur pour la conception de nouveaux produits.

Dans la bibliographie, on distingue deux approches pour étudier la fatigue des élastomères. Historiquement, la première approche considérée a été l'étude de la durée de vie du matériau. Après des mesures de durée de vie en fatigue (Cadwell *et al.*, 1940; André *et al.*, 1999), les auteurs se sont ensuite intéressés à sa prédiction (Mars et Fatemi 2005; Saintier *et al.* 2006a,b; Verron et Andriyana 2008 par exemple). La deuxième approche consiste à s'intéresser à la propagation des fissures de fatigue. En 1953, Rivlin et Thomas ont étudié les aspects énergétiques de la propagation de fissures quasi-statiques dans les élastomères, puis Lake *et al.* (1965; 1995) entre autres ont appliqué à la propagation en fatigue les outils alors developpés. Ces deux approches sont détaillées dans la revue bibliographique de Mars et Fatemi (2002) et dans les thèses de doctorat de l'Institut de Recherche en Génie Civil et Mécanique (Ostoja-Kuczynski, 2005; Le Cam, 2005; Andriyana, 2006; Aït-Bachir, 2010) auxquelles le lecteur peut se référer. Ces différentes études ont notamment montré que le caoutchouc naturel possède d'excellentes propriétés en fatigue multiaxiale - grande durée de vie et faible vitesse de propagation des fissures - mais sans pour autant parvenir à les expliquer. Il est généralement admis dans la bibliographie que le phénomène de cristallisation sous contrainte, c'est-à-dire la capacité du matériau à cristalliser lorsqu'il est déformé, en est à l'origine, bien que le lien entre ces propriétés macroscopiques et la microstructure du matériau n'a jamais été établi.

L'objectif de la présente thèse est de comprendre l'origine des très bonnes propriétés en fatigue multiaxiale du caoutchouc naturel, en proposant de nouvelles approches à une échelle plus fine que l'échelle macroscropique des pièces et des éprouvettes qui est généralement considérée par les mécaniciens. Ma thèse fait suite à celle de Le Cam (2005) qui a étudié la fatigue des élastomères à l'échelle des fissures et micro-fissures. Ici, nous avons choisi d'étudier le caoutchouc naturel vulcanisé et chargé au noir de carbone, qui est couramment utilisé dans l'industrie.

L'étude de la fatigue multiaxiale du caoutchouc naturel à une petite échelle est un problème très complexe et aucune étude à ce jour ne l'a abordé dans sa globalité. Nous avons identifié trois facettes du problème :

– tout d'abord, l'*échelle d'étude*. Nous avons choisi d'étudier la fatigue à deux échelles différentes : une échelle que nous appelons mésoscopique, qui est celle des fissures et micro-fissures, et l'échelle macromoléculaire qui permet d'étudier les changements de

phase et la cristallisation du matériau ;
- ensuite, les *deux approches classiques de la fatigue* : l'approche en durée de vie d'une part et celle en propagation des fissures d'autre part peuvent être adoptées ;
- enfin, le *chargement mécanique* est un aspect important. Compte tenu de la complexité du problème, nous nous sommes limités à deux types de chargement : la fatigue uniaxiale et la déformation quasi-statique multiaxiale en contraintes planes.

Il n'est bien entendu pas possible d'aborder ce problème avec exhaustivité dans une seule étude ; nous avons donc choisi trois axes d'étude, qui sont schématisés sur la figure 1 :

1. l'étude à l'échelle mésoscopique de la propagation des fissures de fatigue uniaxiale ;
2. l'étude de la cristallisation sous contrainte en déformation multiaxiale ;
3. et l'étude de la cristallisation sous contrainte en fatigue uniaxiale.

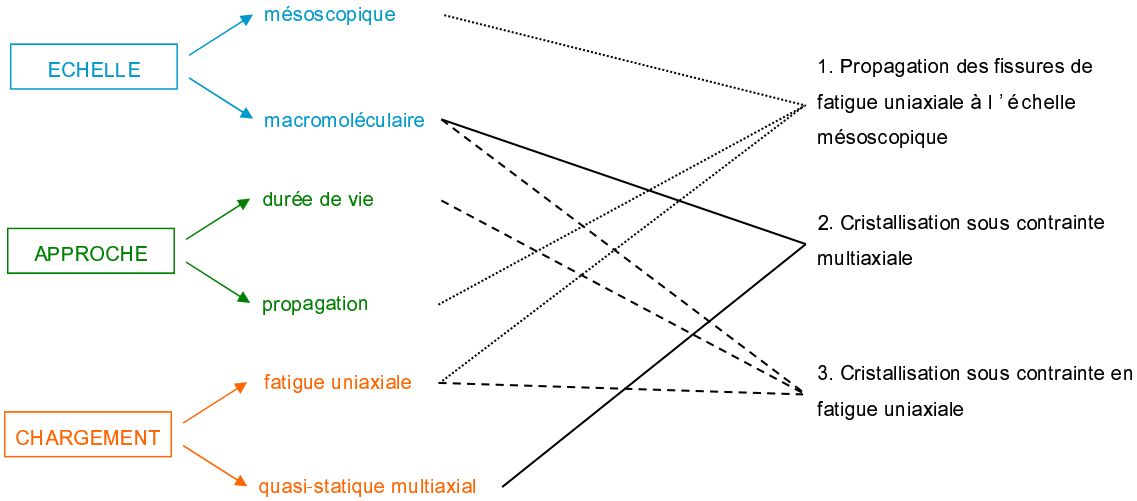

FIGURE 1 – Représentation schématique des trois facettes du problème (en couleurs) et des axes d'étude choisis (en noir).

Pour les études de la cristallisation, c'est-à-dire à l'échelle macromoléculaire, j'ai effectué des essais de diffraction des rayons X au synchrotron Soleil (Gif-sur-Yvette, France).

Le présent mémoire est présenté sous la forme d'une série d'articles tels qu'ils ont été publiés ou soumis. L'état de l'art, la méthode expérimentale et les résultats sont présentés et discutés, notamment au regard de la littérature, au fur et à mesure des articles. Cependant, certains travaux réalisés pendant ma thèse n'apparaissent pas dans ces articles, en particulier ceux ayant permis d'établir la méthode expérimentale ; un chapitre préliminaire est donc dédié aux trois étapes principales de cette élaboration. Puis, les articles font chacun l'objet d'un chapitre et sont regroupés en quatre parties.

Dans la première partie, intitulée « Echelle mésoscopique » et comprenant un seul chapitre, nous nous intéressons aux mécanismes de propagation des fissures dans le cas de la fatigue uniaxiale. L'objectif de cette partie est de comprendre les mécanismes de dissipation à l'échelle mésoscopique qui contribuent aux excellentes propriétés en fatigue du caoutchouc naturel. A l'issue de cette étude, nous obervons que l'échelle mésoscopique ne suffit pas pour relier les propriétés mécaniques du matériau et la cristallisation sous contrainte de manière satisfaisante.

Dans la suite du manuscrit, nous nous intéressons donc à une échelle d'étude plus fine, l'échelle macromoléculaire qui est celle des mécanismes de cristallisation du matériau et qui

a été étudiée par diffraction des rayons X de rayonnement synchrotron. Ainsi, la deuxième partie intitulée « Caractérisation de la cristallisation sous contrainte du matériau » comporte un chapitre qui s'intéresse en détails à la cristallisation sous contrainte du caoutchouc naturel non chargé et chargé au noir de carbone sous chargement de traction quasi-statique uniaxiale. Ce type d'étude est aujourd'hui assez classique. Toutefois, ceci permettra de caractériser notre matériau et de fournir des repères pour les parties suivantes, mais ausi de dresser un bilan de l'état de l'art de la cristallisation sous contrainte du caoutchouc naturel mesurée par diffraction des rayons X.

Nous abordons ensuite la cristallisation sous contrainte du caoutchouc naturel soumis à des déformations multiaxiales dans la troisième partie intitulée « Multiaxialité ». Celle-ci est composée de deux chapitres. En premier lieu, la cristallisation sous contrainte est étudiée en déformation uniaxiale et équibiaxiale. Ce chapitre montre que la multiaxialité de la déformation a un effet important sur l'orientation des cristallites ; cet aspect de la cristallisation sous contrainte multiaxiale est détaillé ensuite. Puis, dans un deuxième chapitre, nous nous intéressons à l'effet du chemin de chargement sur l'orientation des cristallites.

Dans la quatrième et dernière partie, intitulée « Fatigue uniaxiale », deux thèmes sont abordés. Tout d'abord, dans un premier chapitre, nous nous intéressons à la cristallisation sous contrainte au cours d'un seul cycle de traction uniaxiale, mais à grande vitesse de déformation, c'est-à-dire à une vitesse similaire à celles utilisées lors d'essais de fatigue. Ensuite, l'effet de la répétition de ces cycles rapides est abordé, dans deux chapitres dédiés à la cristallisation sous contrainte en fatigue uniaxiale : l'un s'intéresse aux caractéristiques des cristallites et à leur évolution, l'autre se concentre sur l'évolution du degré de cristallinité au cours de la fatigue pour différents niveaux de chargement.

Chapitre 1

Considérations préliminaires sur la méthode expérimentale

Le format choisi pour ce manuscrit - une série d'articles - ne permet pas d'exposer tous les travaux réalisés pendant la thèse. En particulier, certaines difficultés expérimentales qui ont été rencontrées n'y sont pas décrites. L'objet de ce chapitre préliminaire est donc de présenter trois points importants de la méthode expérimentale ayant nécessité une attention particulière :

- la conception et la réalisation d'une machine de fatigue multiaxiale dédiée aux essais in-situ de diffraction des rayons X au synchrotron Soleil ;
- la conception d'éprouvettes de traction équibiaxiale pour des matériaux mous en grandes déformations ;
- et la méthode d'analyse de clichés de diffraction obtenus à Soleil.

Dans ce chapitre, nous utiliserons, par commodité, la notation anglo-saxone NR (pour natural rubber) pour désigner le caoutchouc naturel.

1.1 Conception et réalisation d'une machine de fatigue multiaxiale

L'objectif des essais réalisés au synchrotron Soleil (Gif-sur-Yvette, Fance) lors de ma thèse était de mesurer la cristallisation sous contrainte du caoutchouc naturel par diffraction des rayons X lors d'essais in-situ de fatigue uniaxiale et de traction équibiaxiale. Il était donc nécessaire d'acquérir une machine de fatigue multiaxiale pouvant être utilisée sur la ligne DiffAbs du synchrotron Soleil. Il n'était pas possible d'acheter une machine du commerce, tant pour des raisons budgétaires que pour des raisons pratiques, aucune machine commercialisée ne correspondant parfaitement aux besoins. J'ai donc dû la concevoir et la réaliser dans le cadre de ma thèse.

Il s'agit d'une machine de traction-compression plane bi-axiale, permettant la déformation d'éprouvettes planes cruciformes et d'éprouvettes uniaxiales « haltères » classiques. Les critères de conception de la machine étaient nombreux :

- adaptée à la ligne DiffAbs du synchrotron Soleil, c'est-à-dire respectant de très fortes contraintes en termes d'encombrement et de poids ;
- permettant de réaliser des essais de fatigue en grandes déformations dans un temps « raisonnable », c'est-à-dire avec une fréquence de quelques hertz, et durant plusieurs heures sans interruption ;
- permettant de réaliser des essais de traction équibiaxiale ;

- permettant d'atteindre des niveaux de déformation suffisament élevés pour observer la cristallisation du caoutchouc ;
- synchronisée avec les outils de contrôle de la ligne de diffraction, notamment pour assurer des temps de pause très courts durant les essais de fatigue ;
- garantissant une grande précision et une grande répétabilité des déformations imposées aux éprouvettes, soit une parfaite synchronisation entre les vérins et une grande précision des déplacements ;
- permettant de garder la partie utile de l'éprouvette fixe au cours des essais de traction ;
- polyvalente, pour des essais futurs : large gamme de vitesse, charge maximale des vérins élevée, pilotage des vérins programmable, utilisation avec différents types d'éprouvette, essais en traction et compression, etc. ;
- pouvant être transportée facilement, donc démontable ;
- et respectant le budget déterminé.

La machine de fatigue multiaxiale finalement réalisée, ainsi que le tableau électrique de commande, sont montrés sur la figure 1.1.

Les différentes étapes de conception et de réalisation de cette machine ont été les suivantes :

1. Le choix des vérins et des différents éléments électroniques de contrôle. Nous avons retenu un système de quatre vérins linéaires de traction - compression. La charge maximale des vérins est ± 500 N et leur course est 70 mm. Chaque vérin est controlé par un variateur numérique individuel. Dans les systèmes classiques de pilotage, l'un des variateurs est généralement défini comme le variateur « père », par opposition aux autres variateurs dits « enfants ». Le variateur « père » est alors le seul à être programmé et piloté par un système extérieur (un opérateur, un ordinateur, le système de pilotage de la ligne DiffAbs, etc.), et celui-ci relaye les ordres aux variateurs « enfants ». Ce système, économique et simple, présente le risque d'un léger retard de phase des variateurs « enfants » sur le variateur « père ». La synchronisation des quatre vérins étant essentielle pour nos essais, nous avons finalement choisi d'ajouter une étape dans la hiérarchie de pilotage de la machine en utilisant un boîtier de commande électronique qui relaye les informations aux quatre variateurs simultanément.
2. La conception du tableau électrique. Celui-ci est nécessaire pour assurer la communication entre les différents éléments de contrôle cités ci-dessus, mais également avec les systèmes de pilotage existant sur la ligne DiffAbs. De plus, des éléments de sécurité, comme un « coup de poing » d'arrêt d'urgence et des disjoncteurs, devaient être ajoutés. Les détails de la conception et la réalisation du tableau ont été sous-traités à une entreprise spécialisée.
3. La conception des mors. Dans le cadre d'essais de traction en grandes déformations sur des éprouvettes plates, la principale difficulté lors de l'utilisation de machines standards est le glissement des éprouvettes dans les mors. En effet, lors d'un essai de traction uniaxiale, la variation d'épaisseur d'une éprouvette est proportionnelle à la racine de l'extension. Par exemple, si l'extension de l'éprouvette est $\lambda = 4$, ce qui est très courant pour des essais sur du caoutchouc naturel, alors l'épaisseur de l'éprouvette est divisée par 2. Avec des mors classiques, c'est-à-dire deux plaques resserrées de part et d'autre de l'éprouvette, celle-ci glisse. Pour résoudre ce problème, la meilleure solution est l'emploi de mors hydrauliques qui assurent une pression constante des plaques sur l'éprouvette, s'adaptant ainsi à la diminution de son épaisseur. L'inconvéniant majeur de ces mors est leur encombrement, incompatible avec les dimensions imposées par la ligne de diffraction. J'ai donc plutôt choisi des mors

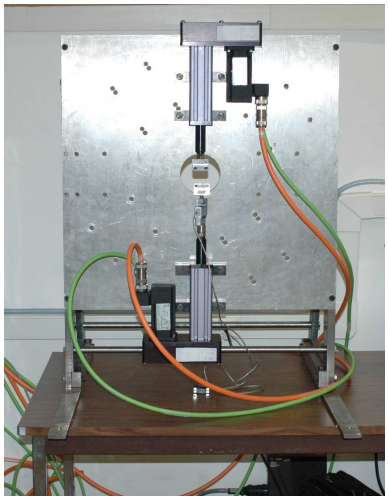

(a) Avant de la machine dans une configuration uniaxiale.

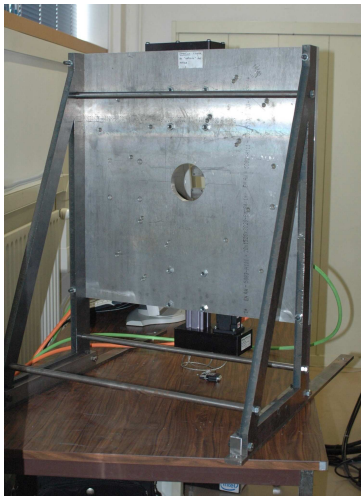

(b) Arrière de la machine.

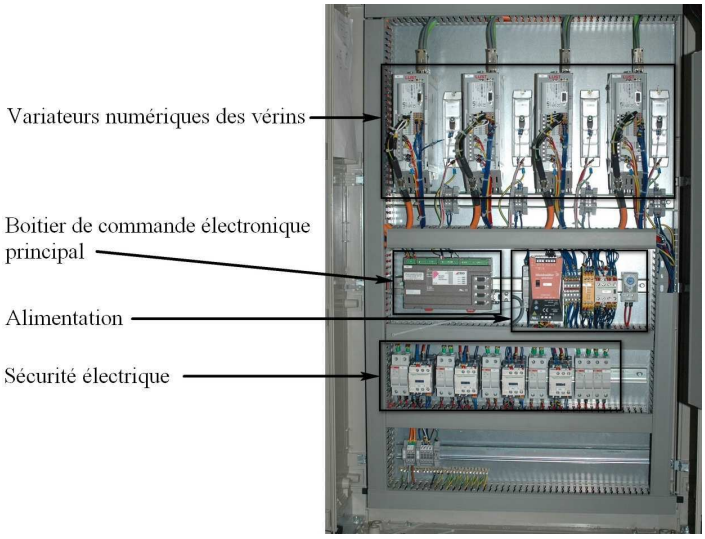

(c) Tableau électrique.

FIGURE 1.1 – Machine de fatigue multiaxiale conçue et réalisée dans le cadre de la thèse pour les essais de diffraction des rayons X au synchrotron Soleil.

mécaniques simples, mais avec une « gouttière » permettant l'utilisation d'éprouvettes dont les extrémités sont plus épaisses, tel un bourelet, ce qui permet de retenir l'éprouvette même si le contact entre les mors et la surface de l'éprouvette n'est plus assuré.

4. La conception du support des vérins adapté au diffractomètre de la ligne DiffAbs, la réalisation des plans techniques de fabrication et le montage de l'ensemble. Le dimensionnement des différentes pièces a été réalisé avec un outil commercial de conception assistée par ordinateur (CAO) et une brève étude de vibrations. Quant au choix des matériaux, la plaque principale de support des vérins a été réalisée en alliage d'aluminium afin de limiter le poids de la machine, et les autres pièces ont été réalisées en acier. Les vérins peuvent être montés sur la plaque avec différentes positions, en fonction de la taille de l'éprouvette testée.
5. La programmation du système de contrôle des vérins. Le langage de programmation utilisé, appelé MotionPerfect ®, est propre au système. Il a donc fallu l'apprendre avant de pouvoir programmer les différents essais. C'est aussi lors de cette étape qu'a été conçue la communication entre la machine de fatigue et le système de pilotage de la ligne DiffAbs, afin d'assurer la meilleure synchronisation possible.

La figure 1.2 montre la machine en place sur la ligne DiffAbs à Soleil et les fortes contraintes liées à l'encombrement de la machine lors de sa conception.

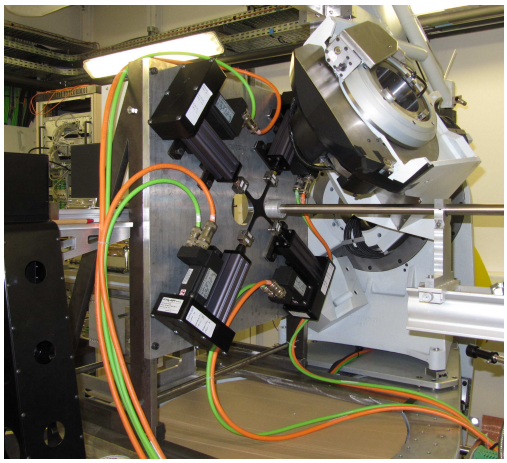

(a) Avant de la machine.

(b) Arrière de la machine avec au premier plan le détecteur MAR345.

FIGURE 1.2 – Machine de fatigue multiaxiale sur le ligne DiffAbs du synchrotron Soleil.

1.2 Conception d'une éprouvette biaxiale

Il n'existe pas d'éprouvettes standards pour réaliser des essais de traction équibiaxiale, comme c'est le cas pour les essais uniaxiaux, alors même que la géométrie de telles éprouvettes n'est pas triviale. En effet, si une simple éprouvette plane carrée est fixée dans quatre mors standards, alors le système est trop contraint et l'éprouvette ne peut pas être étirée en grandes déformations comme l'illustre le schéma de principe de la figure 1.3. Si une éprouvette plane cruciforme simple est utilisée, alors la déformation au point central de l'éprouvette est bien équibiaxiale, mais le niveau de déformation est très faible par rapport au niveau de déformation dans les bras de la croix. Une géométrie d'éprouvette plus complexe est donc nécessaire pour réaliser des essais de traction équibiaxiale.

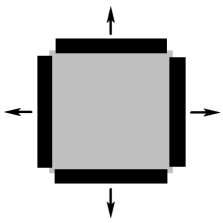

FIGURE 1.3 – Schéma de principe d'une éprouvette simple carrée. Celle-ci ne peut pas être étirée en grandes déformations avec 4 mors standards (représentés en noir).

1.2.1 Critères de conception

Le but de l'étude était de déterminer une géométrie d'éprouvette cruciforme répondant aux critères suivants :

1. niveau de déformation au centre de l'éprouvette le plus élevé possible et suffisant pour atteindre le seuil de cristallisation du caoutchouc ;
2. pas de rupture de l'éprouvette, notamment en dehors de la zone centrale ;
3. homogénéité de la déformation équibiaxiale sur une zone plus grande que la zone d'irradiation aux rayons X, c'est-à-dire prenant en compte la taille du faisceau synchrotron ainsi que son déplacement éventuel au cours du temps ;
4. respect des contraintes technologiques : encombrement, mise en œuvre, charge maximale des vérins ;
5. épaisseur au centre de la pièce suffisament petite pour obtenir un cliché de diffraction faiblement bruité après 5 secondes d'exposition aux rayons X, et suffisament grande pour ne pas endommager l'éprouvette lors de cette exposition.

La principale difficulté lors de cette étude a résidé dans les nombreuses inconnues liées aux critères cités ci-dessus. En effet, pour des raisons pratiques, il a été nécessaire de déterminer la géométrie des éprouvettes alors que la conception de la machine de traction était en cours, que les conditions expérimentales précises d'essais au synchrotron n'étaient pas encore déterminées et que le matériau n'avait pu être caractérisé. Ainsi, les inconnues étaient entre autres :

- la loi de comportement du matériau ;
- le seuil de cristallisation du matériau en traction uniaxiale et en traction équibiaxiale ;
- la taille minimale de la zone homogène nécessaire.

Pour cette raison, le but de l'étude était de trouver un « bon » compromis respectant au mieux l'ensemble des contraintes, sans appliquer de critères discriminants quantifiés. De plus, dans un souci de simplicité, aucun calcul d'optimisation n'a été effectué. L'étude qui suit a en partie été menée en collaboration avec deux étudiants de Master durant l'année 2009-2010.

1.2.2 Méthode expérimentale

Une étude bibliographique a permis de déterminer différentes solutions technologiques proposées par d'autres auteurs pour des essais sur métaux (Demmerle et Boehler, 1993; Hannon et Tiernan, 2008) et matériaux mous (Yu *et al.*, 2002; Waldman et Lee, 2005; Helfenstein *et al.*, 2010) ; ces solutions sont :

- un amincissement du centre de l'éprouvette ;
- un évidements des bras ;

– des bras de forme trapézoïdale, c'est-à-dire plus étroits vers le centre.

Finalement, nous avons retenu une croix simple à bras de largeur régulière. Dans un premier temps, nous avons déterminé la longueur des bras permettant de satisfaire le critère n° 3, c'est-à-dire des bras suffisamment longs pour respecter le principe de Saint-Venant. Dans un deuxième temps, nous avons aminci l'éprouvette au centre afin de satisfaire les critères n° 1,2 et 5.

La déformation des éprouvettes a été calculée par éléments finis avec le logiciel Abaqus ®. L'approche est exclusivement cinématique, les conditions aux limites sont données en déplacement. Nous avons utilisé des éléments finis linéaires, une loi de comportement néo-Hookéenne. Les plans de symétrie de l'éprouvette permettent de simuler un quart de celle-ci uniquement. Enfin, pour la première partie de l'étude, nous avons utilisé une représentation 2D de l'éprouvette en contrainte plane ; dans la deuxième partie une représentation 3D était nécessaire.

1.2.3 Mise en œuvre et résultats

Longueur de bras

Afin de choisir la plus petite longueur de bras permettant la meilleure homogénéité dans la zone centrale, nous avons d'abord établi trois critères d'homogénéité :

– biaxialité : la déformation est biaxiale si les termes hors-diagonaux du tenseur symétrique des déformations d'Euler-Almansi $\mathbf{e}$ (liés au cisaillement) sont faibles comparé aux termes de la diagonale (liés aux extensions) :

$$\sqrt{\left(\frac{e_{12}}{e_{11}}\right)^2 + \left(\frac{e_{12}}{e_{22}}\right)^2} \ll \epsilon, \tag{1.1}$$

– équibiaxialité : la déformation est équibiaxiale si les deux termes de la diagonale sont proches :

$$\sqrt{\frac{(e_{11} - e_{22})^2}{e_{11}^2 + e_{22}^2}} \ll \epsilon, \tag{1.2}$$

– niveau de déformation : la déformation est homogène si en tout point de la zone une mesure équivalente du niveau de déformation est proche de sa valeur au point central de l'éprouvette (unique point où la déformation est parfaitement équibiaxiale) :

$$\sqrt{\frac{\left(e_{11} - e_{11}^{\text{central}}\right)^2 + \left(e_{22} - e_{22}^{\text{central}}\right)^2}{\left(e_{11}^{\text{central}}\right)^2 + \left(e_{22}^{\text{central}}\right)^2}} \ll \epsilon, \tag{1.3}$$

où $\mathbf{e}^{\text{central}}$ est la déformation au point central de l'éprouvette.

Pour une longueur de bras donnée, l'homogénéité de la déformation au centre de l'éprouvette dépend du niveau de déformation imposé, donc des conditions limites. Ainsi, une première série de simulations a été réalisée afin de déterminer, pour cinq longueurs de bras différentes, les conditions aux limites nécessaires pour obtenir les mêmes niveaux de déformation au centre des éprouvettes. Ensuite, les trois critères d'homogénéité sont calculés pour les cinq géométries. La figure 1.4 (a) montre une éprouvette dans l'état non déformé et les figures 1.4 (b) à (d) montrent les niveaux d'homogénéité selon les trois critères (représentation dans l'état déformé). Enfin, la valeur maximale de chacun des trois critères

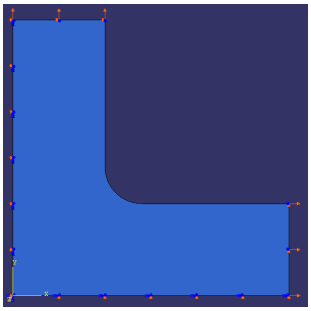

(a) Etat non déformé.

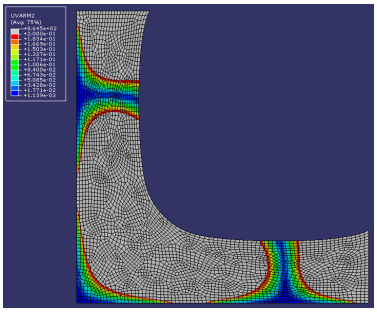

(b) Critère de biaxialité.

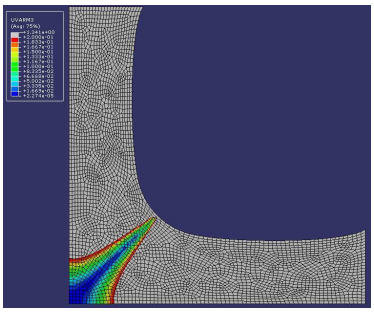

(c) Critère d'équibiaxialité.

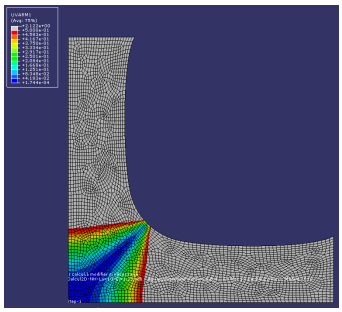

(d) Critère de niveau de déformation.

FIGURE 1.4 – Exemple de calcul des critères d'homogénéité.

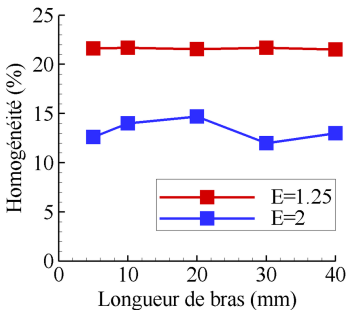

(a) Critère de biaxialité.

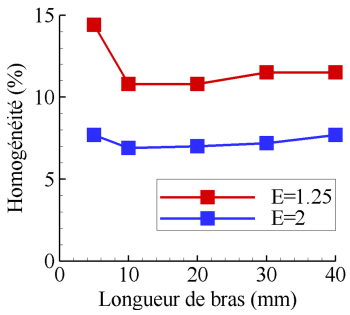

(b) Critère d'équibiaxialité.

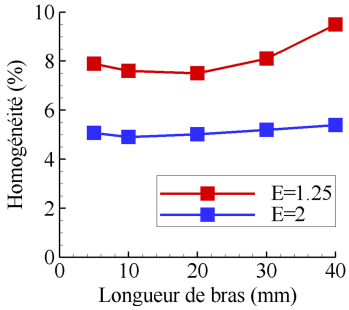

(c) Critère de niveau de déformation.

FIGURE 1.5 – Valeur maximale des trois critères d'homogénéité dans une zone de rayon 2 mm dans l'état non déformé au centre de l'éprouvette, pour deux niveaux de déformation locale E, en fonction de la longueur de bras de l'éprouvette cruciforme.

d'homogénéité dans une zone de rayon 2 mm dans l'état non déformé au centre de l'éprouvette a été relevé pour deux niveaux de déformation différents. La figure 1.5 montre ces valeurs pour les différentes longueurs de bras.

Finalement, la longeur de bras retenue au terme de cette première phase est la plus petite donnant de bons résultats, c'est-à-dire 10 mm.

Amincissement de la zone centrale

Compte tenu de la forme des iso-valeurs d'homogénéité au centre de l'éprouvette (voir fig. 1.4) et d'études précédentes sur les métaux (Demmerle et Boehler, 1993; Hannon et Tiernan, 2008), trois amincissements ont été étudiés :

- amincissement circulaire de 25 % de l'épaisseur initiale,
- amincissement circulaire de 50 % de l'épaisseur initiale,
- amincissement cruciforme de 50 % de l'épaisseur initiale.

La figure 1.6 montre deux des géométries étudiées. Pour chacun de ces amincissements, le

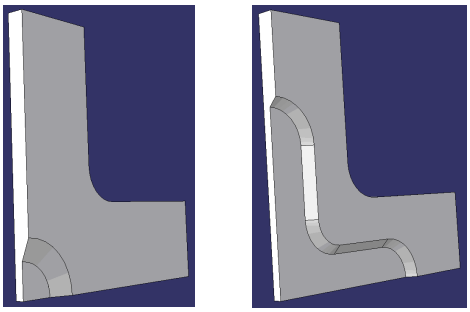

(a) Amincissement circulaire de 50 %.

(b) Amincissement cruciforme de 50 %.

FIGURE 1.6 – Deux amincissements étudiés, dans l'état non déformé.

niveau de déformation au point central de l'éprouvette est calculé en fonction des conditions aux limites en déplacement imposées. La figure 1.7 montre cette déformation en fonction de la déformation imposée aux bras. Les trois amincissements sont efficaces, puisque l'extension au centre de l'éprouvette est très proche de celle imposée aux bras. Si l'éprouvette était une simple croix ne présentant aucun amincissement, la déformation au centre serait très faible alors que les bras seraient eux très étirés.

L'amincissement retenu est celui permettant d'obtenir les plus grandes déformations locales, soit l'amincissement circulaire de 50 %.

Conclusion

Finalement, la géométrie retenue est présentée sur la figure 1.8. Le bourrelet à l'extrémité des bras permet simplement de fixer les éprouvettes dans les mors de la machine de fatigue biaxiale. Le respect du critère n° 4 (force de réaction dans les bras inférieure à la charge maximale des vérins, encombrement de l'éprouvette) a été vérifié a posteriori.

1.2.4 Déformations non équibiaxiales

La géométrie des éprouvettes a été déterminée uniquement dans le but de réaliser des essais de traction équibiaxiales. Mais après la réalisation des éprouvettes, nous avons constaté que celles-ci pouvaient également être utilisées pour obtenir des déformations non

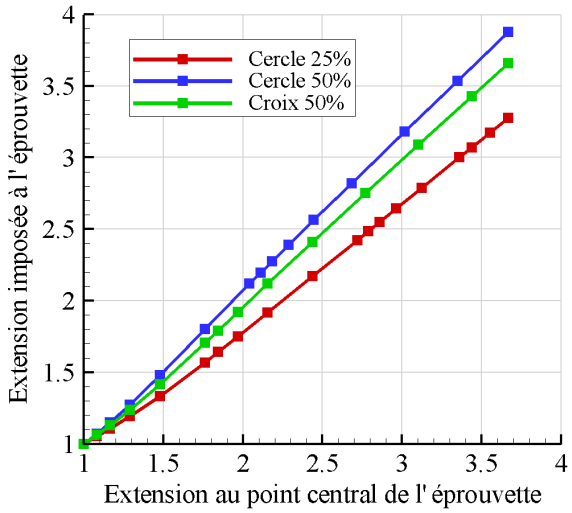

FIGURE 1.7 – Déformation locale au point central de l'éprouvette en fonction de la déformation globale appliquée aux bras, pour trois géométries d'amincissement différentes.

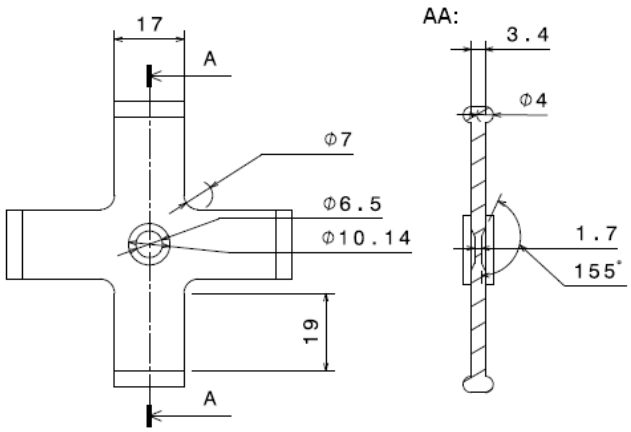

FIGURE 1.8 – Géométrie d'éprouvette retenue pour les essais en déformation multiaxiale.

équibiaxiales en imposant des déplacements différents aux bras non opposés deux à deux. Ainsi, en imposant un déplacement plus faible à deux bras opposés qu'aux deux autres bras, la déformation au centre de l'éprouvette est biaxiale mais non équibiaxiale. Si seuls deux bras opposés sont étirés alors que les deux autres sont uniquement maintenus dans leur position initiale, alors l'état de déformation au centre de l'éprouvette est intermédiaire entre la traction uniaxiale et le cisaillement pur. Le tenseur de déformation au centre de l'éprouvette en fonction du déplacement imposé des bras a été mesuré expérimentalement en filmant les essais de traction et grâce au logiciel de suivi de points Tema motion ®. Comme en déformation équibiaxiale l'homogénéité de la déformation est très peu influencée par la longueur des bras de l'éprouvette (voir fig. 1.5), nous avons estimé que la taille de la zone homogène de déformation était peu influencée par la non-équibiaxialité de la déformation imposée à l'éprouvette.

1.3 Méthode d'analyse des clichés de diffraction

1.3.1 Préambule

Les essais de diffraction des rayons X réalisés au synchrotron Soleil en septembre 2010 dans le cadre de ma thèse étaient les premiers essais de diffraction (de rayonnement synchrotron ou non) réalisés par l'équipe Matériaux, Procédés et Technologie des Composites de l'Institut de Recherche en Génie Civile et Mécanique (GeM) à laquelle j'appartiens. L'analyse de clichés de diffraction ne faisait donc pas partie des compétences de l'équipe et une grande partie de ma thèse a été consacrée à l'acquisition de ces connaissances et compétences. J'ai donc choisi de développer mon propre outil d'analyse des clichés de diffraction afin d'acquérir une expertise et d'en maîtriser toutes les étapes. Ainsi, plutôt que d'utiliser l'un des nombreux logiciels libres ou commerciaux tels que Fityk ou PeakFIT ® couramment employés pour l'analyse de diffractogrammes, j'ai préféré écrire intégralement un programme Matlab ® d'analyse de clichés de diffraction. Ceci a représenté un investissement en temps très important mais m'a permis de contrôler chaque étape de l'analyse et m'a amené à avoir un regard critique sur les méthodes proposées dans la littérature et celle utilisée pour ma thèse.

Dans cette partie, je présente dans un premier temps la méthodologie retenue pour l'analyse des clichés de diffraction. Puis dans un deuxième temps, j'apporte une analyse critique de cette méthodologie et des différentes grandeurs mesurées. Par souci de concision, la théorie de la diffraction des rayons X par les matériaux cristallins et semi-cristallins, ainsi que les différents travaux théoriques qui s'y rapportent ne sont pas expliqués ici. En effet, le lecteur pourra facilement, si nécessaire, se référer à divers ouvrages comme par exemple l'ouvrage de référence de Guinier (1963).

1.3.2 Méthodologie

La figure 1.9 montre un exemple de cliché de diffraction obtenu au synchrotron Soleil, avant tout traitement de données. Il s'agit d'une matrice d'intensité, réalisée à partir d'un détecteur CCD (Charge Coupled Device ou dispositif à transfert de charges) de type MAR345 qui est un détecteur circulaire de diamètre 345 mm. La taille de la matrice est 1024 pixels. A partir d'un tel cliché de diffraction, plusieurs traitements de données successifs sont nécessaires pour finalement obtenir les informations voulues sur la phase cristallisée du NR.

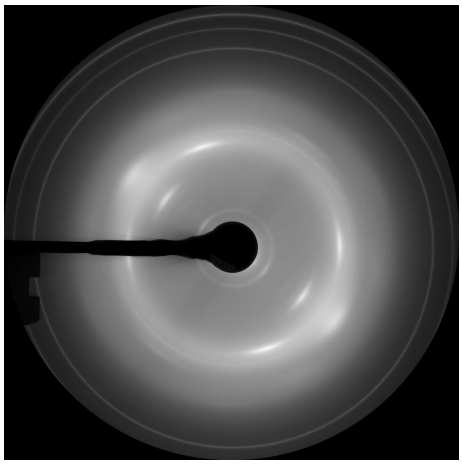

FIGURE 1.9 – Exemple de cliché de diffraction d'un NR chargé au noir de carbone en traction uniaxiale, avant tout traitement de données.

Correction des clichés

Lors d'un essai de diffraction des rayons X, l'intensité de photons diffractés mesurée par un détecteur en aval de l'éprouvette dépend d'un grand nombre de facteurs :

- les caractéristiques cristallographiques de l'éprouvette : c'est ce que l'on cherche à mesurer ;
- la diffusion des photons par l'air ;
- l'intensité du faisceau de photons incidents ;
- l'épaisseur de l'éprouvette ;
- les conditions expérimentales, comme par exemple la sensibilité de chaque cellule du détecteur et la diffraction de photons par les bords du « beam-stop » utilisé pour absorber les photons transmis par l'éprouvette.

Or, ces facteurs varient d'un essai à l'autre. Pour comparer les résultats des différents essais et conclure quant aux caractéristiques de la phase cristallisée du matériau, il est donc nécessaire de d'abord corriger les clichés de diffraction enregistrés par le détecteur.

Pour cela, nous utilisons une méthode détaillée dans l'Annexe A. Pour réaliser cette correction, on considère trois expériences : l'une avec une éprouvette dans l'état déformé d'épaisseur d, qui est l'expérience principale, une autre sans éprouvette et une troisième avec une éprouvette dans l'état non déformé d'épaisseur d_0, ces deux dernières étant des essais de référence. La figure 1.10 schématise les expériences avec éprouvette. L'intensité du faisceau de photons, arrivant par la gauche, est mesurée par la diode PIN (Positive Intrinsic Negative) 1. Une partie de ces photons est transmise à la diode PIN 2. L'autre partie est diffusée par l'air et diffractée par l'éprouvette si elle est présente, son intensité est mesurée par le détecteur.

Les calculs sont largement inspirés par ceux de Ran *et al.* (2001). On note que la différence principale entre le cas étudié ici et le cas étudié par Ran *et al.* est la présence de la diode PIN 1 à une distance non-nulle de l'échantillon. Les détails du calcul sont présentés dans l'Annexe A.

Résumons les notations introduites :

- I_1^{SE}, I_1^{AE}, I_1^{NE}, I_1^{E} : intensité incidente mesurée par la diode PIN 1 dans les cas sans éprouvette (SE), avec une éprouvette (AE), avec une éprouvette non étirée (NE) et avec une éprouvette étirée (E) ;
- I_2^{SE}, I_2^{AE}, I_2^{NE}, I_2^{E} : intensité mesurée par la diode PIN 2 dans les cas sans éprouvette

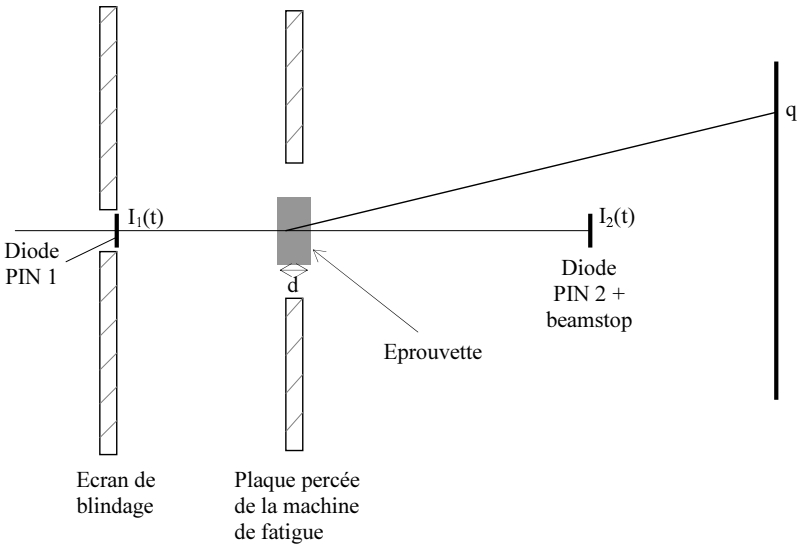

FIGURE 1.10 – Expérience avec éprouvette, dans l'état déformé ou non déformé.

(SE), avec une éprouvette (AE), avec une éprouvette non étirée (NE) et avec une éprouvette étirée (E) ;
- $I_{\mathrm{d}}^{\mathrm{SE}}(q)$, $I_{\mathrm{d}}^{\mathrm{AE}}(q)$: intensité mesurée par le détecteur dans les cas sans éprouvette (SE) et avec une éprouvette (AE) en chaque point q du détecteur ;
- d_0, d : épaisseur initiale de l'éprouvette et épaisseur lors de l'essai principal ;
- 2θ : angle de diffraction, appelé angle de Bragg.

Dans un premier temps, on corrige le cliché de diffraction, c'est-à-dire l'intensité $I_{\mathrm{d}}^{\mathrm{AE}}(q)$, de la diffusion des photons par l'air et du bruit expérimental. Avec les notations introduites, la diffraction « corrigée » $\mathcal{S}(q)$ est donnée par :

$$\mathcal{S}(q) = \frac{d_0}{d}\left[\frac{I_d^{\mathrm{AE}}(q)}{I_2^{\mathrm{AE}}} - \frac{I_d^{\mathrm{SE}}(q)}{I_2^{\mathrm{SE}}}\right]. \tag{1.4}$$

Cette dernière est fonction des intensités mesurées par le détecteur et par la diode PIN 2 au cours de l'essai et lors d'un essai de référence sans éprouvette, de l'épaisseur initiale de l'éprouvette d_0 et de son épaisseur d au moment de l'essai qui est inconnue.

Dans un deuxième temps, il est nécessaire de corriger l'intensité du faisceau incident qui varie légèrement au cours des quelques jours d'essai au synchrotron et de calculer l'épaisseur de l'éprouvette d en fonction des différentes intensités mesurées par les diodes PIN. Finalement, le cliché de diffraction utilisé pour mesurer les caractéristiques cristallographiques du matériau est donné par l'intensité corrigée :

$$\mathcal{S}'(q) = \frac{\ln\left(\frac{I_2^{\mathrm{SE}}/I_1^{\mathrm{SE}}}{I_2^{\mathrm{NE}}/I_1^{\mathrm{NE}}}\right)}{\ln\left(\frac{I_2^{\mathrm{SE}}/I_1^{\mathrm{SE}}}{I_2^{\mathrm{E}}/I_1^{\mathrm{E}}}\right)}\left(\frac{I_d^{\mathrm{AE}}(q)}{I_2^{\mathrm{AE}}} - \frac{I_d^{\mathrm{SE}}(q)}{I_2^{\mathrm{SE}}}\right), \tag{1.5}$$

où I_1^{SE}, I_2^{SE} et $I_d^{\mathrm{SE}}(q)$ sont mesurées lors d'un même essai de référence sans éprouvette, I_1^{NE} et I_2^{NE} sont mesurées lors d'un deuxième essai de référence avec une éprouvette non étirée (en réalité, deux essais : l'un avec une éprouvette uniaxiale et l'autre avec une éprouvette biaxiale selon les clichés qui doivent être corrigés), et enfin I_1^{E}, I_2^{E}, I_2^{AE} et $I_d^{\mathrm{AE}}(q)$ sont les mesures effectuées durant l'essai que l'on cherche à analyser.

En pratique, pour réaliser cette correction, les étapes suivantes sont réalisées par le programme Matlab :

– analyse géométrique d'une image avec éprouvette afin de déterminer *(i)* la position du faisceau incident de photons, donné par le centre des anneaux de diffraction du ZnO présent dans le matériau (voir fig. 1.9) et *(ii)* la distance entre le détecteur et l'éprouvette, donnée par la position de ces anneaux ;
– transformation de toutes les images (avec et sans éprouvette) en coordonnées polaires grâce aux paramètres déterminés précédemment. On note qu'il n'est pas possible de déterminer le centre du faisceau sur une image sans éprouvette. On suppose donc que le faisceau ne s'est pas déplacé entre l'essai de référence sans éprouvette et l'essai traité ;
– correction du bruit expérimental, de l'épaisseur de l'éprouvette, de la diffusion de l'air et de la variation d'intensité de photons incidents en tout point du cliché de diffraction, selon l'équation (1.5).

Identification et modélisation des différentes phases en présence

A l'issue de l'étape de correction, les données expérimentales consistent en une carte d'intensité que nous noterons par la suite $I(\beta, 2\theta)$ où β est l'angle azimuthal et 2θ l'angle de Bragg de diffraction comme le montre la figure 1.11.

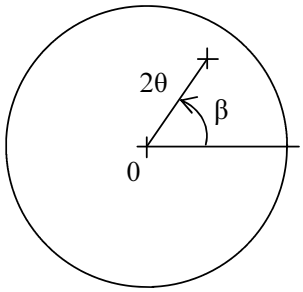

FIGURE 1.11 – Définition de l'angle de Bragg 2θ et de l'angle azimuthal β.

Réduction du problème Les clichés de diffraction du NR en traction uniaxiale ou multiaxiale présentent deux symétries par réflexion, les axes de symétrie étant la direction principale de traction et la normale à cette direction. Ces symétries sont utilisées pour réduire les données et les axes de symétrie sont identifiés à chaque essai. Cependant, le cliché n'est pas réduit à un quart de cercle. En effet, cela aurait pour conséquence de couper de nombreuses taches de diffraction qui seraient alors beaucoup plus difficiles à modéliser par la suite. Le cliché est donc réduit à un intervalle d'angle azimuthal de 100° à 120° selon l'étalement des taches de diffraction.

De plus, les données aux petits et aux grands angles de Bragg 2θ sont également supprimés pour conserver l'intervalle $2\theta = [8°; 27,1°]$.

Séparation des contributions isotrope et anisotrope L'intensité $I(\beta, 2\theta)$ est séparée en deux contributions, l'une isotrope $I_{iso}(2\theta)$ et l'autre anisotrope $I_{aniso}(\beta, 2\theta)$, selon les méthodes de Nogales *et al.* (2001), et Ran *et al.* (2001) : pour chaque valeur de 2θ, on cherche le minimum de $I(\beta, 2\theta)$ sur tout l'intervalle de β, qui est l'intensité isotrope I_{iso}. Ensuite, I_{aniso} est la différence entre I et I_{iso} :

$$I(\beta, 2\theta) = I_{iso}(2\theta) + I_{aniso}(\beta, 2\theta). \tag{1.6}$$

En pratique, le maillage initial des clichés de diffraction est carré puis est décrit en coordonnées polaires pour séparer les phases isotrope et anisotrope. Pour des raisons numériques, le minimum de $I(\beta, 2\theta)$ n'est donc pas recherché pour chaque valeur de 2θ mais pour des intervalles de 2θ. La taille de cet intervalle doit être fixée avec précaution : s'il est trop petit la fonction $I_{aniso}(\beta)$ est définie par un nombre de points trop faible, s'il est trop grand c'est alors la fonction $I_{iso}(2\theta)$ qui est mal définie.

Extraction et déconvolution des spectres A ce stade, il est possible d'extraire différents spectres de diffraction :

- $I(\beta)$ et $I_{aniso}(\beta)$ pour différents intervalles de 2θ ;
- $I(2\theta)$, $I_{aniso}(2\theta)$ et $I_{iso}(2\theta)$ pour différents intervalles de β.

Comme précédemment, les spectres ne peuvent pas être définis pour une seule valeur de 2θ ou β ; ils sont définis pour des intervalles de petites tailles de 2θ et β. La taille de ces intervalles, c'est-à-dire l'unité du repère polaire créé à partir du repère cartésien initial, est un compromis :

- si les intervalles sont très petits, alors certaines mailles du maillage polaire ne contiennent aucun noeud du maillage initial ; les fonctions d'intensité sont alors définies par un nombre de points trop faible ;
- si les intervalles sont très grands, alors chaque maille contient un très grand nombre de noeuds ; les fonctions sont alors lissées car les extrema locaux sont moyennés avec des points très éloignés donc d'intensités très différentes.

En pratique, la taille des intervalles en 2θ est environ $0,04°$, soit environ 500 intervalles pour définir la portion de cercle comprise dans $[8° ; 27,1°]$, la taille des intervalles en β est environ $0,6°$, soit environ 160 intervalles pour définir le quart de cercle. Pour chaque cliché, il existe autant de spectres que d'intervalles.

Ensuite, les spectres sont classiquement modélisés par des sommes de fonction de Pearson VII (Saintier, 2000; Rouvière *et al.*, 2007) qui sont définies par :

$$p(x) = \frac{1}{\left(1 + \left(\frac{(x-position)*2^{2/m}}{largeur}\right)^2\right)^m}, \tag{1.7}$$

où *position* est l'abscisse du centre de la fonction, $largeur$ est la demi-largeur de la fonction et m est un paramètre de forme. Le paramètre m détermine l'étalement du pied de la fonction. Pour limiter la taille des problèmes à résoudre lors de la modélisation des spectres, m n'est pas considéré comme un paramètre ; on fixe $m = 2$, cette valeur étant le meilleur compromis pour une trentaine de spectres testés très variés : déformations uniaxiales et biaxiales, matériau faiblement et fortement cristallisé, spectres en 2θ et en β. Par ailleurs, j'ai observé que la meilleure valeur de m varie avec la formulation et/ou le procédé de réticulation du NR étudié.

Des détails sur la modélisation des spectres seront apportés par la suite, où de nombreux exemples seront donnés. Toutefois, le lecteur peut voir un exemple de modélisation et déconvolution de spectres sur la figure 1.14, qui sera commentée par la suite. De plus, ces spectres illustrent la séparation en phases isotrope et anisotrope : la figure 1.14 (a) représente l'intensité totale, qui est la somme des intensités isotrope et anisotrope présentées sur les figures 1.14 (b) et (c) respectivement.

Identification des phases en présence Une fois l'ensemble des spectres modélisés et déconvolués, il est nécessaire d'identifier les différentes phases en présence dans le matériau. Le NR étant un matériau semi-cristallin, il co-existe une phase cristallisée et une phase

amorphe. Chacune de ces phases peut être orientée ou non-orientée. Plusieurs auteurs ont montré que le taux de phase amorphe orientée dans le NR est très faible (Toki *et al.*, 2002; Murakami *et al.*, 2002). Comme elle est également difficile à mesurer, nous avons décidé de ne pas la quantifier. Par ailleurs, il est établi qu'en traction uniaxiale, la phase cristallisée est fortement orientée. Dans ce cas, la phase cristallisée correspond donc à I_{aniso} et la phase amorphe à I_{iso}. Dans le cas des déformations équibiaxiales, la phase cristallisée est elle aussi isotrope (comme nous le montrerons au Chapitre 4) et ne peut donc pas être séparée simplement de la phase amorphe. Dans ce cas, la modélisation des spectres est réalisée directement à partir de l'intensité totale $I(\beta, 2\theta)$. Cependant, l'identification des phases cristallisée et amorphe ne pose pas de problème, comme cela sera montré au Chapitre 4. De plus, d'autres taches et pics sont visibles sur les clichés et les spectres de diffraction, qui proviennent des adjuvants du NR tels que le ZnO et l'acide stéarique, et sont eux aussi identifiés en fonction de leurs angles de Bragg.

Mesures des caractéristiques cristallographiques du NR

La figure 1.12 montre l'exemple d'un cliché de diffraction corrigé en traction uniaxiale sur lequel les différents pics de diffraction ont été identifiés. A partir de l'intensité et des

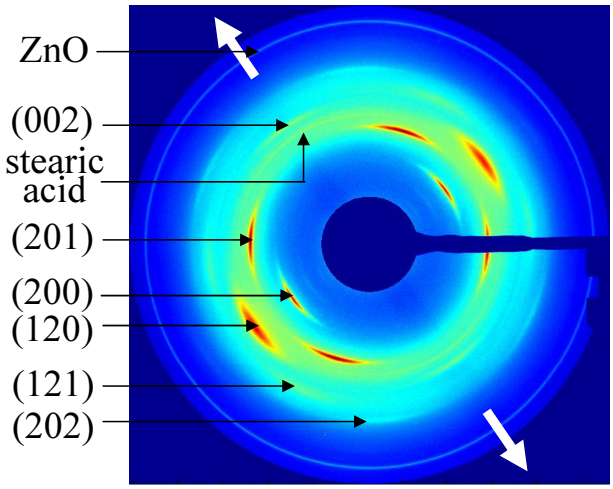

FIGURE 1.12 – Exemple d'un cliché de diffraction corrigé en traction uniaxiale, les différents pics de diffraction sont identifiés par leurs indices de Miller. La direction de traction est montrée par les flèches blanches.

paramètres de forme de ces différentes taches, il est possible de mesurer les caractéristiques cristallographiques du matériau :

- l'angle de Bragg 2θ du point d'intensité maximale des taches permet de calculer la distance interreticulaire d_{hkl} des plans de diffraction (hkl) associés, puis d'en déduire les paramètres de maille ;
- l'angle azimuthal β du centre des taches donne l'orientation moyenne des cristallites dans le matériau ;
- la largeur à mi-hauteur en 2θ des taches permet de calculer la taille des cristallites ;
- la largeur à mi-hauteur en β donne la variation de l'orientation des cristallites ;
- enfin, le taux de cristallinité est mesuré à partir de l'intégrale des intensités.

Ces différentes mesures sont schématisées sur la figure 1.13 et expliquées aux paragraphes suivants. La justification des calculs réalisés sera présentée dans la partie suivante « Analyse critique des grandeurs mesurées ».

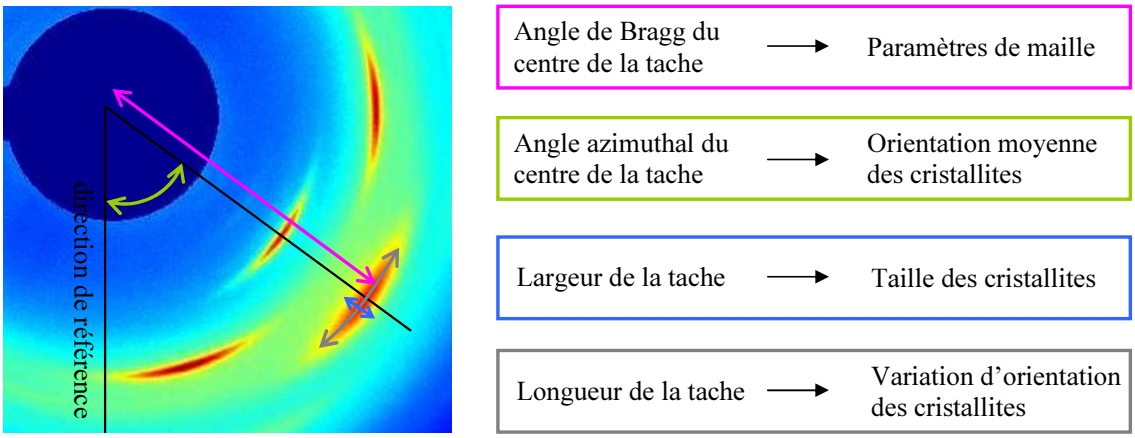

FIGURE 1.13 – Représentation schématique des différents paramètres cristallographiques mesurés à partir d'un cliché de diffraction.

Paramètres de maille A ce jour, il n'y a pas de concensus sur le type de maille du caoutchouc naturel cristallisé sous contrainte, celle-ci étant décrite soit comme monoclinique (Bunn, 1942; Takahashi et Kumano, 2004) soit comme orthorombique (Immirzi *et al.*, 2005; Rajkumar *et al.*, 2006). Ici, nous avons choisi de nous baser sur les études les plus récentes, celles de Immirzi *et al.* (2005) et Rajkumar *et al.* (2006), qui montrent que la maille est orthorombique, c'est-à-dire de forme parallépipédique rectangle.

Pour déterminer les paramètres de maille, qui sont les trois dimensions a, b et c de ce parallépipède, on détermine la distance interreticulaire d_{hkl} de chaque plan cristallin :

$$d_{hkl} = \lambda/2 \sin\theta, \tag{1.8}$$

où λ est la longueur d'onde et θ est l'angle de Bragg du centre de la tache de diffraction (hkl), c'est-à-dire de la position de la fonction de Pearson modélisant le pic (hkl). Ensuite, les paramètres a, b et c sont calculés grâce à la relation entre distance interreticulaire, indices de Miller et paramètres de maille :

$$d_{hkl} = \sqrt{\frac{1}{\frac{h^2}{a^2} + \frac{k^2}{b^2} + \frac{l^2}{c^2}}}. \tag{1.9}$$

Taille et volume des cristallites A partir de la largeur à mi-hauteur ($\mathrm{LMH}_{2\theta}$) en 2θ des taches (hkl), l'équation de Scherrer permet de calculer la taille moyenne des cristallites l_{hkl} dans la direction normale aux plans (hkl) :

$$l_{hkl} = \frac{k\lambda}{\mathrm{LMH}_{2\theta} \cos\theta}, \tag{1.10}$$

où k est un paramètre de forme.

Un indice du volume moyen des cristallites est donné par :

$$\overline{V} = l_{200} \cdot l_{201} \cdot l_{120} \tag{1.11}$$

Variation d'orientation des cristallites La variation d'orientation des cristallites par rapport à leur orientation moyenne est simplement donnée par :

$$\psi_{hkl} = \mathrm{LMH}_{\beta}/2, \tag{1.12}$$

où ψ_{hkl} est la désorientation moyenne des plans (hkl) et LMH_{β} est la largeur à mi-hauteur des pics (hkl) en angle azimuthal β.

Indice de cristallinité Deux indices de cristallinité différents sont mesurés : un indice simple χ et un indice plus long à calculer χ'. L'indice χ est calculé à partir des deux spectres extraits à l'angle de Bragg passant par les taches intenses (120) et (200) :

$$\chi = \frac{\int_{2\theta} I_{crist}}{\int_{2\theta} I_{crist} + \int_{2\theta} I_{amorphe}}, \tag{1.13}$$

où $\int_{2\theta} I_{crist}$ et $\int_{2\theta} I_{amorphe}$ sont les intégrales linéaires sur 2θ de l'intensité des pics des phases cristallisée et amorphe respectivement. Cet indice est proportionnel au taux de cristallinité du matériau. Cependant, l'indice de proportionnalité varie avec la forme des reflections sur les clichés et donc avec la multiaxialité de la déformation : pour un même taux de cristallinité, un anneau sera beaucoup moins intense qu'une tache très localisée car l'intensité est répartie sur une surface du cliché beaucoup plus grande. Pour cette raison, il peut être nécessaire de considérer l'indice χ', qui lui est calculé à partir de la modélisation de tous les spectres en 2θ du cliché :

$$\chi' = \frac{\iint_{\beta,2\theta} I_{crist}}{\iint_{\beta,2\theta} I_{crist} + \iint_{\beta,2\theta} I_{amorphe}}, \tag{1.14}$$

où $\iint_{\beta,2\theta} I_{crist}$ et $\iint_{\beta,2\theta} I_{amorphe}$ sont les intégrales surfaciques (en β et 2θ) de l'intensité des pics des différentes phases.

Nombre de cristallites par unité de volume On calcule un indice du nombre de cristallite par unité de volume irradié :

$$N = \chi \frac{\pi R^2}{\overline{V}} \frac{d_0}{\sqrt{\lambda}}, \tag{1.15}$$

où R est le rayon du faisceau de photons à mi-hauteur, λ l'extension de l'éprouvette et d_0 l'épaisseur de l'éprouvette dans l'état non déformé.

1.3.3 Analyse critique des grandeurs mesurées

Modélisation des spectres

Si la modélisation des spectres par des sommes de fonction de Pearson est en théorie très simple, on constate en pratique de nombreuses difficultés. Différentes méthodes sont employées dans la littérature, pouvant aboutir à des résultats parfois très différents pour un même cliché de diffraction. Pour comparer les différents résultats expérimentaux obtenus, il est bien sûr nécessaire d'utiliser la même méthode d'analyse. Mais la méthode la plus satisfaisante est aussi la plus longue à appliquer : une journée de travail complète est nécessaire pour analyser un seul cliché de diffraction. Aussi, j'ai choisi d'utiliser différentes méthodes en fonction de la précision souhaitée. Pour chaque article présenté ci-après, tous les résultats ont été obtenus avec une même méthode d'analyse, cependant cette méthode varie d'un article à l'autre.

Dans cette partie, j'expose les différentes méthodes et leurs avantages et inconvénients respectifs. Pour illustrer mes propos, j'ai choisi de montrer les résultats obtenus pour un essai de traction uniaxiale quasi-statique sur du NR chargé au noir de carbone (il s'agit de l'essai présenté au Chapitre 3). Pour chaque cliché de diffraction, les spectres sont extraits aux angles azimuthaux des taches (120) et (200). L'extension λ de l'éprouvette, et donc le taux de cristallinité du matériau, varient selon les exemples choisis.

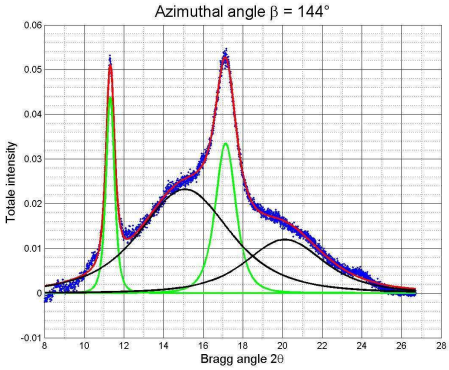

(a) Intensité totale.

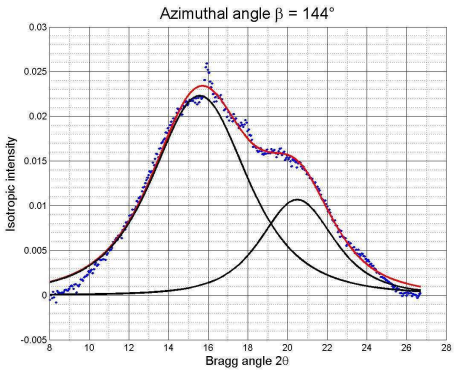

(b) Intensité isotrope.

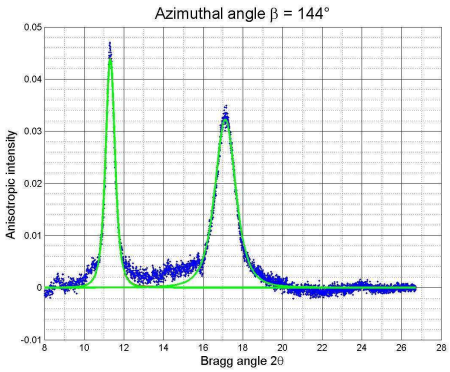

(c) Intensité anisotrope.

FIGURE 1.14 – Exemple de modélisation et déconvolution pour un même cliché : (a) en modélisant directement l'intensité totale ou (b)-(c) en séparant d'abord les phases isotrope et anisotrope. Légende : points bleus = données expérimentales, courbes noires = fonctions attribuées à la phase amorphe, courbes vertes = fonctions attribuées à la phase cristallisée, courbes rouges = somme des fonctions.

Premièrement, la figure 1.14 donne deux exemples de modélisation de spectres : un spectre d'intensité totale directement extrait du cliché (fig. 1.14 (a)) et deux spectres extraits après séparation des phases isotrope et anisotrope (fig. 1.14 (b) et (c)). Pour cet exemple, où le taux de cristallinité est très élevé, les deux méthodes donnent des résultats identiques et satisfaisants. Cependant, on observe sur la fig. 1.14 (b) une première difficulté : la modélisation du petit pic d'acide stéarique à l'angle $2\theta \approx 16°$, qui est très fin et peu intense. La figure 1.15 montre un exemple de déconvolution de spectre d'intensité isotrope, avec ou non une fonction attribuée à l'acide stéarique. Dans le cas de la fig. 1.15 (b), c'est-à-dire avec un troisième fonction représentant le pic d'acide stéarique, la convergence du programme Matlab est très longue (temps de calcul multiplié par 5 environ par rapport au cas de la figure 1.15 (a)). Mais surtout on observe que dans ce cas la modélisation de la phase amorphe du NR n'est pas améliorée : l'intensité maximale de la phase amorphe (à $2\theta \approx 15.6°$) est surestimée de la même manière, que l'acide stéarique soit représenté par une troisième fonction ou non. Pour cette raison, nous avons choisi par la suite de ne pas attribuer de fonction à ce pic. Cette difficulté n'apparaît pas dans le cas du spectre d'intensité totale (fig. 1.14 (a)) car le pic d'acide stéarique est alors masqué par le pic (120) de NR.

Lorsque le taux de cristallinité est plus faible, la déconvolution des différentes fonctions

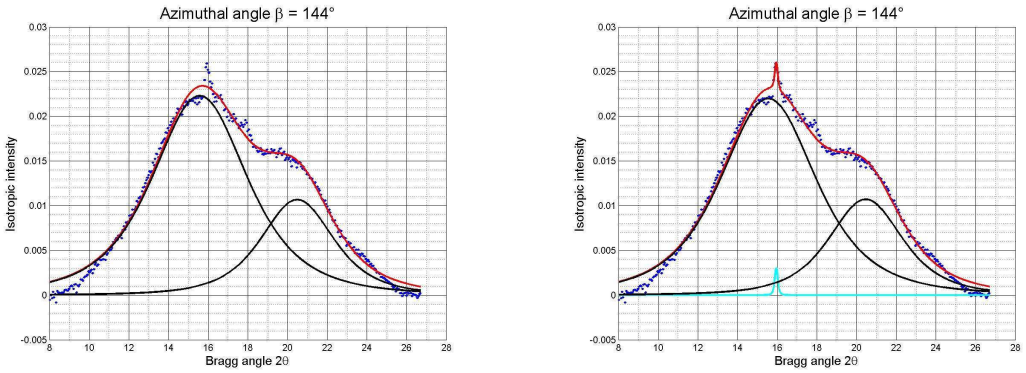

(a) (b)

FIGURE 1.15 – Modélisation du spectre d'intensité isotrope : (a) sans pic d'acide stéarique et (b) avec un pic d'acide stéarique. Légende : points bleus = données expérimentales, courbes noires = fonctions attribuées à la phase amorphe, courbe cyan = fonction attribuée à l'acide stéarique, courbes rouges = somme des fonctions.

à partir d'un spectre d'intensité totale est parfois difficile à réaliser. La figure 1.16 (a) montre par exemple la modélisation d'un spectre d'intensité totale ; la somme des fonctions attribuées à la phase amorphe est représentée par la courbe cyan. Or, celle-ci est

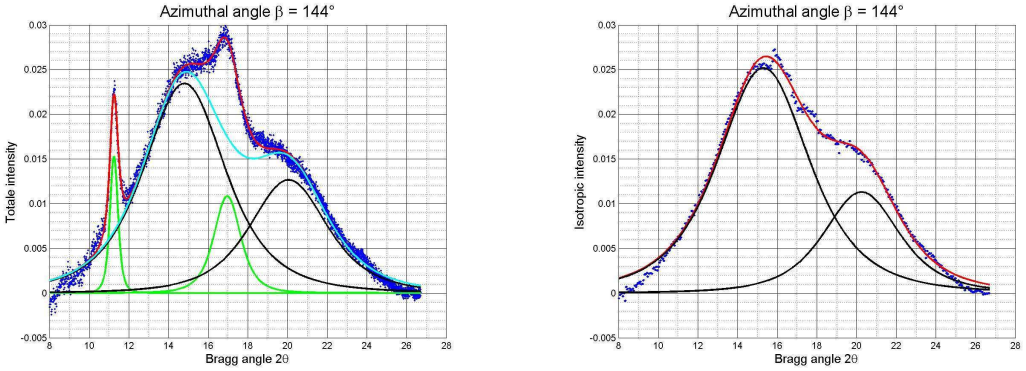

(a) (b)

FIGURE 1.16 – Modélisation de l'intensité de la phase amorphe à partir (a) du spectre d'intensité totale et (b) du spectre d'intensité isotrope. Légende : points bleus = données expérimentales, courbes noires = fonctions attribuées à la phase amorphe, courbe cyan = somme des fonctions attribuées à la phase amorphe, courbes vertes = fonctions attribuées à la phase cristallisée, courbes rouges = somme des fonctions.

largement sous-estimée (à $2\theta \approx 18°$) au profit de la phase cristallisée, comme le montre la figure 1.16 (b) qui représente le spectre d'intensité isotrope extrait du même cliché. En effet, dans le cas de la traction uniaxiale, l'intensité isotrope est due uniquement à la phase amorphe du NR ; les courbes noires sur les fig. 1.16 (a) et (b) devraient donc être identiques, ce qui n'est pas le cas.

La modélisation des spectres d'intensité totale pose également problème lorsque le taux de cristallinité est très faible comme le montre la figure 1.17. En effet, sur la figure 1.17 (a), le pic (120) de NR n'est pas visible sur le spectre d'intensité totale, alors qu'il est visible sur le spectre d'intensité anisotrope de la figure 1.17 (b), bien que ces spectres soient extraits du même cliché. Ainsi, la déconvolution du spectre d'intensité totale conduit à une forte

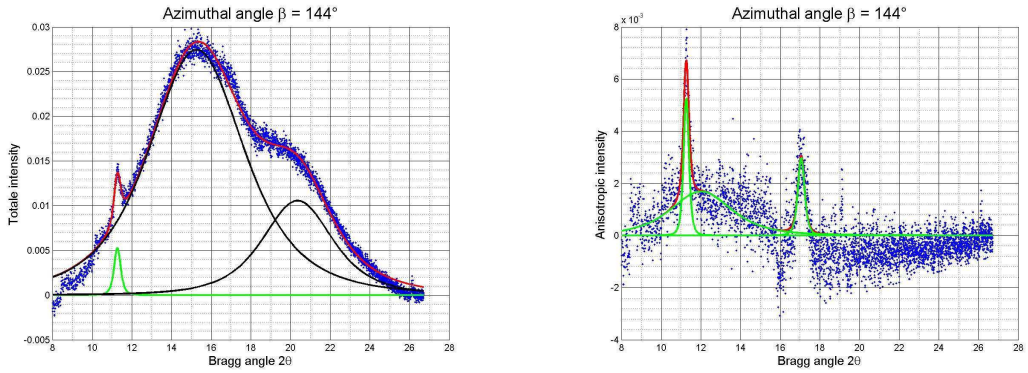

(a) (b)

FIGURE 1.17 – Modélisation de l'intensité de la phase cristallisée à partir (a) du spectre d'intensité totale et (b) du spectre d'intensité isotrope.

sous-estimation de la phase cristallisée du NR.

Lors de la modélisation de spectres de diffraction, certains auteurs suppriment ce que l'on appelle couramment la « baseline », c'est-à-dire une fonction souvent linéaire qui est soustraite du spectre afin que l'intensité finale soit nulle aux extrémités de l'intervalle de 2θ étudié (Marchal, 2006; Rouvière *et al.*, 2007). C'est ce qui a été fait pour tous les spectres montrés jusqu'ici. Cette pratique se justifie principalement pour des raisons mathématiques, puisque les fonctions de Pearson sont des fonctions qui tendent vers 0 en $\pm\infty$. Cependant, la suppression de cette fonction à deux inconvénients majeurs : *(i)* elle conduit à une sous-estimation importante de la phase amorphe en réduisant de près de 50 % l'intensité totale et *(ii)* elle modifie la forme des différents pics en introduisant une réduction non symétrique de l'intensité, ce qui peut rendre la modélisation et la déconvolution plus difficile. J'ai donc choisi de ne pas supprimer cette baseline, mais de la modéliser en même temps que les autres fonctions. Pour des raisons pratiques, j'ai choisi de la modéliser par une fonction de Pearson VII également. En effet, il n'existe pas d'argument lié à un phénomène physique justifiant l'emploi d'une fonction mathématique particulière. De plus, on observe que la forme de la fonction - de Pearson, linéaire ou gaussienne - ne modifie pas le résultat final. La déconvolution de la baseline peut être réalisée sur tous les spectres, d'intensité totale, isotrope et anisotrope, comme le montre la figure 1.18. On note que l'intensité de la baseline est très élevée par rapport à l'intensité totale de la phase amorphe - près de 50 %. Ceci est principalement dû au fait que l'intervalle de 2θ étudié ici est petit par rapport aux angles de diffusion de la phase amorphe du NR. Si l'intervalle était plus grand, on observerait une décroissance progressive de l'intensité aux extrémités du spectre. Ici, on mesure uniquement le « sommet » de la fonction de diffusion de la phase amorphe.

La conservation de la baseline lors de la modélisation et de la déconvolution des spectres introduit une nouvelle difficulté. En effet, comme pour les autres fonctions, il est nécessaire d'attribuer la baseline à l'une des phases en présence dans le matériau. Dans le cas des spectres d'intensité totale et d'intensité isotrope, il est assez naturel de l'attribuer à la phase amorphe du NR. Mais la présence d'une baseline non nulle dans les spectres d'intensité anisotrope peut s'expliquer de deux manières :

- il peut s'agir d'un artefact lié à la méthode expérimentale, par exemple à la diffusion des photons dû au bord du beam-stop. Cette hypothèse est confortée par le fait qu'une telle anisotropie est également visible lorsque le matériau n'est pas étiré ;
- cette diffusion anisotrope peut également être due à une phase amorphe orientée du

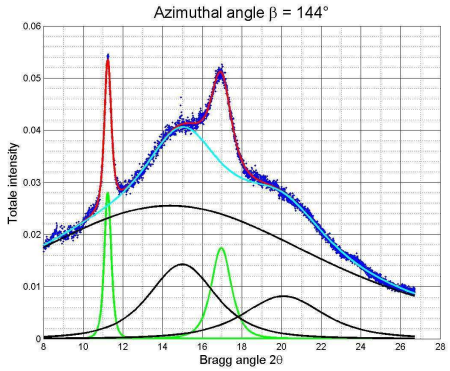

(a) Intensité totale.

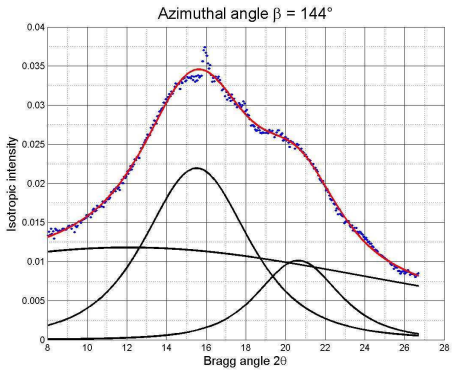

(b) Intensité isotrope.

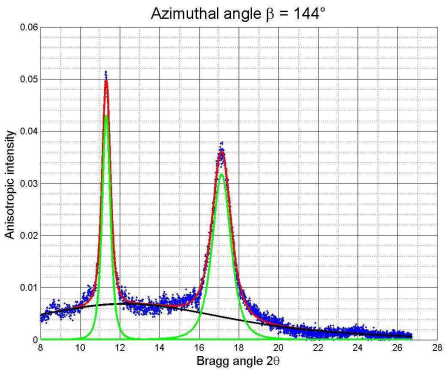

(c) Intensité anisotrope.

FIGURE 1.18 – Modélisation et déconvolution des spectres sans suppression de la baseline.

NR, ce que nous n'avons pas pu confirmer.
Il est donc possible d'associer la baseline du spectre d'intensité anisotrope soit à la phase amorphe du NR, soit à la phase cristallisée du NR, soit à un autre phénomène physique et donc de ne pas tenir compte de cette fonction lors du calcul des taux des différentes phases en présence. A défaut d'argument concluant, j'ai choisi de l'attribuer à la phase amorphe. A titre d'exemple, la figure 1.19 représente la somme des spectres d'intensité isotrope et anistrope de la fig. 1.18 (b) et (c), ce qui permet donc de reconstruire un spectre d'intensité totale *après* avoir déconvolué séparemment les deux spectres. Sur cette

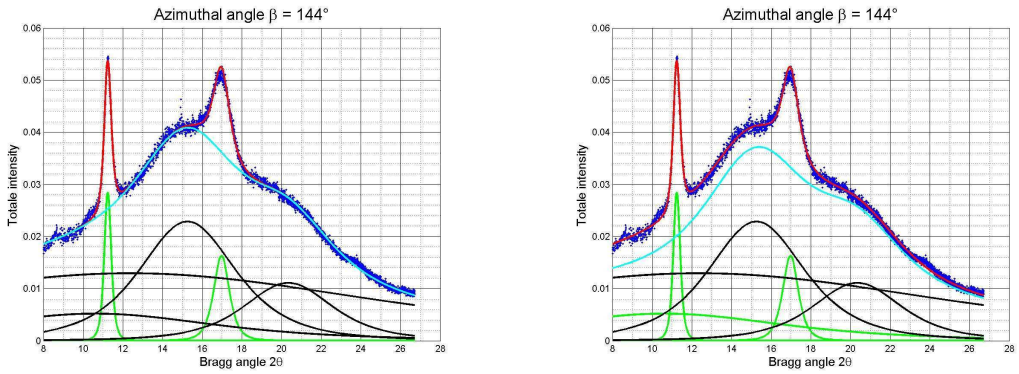

(a) (b)

FIGURE 1.19 – Reconstitution du spectre d'intensité totale à partir des spectres d'intensité isotrope et anisotrope de la fig. 1.18 *après* déconvolution des spectres. (a) La baseline du spectre d'intensité anisotrope est attribuée à la phase amorphe du NR ; (b) cette baseline est attribuée à une autre phase. Les courbes cyan représentent la somme des fonctions attribuées à la phase amorphe.

figure, les courbes cyan représentent la somme des fonctions attribuées à la phase amorphe du NR. Dans le premier cas la baseline du spectre d'intensité anisotrope est attribuée à cette phase (fig. 1.19 (a)), dans le deuxième cas seules les fonctions déconvoluées sur le spectre d'intensité isotrope sont attribuées à la phase amorphe (fig. 1.19 (b)). La méthode retenue ici est donc celle illustrée par la fig. 1.19 (a).

Enfin, la conservation de la baseline permet d'améliorer la modélisation des pics de la phase cristallisée lorsque le taux de cristallinité est très faible. Par exemple, la figure 1.20 montre la modélisation d'un spectre d'intensité anistrope lorsqu'une baseline linéaire est d'abord supprimée (fig. 1.20 (a)) et lorsqu'elle est conservée (fig. 1.20 (b)). Lorsqu'une baseline est supprimée avant la modélisation d'un spectre, une fonction linéaire est alors généralement choisie pour cette baseline puisqu'elle ne nécessite pas de déconvolution préalable pour en déterminer les paramètres. Mais une telle fonction n'est pas toujours optimale pour décrire la baseline, comme le montre la fig. 1.20. En effet, sur la fig. 1.20 (a), l'intensité est négative pour $2\theta \in [15°\ 26°]$, ce qui n'a aucun sens physique et n'est pas modélisable par des fonctions de Pearson. Pour cette raison, c'est la méthode illustrée par la fig. 1.20 (b) qui est retenue.

Pour résumer, la modélisation des spectres de diffraction n'est pas simple et nécessite de faire des choix parfois arbitraires quant à la méthode employée. Ici, j'ai choisi :

- de ne pas modéliser le pic d'acide stéarique pour des raisons de temps de calcul ;
- de séparer les phases isotrope et anisotrope avant la modélisation des spectres, afin d'améliorer la précision et malgré l'augmentation du temps de calcul ;
- de ne pas supprimer la baseline des spectres pour mieux décrire la réalité du phéno-

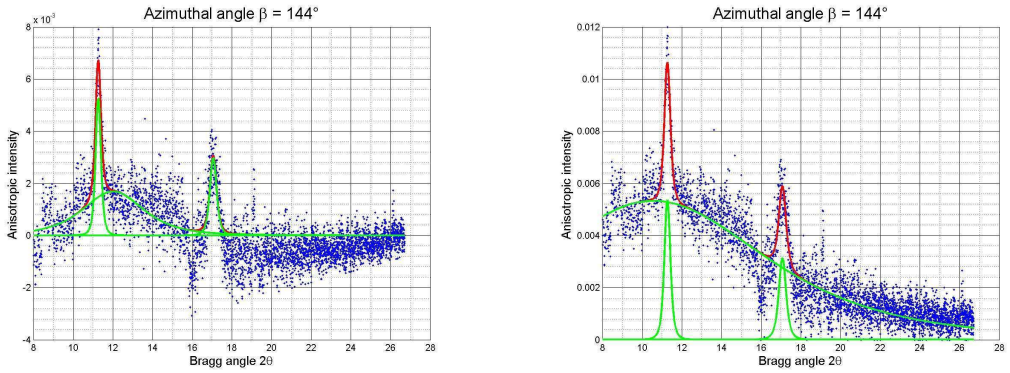

(a) (b)

FIGURE 1.20 – Modélisation d'un spectre d'intensité anisotrope lorsque (a) la baseline est d'abord supprimée et (b) lorsqu'elle est conservée.

mène physique et pour améliorer la précision de la modélisation ;
– d'attribuer la baseline du spectre d'intensité anisotrope à la phase amorphe du NR, orientée ou non.

Bilan Ces différents choix quant à la méthode de modélisation des spectres ont un effect direct sur l'indice de cristallinité calculé ensuite, en surestimant ou sous estimant les différentes phases en présence. L'indice χ est calculé à partir des spectres extraits à l'angle azimuthal correspondant au centre des taches (200) et (120) du NR (voir l'équation (1.13) p. 21). Dans le cas de l'essai de traction uniaxiale quasi-statique réalisé sur un NR chargé au noir de carbone, χ a été calculé par différentes méthodes de modélisation des spectres ; les différents résultats sont présentés sur la figure 1.21. La méthode de modélisation des spectres est différente pour chaque courbe : elle est précisée dans le tableau de légende de la figure. Comme on pouvait s'y attendre (fig. 1.15), la modélisation de l'acide stéarique ne modifie pas le résultat en terme d'indice de cristallinité (comparaison entre les carrés bleus et les croix bleues). La séparation des phases isotrope et anisotrope avant la modélisation des spectres a elle un effet important sur l'indice de cristallinité (comparaison entre triangles et carrés de la même couleur), surtout pour les faibles taux de cristallinité. De même, la suppression de la baseline avant la déconvolution des spectres double l'indice de cristallinité (comparaison entre les triangles, et entre les carrés rouges et bleus) en divisant par deux l'intensité des pics de la phase amorphe. Enfin, l'attribution de la baseline du spectre d'intensité isotrope à la phase amorphe modifie aussi fortement l'indice de cristallinité (comparaison entre les carrés jaunes et rouges). Bien sûr, l'effet de la méthode de modélisation choisie est identique lorsque l'indice de cristallinité utilisé est χ', qui est calculé à partir du cliché complet et pas uniquement d'un angle de Bragg.

Enfin, on note que malgré cette grande variation des résultats en fonction de la méthode utilisée, il est très rare que les auteurs de publications sur la cristallisation du NR donnent des détails sur leur méthode de modélisation des spectres ou proposent un exemple de déconvolution.

La modélisation des spectres permet aussi d'extraires différentes grandeurs (indice de cristallinité, taille et orientation des cristallites, paramètres de maille, etc.) qui ont été données précédemment. Par la suite, nous critiquons le choix de ces grandeurs.

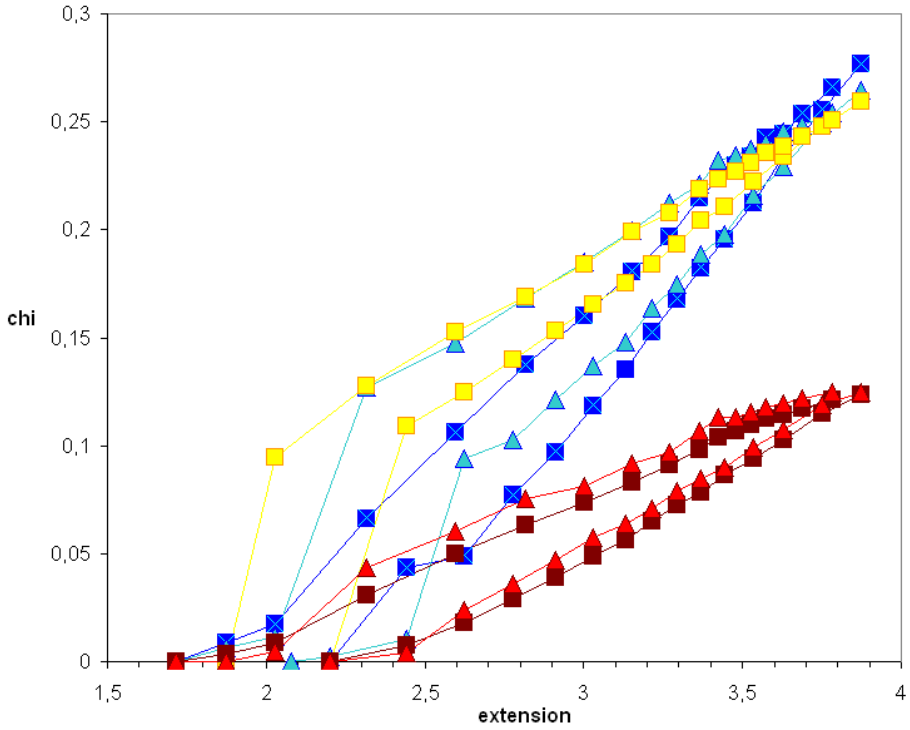

(a)

	Modélisation de l'acide stéarique	Phases isotrope et anisotrope séparées	Baseline supprimée avant modélisation	Baseline attribuée à la phase amorphe du NR
×	oui	oui	oui	-
■	non	oui	oui	-
▲	non	non	oui	-
■	non	oui	non	non
■	non	oui	non	oui
▲	non	non	oui	oui

(b) Légende.

FIGURE 1.21 – Evolution de l'indice de cristallinité χ au cours d'un essai de traction quasi-statique en fonction des méthodes de modélisation des spectres de diffraction.

Indice et taux de cristallinité

Le taux de cristallinité massique d'un matériau est donné par :

$$X = \frac{\mathcal{I}_{crist}}{\mathcal{I}_{crist} + \mathcal{I}_{amorphe}}, \tag{1.16}$$

où $\mathcal{I}_{crist}$ et $\mathcal{I}_{amorphe}$ sont les intégrales surfaciques (en 2θ et β) des intensités des phases cristallisée et amorphe respectivement. L'intervalle de 2θ considéré est limité *(i)* aux petits angles par la présence d'un beam-stop obligatoire pour ne pas saturer le détecteur et *(ii)* aux grands angles par la taille du detecteur. Cependant, si la structure cristallographique du NR n'est pas modifiée aux cours des essais, c'est-à-dire si *(i)* les angles de diffraction des différents plans cristallographiques de la phase cristallisée et *(ii)* la fonction de diffusion de la phase amorphe ne sont pas modifiés, alors le ratio X calculé pour un intervalle de 2θ est toujours proportionnel au ratio X calculé pour toutes les valeurs de 2θ ; le cœfficient de proportionnalité dépend uniquement de l'intervalle de 2θ. Ainsi, l'indice de cristallinité χ' défini à l'équation (1.14) (page 21) est proportionnel au vrai taux de cristallinité du matériau, bien que le coefficient de proportionnalité soit inconnu.

De même, lorsque l'intervalle de β est réduit, comme par exemple pour l'indice χ défini à l'équation (1.13) (page 21) où l'intervalle de β est réduit à une seule valeur, alors l'indice est bien proportionnel au taux X. Mais l'indice de proportionnalité entre les deux ratios varie si l'orientation des cristallites varie. Par exemple, si les cristallites sont orientées aléatoirement ; alors l'intensité des photons diffractés par celles-ci est répartie sur un anneau. Alors que si les cristallites sont toutes orientées dans la même direction, l'intensité est concentrée sur une tache très étroite. Ainsi, l'intégrale surfacique de cette intensité peut être identique, alors que la valeur de l'intensité à un angle β donné varie : elle est beaucoup plus grande au centre de la tache qu'en tout point de l'anneau. Pour cette raison, l'indice χ ne peut pas être utilisé lors de la comparaison de différents essais de déformation multiaxiale et χ' est utilisé.

En revanche, la méthode parfois employée qui consiste à calculer un indice de cristallinité à partir de spectres dont la baseline a été supprimée, ne respecte pas la proportionnalité entre l'indice et le taux de cristallinité, comme le montre les deux équations suivantes :

$$\chi_1 = \frac{\mathcal{I}_{crist}}{\mathcal{I}_{crist} + \mathcal{I}_{amorphe} + \mathcal{I}_{baseline}}, \tag{1.17}$$

$$\chi_2 = \frac{\mathcal{I}_{crist}}{\mathcal{I}_{crist} + \mathcal{I}_{amorphe}}, \tag{1.18}$$

où $\mathcal{I}_{crist}$, $\mathcal{I}_{amorphe}$ et $\mathcal{I}_{baseline}$ sont les intégrales des fonctions attribuées à la phase cristallisée, à la phase amorphe autre que la baseline et à la baseline, respectivement. En supprimant la baseline avant la déconvolution des spectres, et donc en la supprimant du calcul de l'indice de cristallinité, χ_2 n'est pas proportionnel à χ_1 et donc au vrai taux de cristallinité du matériau X.

On note qu'une grande variété d'indices de taux de cristallinité est utilisée dans les publications sur la cristallisation sous contrainte du NR. De nombreux auteurs utilisent des indices très proches de l'indice χ (Saintier, 2000; Toki *et al.*, 2002; Albouy *et al.*, 2005; Toki *et al.*, 2006; Tosaka *et al.*, 2006; Rault *et al.*, 2006a,b; Kohjiya *et al.*, 2007; Rouvière *et al.*, 2007). D'autres auteurs ne mesurent que l'intensité de la phase cristallisée sans calculer de ratio (Toki *et al.*, 2000; Murakami *et al.*, 2002; Miyamoto *et al.*, 2003; Trabelsi *et al.*, 2003b, 2004; Poompradub *et al.*, 2005; Marchal, 2006; Ikeda *et al.*, 2007). Quelques auteurs utilisent un ratio similaire à χ' (Toki *et al.*, 2004; Tosaka *et al.*, 2004a).

Enfin, certains auteurs emploient une méthode assez différente, dite « de Mitchell » ou « de Mitchell simplifiée », qui consiste à mesurer la variation d'intensité de la phase amorphe entre un état totalement amorphe et un état semi-cristallin (Dumbleton et Bowles, 1966; Sahores, 1973; Lee et Donovan, 1987; Alexander *et al.*, 1995; Cyr *et al.*, 1998; Trabelsi *et al.*, 2002, 2003b,a, 2004; Chenal *et al.*, 2007a,b).

Volume des cristallites

L'équation (1.11) (page 20) définit l'indice de volume moyen des cristallites $\overline{V}$ comme le produit des dimensions moyennes des cristallites dans trois directions différentes. Trois points sont intéressants à observer :

- la forme des cristallites de NR, probablement irrégulière et variable, n'a jamais été déterminée. Il n'est donc pas possible de calculer le volume réel des cristallites. Cependant, quelle que soit la forme d'un objet, son volume est proportionnel au produit de ses dimensions dans trois directions non parallèles quelconques ;
- le coefficient de proportionnalité entre le volume réel et le volume calculé de l'objet n'est constant que si la forme et les proportions de l'objet restent consantes. Ici, cette hypothèse est probablement fausse. Cependant, on observe qu'au cours d'un essai de traction uniaxiale quasi-statique, les ratios entre les différentes dimensions des cristallites évoluent peu (voir Chapitre 3). On suppose donc que la forme des cristallites n'est pas beaucoup modifiée par le niveau de déformation ;
- enfin, il est évident que le produit de moyennes n'est pas égal à la moyenne des produits. Ainsi, le volume calculé à partir des dimensions moyennes des cristallites n'est pas le volume moyen des cristallites et plus la dispersion de la taille des cristallites est grande, plus l'erreur est importante.

Ainsi, le terme $\overline{V}$ est un bon indicateur qualitatif de l'évolution du volume moyen des cristallites au cours d'un essai mais n'est pas une grandeur proportionnelle au volume moyen réel des cristallites.

Nombre de cristallites par unité de volume

L'équation (1.15) (page 21) définit un indice du nombre de cristallites par unité volume irradié. Cette grandeur n'étant pas usuelle pour l'étude de la cristallisation sous contrainte du caoutchouc, je détaille ici comment elle est introduite et les différentes hypothèses faites au cours du calcul.

Dans le volume de matériau irradié par les rayons X, il existe I familles de cristallites $(n_i, v_i)_{1\leq i\leq I}$ qui sont composées de n_i cristallites de volume v_i. Grâce aux essais de diffraction, il est possible de connaître le taux de cristallinité massique du matériau χ et le volume moyen des cristallites $\overline{V}$ (dans certaines limites comme expliqué précédemment). Le volume total de la phase cristallisée est la somme du volume de toutes les cristallites mais aussi le nombre total de cristallites N multiplié par le volume moyen des cristallites :

$$N\overline{V} = \sum n_i v_i. \tag{1.19}$$

Ensuite, le taux de cristallinité volumique χ_v du matériau est le rapport du volume de la phase cristallisée et du volume total du matériau V, soit :

$$\chi_v = \frac{\sum n_i v_i}{V}. \tag{1.20}$$

A partir des équations (1.19) et (1.20), il vient :

$$N = \chi_v \frac{V}{\overline{V}}. \tag{1.21}$$

Enfin, l'éprouvette étant perpendiculaire au faisceau de photons, le volume total du matériau irradié V est :

$$V = \pi R^2 d, \tag{1.22}$$

où d est l'épaisseur de l'éprouvette et R est le rayon du faisceau de photons. Finalement, en supposant que le matériau est incompressible ce qui induit une erreur faible dans le cas des élastomères, on obtient :

$$V = \pi R^2 \frac{d_0}{\sqrt{\lambda}}. \tag{1.23}$$

Donc, finalement

$$N = \chi \frac{\pi R^2 d_0}{\sqrt{\lambda}\overline{V}}, \tag{1.24}$$

en supposant que le taux de cristallinité massique est égal au taux de cristallinité volumique. Enfin, en pratique, on considère que le rayon du faisceau R est la demi-largeur à mi-hauteur de la fonction de distribution des photons au point focal et que celle-ci est constante d'un essai à l'autre, donc au cours du temps.

Première partie

Échelle mésoscopique

Dans cette première partie, nous nous intéressons à l'échelle des fissures et micro-fissures de fatigue, appelée ici « échelle mésoscopique » par comparaison avec d'une part l'échelle des éprouvettes et des pièces - souvent utilisée pour l'étude de la durée de vie en fatigue du caoutchouc - et d'autre part l'échelle des macromolécules - qui sera l'objet des parties suivantes.

Cette partie contient un unique chapitre, dont les références exactes et le résumé sont donnés ci-dessous. Le but de ce chapitre est de comprendre le mécanisme de propagation des fissures de fatigue dans le caoutchouc naturel chargé au noir de carbone et de le relier à la faible vitesse de propagation des fissures observée par d'autres auteurs (Lake et Lindley 1965; Lake 1995 par exemple). Pour cela, des essais de propagation in-situ sont réalisés, afin d'observer au microscope électronique à balayage (MEB) la morphologie des pointes de fissures puis la propagation de ces fissures en fatigue.

In-situ SEM study of fatigue crack growth mechanism in carbon black-filled natural rubber

S. Beurrot, B. Huneau, E. Verron
Publié dans Journal of Applied Polymer Science, 117 :2010, 1260-1269

Une micro-machine de traction placée dans la chambre d'un microscope électronique à balayage est utilisée pour réaliser des essais de fatigue *in-situ* sur un élastomère *cis*-1,4-polyisoprène chargé au noir de carbone ; la pointe de fissure est observée en temps réel pendant la propagation de la fissure. Ces observations permettent de décrire en détails la morphologie de la pointe de fissure, de comprendre le mécanisme de propagation de fissure de fatigue et d'expliquer le phénomène de branchement à l'échelle de la microstructure. Enfin, ces résultats sont reliés aux excellentes propriétés en fatigue du caoutchouc naturel et à la cristallisation sous contrainte.

Chapitre 2

Mécanisme de propagation de fissure de fatigue

2.1 Introduction

Carbon Black-filled Natural Rubber (CB-NR) exhibits longer fatigue life than other elastomeric materials (Beatty, 1964). Number of mechanical studies have been proposed to quantify the long-term durability of this material (see Lake 1995; Mars et Fatemi 2002 and the references herein). Nevertheless, only few recent papers investigate the microstructural aspects of fatigue crack growth in rubber (Le Cam *et al.*, 2004; Hainsworth, 2007); in these studies, fatigue tests are first conducted until a sufficiently long fatigue crack develops in the sample, then this sample is stretched and the open crack is observed in a Scanning Electron Microscope (SEM). Moreover, Le Cam *et al.* (2004) developed an original "microcutting" technique which permits to observe fatigue damage behind the crack tip and then to propose a scenario of fatigue crack growth in NR.

The aim of the present paper is to verify this previously proposed mechanism and to enrich the understanding of the phenomena involved during fatigue crack growth at the microstructural scale. In this purpose, in-situ SEM fatigue experiments are conducted thanks to a micro-tensile testing machine and crack propagation is observed in real-time. Indeed, we believe that only such observations enable to unquestionably establish the scenario.

The experimental procedure is first described in details. Then, the next section presents the thorough description of the crack tip, clarifies the scenario of crack propagation and explains how secondary cracks appear. Finally, these results are discussed in the light of both macroscopic fatigue properties and strain-induced crystallization of natural rubber.

2.2 Experimental procedure

The aim of the present experiments is to observe the evolution of the crack tip during rubber fatigue crack propagation, *in real-time*. The experiments are conducted in three steps: *(i)* the specimen is precut with a scalpel, *(ii)* a classical fatigue experiment is then conducted in a standard machine until a fatigue crack propagates and *(iii)* the experiment is continued in a micro-tensile testing machine placed in a SEM.

2.2.1 Apparatus

The micro-tensile testing machine is shown in Figure 2.1; it was designed by Deben UK Limited especially for soft materials (the distance between the clamps varies from 20 mm to 40 mm). This machine is sufficiently small-sized to be placed in the chamber of a SEM, it is

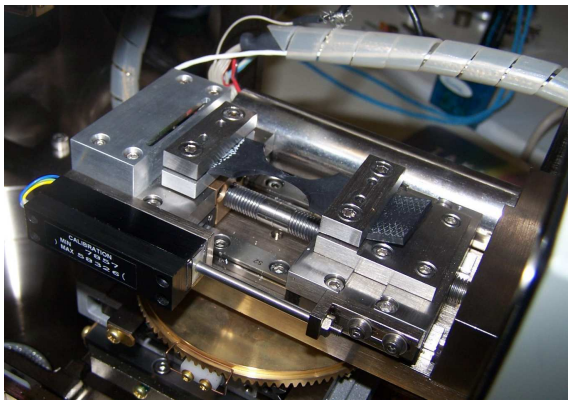

Figure 2.1: Micro-tensile testing machine

monitored by a computer connected via a leak-free connector, and the double screw driving system leads to easy observation because the centre of the sample, i.e. the position of the crack tip, does not change during loading. Nevertheless, two major difficulties are due to the characteristics of the machine. First, its size and the limited distance between the clamps constrain both size and shape of the samples. Indeed, a special design of samples is needed to induce large strain in the vicinity of the crack. Second, as the relative speed of the clamps can vary from 0.1 mm/min to 2 mm/min, the maximum frequency of a fatigue test is 0.83 mHz, such value leading to days-long experiments. This is the reason why samples are pre-cut and the fatigue crack is first propagated in a classical tensile-testing machine.

2.2.2 Material and design of the sample

The material considered here is an industrial 43 phr CB-NR, provided in 2 mm thick calendered sheets.

As mentioned above, a special shape of sample was chosen in order to achieve large strain in crack vicinity and to propagate it; the corresponding geometry is shown in Figure 2.2. To ensure that the deformation is predominantly uniaxial extension, we performed

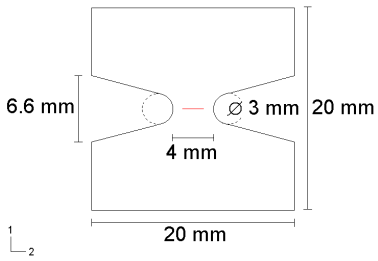

Figure 2.2: Geometry of samples

a finite element simulation of the sample (without a precut) for a 20 mm long sample

stretched to 40 mm long. In that case, the engineering strain tensor in the center of the sample is:

$$P = \begin{bmatrix} 1.40 & 0.02 & 0 \\ 0.02 & -0.71 & 0 \\ 0 & 0 & -0.70 \end{bmatrix}, \tag{2.1}$$

where the directions are defined in Fig. 2.2. The first component corresponds to a stretch ratio of about 400% and the other components are negligible, so the deformation at crack tip is nearly uniaxial.

2.2.3 Procedure

(i) The first step consists in pre-cutting the sample to localize the crack in its centre. This cut is made with a scalpel and the resulting crack is less than 1 mm deep and between 2 and 3 mm long.

(ii) To reduce the duration of the fatigue experiment, a fatigue crack is initiated from the precut in a standard fatigue machine. Fully relaxing cycles of stretch amplitude 200% are considered and the strain rate is chosen to limit self-heating, in order to not superimpose thermal damage to mechanical damage. Practically, it corresponds to frequencies less than 1 Hz. Finally this first part of the fatigue test performed in a standard machine is stopped after the crack has propagated of about 50% of precut deepness.

(iii) Finally, the experiment is continued in the small scale tensile machine. Loading conditions are identical to those of *(ii)* except the frequency which is 0.83 mHz. Observation is made in a Jeol 6060LA SEM using secondary electrons imaging. Note that if a too high power electron beam is used, crack tip is damaged: microscopic cracks develop perpendicular to the loading direction. To overcome this difficulty, four parameters need to be lowered to reduce the energy of the electron beam per unit area: the probe current, the accelerating voltage, the magnification and the exposure time. Once these parameters set, the fatigue experiment is stopped once per cycle at maximum stretch to photograph the crack tip.

2.2.4 Remark on the validity of the experimental method

Recall that the objective of the experiments is to establish the fatigue crack growth mechanism in ambient air at conventional frequencies (about 1 Hz) and that in-situ observations cannot be conducted with those experimental conditions. So, an essential prerequisite is to check that the mechanism is not affected by this change of experimental conditions. First, assuming that a given mechanism always leads to similar crack tip morphologies, we verified that crack tips before and after in-situ fatigue tests have the same characteristics: similar microstructural features with the same sizes and proportions. Second, we verified *a posteriori* that the change in experimental conditions does not influence the mechanism by examining the fracture surface of the samples: the transition between the pre-cut step *(i)* and the conventional fatigue step *(ii)* is visible, but the one between conventional *(ii)* and in-situ *(iii)* fatigue tests is not.

2.3 Mechanism of fatigue crack propagation

2.3.1 Description of the crack tip

Figures 2.3 and 2.4 present respectively the front view and the side view of the fatigue crack tip. In the former figure, tensile direction is indicated by white arrows and the

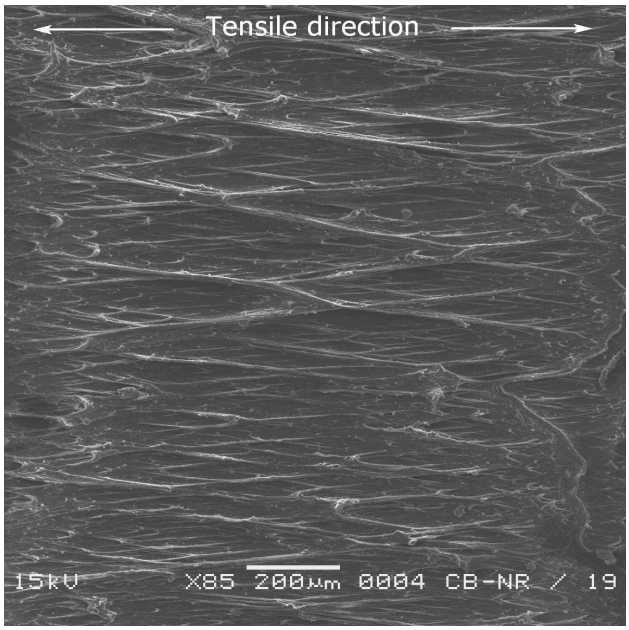

Figure 2.3: Top view of a representative crack tip

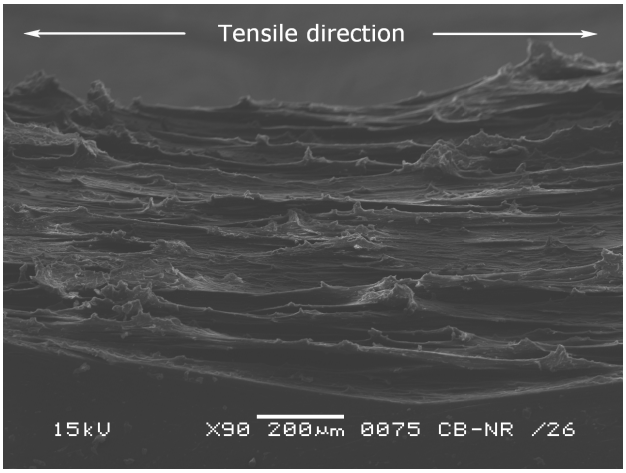

Figure 2.4: Side view of a representative crack tip

propagation direction is normal to the photomicrograph. As observed previously (Le Cam *et al.*, 2004; Hainsworth, 2007), the crack tip is composed of number of diamond-shaped zones separated by ligaments. The pattern of ligaments and diamond-shaped zones can be described as multi-scaled because large diamond-shaped zones delimited by large ligaments are themselves made up of smaller zones delimited by smaller ligaments. Fig. 2.4 shows that the crack tip is a 'hilly landscape': the diamond-shaped zones are flat and smooth compared to the ligaments, and those ligaments emerge from the smooth surfaces. The

most noticeable characteristic of the crack tip is the pattern regularity. Surprisingly, the ligaments are not parallel to the tensile direction. In fact, they are parallel to two directions which are symmetric with respect to the tensile direction. The angle between the direction of ligaments and the loading direction decreases with the extension of the sample. Consequently, at a given deformation even if the size of diamond-shaped zones varies, all of them have the same length-width ratio. For instance, in Fig. 2.3, this ratio is 4 to 1. Nevertheless, the size of the diamond-shaped zones is not uniform; indeed the knots of the pattern are not regularly located.

Then, we examine more precisely the ligaments. They vary in shape and size. First, they can be compared in regard to their size: *(1)* large ligaments delimit large diamond-shaped zones, *(2)* intermediate-sized ligaments delimit small diamond-shaped zones and finally *(3)* the smallest ligaments are those contained in the small diamond-shaped zones. Second, ligaments can also be compared in regard to their shape. It leads to four types of ligaments defined by the form of their section as shown in Figure 2.5: those with uniform width along their height (mostly large ligaments) (Fig. 2.5 (a)), those with a large base (mostly intermediate-sized and small ligaments) (Fig. 2.5 (b)), those with a narrow base (large and intermediate-sized ligaments) (Fig. 2.5 (c)) and finally those which form a bridge (very rare, small ligaments) (Fig. 2.5 (d)). Finally, the crack tip also contains another relief

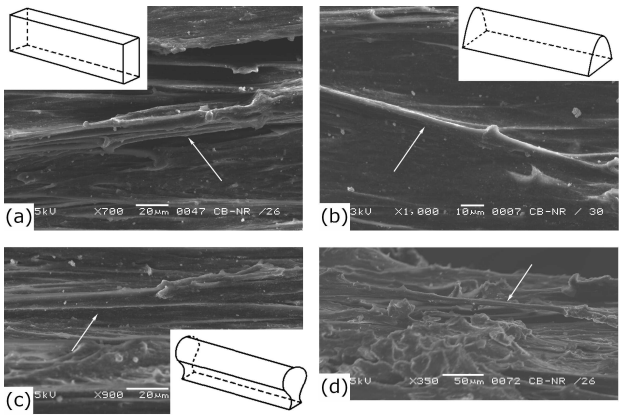

Figure 2.5: SEM pictures and schemes of the four main ligaments shapes: (a)ligament with uniform width (b)ligament larger at the base (c)ligament larger at the top (d)ligament shaped as a bridge

feature shown in Figure 2.6. As it will be established in the following, it corresponds to previously broken and then shrunk ligaments. They are located at the knots of the pattern, i.e. at the intersection of the ligaments.

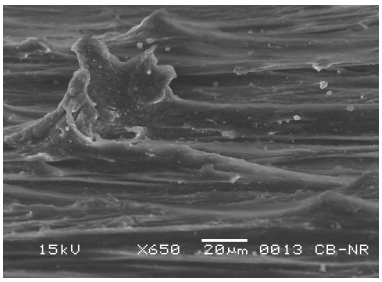

Figure 2.6: Example of a shrunk ligament

The previous description was devoted to rubber matrix, but as the material considered in this study is an industrial CB-NR, it contains a lot of different inclusions. Most of them are zinc , in both diamond-shaped zones and ligaments, or carbon black agglomerates in diamond-shaped zones. In most of the cases, they are contained in elliptical cavities.

Finally, Figure 2.7 summarizes the description of the crack tip microstructure: the left-hand drawing shows the front view and presents the different elements described above, and the right-hand drawing is a side view which highlights the relief of the crack front. 2.1 gives the mean sizes and quantities of those features measured on a 500 μm $\times$ 800 μm area of a given crack tip. The sample and the area were chosen for their representativeness.

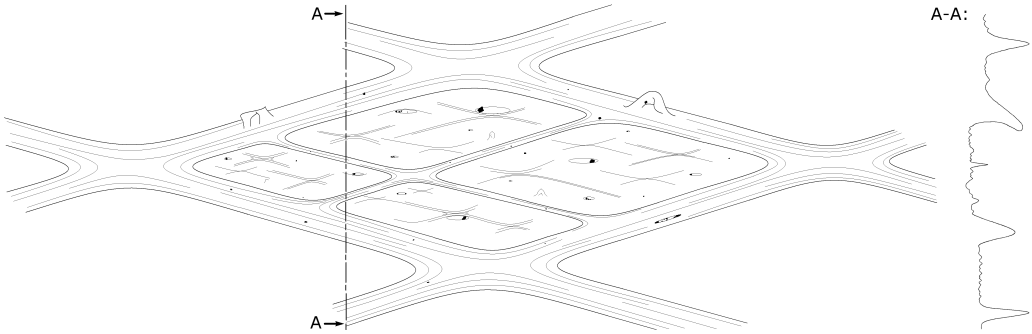

Figure 2.7: Open crack tip (top view and section)

2.3.2 How does the crack propagate?

Figure 2.8 shows six SEM images of a 0.5 mm^2 area of the crack tip taken respectively for the maximum stretch of in-situ fatigue cycles 1, 10, 21, 31, 41 and 51. The micromechanism of fatigue crack growth in rubber can be established thanks to this figure. From one SEM image to another, it clearly appears that all the crack tip zones are affected by crack growth: positions of ligaments change with loading as shown by the white lines drawn on images. It means that the crack front is a surface rather than a line. Moreover, the evolution of the diamond-shaped zones suggests a three-step mechanism for crack propagation as emphasized in Figure 2.9. In order to describe this evolution, we choose Fig. 2.9 (a) as the reference state of the zones. Under loading, zones become larger (see changes between Fig. 2.9 (a), (b) and (c)), and cavities and inclusions appear on the surface (see Fig. 2.9 (c)). It means that the matter tears and the zone grows deeper in the direction normal to the crack surface, i.e. the direction of crack growth (it can not be seen in the figure). The more the zone goes deeper, the more the ligaments which delimit it are stretched. Then after a few number of cycles, one of these ligaments breaks (see Fig. 2.9 (d)) and shrinks (see Fig. 2.9 (e)). This breakage is not instantaneous: it lasts from one to ten cycles depending on the size and shape of the ligament and of the local microstructure. Two different evolutions of the microstructure are observed: a new ligament may emerge or the two diamond-shaped zones separated by the broken ligament may coalesce as shown in Fig. 2.9 (f). In both cases, the matter reorganizes itself in a large vicinity of the broken ligament through the displacement of ligaments and diamond-shaped zones. In fact, this mechanism repeats itself in every diamond-shaped zone of the crack front. From a temporal point of view, this phenomenon occurs in a continuous manner with different velocities in each point. From a spatial point of view, it can happen simultaneously in different locations of the crack front.

Element type	Mean size (μm or μm^2 or μm^3)	Quantity observed on the chosen sample
Large diamond-shaped zones	200 × 800	4
Small diamond-shaped zones	100 × 400	20 (from 3 to 8 per large zone)
Large ligaments	(width × height × length) 20 × 50 × 600	4
Intermediate-sized ligaments	(width × height × length) 10 × 25 × 300	around 100
Small ligaments	(width × height × length) 1 × 5 × 50	several hundreds
Zinc oxides	diameter < 10 (exceptionally 20)	several hundreds
Cavities around zinc oxides	elliptical: 7 × 20	several tens
Carbon black agglomerates	diameter: 50	1
Cavities around agglomerates	elliptical: 50 × 200	1
Shrunk ligaments	diameter: from 1 to 100	around 100
Ligaments with uniform width	-	2/3 of all large ligaments, 1/4 of all intermediate-sized ligaments, 1/4 of all small ligaments
Ligaments with a large base	-	1/2 of all intermediate-sized ligaments, 3/4 of all small ligaments
Ligaments with a narrow base	-	1/3 of all large ligaments, 1/4 of all intermediate-sized ligaments
"Bridge" ligaments	-	1% of all small and intermediate-sized ligaments

Table 2.1: Sizes and quantities of the elements measured on a 500 μm × 800 μm area of a given crack tip

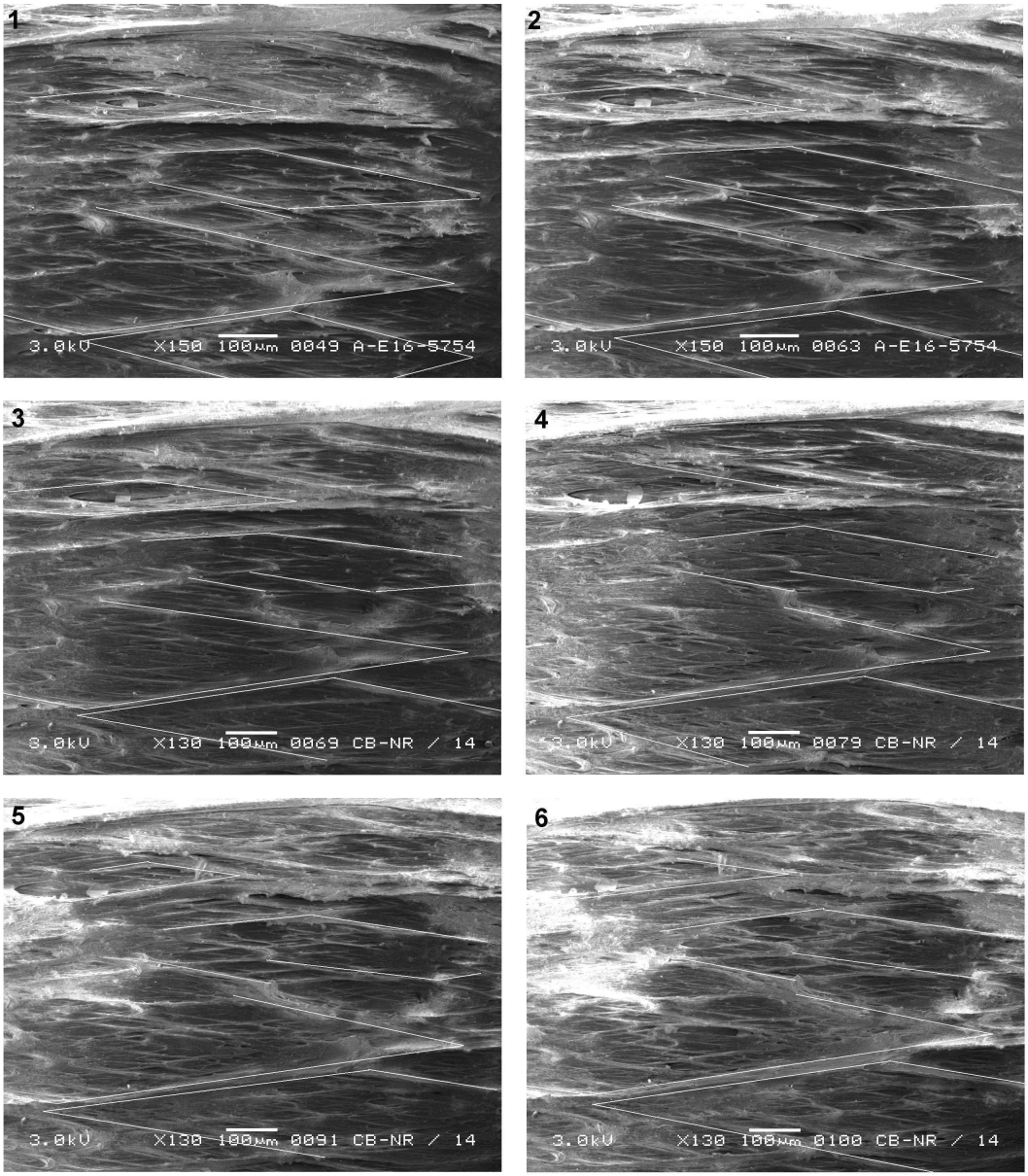

Figure 2.8: Evolution of a crack tip during cyclic loading after respectively 1, 10, 21, 31, 41 and 51 in-situ cycles

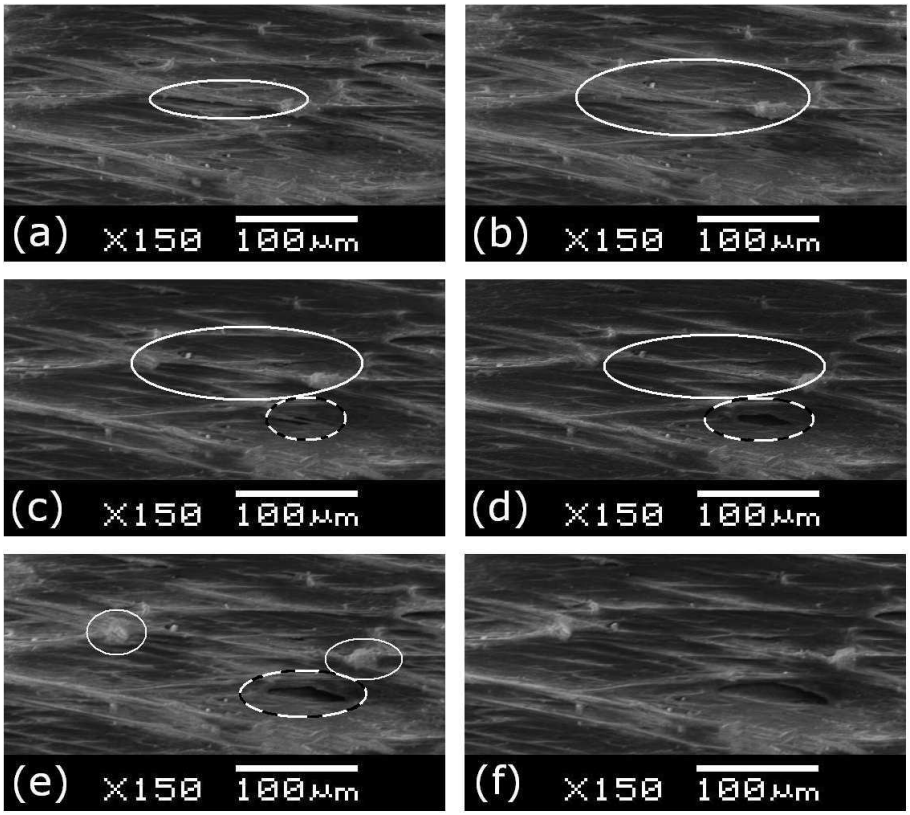

Figure 2.9: Successive photographs of the same detail of a crack tip during the rupture of a ligament after respectively 1, 3, 4, 5, 6 and 8 in-situ cycles

To close this section, we summarize the main elements of the previous mechanism with the help of a five-step scenario as depicted in Figure 2.10.

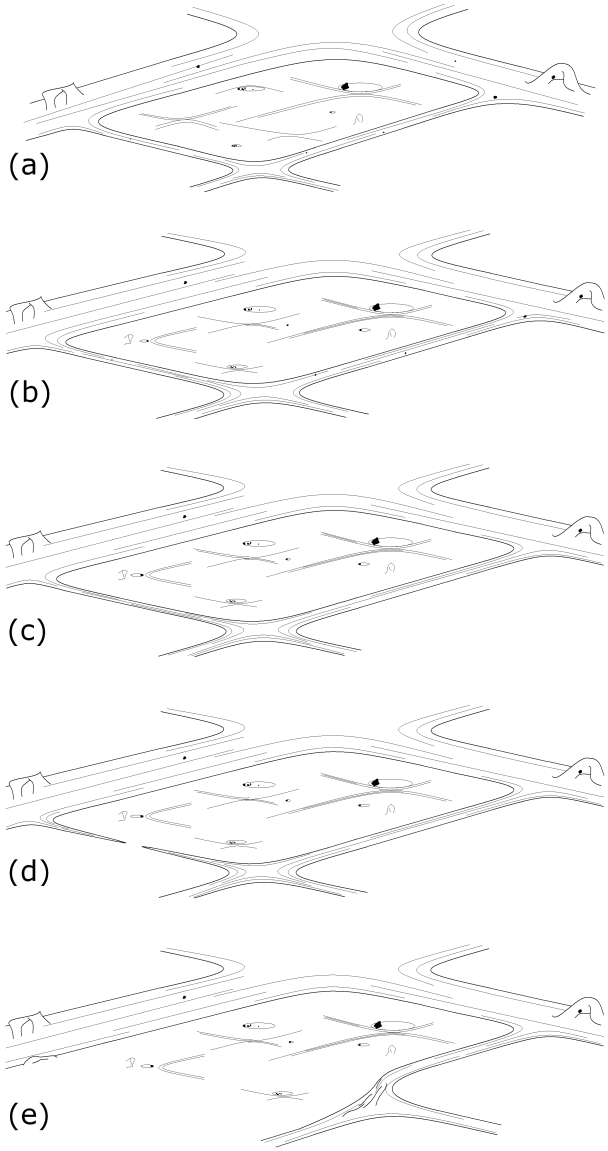

Figure 2.10: Fatigue crack propagation mechanism

(a) Fig. 2.10 (a) presents the initial state of a diamond-shaped zone and its delimiting ligaments; it is a detail of the drawing of the crack tip in 2.7,

(b) the diamond-shaped zone grows larger and deeper, showing new inclusions and ligaments (see Fig. 2.10 (b)),

(c) as a consequence, ligaments which delimit the zone are stretched and one of them gets thinner than in the previous cycle (see Fig. 2.10 (c)),

(d) eventually, this ligament breaks (see Fig. 2.10 (d)),

(e) finally, the matter reorganizes itself through coalescence of the diamond-shaped zone with one of its neighbours (see Fig. 2.10 (e)).

2.3.3 How do secondary cracks appear?

In the previous sections, the crack was observed only when opened. However, the study of the closed crack exhibits the path of a fatigue crack in natural rubber. To perform these observations, samples are cut in two with a scalpel along the plane defined by the tensile and propagation directions in the middle of the crack as shown in Figure 2.11. Figure 2.12

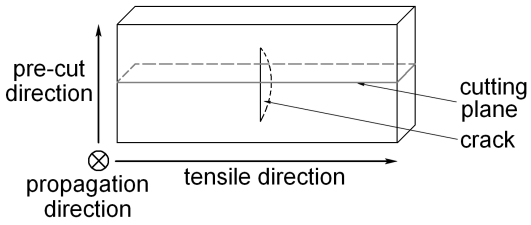

Figure 2.11: Cutting plane of the specimens after fatigue tests

presents the side view of the crack which is slightly open to observe more easily the crack path. It highlights the main crack path which is normal to the tensile direction and several

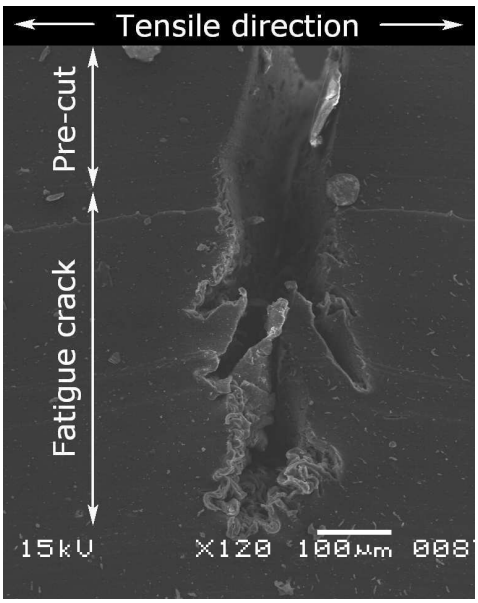

Figure 2.12: Crack path observed in a cut sample

secondary cracks. Similarly to Hamed (1994), the term "secondary crack" refers to short deviated cracks developed from the main one. Their length varies from 10 μm to 100 μm. In order to establish the scenario of secondary cracks formation also called "crack branching phenomenon", it is necessary to determine how diamond-shaped zones evolve relatively to the others. In this purpose, the crack tip is observed with a different orientation from the previous images (Figs. 2.8 and 2.9): samples are rotated 90° in the SEM chamber to change the orientation of the ligaments with respect to the secondary electron detector. The obtained image is presented in Figure 2.13; it emphasizes the relief of the crack tip due to the shadow contrast. It shows that all diamond-shaped zones are not in the same plane: some of them are deeper than others (see those indicated by white arrows in Fig. 2.13).

The crack propagation mechanism proposed in Sec. 2.3.2 does not take into account kinetics. The presence of diamond-shaped zones of different deepness in Fig. 2.13 suggests

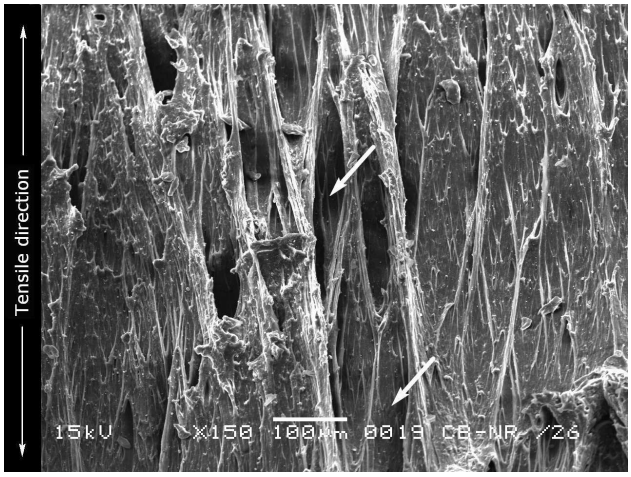

Figure 2.13: Top view of a crack tip – 90° rotated specimen in the chamber of the specimen

that even though the diamond-shaped zones evolve in a continuous manner, they do not grow deeper at the same speed. Moreover, recalling that the crack front is a surface rather than a line, the crack branching scenario will be established with the help of Figure 2.14. It shows the evolution under fatigue loading of three contiguous diamond-shaped zones

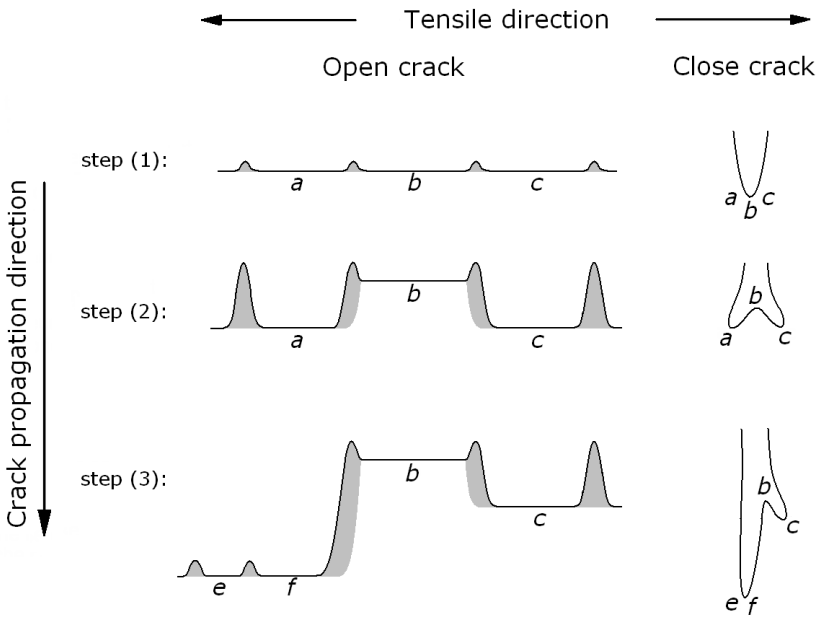

Figure 2.14: Branching phenomenon mechanism

(a,b,c) located at the crack front surface. It is a simplified representation of the crack tip cross-section: the right-hand drawings describe the close crack with the same view as in Fig. 2.12 and the left-hand drawings show the same crack but opened. To simplify the discussion, the scenario is established by considering three successive steps:

(1) Initially, the three diamond-shaped zones a, b and c are separated by ligaments (grey in the figure) and have the same depth. When the crack is closed, there is only one branch.

(2) Later on, when the crack has propagated, zones a and c have grown deeper than zone

b. So, the close crack presents two similar branches. The main crack will develop from one or the other (*a* or *c*).

(3) As the crack continues to propagate, one of the two previous branches will become the main crack due to both local mechanical conditions and microstructure. In the figure, zone *a* has become the main crack, and turned into two new diamond-shaped zones *e* and *f* because the former ligaments which delimited zone *a* broke and new ones appeared; zone *b* does not evolve anymore because it is partially relaxed; and zone *c* forms a secondary crack.

During crack propagation, the elementary scenario described above repeats: zones *e* and *f* will evolve in the same manner as zones *a*, *b* and *c* in step (1). It is to note, that zones *a*, *b*, *c* can be three single diamond-shaped zones or three groups of several zones.

Finally, the crack branching scenario enable us to explain the roughness of the fracture surface morphology shown in Figure 2.15. More precisely, the fracture surface contains

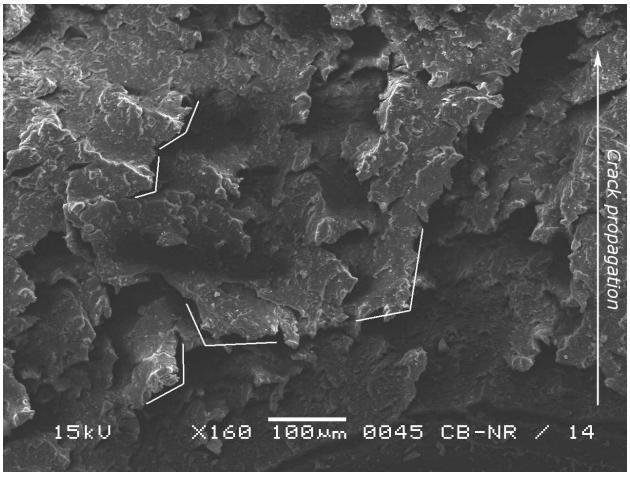

Figure 2.15: Detail of the fracture surface (top view)

numerous "leaves", i.e. thin pieces of matter orientated toward the initiation zone of the crack; their size varies between 10 μm and 100 μm similarly to the length of secondary cracks. In fact, the matter which separates secondary cracks from the main crack when we observe the close crack corresponds to the leaves on the fracture surface; this is shown in Figure 2.16: Fig. 2.16 (a) is the sketch of the close crack shown in Fig. 2.12 and Fig. 2.16 (b) is the sketch of the fracture surface side view Fig. (2.15).

2.4 Discussion

Recently, some authors performed interrupted fatigue tests and observed stretched samples in SEM (Le Cam *et al.*, 2004; Hainsworth, 2007). Le Cam *et al.* observed the damage induced by fatigue and proposed the mechanism of crack propagation in natural rubber. Nevertheless, only observations performed during crack propagation enable to unquestionably establish this mechanism. Here, in-situ SEM experiments have been conducted to observe fatigue crack propagation in rubber in real-time. If such experiments have been already conducted for metallic materials (Crepin *et al.*, 2000), to our knowledge, the present work is the first attempt to apply this technique to rubber materials. Some experimental difficulties have been overcome. These difficulties are mainly due to the non-conductive nature of polymers: first the build-up charge leads to low-quality images, and second the

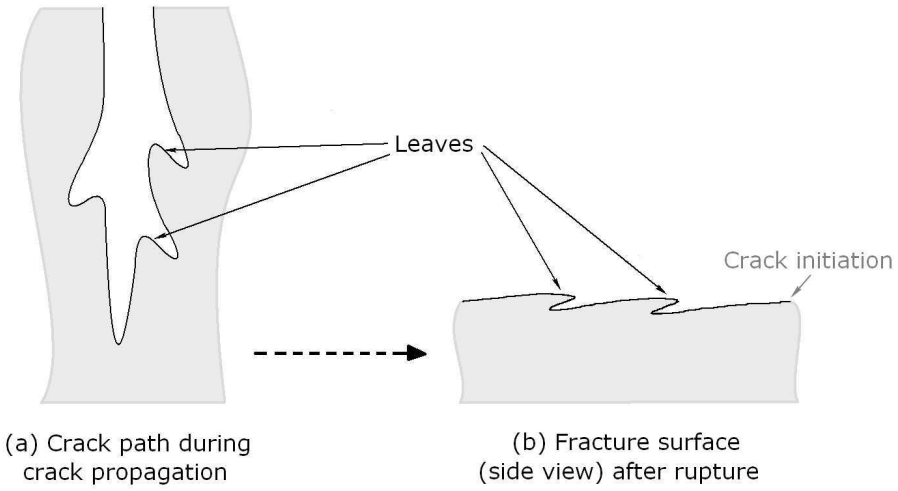

Figure 2.16: Origin of the fracture surface leaves

electron beam causes radiation damage which alters the material. It can lead to false interpretation as underlined by White et Thomas (1984). The classical way to counter these difficulties consists in applying a conductive coating to the sample; in our case this solution could not be applied because the coating layer would have been destroyed by cyclic loading. As detailed in Sec. Experimental procedure, we reduce the energy of the electron beam per unit area.

With this careful procedure, we are able to highly improve the description of both crack tip morphology and propagation mechanism we previously published (Le Cam *et al.*, 2004). First, the crack tip description is enriched: ligaments morphology and orientation were thoroughly investigated. Second, the present mechanism of crack propagation is in good agreement with the previous one, except for the perpendicular micro-cracks and the cavities which were observed by Le Cam et al. and not here. In fact, those micro-cracks were due to the electron beam; moreover, we believe that what was called a cavity in our previous study was only a smooth hollow which deepness was overestimated. Third, additional experiments allow to explain both crack branching and rough surface morphology in NR under fatigue loading conditions.

The microscopic mechanism presented above explains the great fatigue properties of NR at the macroscopic scale: long fatigue life (Mark *et al.*, 2005) and low crack growth rate (Lake, 1995; Papadopoulos *et al.*, 2008). Indeed, the ligaments of the crack tip resist to crack propagation in two ways: they induce a surface crack front rather than a tearing line as well as branched cracks which both help to dissipate energy and then hold up crack advance as previously argued by Hamed (1994).

The great fatigue properties of NR are usually correlated with its ability to crystallize under deformation. In order to relate this property to our results, we will now compare NR to Styrene Butadiene Rubber (SBR), an elastomer which does not exhibit strain-induced crystallization. More precisely, a similar study has been conducted for a SBR material with the same amount of carbon black fillers than in the NR considered here. It highlights three main differences between NR and SBR fatigue crack growth mechanisms:

– as shown in Figure 2.17 (a) as compared to Fig. 2.11 (b), the crack tip of SBR does not present ligaments. Even though we observe sort of filaments parallel to tensile direction, the crack tip is very smooth and experiments reveal that those filaments

do not resist to crack propagation as ligaments do in NR,
- the in-situ crack propagation observation also shows that in SBR the crack front is a line rather than a surface as in NR,
- the close crack in Figure 2.17 (b) shows that crack branching does not occur in SBR contrary to what is observed in NR (see Fig. 2.12).

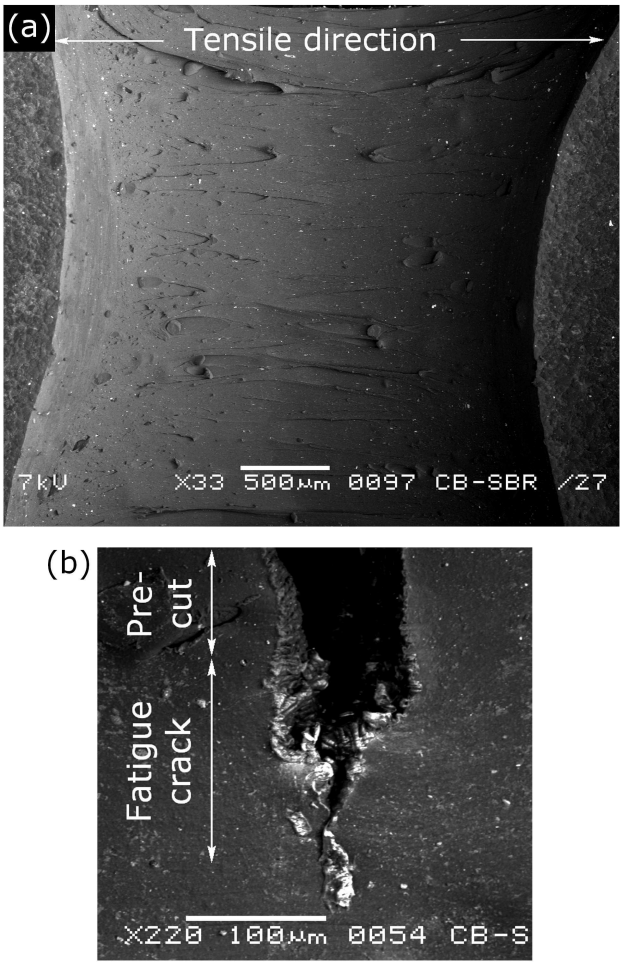

Figure 2.17: SBR specimen: (a) front view of the open crack tip (b) side view of the close crack

This comparison demonstrates that the heterogeneity of the microstructure at the crack tip (ligaments, diamond-shaped zones) is a consequence of strain-induced crystallization in NR.

2.5 Conclusion

Fatigue crack growth in natural rubber has been observed in real-time thanks to in-situ fatigue experiments in a scanning electron microscope. The careful and original procedure used in this study has enabled us to highly improve our knowledge of fatigue crack propagation:

1. The crack tip morphology has been thoroughly described. It is composed of ligaments which form a regular pattern of diamond-shaped zones as the ligaments are surprisingly not parallel to the tensile direction but to two directions symmetric with respect to the

tensile direction. Sizes and shapes of the ligaments and inclusions found at the crack tip has also been detailed.

2. The scenario of fatigue crack growth has been established. We have observed that the crack front is a surface rather than a line and that the elementary mechanism of crack propagation in one diamond-shaped zone repeats itself simultaneously in different locations of the crack tip.
3. Moreover, as this phenomenon occurs with different velocities in each point of the crack tip, we have explained the mechanism of initiation and propagation of branched cracks and also the roughness of fracture surfaces of NR.
4. The crack growth mechanism has been related to the great fatigue properties at the macroscopic scale (low crack growth rate and long fatigue life): both the surface crack front and the branched cracks dissipate energy and hold up crack advance.
5. A similar study conducted for styrene butadiene rubber have demonstrated that the heterogeneity of the microstructure at the crack tip is a consequence of strain-induced crystallization in NR.

At the close of this study, the mechanism of fatigue crack propagation in NR is qualitatively well-established; further investigations are now required to quantify the heterogeneity of some physical quantities, for example crystallinity and strain, at the crack tip.

2.6 Acknowledgment

The authors are thankful to Trelleborg Automotive for providing the material for this study.

Deuxième partie

Caractérisation de la cristallisation sous contrainte du matériau

L'étude des fissures de fatigue à l'échelle mésoscopique a permis de comprendre - au moins en partie - les mécanismes de dissipation qui expliquent les très bonnes propriétés en fatigue du caoutchouc naturel. Toutefois, cette échelle ne permet pas d'identifier le lien entre ces propriétés et la cristallisation sous contrainte du matériau, alors qu'il est généralement admis que ce phénomène est à l'origine de la grande durée du vie en fatigue du caoutchouc naturel.

Le phénomène de cristallisation sous contrainte fait donc l'objet de cette partie et des parties suivantes, il est étudié par diffraction des rayons X. Dans le chapitre constituant cette partie, dont les références sont données ci-dessous, nous nous intéressons à un cycle de traction uniaxiale quasi-statique. L'objectif est de caractériser la cristallisation du caoutchouc naturel, non chargé et chargé au noir de carbone, afin de définir les phénomènes qui seront utilisés comme référence lorsque nous étudierons les déformations multiaxiales et la fatigue dans les parties suivantes.

Strain-induced crystallization in unfilled and carbon black-filled natural rubber as revealed by X-ray diffraction

S. Beurrot-Borgarino, B. Huneau, E. Verron
Soumis à Journal of Applied Physics

L'évolution de la cristallisation sous contrainte lors d'un cycle de traction quasi-statique dans le caoutchouc naturel non chargé et chargé au noir de carbone est mesurée et comparée grâce à la diffraction des rayons X aux grands angles (WAXD). En premier lieu, nous montrons que l'évolution du degré de cristallinité durant un cycle est principalement due à la nucléation et la fusion de cristallites plutôt qu'à un changement de tailles des cristallites. Ensuite, l'évolution des caractéristiques des cristallites, c'est-à-dire les paramètres de maille, le volume de la maille élémentaire et le nombre, la taille, le volume et la désorientation des cristallites, est mesurée. Cela permet de mettre en évidence l'existence de deux extensions spécifiques qui correspondent à des changements de mécanisme de cristallisation importants.

Chapitre 3

Cristallisation sous contrainte du caoutchouc naturel non chargé et chargé au noir de carbone lors d'un cycle quasi-statique

3.1 Introduction

Natural rubber (NR), cis-1,4-polyisoprene, is a material widely used for engineering applications because of its great mechanical properties, such as a high tensile strength, a remarkable crack growth resistance and its ability to withstand very large elastic strain. Those properties are partly attributed to the material's ability to crystallize under strain. Strain-induced crystallization (SIC) of NR has been thoroughly studied by several experimental techniques, for example X-ray diffraction, birefringence, volume change, stress relaxation or calorimetry. In particular, wide-angle X-ray diffraction (WAXD) has been used to measure the evolution of the degree of crystallinity of NR during quasi-static tensile tests, but also to measure the characteristics of the crystallites, such as their size and orientation (Trabelsi *et al.*, 2003b, 2004; Tosaka *et al.*, 2004b; Poompradub *et al.*, 2005; Chenal *et al.*, 2007a,b). For a complete review of those works, the reader can refer to Huneau (2011).

The effect of fillers on SIC of NR has been less studied, and in particular the effect of carbon black which is very often used in elastomeric industrial parts to enhance the tensile strength of NR. The major recent studies on the subject are those of Trabelsi *et al.* (2003b) and Poompradub *et al.* (2005) who obtained some contradictory results. Furthermore, the knowledge on SIC of NR did not enable so far to relate SIC and NR outstanding mechanical properties.

The objective of this article is *(i)* to the measure the evolution of the crystalline phase in unfilled and carbon black-filled NR during a quasi-static tensile test as measured by WAXD technique and *(ii)* to propose a mechanism of SIC in both materials.

3.2 Experimental method

3.2.1 Material and samples

The materials in this study are natural rubber, either unfilled or filled, cross-linked with 1.2 phr (per hundred of rubber) of sulphur and 1.2 phr of CBS accelerator. It also contains ZnO (5 phr) and stearic acid (2 phr) ; the filled NR contains 50 phr of N330 carbon black. In the following, unfilled NR is sometimes abbreviated to 0-NR and carbon black-filled NR to CB-NR.

The samples are classical flat dumbbell specimen with a 10 mm gauge length and a 2 mm $\times$ 4 mm section.

3.2.2 Synchrotron

The synchrotron measurements are carried out at the DiffAbs beamline in the French national synchrotron facility SOLEIL (proposal number 20100096). The wavelength used is 1.319 Å and the beam size is 0.3 mm in diameter at half-maximum. The 2D WAXD patterns are recorded by a MAR 345 CCD X-ray detector. The exposure time is 2 seconds. A PIN-diode is used in order to make an accurate correction of air scattering.

3.2.3 Procedure

In order to lower the residual elongation of the sample due to Mullins and viscous effects, both samples are pre-cycled just before testing (5 cycles) at a higher strain than during the tests. The samples are stretched at 0.012 mm.s^{-1}. The 0-NR sample is elongated of 130 mm, which corresponds to the local stretch ratio λ=5.81. The total duration of the cycle is about 3 hours and it corresponds to a mean stretch ratio rate along the cycle of $\dot{\lambda} = 0.54.10^{-3}$ s^{-1}. For the CB-NR sample, the elongation is 90 mm which corresponds to λ=4.02 and $\dot{\lambda} = 1.06.10^{-3}$ s^{-1}; it is about a two-hour cycle. A scattering pattern is recorded every 98 seconds. The local stretch ratio λ at the center of the sample is measured continuously by an optical method.

3.2.4 Scattering pattern analysis

Here, small angles scattering is not investigated; the range of diffraction angles is $2\theta \in [8°, 26.7°]$. We used the (012) reflections of Cr_2O_3 powder placed on each side of a specimen to calibrate the diffraction angles 2θ (a = 4.9590 Å and c = 1.3596 Å). An air scattering pattern (without any sample) is first collected and is used to correct the patterns. Moreover, the change in thickness of the sample under extension and the change of intensity of the incident photons are also considered. All these corrections are performed by following the well-established method of Ran *et al.* (2001). An example of corrected diffraction pattern is given in Figure 3.1.

The intensity of photons diffracted by the isotropic phases in the material $I_{iso}(2\theta)$ is extracted from the diffraction patterns by considering the minimum intensity along the azimuthal angle β for each Bragg angle 2θ. Then, the intensity of photons diffracted by the anisotropic phases $I_{ani}(2\theta, \beta)$ is calculated as the difference between the total intensity of photons diffracted $I_{total}(2\theta, \beta)$ and $I_{iso}(2\theta)$. The spectra extracted from $I_{ani}(2\theta, \beta)$ and $I_{iso}(2\theta)$ are classically fitted by series of Pearson functions (Toki *et al.*, 2000; Trabelsi *et al.*, 2003a; Rault *et al.*, 2006a; Chenal *et al.*, 2007b). Figures 3.2 (a) and (b) present examples of fitting and deconvolution of a (2θ,I_{iso}) spectrum and a (2θ,I_{ani}) spectrum, respectively.

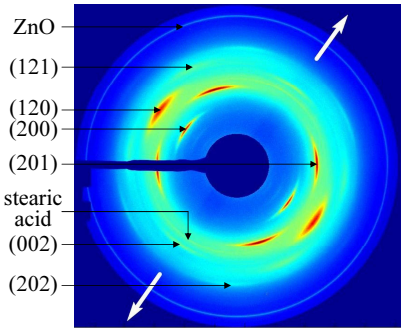

Figure 3.1: (Color online) Example of diffraction pattern of crystallized NR. The white arrows show the tension direction. The Miller indices of the planes corresponding to the diffraction arcs are also indicated in the figure.

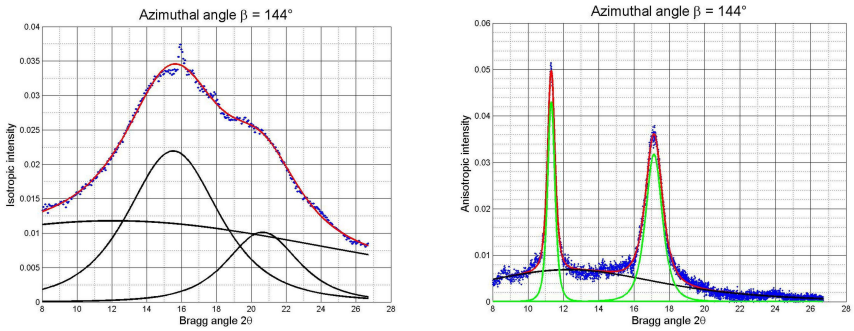

(a) (b)

Figure 3.2: (Color online) Examples of deconvolution of (a) a spectrum (2θ,I_{iso}) and (b) a spectrum (2θ,I_{ani}) fitted by series of Pearson functions.

An index of crystallinity χ is calculated with the same method than Albouy *et al.* (2005):

$$\chi = \frac{\mathcal{I}_{\text{cryst}}}{\mathcal{I}_{\text{cryst}} + \mathcal{I}_{\text{amorphous}}} \tag{3.1}$$

where $\mathcal{I}_{\text{cryst}}$ is the integrated intensity of the (120) and (200) peaks (measured on one (2θ,I_{iso}) spectrum at the azimuthal angle of highest intensity of the peaks) and $\mathcal{I}_{\text{amorphous}}$ is the integrated intensity of the amorphous halo, considered equal to the intensity I_{iso} integrated on one spectrum as well.

The lattice parameters of the crystall cell of the polyisoprene are calculated considering an orthorhombic crystal system, as recently determined by Immirzi *et al.* (2005) and Rajkumar *et al.* (2006). On the scattering pattern, we identify 18 diffraction arcs that result from the diffraction due to 6 different planes (see Fig. 3.1). As only three lattice parameters (a, b and c) must be calculated, each of them is the average of two values measured from the arcs due to two different diffraction planes. The volume of the unit cell V is simply calculated from the lattice parameters:

$$V = abc. \tag{3.2}$$

Similarly to others (Trabelsi *et al.*, 2003a,b, 2004; Tosaka *et al.*, 2004b; Poompradub *et al.*, 2005; Chenal *et al.*, 2007a), the crystallites size is deduced from the Scherrer formula (Guinier, 1963):

$$l_{hkl} = \frac{K\lambda}{\text{FWHM}_{2\theta}\cos\theta}, \tag{3.3}$$

where l_{hkl} is the crystallites size in the direction normal to the hkl diffraction plane, K is a scalar which depends on the shape of the crystallites (here we adopt 0.78 as Trabelsi *et al.* (2003a)), λ is the radiation wavelength, θ is the Bragg angle and $\text{FWHM}_{2\theta}$ is the full width at half-maximum of the peak hkl in 2θ. An index of the volume of the crystallites $\overline{V}_{\text{cryst}}$ is calculated from the crystallites size in three different directions:

$$\overline{V}_{\text{cryst}} = l_{200} \cdot l_{120} \cdot l_{201}. \tag{3.4}$$

As the geometrical shape of the crystallites in NR remains unknown, it is not possible to calculate the real volume of the crystallites. But in the hypothesis that this shape does not change with strain and fillers, $\overline{V}_{\text{cryst}}$ is proportional to the real mean volume of the crystallites.

Assuming the incompressibility of the material, and that the volume crystallinity is equal to the mass crystallinity, we calculate an index of number of crystallites per unit volume N:

$$N = \frac{\chi V_{\text{irradiated}}}{\overline{V}_{\text{cryst}}}. = \frac{\chi}{\overline{V}_{\text{cryst}}}\frac{\pi R^2 t_0}{\sqrt{\lambda}}, \tag{3.5}$$

where $V_{\text{irradiated}}$ is the volume irradiated by the X-ray beam, R is the radius at half-maximum of the beam, t_0 is the thickness of the sample in the undeformed state and λ is the local stretch ratio of the sample. Then, N is proportional to the real number of crystallites per unit volume.

Finally, the misorientation ψ_{hkl} compared to the mean orientation of the hkl diffraction planes in the crystallites is simply given by half the full width at half-maximum (FWHM_{β}) of the peaks, measured on the azimuthal profiles of the reflection.

3.3 Results and discussion

3.3.1 Stress and crystallinity

Figures 3.3 and 3.4 show the evolution of the nominal stress P and the index of crystallinity χ respectively with the stretch ratio λ, for unfilled (0-NR) and carbon black-filled (CB-NR) NR. Our results are very similar to those obtained by other authors which have

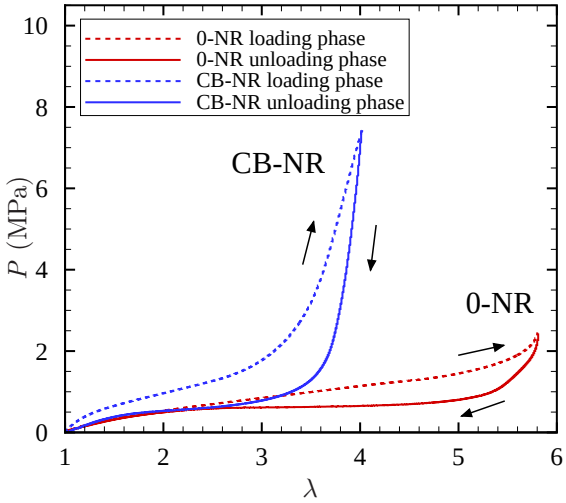

Figure 3.3: (Color online) Evolution of the nominal stress P with the stretch ratio λ for unfilled (0-NR) and filled (CB-NR) natural rubber.

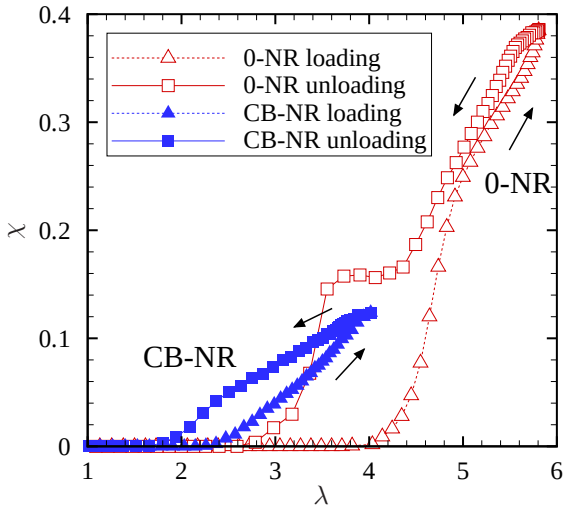

Figure 3.4: (Color online) Evolution of the index of crystallinity χ during a low strain rate cycle for unfilled (0-NR) and carbon black-filled (CB-NR) natural rubber.

been highly discussed already and therefore will only be summarized as follow:

- in Fig. 3.4 we observe an onset of crystallization λ_C and an onset of melting λ_M,
- the fillers in the material increase the stress and the crystallinity. But the maximum crystallinity reached during the cycle is much lower. They also decrease λ_C and λ_M.

We note that the plateau of crystallinity observed during the unloading phase of the 0-NR cycle corresponds to the phenomena called "inverse yielding effect", which have been

observed and studied by Trabelsi *et al.* (2003b) and Albouy *et al.* (2005); it is due to an inhomogeneous deformation along the sample.

3.3.2 Lattice deformation of the crystallites

Figure 3.5 shows the evolution of the lattice parameters a, b and c (Fig. 3.5 (a), (b) and (c) respectively) and of the unit cell volume (Fig. 3.5 (d)) with the stretch ratio, for unfilled and filled NR. Their evolution is quite similar for both materials. We observe that

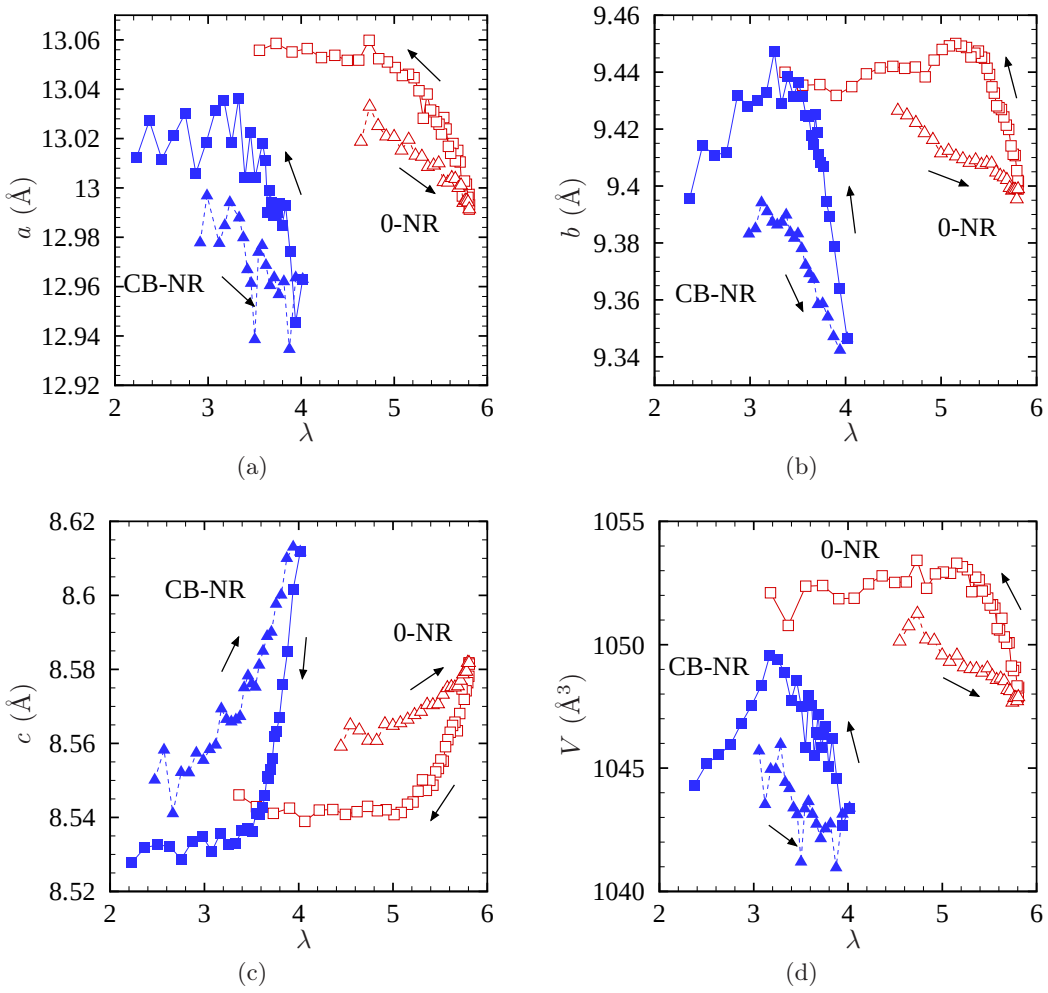

Figure 3.5: (Color online) Evolution of the lattice parameters and unit cell volume during a low strain rate cycle for unfilled (0-NR, unfilled red symbols) and carbon black-filled (CB-NR, filled blue symbols) NR. (a): lattice parameter a. (b): lattice parameter b. (c): lattice parameter b. (d): unit cell volume. Loading phase: triangles; unloading phase: squares.

the parameters a and b and the unit cell volume decrease with the stretch ratio λ whereas the parameter c increases with λ. It means that when the material is stretched, the unit cells are elongated in the direction of tension, which is the c-direction, and contracted in the two other directions. Furthermore, the crystallized phase is compressed as the volume of the unit cell decreases. Those results have already been shown by Tosaka *et al.* (2004b), Tosaka (2007) and Poompradub *et al.* (2005). But in those studies, the measurements performed during loading and unloading phases of the cycle were not differentiated. Here,

we also observe that the evolution of the unit cell with the stretch ratio is different during both phases. More particularly, for a given stretch ratio, the unit cell is less elongated and less compressed during the unloading phase than during the loading phase.

Three differences are observed between unfilled and filled NR:

- in CB-NR, the lattice parameters are quite constant at the beginning of the loading phase between $\lambda = 2.4$ and $\lambda = 3.4$ (due to the scale of λ-axis, the plateau is very short in Fig. 3.5),
- at the end of the unloading phase (from $\lambda = 3.5$ to $\lambda = 2.2$) in CB-NR, b and the volume decrease whereas they are almost constant in 0-NR,
- the unit cell is more elongated and smaller in volume in filled than in unfilled NR.

Quantitatively, the lattice parameters only slightly vary with the stretch ratio: a ranges from 12.71 Å to 12.77 Å in 0-NR and from 12.66 Å to 12.75 Å in CB-NR; b ranges from 9.17 Å to 9.22 Å in 0-NR and from 9.12 Å to 9.21 Å in CB-NR; c ranges from 8.35 Å to 8.40 Å in 0-NR and from 8.34 Å to 8.43 Å in CB-NR. It represents a variation of about 0.5 % for 0-NR and of about 1 % for CB-NR along a cycle. Accordingly, the variation of the unit cell volume along the cycles is very small as well: about 0.5 % in 0-NR and 0.7 % in CB-NR. The three lattice parameters are slightly larger than those previsouly published for both unfilled (Bunn, 1942; Takahashi et Kumano, 2004; Tosaka *et al.*, 2004b; Immirzi *et al.*, 2005; Poompradub *et al.*, 2005; Rajkumar *et al.*, 2006) and filled NR (Poompradub *et al.*, 2005), however this difference is of the same order of magnitude than the discrepancy in the litterature, i.e. about 3 %.

3.3.3 Size and volume of the crystallites

Figure 3.6 shows the size of the crystallites for unfilled NR (from Fig. 3.6 (a) to (f)) and filled NR (from Fig. 3.6 (g) to (l)) in six different directions. The evolution of the mean volume of the crystallites during the two cycles is given in Figure 3.7. The evolution of the volume is of course very similar to the evolution of the size of the crystallites. Those figures lead to the following results:

- the size of the crystallites evolves of about 10 % to 50 %, depending on the material and direction considered,
- the crystallites are slightly smaller in filled than in unfilled NR. Poompradub *et al.* (2005) and Trabelsi *et al.* (2003b) obtained the same result.
- the size ranges from 50 Å to 250 Å for unfilled NR and from 40 Å to 170 Å for filled NR. It is slighly higher than the ones reported by other authors for unfilled NR (Trabelsi *et al.*, 2003b; Tosaka *et al.*, 2004b; Chenal *et al.*, 2007a; Tosaka, 2007). But several authors showed that the size of the crystallites varies significantly with the crosslink density (Trabelsi *et al.*, 2003a; Tosaka *et al.*, 2004b; Tosaka, 2007; Chenal *et al.*, 2007a). This parameter has not been measured for our materials; it is possible that the discrepancy with the bibliography arises from a different crosslink density. For carbon black-filled NR, Poompradub *et al.* (2005) reported a similar size, whereas Trabelsi *et al.* (2003b) obtained much larger crystallites.
- the evolution of the size and volume of the crystallites is the same for both materials and in most directions: during the loading phase, the size of the crystallites decreases with λ; during the unloading phase, it first increases for high stretch ratios and then decreases for small stretch ratios. Moreover, for a given stretch ratio, the crystallites are larger during the loading than during the unloading phase for small stretch ratios, whereas it is the opposite for high stretch ratios, as shown by the "loop" in the figures. Other authors reported the same evolution for unfilled NR (Tosaka *et al.*, 2004b;

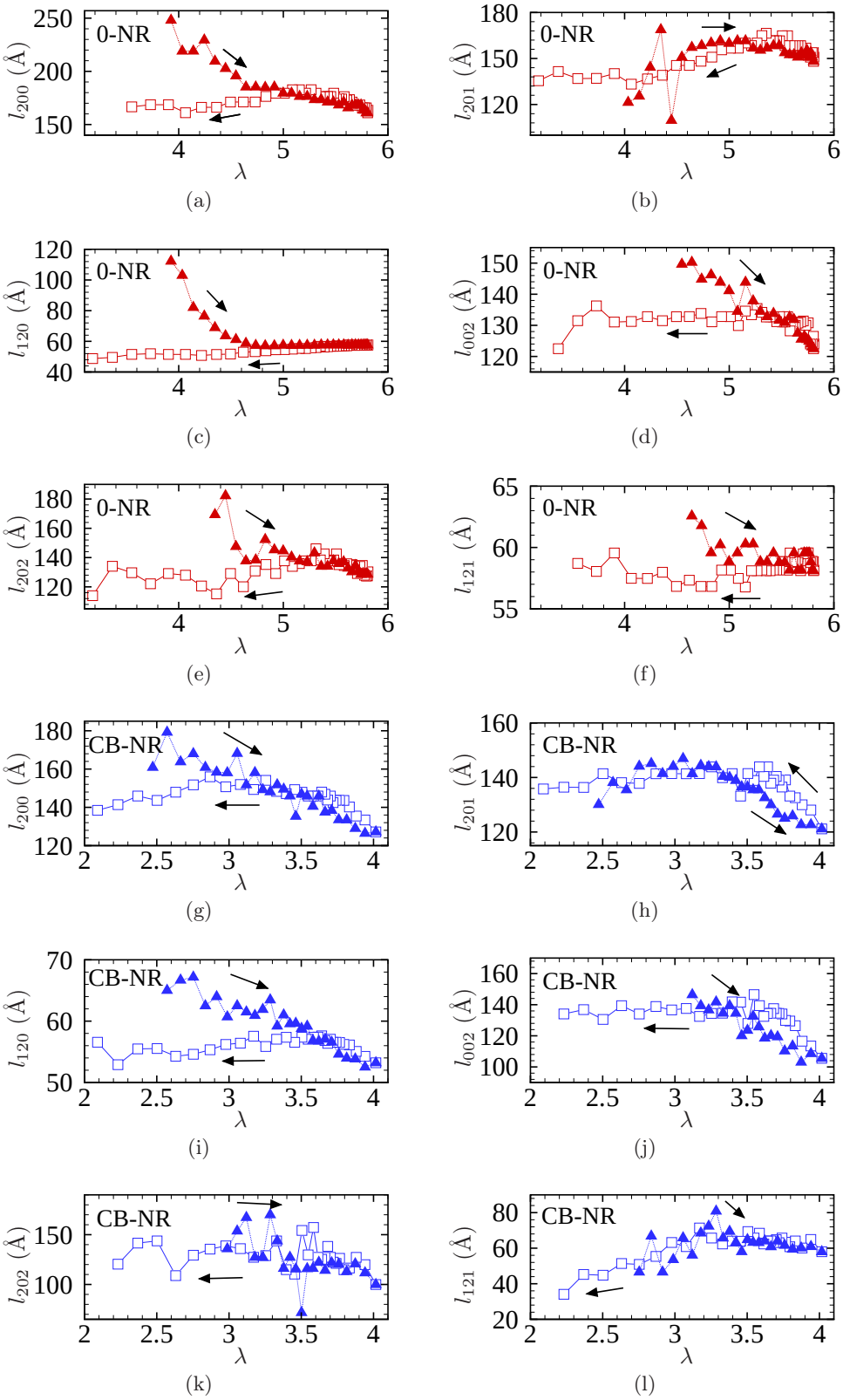

Figure 3.6: (Color online) Evolution of the size of the crystallites during a low strain rate cycle for unfilled (0-NR, red symbols, from (a) to (f)) and carbon black-filled (CB-NR, blue symbols, from (g) to (l)) NR. l_{hkl} is measured in the direction normal to the (*hkl*) diffraction planes. Loading phase: filled triangles; unloading phase: unfilled squares.

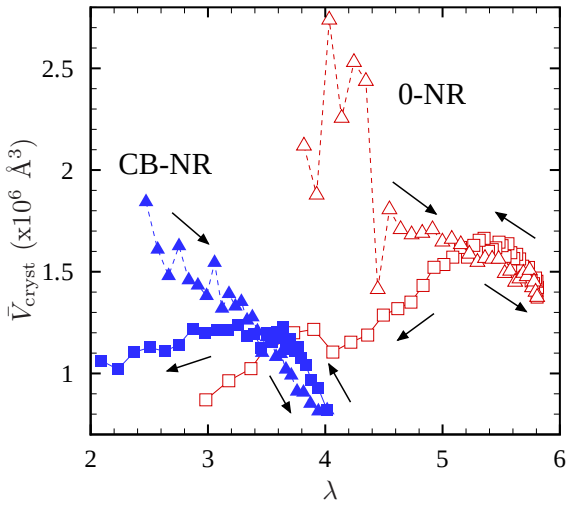

Figure 3.7: (Color online) Evolution of the volume of the crystallites during a low strain rate cycle for unfilled (0-NR, unfilled red symbols) and carbon black-filled (CB-NR, filled blue symbols) NR. Loading phase: triangles; unloading phase: squares.

Tosaka, 2007; Poompradub *et al.*, 2005; Trabelsi *et al.*, 2003a,b, 2004) and filled NR (Trabelsi *et al.*, 2003b; Poompradub *et al.*, 2005), eventhough Trabelsi *et al.* (2003b) concluded to a constant size during the cycle and achieved only small stretch ratios for the carbon black filled NR. Our observation highly differs from the evolution measured by Chenal *et al.* (2007a) who showed that the size increases or is constant with λ for an unfilled NR. As it is not explicitely detailed in the article during which phase of a cycle the measurements were performed, it is possible they were performed during the unloading phase, which would be more consistent with our results and other authors' results.

3.3.4 Number of crystallites

The evolution of the number of crystallites per unit volume of material N with the stretch ratio is presented in Figure 3.8. It is very similar to the evolution of the index of crystallinity: it increases with λ; it is higher during the unloading phase than during the loading phase; crystallites first appear at the threshold of crystallization λ_C and the material is amorphous for stretch ratios smaller than the threshold of melting λ_M; λ_M is lower than λ_C; finally there are more crystallites in filled NR than in unfilled NR for a given stretch ratio but the maximum number of crystallites reached is much smaller.

Figs. 3.4, 3.7 and 3.8 demonstrate that the evolution of the degree of crystallinity along a cycle is mostly due to the nucleation and melting of crystallites, rather than to the change in size of the existing crystallites. During the loading phase, the decrease of $\overline{V}_{cryst}$ with λ is over-compensated by the large increase in N, it results in an increase in χ. Moreover, the hysteresis of χ observed in Fig. 3.4 arises from a larger number of crystallites during the unloading phase than during the loading phase. Finally, the higher maximum degree of crystallinity reached in unfilled NR compared to carbon black-filled NR is due to both larger crystallites and mainly a larger number of crystallites.

It is to note that for very high stretch ratios, the number of crystallites measured during the unloading phase is lower than during the loading phase: we observe a very small "loop" in both CB-NR and 0-NR curves in Fig. 3.8. It might by due to the method of

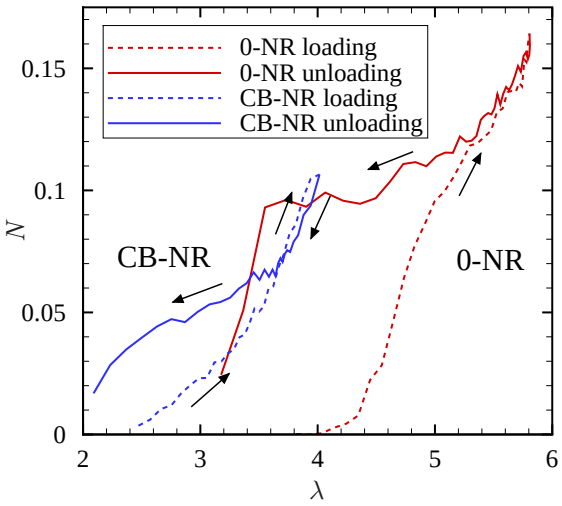

Figure 3.8: (Color online) Evolution of the number of crystallites per unit volume of undeformed material during the low strain rate cycles for unfilled (0-NR) and carbon black-filled (CB-NR) natural rubber.

measurement. Indeed, to calculate the number of crystallites it is necessary to assume that the material is incompressible. But it is established that *(i)* amorphous elastomer is not incompressible, *(ii)* the density increases when rubber crystallizes (Le Cam, 2010) and *(iii)* the volume of the unit cells of the crystallites decreases with λ as shown in Fig. 3.5 (d). For this reason, these "loops" are not discussed here as they may only be an artifact.

3.3.5 Misorientation of the crystallites

Figure 3.9 gives the misorientation compared to the mean orientation of six different diffraction planes of the crystallites during a cycle for unfilled NR and five different planes for filled NR. The misorientation of the sixth plane (121) is not given as the results are too noisy to be conclusive. Their evolution during a cycle is very different in unfilled and filled NR:

- In unfilled NR (Fig. 3.9 (a) to (f)), the misorientation slightly decreases with λ during the loading phase. During the unloading phase, it evolves in three stages: it first slightly decreases, then it increases significantly, finally it is nearly constant at the end of the cycle. The misorientation is higher during most of the unloading phase than during the loading phase. This evolution is similar for the six diffraction planes studied here, expect for the plane (002) at the beginning of the loading phase. It is also similar to the evolution reported by other authors (Trabelsi *et al.*, 2003a,b; Tosaka *et al.*, 2004b; Poompradub *et al.*, 2005; Tosaka, 2007).
- In filled NR (Fig. 3.9 (g) to (k)), the misorientation increases at the beginning of the loading phase and then slightly decreases. During the unloading phase, it first decreases and then slightly increases or is constant, depending on the diffraction planes considered. The misorientation is higher during the loading phase than during the unloading phase. Trabelsi *et al.* (2003b) showed the same result, but only for small stretch ratios. Poompradub *et al.* (2005) obtained very different results: they observed that the evolution of the misorientation is similar in filled and in unfilled NR.
- Quantitatively, the misorientation of the crystallites does not change much during

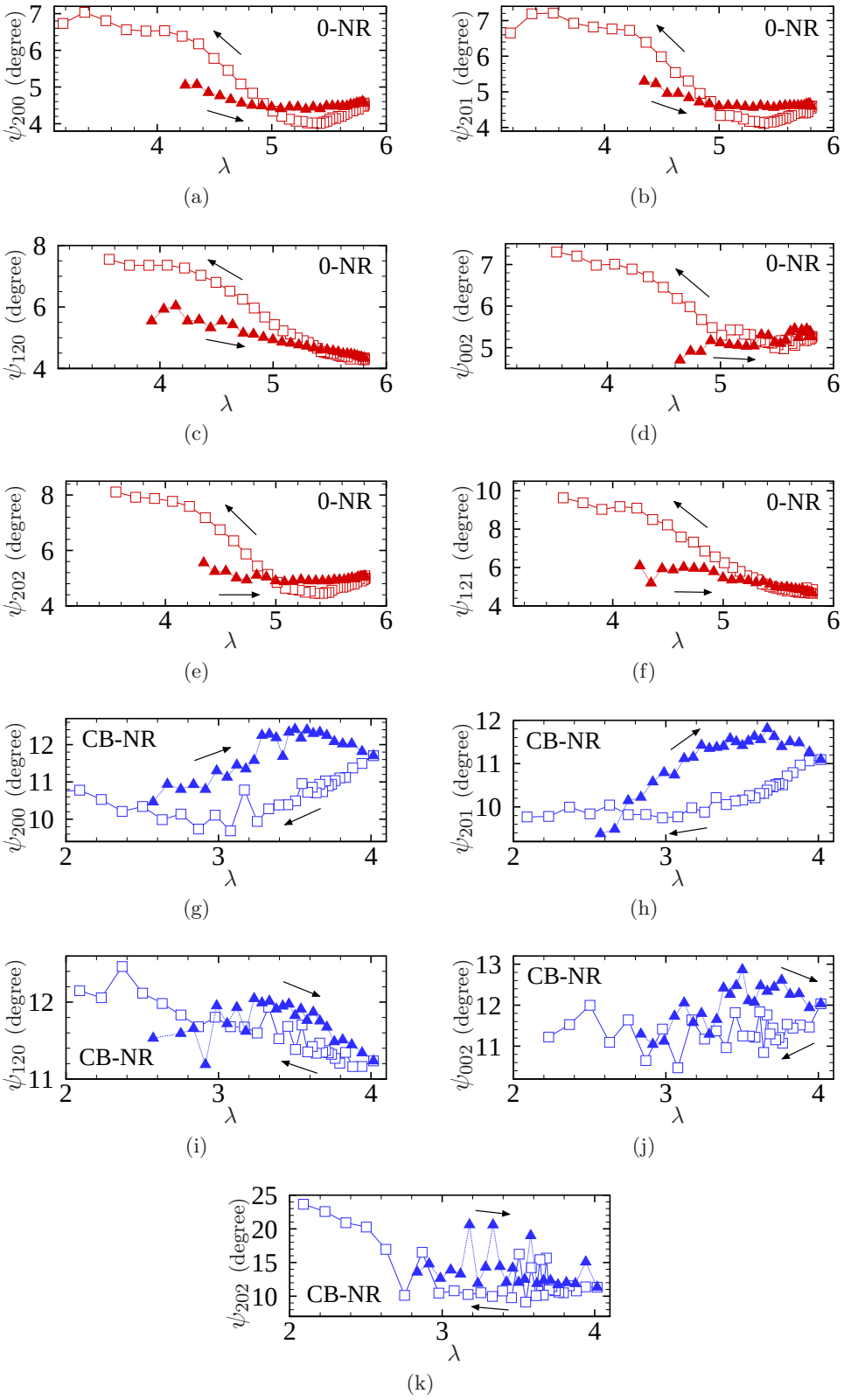

Figure 3.9: (Color online) Evolution of the misorientation of the diffraction planes of the crystallites compared with their mean orientation during a low strain rate cycle for unfilled (0-NR, red symbols, from (a) to (f)) and carbon black-filled (CB-NR, blue symbols, from (g) to (k)) NR. The Miller indices *hkl* are given in the ordinate of the graph ψ_{hkl}. Loading phase: filled triangles; unloading phase: unfilled squares.

a cycle and is twice larger in filled NR than in unfilled NR: it ranges from about $\pm 4°$ to $\pm 8°$ in 0-NR and from $\pm 10°$ to $\pm 13°$ in CB-NR. Those values are similar to those measured by other authors (Trabelsi *et al.*, 2003a,b; Tosaka *et al.*, 2004b; Poompradub *et al.*, 2005; Chenal *et al.*, 2007a; Tosaka, 2007) except for two studies. Poompradub *et al.* (2005) showed that in unfilled NR the misorientation of the crystallites is very close (but smaller) to the misorientation in filled NR. Trabelsi *et al.* (2003b) obtained larger misorientation in filled NR: it varies from $\pm 17°$ to $\pm 20°$.

3.4 SIC mechanism in unfilled and filled NR

In Figure 3.10 we propose a simple model of the evolution of the characteristics of the crystallites during a low strain rate cycle in unfilled and filled NR, i.e. the lattice parameters and the unit cell volume (Fig. 3.10 (c) to (f)), the crystallites volume (Fig. 3.10 (g) and (h)) and the crystallites misorientation (Fig. 3.10 (i) and (j)). Moreover, the evolution of the nominal stress is reminded in Fig. 3.10 (a) and (b). This model is purely qualitative and the quantitative differences between the two materials are not reported here. For this reason, no scales are given for the different axes.

In this section, we first justify the assumptions of this model. Then, with the help of our model we discuss whether or not crystallites evolve during a cycle once they are nucleated. Further, we propose a mechanism of strain-induced crystallization in unfilled NR. Finally, the mechanism of SIC in carbon black-filled NR and the differences between unfilled and filled NR are discussed.

3.4.1 SIC model

In 0-NR, during the loading phase, the evolution of the different characteristics with λ is monotonous. On the contrary, we observe in Figs. 3.7, 3.9 (a) to (f) and 3.5 changes of slope during the unloading phase; they occur roughly at the same stretch ratio for all the characteristics. In the following, this specific stretch ratio is called λ_u^* (u as *unloading*) and its value is about $\lambda_u^* = 5.4$. This value is approximative and not very easy to determine as the changes of slope are gradual, particularly for the lattice parameters. In order to exacerbate the different phases of evolution of the crystallites along a cycle, we choose sharp changes of slope in Fig. 3.10. Moreover, for the same reason and to simplify the interpretation of those evolutions in term of SIC mechanism, the very slight increases or decreases of values are modelized as constant, such as the lattice parameters and the unit cell volume at the end of the unloading phase and such as the misorientation of the crystallites at the end of the loading phase. Furthermore, as described in the section *Results and discussion*, the evolution of the crystallites misorientation with the stretch ratio varies from one diffraction plane to another. In particular, ψ_{002} increases during the loading phase whereas the misorientation of the five other planes decreases. Moreover the change of slope during the unloading phase occurs around $\lambda = 5.7$ for the planes (120) and (121) and not around $\lambda_u^* = 5.4$. For the model, we considered only the "average" evolution of the various ψ_{hkl}, i.e. the evolution shared by most of the diffraction planes, as shown in Fig. 3.10 (g).

As already reported in the section *Results and discussion*, the evolution of the lattice parameters, the unit cell volume and the crystallites volume in CB-NR is quite similar to their evolution in 0-NR (see Figs. 3.7, 3.9 (g) to (k) and 3.5). As in 0-NR, the changes of slope during the unloading phase occur at the same stretch ratio, $\lambda_u^* = 3.6$ for this material. As the onsets of crystallization λ_C and melting λ_M are lower for CB-NR than for 0-NR, it is

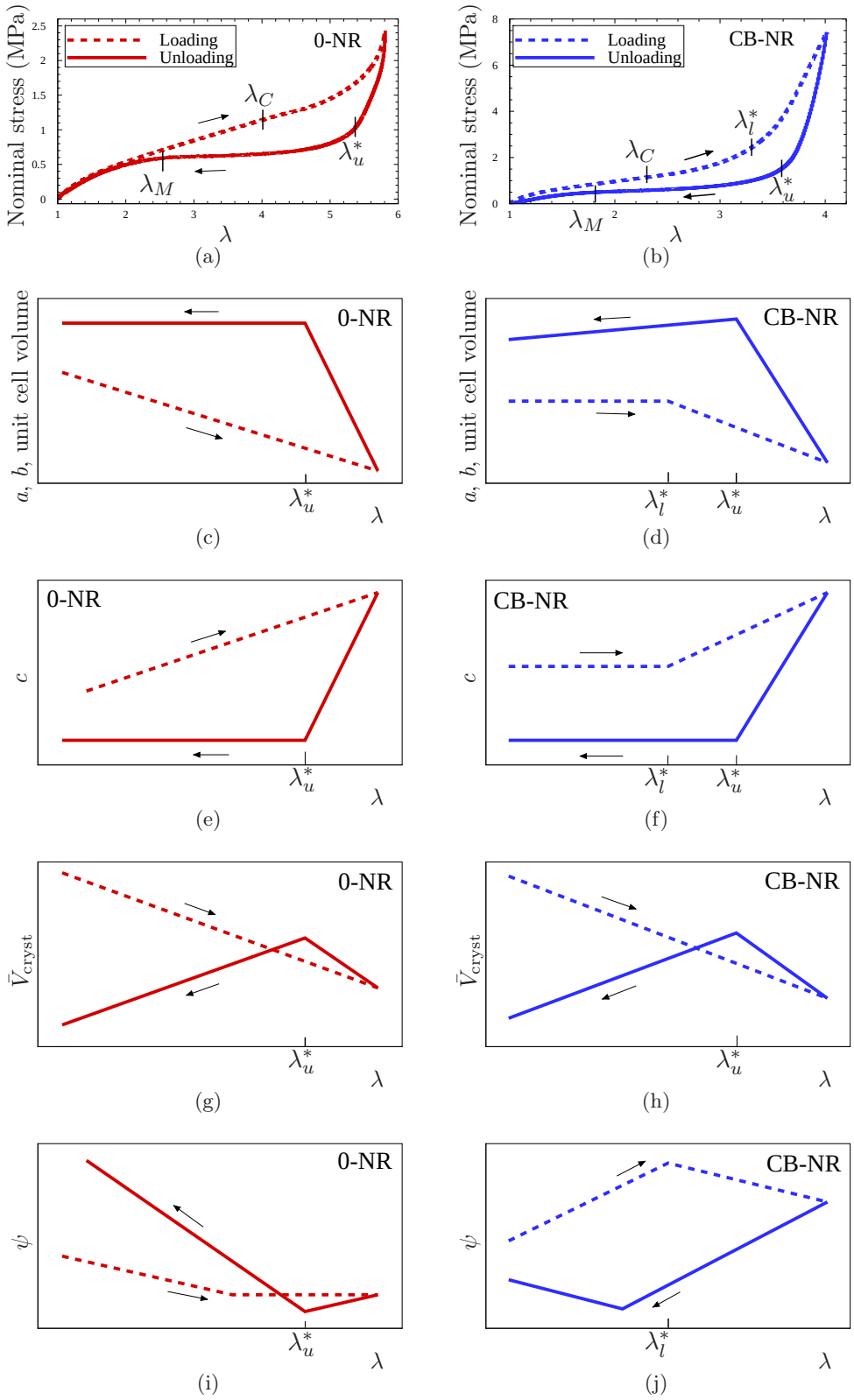

Figure 3.10: (Color online) Model of the evolution of the nominal stress and of the different characteristics of the crystallites during a low strain rate cycle in unfilled (0-NR) and carbon black-filled (CB-NR) NR.

not surprising to observe a lower λ_u^* as well. Contrary to unfilled NR, we observe in carbon black-filled NR a second characteristic stretch ratio $\lambda_l^* = 3.3$ (l as *loading*). It corresponds to a change of slope of the lattice parameters, the unit cell volume and the misorientation of the crystallites during the loading phase of a cycle. As for 0-NR, the evolution of the misorientation varies from one diffraction plane to another and only the "average" evolution is modelized in Fig. 3.10 (j). Also, the evolution of the different crystallites characteristics are as well exacerbated, in order to emphasize the mechanisms involved. Furthermore, it is to note that two changes of slope are isolated, i.e. they do not occur at the same stretch ratio than other changes of slope: the misorientation of the crystallites during the loading phase in unfilled NR and the misorientation during the unloading phase in filled NR.

Finally, the different characteristic stretch ratios λ_C, λ_l^*, λ_u^* and λ_M are reported on the stress-strain curves in Fig. 3.10 (a) and (b). We observe that λ_l^* and λ_u^* correspond to major changes of slope in the stress-strain curves: for $\lambda_l^* < \lambda < \lambda_u^*$, the stiffness of the materials is very high. This model proposed in Fig. 3.10 is a simplification of reality but offers a more adapted base to discuss the mechanism of SIC in NR than the experimental data.

3.4.2 Evolution of a crystallite once nucleated

Before proposing a mechanism of strain-induced crystallization, it is here necessary to recall that any measurement performed by X-ray diffraction experiment is an average over all the crystallites present in the irradiated material; this technique does not allow to measure the dispersion of a characteristic of the crystallites. During the loading phase, the number of crystallites highly increases with the stretch ratio as shown in Fig. 3.8. Therefore, a decrease or an increase of the crystallites characteristics (such as the lattice parameters, the unit cell volume and the crystallites volume and misorientation) with the stretch ratio can be the result of either two phenomena:

- Once a crystallite is nucleated, it does not evolve. But as λ changes, new crystallites nucleate and are different from the crystallites already present in the material. The measured average over all the crystallites is modified.
- A change in λ has an effect on the crystallites already present in the material. All the crystallites are identical and the average quantity changes because all the crystallites change. The new crystallites that nucleate at a given λ are similar to the older modified crystallites.

Similarly, during the unloading phase, the crystallites melt and the uncertainty remains on the origin of a decrease or an increase of an average.

In the following, we determine whether or not the different characteristics of a crystallite already nucleated can evolve with λ by a reasoning by elimination.

As shown in Fig. 3.10 (c) and (d), the lattice parameters a and b decrease with λ during the loading phase. If the lattice parameters of the crystallites already nucleated cannot evolve, it means that at a new higher λ, new crystallites nucleate with smaller lattice parameters. In this hypothesis, at the end of the loading phase, the lattice parameters vary from one crystallite to another but are always smaller than the ones of the crystallites nucleated at the beginning of the cycle. Therefore, after melting of most of the crystallites during the unloading phase, the lattice parameters a and b of the last crystallites which remain in the material at the end of the unloading phase should be equal or smaller to than the ones measured at the beginning of the cycle. But we observe that the averages of a and b are greater at the end of the unloading phase than at the beginning of the loading phase. This contradiction means that the parameters a and b of each crystallite evolve

with λ, and are probably equal for all the crystallites for a given stretch ratio. The same reasoning applied to the unit cell volume and to the lattice parameter c demonstrates that those evolve as well with the stretch ratio along the lifetime of the crystallites. The same reasoning can be applied to CB-NR as well.

Similarly, in unfilled NR, the misorientation of the crystallites decreases with λ along the loading phase. Considering that the orientation of a crystallite cannot change, then at the end of the loading phase, the crystallites have different misorientations but always lower than the one measured at the beginning of the cycle. Therefore, it is not possible that at the end of the unloading phase the average misorientation of the last crystallites is greater than at the beginning of the loading phase. For this reason, we conclude that the orientation of a crystallite evolves during a stretching cycle. It is not possible to apply the same reasoning to carbon black-filled NR; but we believe that if crystallites in unfilled NR have the ability to change their orientation during a cycle, crystallites in filled NR have too.

Finally, it is difficult to prove whether or not the volume of a crystallite may change once nucleated. Tosaka *et al.* (2004b) suggested that the misorientation of a crystallite is related to its size because it is bent. This would mean that $\overline{V}_{cryst}$ and ψ would be correlated, and that a given change in $\overline{V}_{cryst}$ would always lead to the same change in ψ; it is clearly not the case here (see Fig. 3.10 (g) to (j)). Moreover, the change in $\overline{V}_{cryst}$ cannot be explained by the change in the unit cell volume: the orders of magnitude are very different, and during the unloading phase the unit cell volume increases when the crystallites volume decreases. It means that of change in volume of a crystallite is due to the addition or the subtraction of macromolecules in it. In this case, we would expect that an increase and a decrease of λ have opposite consequences on the crystallites macromolecules; but we observe that this is not the case as $\overline{V}_{cryst}$ decreases during both loading and unloading phases. Therefore, we believe that it is very improbable that a crystallite volume changes once nucleated.

As a summary:

- the lattice parameters, the unit cell volume and the misorientation evolve along crystallites lifetime, and they are the same for all the crystallites at a given stretch ratio,
- once a crystallite is nucleated, its size and volume probably do not change, i.e. a change in $\overline{V}_{cryst}$ is due to nucleation or melting of crystallites wich have a different volume than the other ones.

Most probably, this description is a simplification of reality and crystallites may coexist in the material with slightly different lattice parameters and misorientation, and the size of a crystallite may change a little along its lifetime. But in a first approach, it may be useful to simplify the very complex physical phenomena at stake in order to be able to propose a mechanism of strain-induced crystallization.

3.4.3 SIC mechanism in unfilled NR

Based on Fig. 3.10, during a low strain-rate cycle, the crystalline phase of unfilled NR evolves in different stages:

1. From $\lambda = 1$ to λ_C, the material is totally amorphous.
2. At λ_C, a first crystallite appears.
3. From λ_C to $\lambda_{\max}$, the number of crystallites increases. As λ increases, the crystallites nucleate with a smaller and smaller size, i.e. they contain less and less macromolecules. The reason for this phenomenon is unknown. It is established that vulcanized NR is not homogeneous and that some macromolecules have a greater mobility

than others. It is possible that the areas of the material where the mobility of the macromolecules is lower are less favourable sites to nucleation: the crystallites appear only at very high stretch ratios and are smaller when they nucleate. We note that this assumption is somewhat similar to the assumptions of Fukahori (2010). Moreover, while the material is more and more stretched, the c-axis of the unit cells of all the crystallites gets better aligned with the tension direction, i.e. the misorientation of the crystallites decreases. It might simply be due to the fact that the crystallites follow the flow of amorphous chains in the tension direction. Finally, during this phase, the unit cell of all the crystallites are elongated in the tension direction and contracted in the two other directions, probably because of the stress which the crystallites are subjected to because of the neighboring amorphous macromolecules. This lattice deformation leads to a decrease in the unit cell volume.

4. At the beginning of the unloading phase, from $\lambda_{\max}$ to λ_u^*, the number of crystallites decreases. It corresponds to a drop of the nominal stress. Also, the local stress applied to the unit cells drops: they are less elongated in the tension direction and less contracted in the two other directions and their volume increases rapidely. During this phase, the crystallites get more aligned which is surprising because the material is less stretched. Finally, $\overline{V}_{\text{cryst}}$ increases which means that the crystallites which melt during this phase are the smallest ones, i.e. the ones which had nucleated at the end of the loading phase. It means that the amorphous part of the macromolecules of those crystallites were stretched close to the onset of melting λ_M when the global stretch ratio was $\lambda_{\max}$.
5. From λ_u^* to λ_M, the evolution of the material and the crystallites is very different, eventhough the number of crystallites decreases at the same rate. The nominal stress is almost constant during this phase. The lattice parameters are now constant, as if the local stress applied to the unit cells was constant too. The a and b-axes are larger and the c-axis is smaller than during the loading phase, as if for a given stretch ratio of the material, the local stress applied to the unit cells was lower during this unloading phase than during the loading phase. The misorientation of the crystallites sharply increases and is even higher than during the loading phase. This increase might reflect a local buckling of the crystallites. Finally, the mean volume of the crystallites decreases, which means that for $\lambda < \lambda_u^*$, the biggest crystallites, i.e. the ones that nucleated at the beginning of the loading phase, melt first. It is surprising and opposite to what happens from $\lambda_{\max}$ to λ_u^*.
6. When the material reaches λ_M, the last crystallite melts.
7. From λ_M to $\lambda = 1$, the material is totally amorphous again and the stress decreases down to zero.

The stretch ratio λ_u^* appears to be a critical stretch ratio at which the mechanisms involved at the macromolecular scale completely change. It is revealed by the changes of slope of the evolution of the crystallites characteristics. It corresponds to an important change of state of the material both at macroscopic and microscopic scales. Indeed, at a macroscopic scale, the stress drops before λ_u^* but is almost constant from λ_u^* to λ_M. At a microscopic scale, for $\lambda < \lambda_u^*$, the lattice parameters are constant and the misorientation of the crystallites increases, which is consistent with a decrease of a local stress applied to the crystallites.

Eventhough this specific stretch ratio has not been particularly noticed by the authors, the experimental data from Trabelsi *et al.* (2003b) and Tosaka *et al.* (2004b) show as well changes of slope at the same stretch ratio on the stress-strain response, the crystallites

misorientation and the crystallites size versus the strain. Trabelsi *et al.* (2003b) and Rault *et al.* (2006a) have described SIC during a low strain-rate cycle in different stages. The onsets of crystallization and melting noted A and E by the authors are the same than the ones noted λ_C and λ_M here. The stretch ratio D is somewhat different from λ_u^*, but it is possible that they correspond to the same phenomenon and that the difference between the two stretch ratios arises only from the method of determination. The authors also noted a specific stretch ratio on the stress-strain curve, called B, during the loading phase. Because it does not corrrespond to any peculiar changes on the crystallized phase of NR, we chose here not to describe it as a specific stretch ratio for SIC in unfilled NR.

3.4.4 Differences between unfilled and filled NR

As described in Section *Results and discussion*, SIC in carbon black-filled NR is quantitavely quite different from SIC in unfilled NR. But qualitatively, the evolution of the crystalline phase during a low strain rate cycle is very close for both materials, as summarized in Fig. 3.10. Two main differences have been highlighted: *(i)* a specific stretch ratio during the loading phase noted λ_l^* exists and *(ii)* the evolution of the misorientation of the crystallites is very different ; they are now discussed.

As shown in Fig. 3.10 (b), the stretch ratio λ_l^* corresponds to a change of slope in the stress-strain curve during the loading phase, i.e. a large increase of the stiffness of the carbon black-filled NR. During the unloading phase, the evolution of the stress is very similar to its evolution for unfilled NR: first a drop of stiffness, then from λ_u^* the stress is almost constant, and finally for $\lambda < \lambda_M$ the stress decreases again.

The evolution of the lattice parameters is quite similar for both materials, as shown in Fig. 3.10 (c), (d), (e) and (f). But in filled NR, the parameters are constant for $\lambda < \lambda_l^*$, as if the crystallites were not as constrained as in unfilled NR. Also, we observe that at the end of the unloading phase, the unit cell volume and the lattice parameters a and b are not constant but slightly decrease which is unexpected.

Eventhough the volume of the crystallites is quantitatively very different in unfilled and filled NR, we observe that its evolution along a cycle is qualitatively similar, as shown in Fig. 3.10 (g) and (h). It suggests that carbon black fillers only have a small effect on crystallites nucleation. In particular, we do not observe any changes of slope at λ_l^*, which is a specific stretch ratio related to presence of carbon black fillers.

Besides, as shown in Fig. 3.10 (i) and (j), the misorientation of the crystallites is very different both quantitatively and qualitatively in the two materials. In filled NR, during the loading phase, the misorientation first increases and then decreases, the change of slope occuring at λ_l^*. During the unloading phase, it first decreases and then increases, but the change of slope occurs at a stretch ratio much lower than λ_u^*. Furthermore, contrary to unfilled NR, the misorientation is significantly lower during the unloading phase than during the loading. This evolution of the misorientation is unexplained yet.

Finally, the stretch ratio λ_l^* appears to be a critical stretch ratio, as λ_u^*, at which a significant change of mechanism occurs, which is revealed by the different changes of slope of the evolution of the crystallites characteristics.

3.5 Conclusion

To summarize the major results of this paper: during a quasi-static tensile cycle of unfilled and carbon black-filled NR, we observe that

- in both rubbers, the degree of crystallinity evolves mainly because of the evolution of N, i.e. the nucleation and melting of new crystallites; once nucleated, the crystallites do not change much in size,
- four specific stretch ratios exist: the onsets of crystallization λ_C and melting λ_M, which had already been observed, but also the stretch ratios λ_l^* (in carbon black-filled NR only) and λ_u^* during the loading and unloading phases respectively. Those stretch ratios are onsets for major changes of mechanism at the macromolecular scale which most probably influence as well the mechanical behavior of the material,
- finally, strain-induced crystallization is qualitatively very similar in unfilled and carbon black-filled NR, i.e. the lattice parameters, the unit cell volume and the size of the crystallites evolve in similar ways, except for the misorientation of the crystallites which evolves in very different ways in the two materials,
- quantitatively, we observe more differences: the crystallites are smaller and more misoriented and the unit cells are smaller in carbon black-filled NR than in unfilled NR.

3.6 Acknowledgment

The authors thank Dr D. Thiaudière, Dr C. Mocuta and Dr A. Zozulya from the DiffAbs beamline in Soleil synchrotron facility and the Soleil staff for their great help during the experiments.

Troisième partie

Multiaxialité

Dans cette troisième partie, nous nous intéressons maintenant à la cristallisation sous contrainte multiaxiale. Cette partie est composée de deux chapitres, dont les références et les résumés sont donnés ci-dessous. Dans le premier chapitre, nous comparons la cristallisation sous contrainte en chargement uniaxial et équibiaxial, et montrons que les cristallites diffèrent principalement par leur orientation. Puis nous étudions plus en détails l'orientation des cristallites en fonction de la multiaxialité de la déformation. Dans le deuxième chapitre, nous abordons l'effet du chemin de chargement sur cette orientation.

Orientation of strain-induced crystallites in natural rubber subjected to multiaxial deformation

S. Beurrot-Borgarino, B. Huneau, E. Verron
Les principaux résultats de cette étude seront soumis à European Physical Journal E

La cristallisation sous contrainte du caoutchouc naturel chargé au noir de carbone en traction multiaxiale est étudiée. Des éprouvettes cruciformes spécifiques et une machine de traction ont été développées pour réaliser des essais de diffraction des rayons X, qui ont été menés sur la ligne DiffAbs du synchrotron Soleil (France). Alors qu'un cliché de diffraction des rayons X classique en traction uniaxiale présente des arcs de diffraction, un cliché en déformation équibiaxiale est composé de deux anneaux intenses qui reflètent la nature non-orientée de la cristallisation sous contrainte. En effet, la cristallisation sous contrainte du caoutchouc naturel en déformation équibiaxiale est isotrope dans le plan de traction, alors qu'elle est fortement orientée en traction uniaxiale. La comparaison entre ces états de déformation montre que la taille des cristallites est du même ordre de grandeur et que les paramètres de maille sont identiques ; seule l'orientation diffère.

Ensuite, l'étude montre que pour tous les états de déformation multiaxiale dans le plan (traction uniaxiale, cisaillement, traction biaxiale), sauf les déformations équibiaxiales, l'axe c de la maille élémentaire des cristallites est parallèle à la direction de plus grande extension. En déformation équibiaxiale, les cristallites ne sont pas orientées dans le plan de traction. La désorientation des cristallites (par rapport à leur orientation moyenne) est constante pour les déformations uniaxiales et le cisaillement pur, et augmente avec la biaxialité dans le cas des déformations biaxiales.

Effect of multiaxial loading path on orientation and misorientation of strain-induced crystallites in carbon black-filled natural rubber

S. Beurrot-Borgarino, B. Huneau, E. Verron
Sera soumis à Journal of Polymer Science Part B : Polymer Physics

L'évolution de l'orientation des cristallites sous contrainte dans le caoutchouc naturel chargé au noir de carbone suivant divers chemins de déformation multiaxiale est mesurée par diffraction des rayons X synchrotron aux grands angles (WAXD). Nous observons que lorsque la multiaxialité de la déformation est modifiée, l'orientation moyenne des cristallites présentes dans le matériau évolue et pour un état de déformation donné ne dépend pas du chemin de déformation parcouru pour parvenir à cet état de déformation.

Chapitre 4

Cristallisation sous contrainte multiaxiale

4.1 Introduction

Natural rubber (NR, cis-1,4-polyisoprene) vulcanizates are widely used in numerous industrial applications because of their specific mechanical properties: they can withstand very large strain ($\approx$ 700-1000 %) before fracture, their tensile strength is quiet large as compared to those of synthetic rubbers, and their fatigue and fracture properties are great. Most of these remarkable features are closely related to their ability to crystallize under strain. Strain-induced crystallization (SIC) of NR has been discovered by Katz in 1925 with the help of X-ray diffraction. This technique has permitted to exhibit the oriented nature of crystallites, to obtain the crystallographic data of NR (Bunn, 1942; Nyburg, 1954) and to relate SIC to the mechanical hysteresis of the stress-strain response (Clark *et al.*, 1941; Toki *et al.*, 2000). This relationship has been recently investigated in real-time by several authors with the help of synchrotron radiation (see Murakami *et al.* 2002; Toki *et al.* 2002, 2003; Trabelsi *et al.* 2003a among others, for a more complete review of these works the reader can refer to Tosaka 2007; Huneau 2011). These studies are now considered essential for the development of SIC models (Tosaka, 2009; Fukahori, 2010) and subsequent constitutive equations (Kroon, 2010).

Most of the previous studies on SIC focused on uniaxial tension. Nevertheless, as engineering applications involve multiaxial loading conditions, the mechanical models must take into account the multiaxiality of the material response; for example, it is well-known that the efficiency of a given constitutive equation for rubberlike materials requires pure shear or biaxial experimental data (Marckmann et Verron, 2006). In this way, the present paper is devoted to the experimental study of equibiaxial strain-induced crystallization of NR by X-ray diffraction using synchrotron radiation. To our knowledge, this is the second study on the influence of biaxiality on strain-induced crystallization of NR: in 1973, Oono *et al.* studied the orientation of crystallites in a stretched thin film of unfilled vulcanized natural rubber at -27°C.

Here, in a first part, we compare *(i)* the lattice parameters of the crystal cell, *(ii)* the size of the crystallites and *(iii)* their orientation when NR is in equibiaxial deformation state and in uniaxial deformation state, at room temperature and for thick samples. We show that the main difference between the crystallized phases in each deformation state is the orientation of the crystallites. Therefore, in a second part, we investigate the orientation of the crystallites of NR subjected to various biaxial deformations. The method of measurement is first applied to three particular cases (uniaxial, biaxial non-equibiaxial and

equibiaxial deformation states) for which the results are detailes. It is then generalized to 82 different multiaxial deformation states.

4.2 Experimental method

4.2.1 Instrumentation

Both uniaxial and equibiaxial experiments have been conducted with the homemade stretching machine shown in Figure 4.1. It is composed of four electrical actuators, which

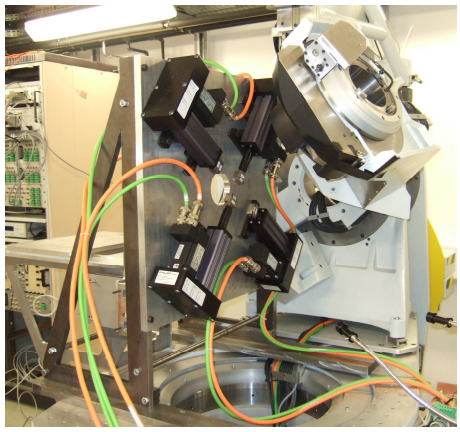

Figure 4.1: Uniaxial and equibiaxial stretching machine in DiffAbs beamline.

displacements can be synchronized or not. Their loading capacity is ±500 N and their stroke is 75 mm each. All the experiments are conducted by prescribing the displacement of these actuators: for equibiaxial tests, the four actuators are used and for uniaxial tests, only two of them are used.

Synchrotron measurements have been carried out at the DiffAbs beamline in the French national synchrotron facility SOLEIL (proposal number 20100096). The wavelength used is 1.319 Å and the beam size is 0.3 mm in diameter at half-maximum. The 2D WAXD patterns are recorded by a MAR 345 CCD X-ray detector. In order to make an accurate correction of air scattering, a PIN-diode is used.

4.2.2 Samples and material

Obtaining biaxial and equibiaxial deformations for soft materials is not an easy task (Demmerle et Boehler, 1993). For our study, we developed a cruciform sample, which is a symmetric cross, thinned at its center in order to achieve higher strain levels without breaking the arms of the sample, as shown in Figure 4.2 (a). Under loading, the arms of the sample are uniaxially stretched, the central part is in a complex deformation state and various multiaxial deformations can be obtained at the center point of the specimen, depending on the amplitudes of stretching of the arms of the cross. For example, if the four arms are equally stretched, the center of the sample is in equibiaxial loading conditions, as in Figure 4.2 (b). Biaxial non-equibiaxial deformationis obtained by stretching two opposite arms more than the two other ones. To obtain planar tension at the center of the sample, two opposite arms are stretched while the two other ones are kept fixed. In all cases, stretching of opposite arms is always symmetric in order to keep the center of the sample fixed and aligned with the beam. In the case of equibiaxial loading conditions,

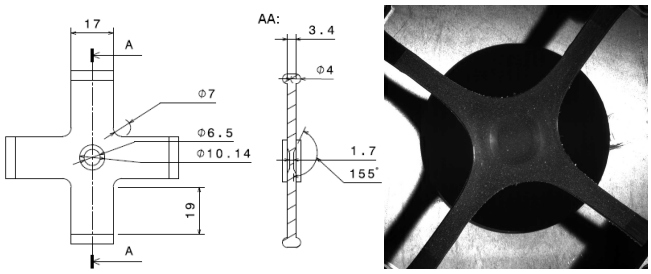

(a) (b)

Figure 4.2: Cruciform sample for multiaxial tests. (a) Dimension of the sample. (b) Sample in equibiaxial loading conditions.

both homogeneity and equibiaxiality were verified by finite element analysis and the zone in which the material is subjected to nearly equibiaxial tension is quiet larger than the beam spot, i.e. about 3 mm^2. Uniaxial samples are classical dumbbell specimens with a 10 mm gauge length and a 2 mm $\times$ 4 mm section. Local strain at the center of both equibiaxial and uniaxial samples are classicaly measured by optical means.

The primary objective of this study was the analysis of SIC in vulcanized NR without fillers. Nevertheless, preliminary equibiaxial experiments showed that, even for the maximum displacement of the actuators, it was not possible to reach sufficient strain for the onset of crystallization. It was then decided to investigate the response of a carbon black-filled NR. As demonstrated by number of authors, experimental results for unfilled and filled NR are identical, apart from a simple amplification factor (see Guth 1945; Mullins et Tobin 1965; Harwood et Payne 1966 among others) even for crystallization (Rault *et al.*, 2006a; Chenal *et al.*, 2007b; Tosaka, 2009). The material was cross-linked by 1.2 phr (parts per hundred of rubber) of sulfur; it also contains ZnO (5 phr) and stearic acid (2 phr). It is filled with 50 phr of N330 carbon black.

4.2.3 Procedure

The stretching unit was placed on the stand of the DiffAbs diffractometer (see Fig. 4.1) in order to keep the beam focused on the centre of the samples. The uniaxial experiments are quasi-static (the actuators speed iss set to 0.012 mm/s) and scattering patterns are recorded every 100 seconds (due to the reading time of the CCD detector). The maximum stretch ratio reached during the test is $\lambda = 4.0$ in the direction of tension. For the multiaxial tests, the actuators speed is 30 mm/s, and one pattern is recorded at maximum deformation once the actuators have stopped. The exposure time is short (1 second for uniaxial tests and 3 seconds for multiaxial tests): it permits to reduce the influence of kinetics of crystallization on the results.

An air scattering pattern (without sample) was first collected and it has been used to correct the patterns. Moreover, the change in thickness of the sample under extension and the change of intensity of the incident photons have also been considered. All these corrections are performed by following the well-established method of Ran *et al.* (2001). Here, small angles scattering is not investigated; the range of diffraction angles is $2\theta \in [8°, 26.7°]$. We used the (012) reflection of Cr_2O_3 powder placed on each side of a specimen to calibrate the diffraction angles 2θ ($a = 4.9590$ Å and $c = 1.3596$ Å).

4.2.4 Scattering pattern analysis

The spectra extracted from the diffraction patterns are classically fitted by series of Pearson functions (Toki *et al.*, 2000; Trabelsi *et al.*, 2003a; Rault *et al.*, 2006a; Chenal *et al.*, 2007b) thanks to a homemade Matlab ®code. The lattice parameters of the crystal cell of the polyisoprene are calculated considering an orthorombic crystal system, as determined by Immirzi *et al.* (2005) and Rajkumar *et al.* (2006). In equibiaxial deformation, only the lattice parameters a and c can be calculated. In uniaxial tension, the parameters a, b and c are calculated from the (200), (120) and (201) reflections respectively.

The crystallites sizes are deduced from the Scherrer formula (Guinier, 1963) as Trabelsi *et al.* (2003a):

$$l_{hkl} = \frac{K\lambda}{\mathrm{FWHM}_{2\theta}\cos\theta} \tag{4.1}$$

where l_{hkl} is the crystallites size in the direction normal to the (hkl) plane, K is a scalar which depends on the shape of crystallites (here we adopt 0.78 as proposed by Trabelsi *et al.* (2003a)), λ is the radiation wavelength, θ is the Bragg angle and $\mathrm{FWHM}_{2\theta}$ is the full-width at half-maximum of the (hkl) reflection in 2θ.

The misorientation ψ_{hkl} (compared to the mean orientation) of the (hkl) diffraction plane in the crystallites is simply given by half the full width at half maximum (FWHM_{β}) of the peaks, measured on the azimuthal profiles of the reflection.

Finally, an index of crystallinity χ is calculated:

$$\chi = \frac{\mathcal{I}_{\mathrm{cryst}}}{\mathcal{I}_{\mathrm{cryst}} + \mathcal{I}_{\mathrm{amorph}}} \tag{4.2}$$

where $\mathcal{I}_{\mathrm{cryst}}$ is the integrated intensity of the crystallized phase reflections and $\mathcal{I}_{\mathrm{amorph}}$ is the integrated intensity of the amorphous halo over a quarter of the diffraction patterns by using their symmetries.

4.3 Results and discussion

4.3.1 Uniaxial loading conditions

The diffraction patterns for filled NR in uniaxial tension are shown in Figure 4.3 in the undeformed (Fig. 4.3 (a)) and deformed states at stretch ratio $\lambda = 4.0$ in the direction of tension (Fig. 4.3 (b)). In the undeformed state, the scattering pattern consists of a diffuse amorphous halo, the (100) reflection of ZnO and a dim arc due to stearic acid. Fig. 4.3 (b) was recorded at maximum strain (λ=4.0); it exhibits reflections of crystallized NR. The diffraction pattern is of course oriented according to the stretching direction (see the white arrows in the figure). The pattern is composed of eight intense reflection arcs corresponding to three different crystallographic planes (200), (201) and (120), ten less intense reflection arcs corresponding to three different crystallographic planes (121), (202) and (002), a co-existing amorphous halo and the ZnO and stearic acid reflections. The X-ray spectra corresponding to the deformed state are shown in Figure 4.4: in the transverse direction which goes through the (200) and (120) arcs (Fig. 4.4 (a)), in the direction that goes through the (201) arcs (Fig. 4.4 (b)), and finally in the loading direction which goes through the (002) arcs (Fig. 4.4(c)).

We obtain several results which will be commented in the following discussion:

– crystalline reflections are consistent with the orthorombic crystal system of the polyisoprene determined by Immirzi *et al.* (2005) and Rajkumar *et al.* (2006),

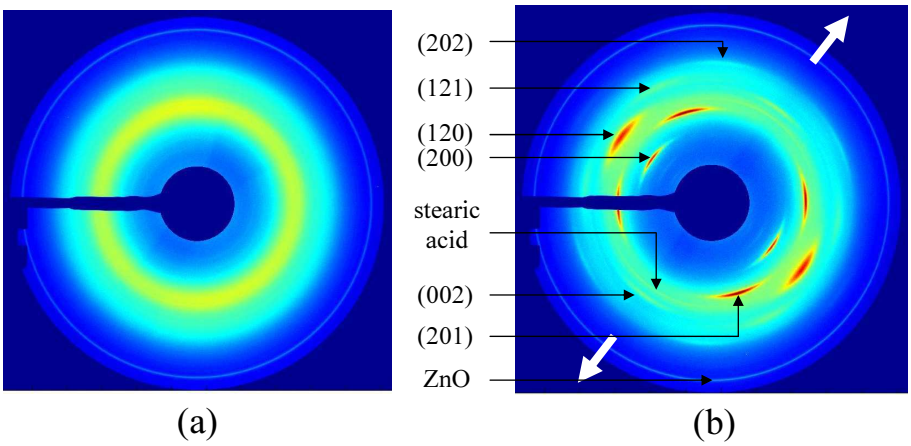

Figure 4.3: WAXD patterns for uniaxial tension conditions: (a) undeformed state, (b) deformed state; the stretch ratio is $\lambda = 4.0$. White arrows show the stretching direction.

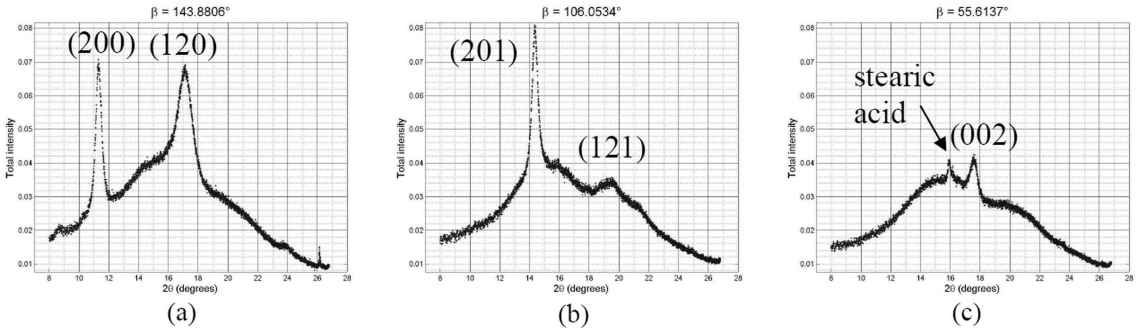

Figure 4.4: X-ray spectrum for uniaxial tension: (a) transverse direction, (b) (201)-direction, (c) loading direction; the stretch ratio in the direction of tension is λ=4.0.

- the lattice parameters are $a = 13.09$ Å, $b = 9.18$ Å and $c = 8.39$ Å,
- the c-axis of the cristal cells in the crystallites are parallel to the tensile direction, as shown by Bunn (1942),
- the misorientation of the (200) and (201) planes of the crystallites are respectively equal to $\psi_{200} = 11.70°$ and $\psi_{201} = 11.09°$,
- the crystallites sizes are l_{200}=127.2 Å and l_{201}=121.1 Å,
- the index of crystallinity is χ=3.37 %.

4.3.2 Equibiaxial loading conditions

Figure 4.5 presents the WAXD patterns for filled NR in equibiaxial tension in the undeformed state (Fig. 4.5 (a)) and deformed state at $\lambda = 2.4$ in every direction of the plane of tension (Fig. 4.5 (b)). Loading directions are given by the white arrows in the figure.

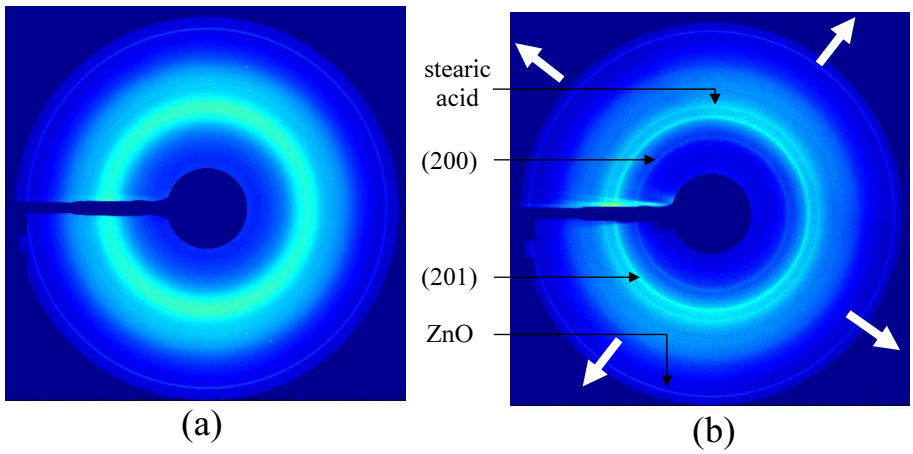

Figure 4.5: WAXD patterns for equibiaxial tension conditions: (a) undeformed state, (b) deformed state; the stretch ratio in every direction of the plane of tension is $\lambda = 2.4$. White arrows show the stretching directions.

As expected, the diffraction pattern in the undeformed state is exactly the same as in the undeformed state in the uniaxial experiment. In the deformed state, the diffraction pattern is composed of two intense rings corresponding to the (200) and (201) diffraction planes, an amorphous halo, and the ZnO and the stearic acid reflections. An X-ray spectrum of the deformed state is shown in Figure 4.6; due to the isotropic nature of the pattern, all radial spectra are identical.

Various results are deduced from Figures 4.5 and 4.6:

- the crystal unit cell is not changed: diffraction angles of the (200) and (201) planes are very close to those observed in uniaxial tension. The corresponding lattice parameters are $a = 13.06$ Å and $c = 8.48$ Å, which differ from the parameters in uniaxial tension of less than 1.1 %,
- reflections of the (200) and (201) planes are full rings: the crystallites are not oriented in the plane of tension,
- the crystallites sizes are l_{200}=149.3 Å and l_{201}=105.2 Å,
- the index of crystallinity is χ=1.09 %.

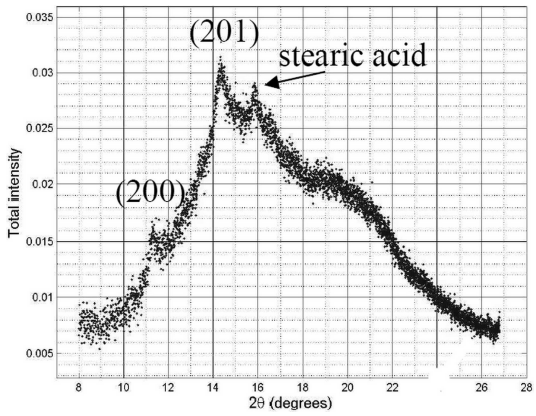

Figure 4.6: X-ray spectrum for equibiaxial tension; the stretch ratio in every direction of the plane of tension is λ=2.4.

4.3.3 Comparison between crystallized phases of NR in uniaxial and equibiaxial loading conditions

The lattice parameters of the crystal cell in uniaxial tension are slightly larger (from 0.1 % to 3.4 %) than those calculated by Poompradub *et al.* (2004) in carbon-black filled NR (a = 12.65 Å, b = 9.16 Å and c = 8.40 Å). No other study on the lattice parameters of crystallized carbon black-filled NR has been published; but we observe that results on unfilled NR vary from one study to another of up to 3.5 % (Bunn, 1942; Takahashi et Kumano, 2004; Tosaka *et al.*, 2004b; Poompradub *et al.*, 2005; Immirzi *et al.*, 2005; Rajkumar *et al.*, 2006). Those discrepencies may arise from the method of measurement of the lattice parameters. Indeed, we observed that for our experiments the results vary of about 3 % depending on the reflections used for the calculation of the lattice parameters (here, the reflections of six different planes are visible on the pattern whereas only three lattice parameters must be calculated). Furthermore, the lattice parameters are the same for uniaxial and equibiaxial loading conditions (the difference being less than 1.1 %) and this comparison is not influenced by the previous discrepancy in the bibliography as the same method has been used. This extends the recent result of Poompradub *et al.* (2004), who demonstrated that the lattice parameters of filled NR only slightly evolve with strain in uniaxial tension: we demonstrate here that they do not change with deformation state either.

Only few studies on crystallization of carbon black-filled NR have been published (Trabelsi *et al.*, 2003b; Poompradub *et al.*, 2005; Chenal *et al.*, 2007b; Toki *et al.*, 2008) and they only concern uniaxial tension. The crystallites sizes obtained in the present study are quite different from those measured by other authors. In fact, the size of the crystallites highly depends on cross-links density (Trabelsi *et al.*, 2003a; Tosaka *et al.*, 2004b; Poompradub *et al.*, 2005; Chenal *et al.*, 2007a), i.e. formulation and processing, especially for filled NR. From the results given in the previous section, one may conclude that crystallites in NR subjected to equibiaxial loading conditions do not have the same size as in uniaxial loading conditions. But we observe in uniaxial tension that crystallites size depends on strain as shown in Table 4.1; similar results are given by Tosaka *et al.* (2004b) and Poompradub *et al.* (2005). In order to compare results in uniaxial and equibiaxial loading conditions, it would then be necessary to measure the crystallites size at similar loading conditions in both uniaxial and equibiaxial tension. But as the deformation states are very different, the stretch ratio is not representative of the loading conditions and other mechanical quantities

Table 4.1: Crystallites size in uniaxial tension for different stretch ratios λ.

λ	2.8	3.4	3.9
l_{200} (Å)	161	147	127
l_{201} (Å)	145	137	121

must be investigated to compare different deformation states. Here, we can only conclude that the size of the crystallites is of the same order of magnitude for both deformation states.

In uniaxial tension, the crystallites are misoriented of about 11°; it is twice smaller than the misorientation measured by Trabelsi *et al.* (2003b) and about 30 % smaller than the misorientation measured by Poompradub *et al.* (2005). This discrepancy may be explained by the difference in cross-link densities, similarly as the difference in crystallites size. In equibiaxial tension, the *b*-axis of the unit cells of the crystallites are not oriented in the plane of tension. This result extends the study of Oono *et al.* (1973) who showed that the crystallites are oriented in the direction perpendicular to the plane of tension in the case of a thin film of NR.

It is well established that the degree of crystallinity of NR highly depends on the level of deformation of NR (Clark *et al.*, 1940). Therefore, as for the crystallites sizes, it is necessary to compare the index of crystallinity in NR in uniaxial and equibiaxial deformations at similar loading levels. The stretch ratio measured here is not sufficient to characterize the loading conditions; further mechanical analysis of the deformation are necessary to discuss the degree of crystallinity.

4.3.4 Orientation of strain-induced crystallites in NR subjected to various multiaxial loading conditions

Figure 4.7 presents the diffraction patterns and azimuthal spectra for filled NR subjected to uniaxial (Fig. 4.7 (a) and (b)), biaxial non-equibiaxial (Fig. 4.7 (c) and (d)) and equibiaxial (Fig. 4.7 (e) and (f)) deformation. Fig. 4.7 (a) exhibits the diffraction reflections of crystallized NR in uniaxial tension. The diffraction pattern is of course oriented according to the stretching direction (see the white arrows in the figure). The diffraction pattern of crystallized NR in biaxial deformation (Fig. 4.7 (c)) is quite similar to the pattern of NR in uniaxial deformation. The pattern is also oriented, according to the first principal direction of tension (direction of highest strain). There are fewer diffraction arcs visible on the pattern and they are less intense and wider. As already shown in the previous section, when filled NR is subjected to equibiaxial deformation (Fig. 4.7 (e)), the diffraction pattern is very different: the diffraction reflections of the crystalline phase are rings and not arcs, and only the reflections corresponding to planes (201) and (200) are visible.

In order to measure the misorientation of the crystallites in NR subjected to the three different deformation states, azimuthal spectra are extracted from the previous diffraction patterns (shown in Fig. 4.7 (b), (d) and (f)) at Bragg angles corresponding to the (200) and (201) diffraction arcs. The width of the reflection arcs in the pattern (i.e. the width at half-maximum of the peaks in the spectra) directly stems for the misorientation of the crystallites: the wider the arcs, the more misoriented the crystallites. In the case of uniaxial and biaxial tension, the position of the (002) arcs (aligned with the direction of tension for the uniaxial test and with the direction of highest strain for the biaxial test) shows that the

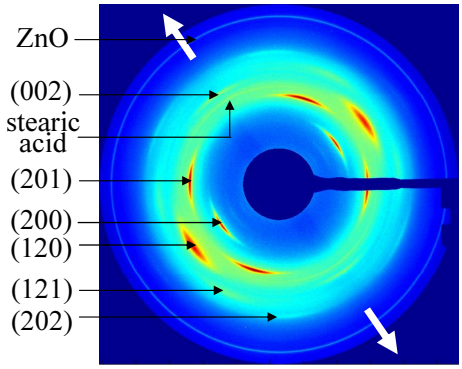

(a) Uniaxial deformation. True strain in the direction of tension: $\epsilon = 1.39$.

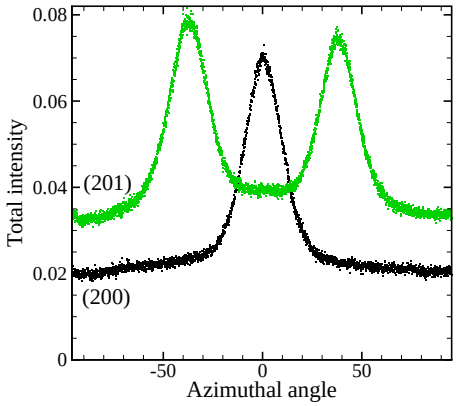

(b) Uniaxial deformation.

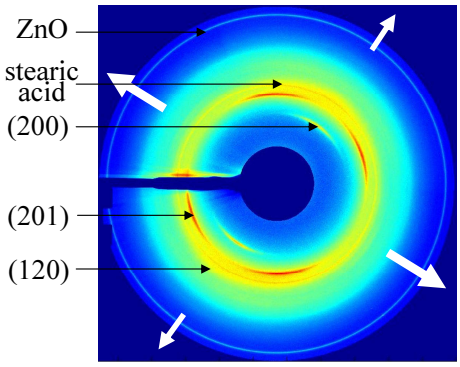

(c) Biaxial deformation. True strains in the directions of tension: $\epsilon_1 = 1.03$ and $\epsilon_2 = 0.34$.

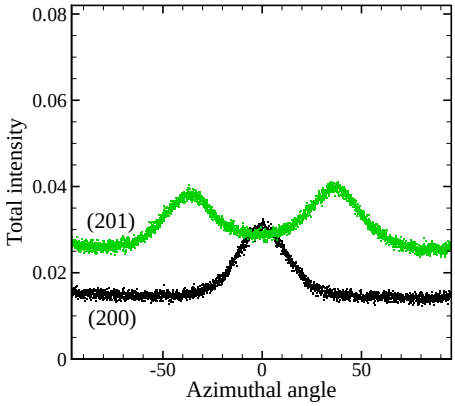

(d) Biaxial deformation.

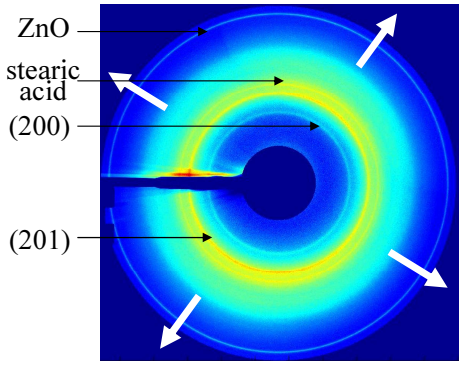

(e) Equibiaxial deformation. True strain in any direction: $\epsilon = 0.88$.

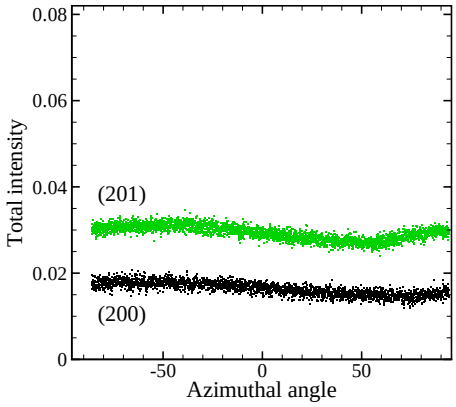

(f) Equibiaxial deformation.

Figure 4.7: (Color online) (a), (c) and (e): scattering patterns of NR in different deformation states. The white arrows in the patterns show the tensile directions. The Miller indices of the different diffraction reflections are given on the left-hand side of the patterns. (b), (d) and (f): azimuthal spectra extracted from the diffraction patterns at Bragg angles $2\theta = 11.3°$ and $2\theta = 14.4°$, corresponding to the diffraction planes (200) and (201) respectively. The origin of the azimuthal angle β is arbitrarily defined as the center of one of the two (200) arcs.

c-axis of the crystall cell of the crystallites is in average oriented along the main direction of tension. As the peaks in the spectra of the biaxial test are wider at half-maximum than the peaks in the spectra of the uniaxial test, the crystallites are more misoriented in NR subjected to biaxial tension than to uniaxial tension: ψ_{200}=11.70° and ψ_{201}=11.09° in uniaxial deformation, and ψ_{200}=15.25° and ψ_{201}=17.03° in biaxial deformation. In the case of equibiaxial loading conditions, the crystallites are not oriented in the plane of tension as already shown. However, a small anisotropy can be observed in the spectra (Fig. 4.7f) due to experimental settings (it can also be observed in patterns of amorphous undeformed samples).

In order to investigate more widely the relationship between the orientation of the crystallites in NR and the multiaxiality of the deformation of the material, 82 multiaxial tensile tests are performed. The true strains in the principal directions ϵ_1 and ϵ_2 of each test are given in Figure 4.8. Figure 4.9 shows the misorientation of the diffraction planes (200),

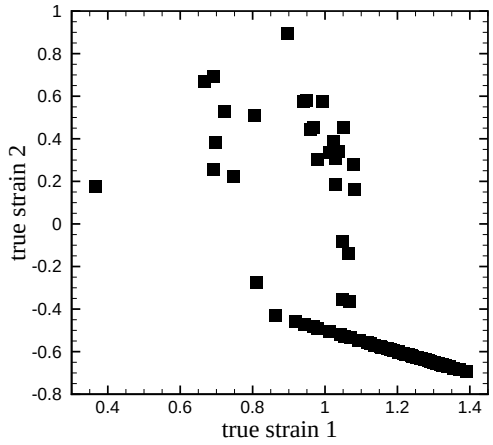

Figure 4.8: Multiaxial tests performed for this study. The tests are characterized by the true strains in the two principal directions ϵ_1 and ϵ_2.

(201) and (120) compared to their mean orientation for different multiaxial deformation states. The multiaxiality of the tests is characterized by the biaxiality factor B, which is the ratio of the true strains: $B = \epsilon_2/\epsilon_1$ where $\epsilon_1 > \epsilon_2$. One can note that $B \in [-0.5; 1]$; $B = -0.5$ for a material subjected to uniaxial deformation; $B = 0$ in the case of planar tension; $B = 1$ for equibiaxial deformation; and when the material is subjected to biaxial non-equibiaxial deformation, $B \in]0; 1[$. We observe that the misorientation of the three diffraction planes (200), (201) and (120) evolve similarly with B: for $B < 0$, the misorientations are small and constant (between ±9° and ±14°) and for $B > 0$, the higher the biaxiality factor, the higher the misorientations (up to ±40°).

In the case of equibiaxial deformation, it is not possible to measure any misorientation of the crystallites compared to their mean orientation as the crystallites are not oriented. We define the misorientations $\psi_{200} = \pm 90°$, $\psi_{201} = \pm 53°$ and $\psi_{120} = \pm 90°$. Indeed, in a diffraction pattern of uniaxially stretched NR, there are two reflection arcs due to the planes (200), separated by 180°; an extension of both arcs of ±90° forms a complete ring. Similarly, there are four reflections arcs due to the planes (201) - the most distant ones from one another are 106° apart - and two arcs due to the planes (120) separated by 180°. Figure 4.10 shows a model of the evolution of the misorientation ψ_{200} with the biaxiality factor B. The misorientations ψ_{201} and ψ_{120} would be modeled exactly in the same manner, only the values of the y-axis would change. When $B \leq 0$, from uniaxial deformation to planar tension, ψ is constant. In this case, the material is stretched in one direction but is

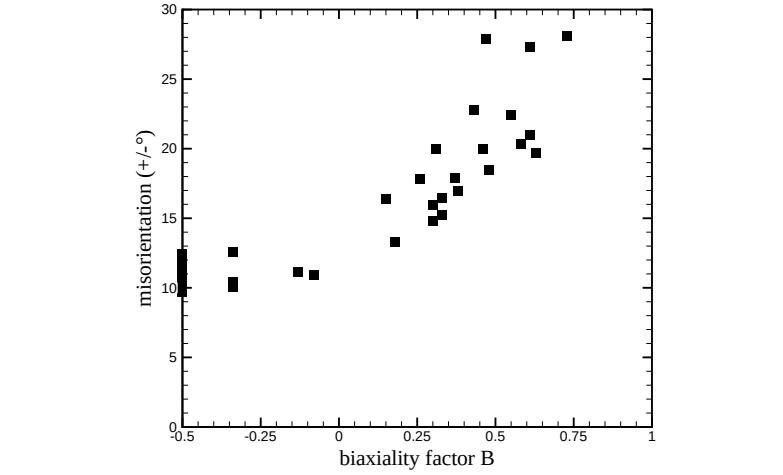

(a) (200)-planes

(b) (201)-planes

(c) (120)-planes

Figure 4.9: Misorientation of the diffraction planes (200), (201) and (120) compared to their mean orientation vs. the biaxiality factor B, B defined as the ratio of the true strains in the two principal directions of the plane of tension. B reflects the multiaxiality of the two-dimensional tests.

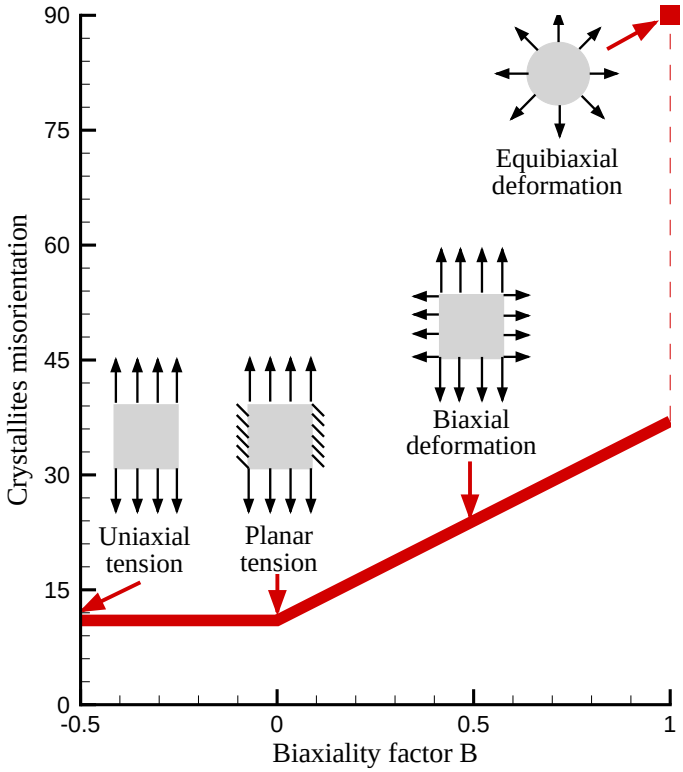

Figure 4.10: (Color online) Model for the evolution of the misorientation of the crystallites with the biaxiality factor B.

either undeformed or compressed in the perpendicular direction (as shown by the schemes in Fig. 4.10). As soon as the material is stretched in the second direction as well, i.e. when $B > 0$ and the deformation is biaxial, the misorientation of the crystallites increases linearly with B. Finally, when $B = 1$ - which corresponds to equibiaxial deformation and equal stretching in every direction on the plane of tension (as shown by the scheme) - the crystallites are not oriented. We believe that the curve is discontinuous at $B = 1$: it means that the crystallites are oriented as soon as the material is more stretched (even slightly) in one direction than in the other one.

4.4 Conclusion

Firstly, this work shows that in carbon black-filled NR subjected to equibiaxial tension, a small crystalline phase co-exists with an amorphous non-oriented phase, as well as in NR subjected to uniaxial tension. The crystallites are similar in uniaxial and equibiaxial tension: their size is of the same order of magnitude and the lattice parameters are identical.

Secondly, the orientation of the crystallites in stretched NR highly depends on the multiaxaility of deformation. The different two-dimensional deformation states can be divided into three groups with respect to the misorientation of the crystallites:

- when the material is stretched in one direction only (from uniaxial to planar tension), the misorientation is constant and small,
- when the material is stretched in two directions (biaxial deformation), the greater the biaxiality, the greater the misorientation,
- when the material is equally stretched in all directions (equibiaxial deformation), the

crystallites are not oriented in the plane of tension.

4.5 Acknowledgement

The authors thank Dr D. Thiaudière, Dr C. Mocuta and Dr A. Zozulya from the DiffAbs beamline in the synchrotron facility Soleil for their great help during the experiments and the Soleil staff for running smoothly the facility.

Chapitre 5

Effet du chemin de chargement sur l'orientation et la désorientation des cristallites

5.1 Introduction

Natural rubber (NR), cis-1,4-polyisoprene, has remarkable mechanical properties which are generally attributed to strain-induced crystallization (SIC). SIC of NR is commonly investigated by wide-angle X-ray diffraction (WAXD) as it offers a very precise way to measure the characteristic of the crystalline phase of the material (Huneau, 2011). Most of the studies focus on uniaxial tension, while NR is widely used in multiaxial loading conditions for engineering applications. In 1973, Oono *et al.* (1973) studied the crystallization of NR subjected to equibiaxial deformation and showed that in such state, the b-axis of the unit cells of the crystallites is normal to the plane of tension whereas the a and c-axes are randomly oriented in the plane of tension. In a previous studies (Beurrot *et al.*, 2011a; Beurrot-Borgarino *et al.*, b), we have shown that for any planar multiaxial deformation state, the c-axis of the unit cells of the strain-induced crystallites in carbon black-filled NR is in average parallel to the direction of highest stretch ratio. Furthermore, the misorientation of the crystallites compared to this mean orientation highly depends on the multiaxiality of the deformation state.

The objective of this study is to determine the effect of the history of mechanical loading of the material on the orientation of the crystallites. If the direction of highest stretch ratio is modified, does the orientation of crystallites changes? Does the misorientation of the crystallites depend only on the strain state at which it is measured, or does it also depend on the previous strain state of the material? To answer this question, X-ray diffraction experiments have been performed in order to measure the orientation and misorientation of strain-induced crystallites in a carbon black-filled NR subjected to several multiaxial loading paths. The results for similar strain states but with different loading paths are then compared.

5.2 Experimental method

5.2.1 Instrumentation

The experiments have been conducted with the homemade stretching machine shown in Figure 5.1. It is composed of four electrical actuators which displacements are synchronized.

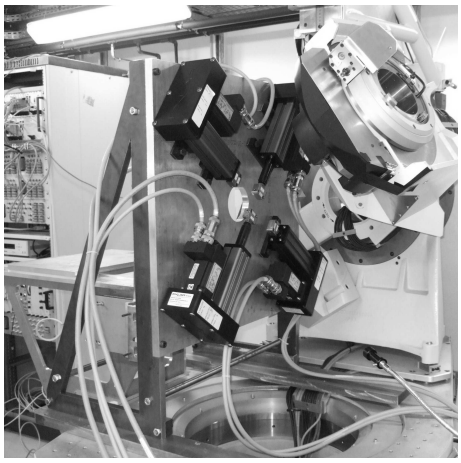

Figure 5.1: Multiaxial stretching machine in DiffAbs beamline in Soleil

Their loading capacity is ±500 N and their stroke is 75 mm each. All the experiments are conducted by prescribing the displacement of these actuators.

The X-ray diffraction experiments have been carried out at the DiffAbs beamline in the French national synchrotron facility SOLEIL (proposal number 20100096). The wavelength used is 1.319 Å and the beam size is 0.3 mm in diameter at half-maximum. The 2D WAXD patterns are recorded by a MAR 345 CCD X-ray detector; the transmitted photons are measured by a PIN-diode in order to make an accurate correction of the sample thickness.

5.2.2 Samples and materials

Obtaining multiaxial deformation for soft materials is not an easy task (Demmerle et Boehler, 1993). For our study, we developed a sample with the cruciform shape shown in Figure 5.2 (a), based on a symmetric cross thinned at its center in order to reach higher strain levels without breaking the arms of the cross sample. Under loading, the arms of

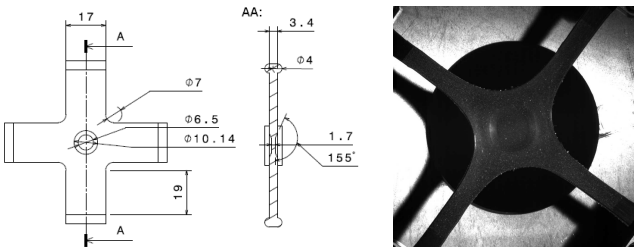

(a) (b)

Figure 5.2: (a) Cruciform sample in undeformed state. (b) Cruciform sample in equibiaxial deformation state

the sample are uniaxially stretched, the central part of the sample is in a complex strain state. The strain state at the center point of the specimen depends on the stretch ratios in each arm. For example, if the four arms are equally stretched, the strain is equibiaxial; if two opposite arms are less stretched than the others, then the center point is in biaxial non-equibiaxial strain state; and if only two arms are stretched, the center point is in planar tension (also referred to as pure shear state). The stretching of opposite arms are always equal in order to keep the center of the sample fixed. The homogeneity of the deformation at the center of the specimen was verified by finite element analysis (not shown here) and

the zone in which the strain is homogeneous is quiet larger than the beam spot, i.e. about 3 mm^2. The cruciform sample in a deformed state is shown in Figure 5.2 (b).

As the cross sample is in a complex state of strain when the arms are stretched, it is difficult to predict the stretch ratios in the center of the sample from the values of displacement of the actuators only. Therefore, all the tests have been filmed and a motion analysis system (Tema motion ®) has been used to track the displacement of points of a pattern painted on the sample. It leads to the determination of the deformation gradient $\mathbf{F}$ from which the two stretch ratios in the directions parallel to the plane of tension are extracted. The general form of the deformation gradient, assuming incompressibility, is :

$$\mathbf{F} = \begin{bmatrix} \lambda & 0 & 0 \\ 0 & \lambda^B & 0 \\ 0 & 0 & \lambda^{-B-1} \end{bmatrix} \tag{5.1}$$

where B is the multiaxiality factor, $B \in [-0.5; 1]$. One can note that $B = -0.5$ for uniaxial tension, $B = 0$ for planar tension and $B = 1$ in the case of equibiaxial tension. When the material is subjected to biaxial (non-equibiaxial) tension, $B \in]0; 1[$. Finally, $B \leq 0$ when the material is stretched in one principal direction only and retracted in the second principal direction of the plane of tension (i.e. uniaxial tension, planar tension or any intermediate state) .

The primary objective of this study was the analysis of SIC in vulcanized NR without fillers. Nevertheless, preliminary equibiaxial experiments showed that, even for the maximum displacement of the actuators, it was not possible to reach sufficient strain at the center of the samples for the onset of crystallization. Therefore, we choose to investigate the response of a carbon black-filled NR. As demonstrated by number of authors, experimental results for unfilled and filled NR are identical, apart from a simple amplification factor (see Guth 1945; Mullins et Tobin 1965; Harwood et Payne 1966 among others); this relationship also applies to crystallization (Rault *et al.*, 2006b; Chenal *et al.*, 2007b; Tosaka, 2009). The material was cross-linked by 1.2 g of sulfur and 1.2 g of CBS accelerator for 100 g of rubber; it also contains 5 g of ZnO and 2 g of stearic acid. It is filled with 50 g of N330 carbon black.

5.2.3 Procedure

The stretching unit was placed on the stand of the DiffAbs diffractometer (see Fig. 5.1) in order to keep the beam focused at the centre of the samples. To lower the Mullins and viscous effects (Mullins et Tobin, 1965), the samples are first equibiaxially stretched five times at a high stretch ratio just before experiments. Furthermore, a new sample is used for each experiment. Figure 5.3 shows the deformation paths applied to the center of the sample for the six experiments performed, in terms of B and λ as defined by Eq. (5.1). For all strain states, the principal direction of highest stretch ratio is x - vertical in Fig. 5.2 (a) - except for the second half of path (f) where the principal direction of highest stretch ratio is y, perpendicular to x. Because of the viscosity of NR and the complex sample shape, it is not possible to change one of the parameters λ and B, and simultaneously keep the second parameter perfectly constant, except in the case of equibiaxial deformation. For example, λ is not constant when B varies in experiments (d), (e) and (f); B is not constant when λ varies in experiments (a) and (b).

The actuators speed was 30 $mm.s^{-1}$. They were stopped and one diffraction pattern was recorded at each square symbols drawn on the paths in Fig. 5.3. The exposure time was set to a minimum, i.e. 3 seconds; it permits to reduce the influence of kinetics of crystallization on the results.

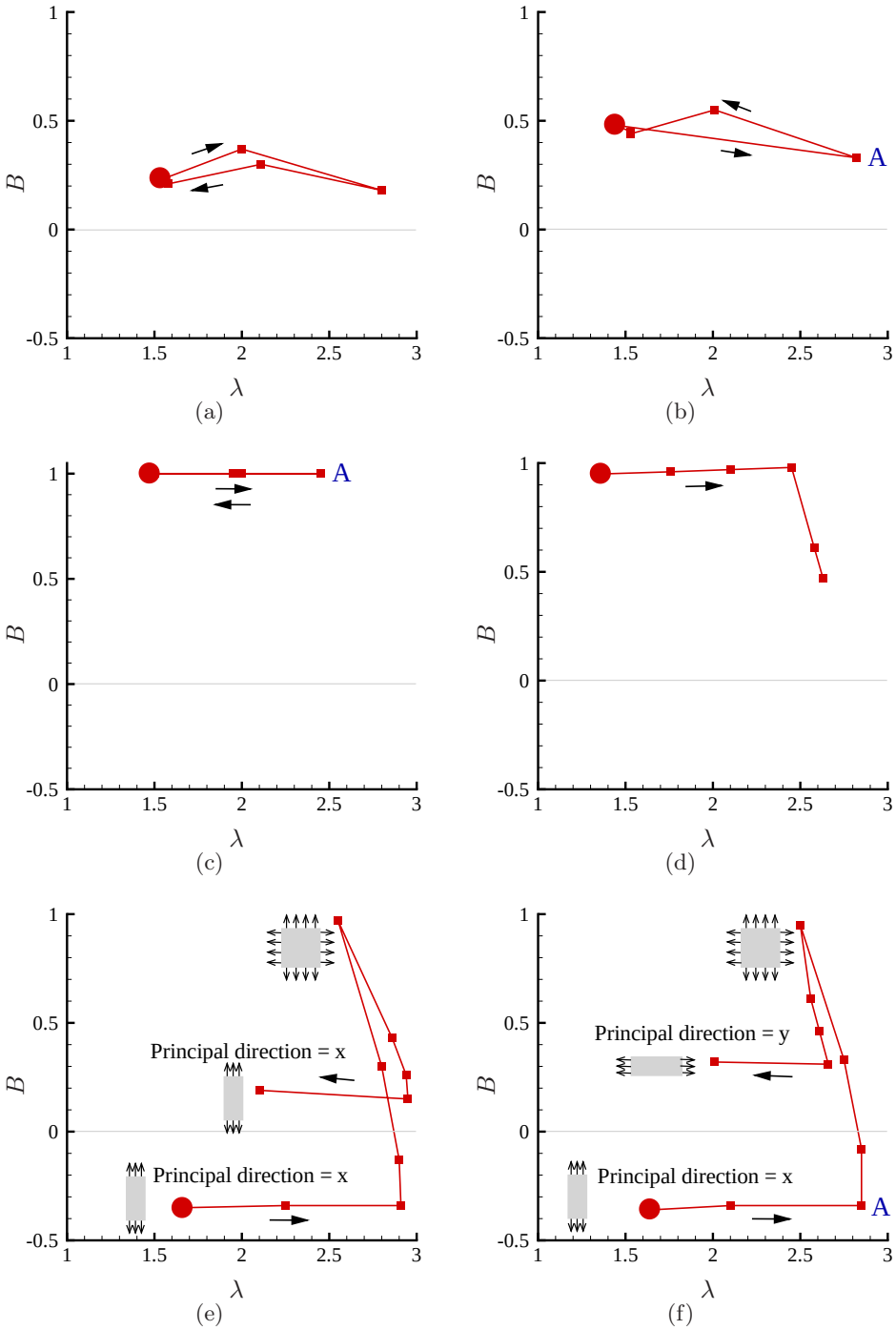

Figure 5.3: (Colore online) Different multiaxial strain paths applied to the center of the sample, defined by λ - highest stretch ratio in the principal direction - and B - biaxility factor. The circles represent the beginning of the path; the undeformed state, which is the starting state of all the experiments, cannot be represented here as B is then undefined. The principal direction of highest stretch ratio is x (vertical in Fig. 5.2 (a)) for all the experiments, except for the last ofur steps of path (f): the principal direction of highest stretch ratio is y, perpendicular to x; for more clarity, the deformation of a representative volume element (RVE) is shown for paths (e) and (f). The letter A refers to specific strain states cited in the text.

An air scattering pattern without sample was first collected and it has been used to correct the patterns. Moreover, the change in thickness of the sample under extension and the change of intensity of the incident photons have also been considered. All these corrections are performed by following the well-established method of Ran *et al.* (2001). Here, small angles scattering was not investigated; the range of diffraction angles is $2\theta \in [8°, 26.7°]$.

5.2.4 Scattering pattern analysis

In uniaxial tension, the reflections of six different diffraction planes (200, 201, 120, 002, 121 and 202) are visible on the diffraction patterns, whereas only the (200) and (201) reflections are visible when the material is submitted to equibiaxial deformation (Beurrot *et al.*, 2011a). For this reason, we choose to focus on the (201) reflections only, in order to be able to measure their evolution for all strain states.

Azimuthal spectra (oppositely to classical Bragg angle spectra) are extracted from the diffraction patterns; they are classically fitted by series of Pearson functions (Toki *et al.*, 2000; Trabelsi *et al.*, 2003a; Rault *et al.*, 2006b; Chenal *et al.*, 2007b). The mean orientation of the crystallites is given by the azimuthal angles of the various peaks in the pattern. The misorientation ψ_{hkl} compared to the mean orientation of the (hkl) diffraction planes is simply given by half the full width at half maximum (FWHM) of the peaks.

Finally, an index of crystallinity χ is calculated:

$$\chi = \frac{\mathcal{I}_{\text{cryst}}}{\mathcal{I}_{\text{cryst}} + \mathcal{I}_{\text{amorph}}} \tag{5.2}$$

where $\mathcal{I}_{\text{cryst}}$ is the integrated intensity of the crystallized phase reflections and $\mathcal{I}_{\text{amorph}}$ is the integrated intensity of the amorphous halo over a quarter of the whole diffraction pattern, using the symmetry of the pattern.

5.3 Results and discussion

5.3.1 Previous results

In a previous study, we showed that the misorientation of the crystallites is very small and equal for every values of $B \leq 0$ (Beurrot-Borgarino *et al.*, b). For this reason, in the following, all the strain states where $B \leq 0$ are grouped together and called "unidirectional stretching" or "1D-stretching"; it corresponds to a state where the material is *(i)* stretched in only one of the principal directions, i.e. $\lambda > 1$ in this direction, and simultaneously *(ii)* free to retract or maintained undeformed in the two other principal directions, i.e. $0.5 \leq \lambda \leq 1$ in those directions. This term groups together uniaxial tension ($B = -0.5$), planar tension ($B = 0$) and all the intermediate strain states. It is opposed to biaxial tension where the material is stretched in two principal directions of the plane, i.e. $\lambda > 1$ in the two directions and $B > 0$. In the following, the term "equibiaxial tension" is used when the stretch ratios are equal in the two directions and "twodirectional stretching" or "2D-stretching" is used when the strain is biaxial but non-equibiaxial.

Figure 5.4 shows the scattering patterns of NR in three different strain states: unidirectional stretching (Fig. 5.4 (a)), twodirectional stretching (Fig. 5.4 (b)) and equibiaxial tension (Fig. 5.4 (c)). Those strain states correspond to the points A in Fig. 5.3 (f), (b) and (c) respectively; they have been reached by keeping the multiaxiality factor B fairly constant when increasing the stretch ratio λ. Azimuthal spectra are extracted from those patterns, at the Bragg angle of the (201) reflections; they are shown in Figure 5.5.

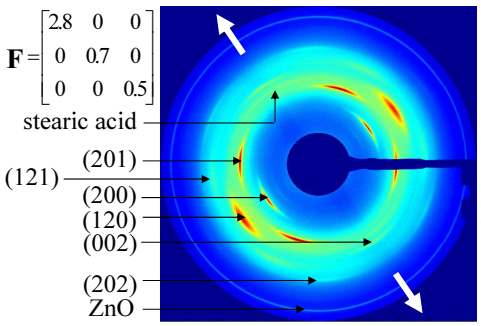

(a) unidirectional stretching, $B = -0.35$.

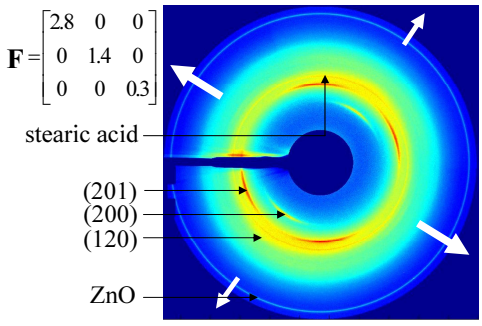

(b) twodirectional stretching, $B = 0.35$.

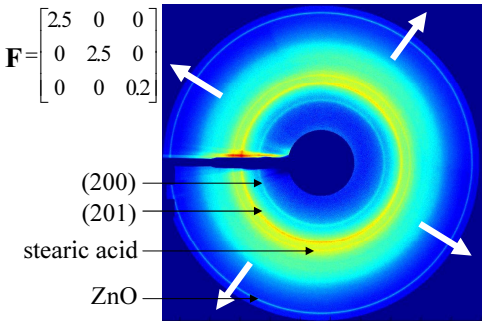

(c) equibiaxial tension, i.e. $B = 1$.

Figure 5.4: Scattering patterns of NR in different strain states. **F** is the deformation gradient; the white arrows show the tensile directions.

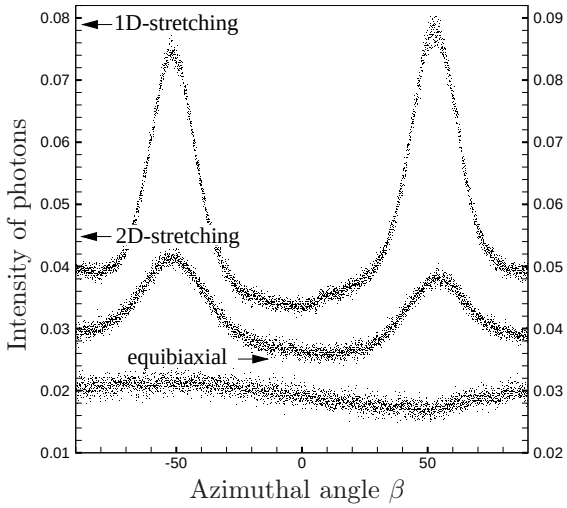

Figure 5.5: Azimuthal spectra at $2\theta = 14.3°$ (Bragg angle of the (201) reflections) for different strain states: unidirectional stretching, twodimensional stretching and equibiaxial tension. The origin of the azimuthal angle β is arbitrarily defined as the tension direction.

Several results on the orientation of the crystallites can be extracted from Fig. 5.4 and 5.5; they are detailed in (Beurrot *et al.*, 2011a) and summarized here:

- in uniaxial and biaxial tension, the c-axis of the unit cells of the crystallites are in average parallel to the direction of highest stretch ratio,
- in equibiaxial tension, the crystallites are not oriented in the plane of tension; it results in annular reflections on the patterns (Fig. 5.4 (c)). The slight anisotropy of the intensity (Fig. 5.5) is an experimental artefact.

Further results can be obtained from additionnal diffraction patterns, as detailed in (Beurrot-Borgarino *et al.*, b):

- in 1D-stretching, the misorientation of the crystallites compared to their mean orientation is constant with B and λ and small: about 10° to 12°,
- in 2D-stretching, the misorientation of the crystallites is larger than in 1D-stretching (the peaks are larger at mid-height in Fig. 5.5). The misorientation increases with B, from about 10° to about 35°.

In the following, we compare the orientation of the crystallites in similar strain states, but obtained reached after different loading paths. Figure 5.6 shows the misorientation of the crystallites ψ_{201} (in black) and the index of crystallinity χ (in brackets) for different steps of the six loading paths; the values have not been calculated for all the steps of the paths, expecially χ.

5.3.2 Equibiaxial tension

We compare here the same strain state ($B \approx 1$ and $\lambda \approx 2.5$) reached after two different loading paths shown in Fig. 5.6:

- step B in path (c): the strain is always equibiaxial along the path,
- step B in path (f): the sample is first 1D-stretched, then B is increased while λ is kept fairly constant.

Figure 5.7 shows the corresponding azimuthal spectra at the Bragg angle of the (201) reflections. In both cases, there are no peaks observed which means that the crystallites are not oriented in the plane of tension. A slight anisotropy is observed for path (f), but it is smaller than for path (c) and is most probably due to an artefact as well, rather than to the loading path. For this reason, ψ_{201}, which is defined as the misorientation of the crystallites compared to their *mean* orientation, cannot be calculated.

5.3.3 Twodirectional stretching

We now compare the orientation of the crystallites when the sample is in 2D-stretching state, obtained (see Fig. 5.6):

- directly, as steps C in paths (a) and (b), i.e. with B fairly constant along the path,
- after 1D-stretching, as steps D in paths (e) and (f),
- after equibiaxial tension, as step E in path (d).

In all cases, the c-axis of the unit cells of the crystallites are in average parallel to the direction of highest stretch ratio, i.e. direction x. As shown in Fig. 5.6, at steps C the misorientation ψ_{201} is equal to 15° (path (a)) and 17° (path(b)); it is the same as steps D in paths (e) ($\psi_{201} = 16°$) and (f) ($\psi_{201} = 19°$). At steps E, which is obtained after equibiaxial tension, the misorientation $\psi_{201} = 30°$ is higher.

We observe that during path (a), ψ_{201} is almost twice larger during the unloading phase of the cycles than during the loading phase, though B is kept fairly constant (see Fig. 5.6). This phenomena has already been observed during uniaxial tensile tests for small values of λ (Trabelsi *et al.*, 2003a; Tosaka *et al.*, 2004b; Tosaka, 2007; Beurrot-Borgarino *et al.*,

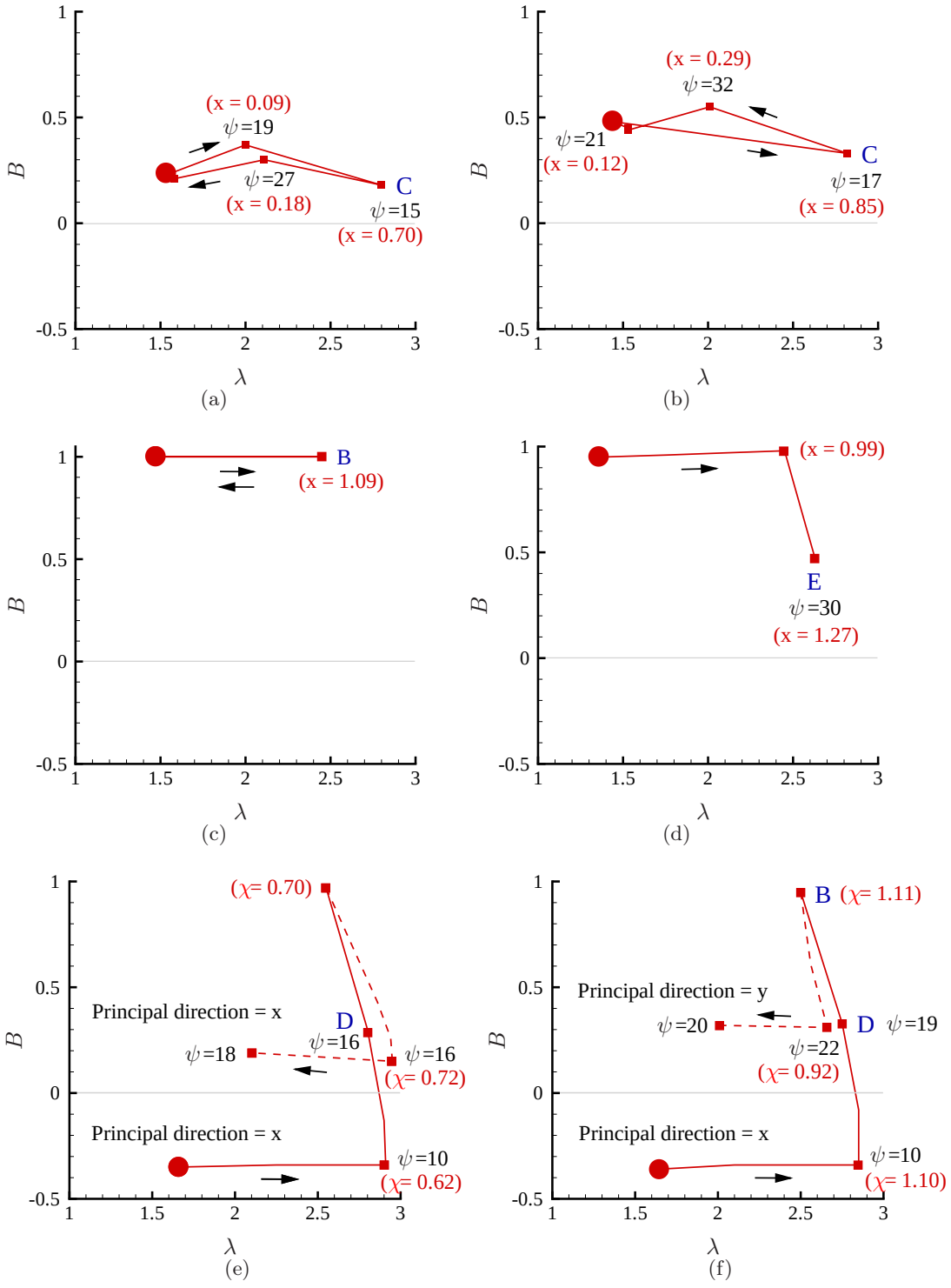

Figure 5.6: (Colore online) Misorientation of the crystallites ψ_{201} (in degrees) and crystallinity index χ (in %) along the deformation paths. The circles represent the beginning of the paths; the letters in capital refer to specific strain states and the dashed lines refer to specific paths cited in the text.

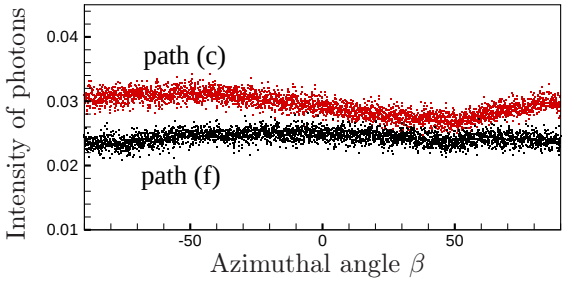

Figure 5.7: Azimuthal spectra at $2\theta = 14.3°$ (Bragg angle of the (201) reflections) of NR in equibiaxial tension reached after two different loading paths (c) and (f), see Fig. 5.3.

c). The origin of this phenomena is unknown, however it may explain the evolution of the misorientation during path (d). Indeed, at the beginning of the path the stretch ratio is increased in the two principal directions; then λ is kept constant while B is decreased, which means that the stretch ratio in the second principal direction decreases (see Eq. (5.1)). Therefore, in this second direction, the path may be seen as a loading phase followed by an unloading phase. This could explain the increase of ψ_{201} observed at step E.

5.3.4 Change in principal direction

As shown in Fig. 5.3, in path (f) the sample is first 1D-stretched and then 2D-stretched in direction x, and finally 2D-stretched in the principal direction y perpendicular to x; between those two last strain states the sample is necessarily in equibiaxial tension. The same loading path is applied in path (e), except that the principal direction remains x along the whole path. During the retraction phase of the paths, represented by dashed lines in Fig. 5.6, the c-axis of the unit cells of the crystallites are in average parallel to the principal tensile direction x or y. It means that during path (f), the crystallites turned of 90° when the direction of highest stretch ratio changes. Moreover, ψ_{201} varies from 16° to 18° in path (e) and from 20° to 22° in path (f); this difference is very small. It is possible that it is not due to the change in principal direction but simply to the difference in B between the two paths.

5.4 Concluding remarks

For the different loading paths studied here, the history of mechanical loading has no significant effect on the mean orientation of the strain-induced crystallites in carbon black-filled NR. For any loading paths, in the case of 1D- and 2D-stretching, the c-axis of the unit cells of the crystallites are in average parallel to the principal tensile direction and the higher the biaxiality, the higher the misorientation of the crystallites. In the case of equibiaxial tension, the crystallites are not oriented in the plane of tension and the crystallized phase is isotropic.

The fact that history of loading has no significant effect of the crystallites orientation even when the stretch ratio λ is maintained fairly constant means that the crystallized phase of the material is free to evolve. More particularly, the crystallites are *in average* free to rotate. As shown by the numbers in brackets in Fig. 5.6, the degree of crystallinity χ does not change significantly when B is increased or decreased and λ is kept constant (see paths (d), (e) and (f)): the number of crystallites remains constant while their orientation in average changes. But this result does not allow to determine whether the crystallites

already nucleated turn when B is modified, or whether the former crystallites are melted and new ones are nucleated with a new orientation. It is probably not possible to determine which of these two scenarios takes place by X-ray diffraction experiments. Indeed, all the measurements are averages over a large volume of material compared to the size of strain-induced crystallites. Finally, this uncertainty leads to other questions, unresolved yet: what are the mechanisms of nucleation and melting of the crystallites at a macromolecular scale in multiaxial deformation? In what mechanical state are the amorphous macromolecules neighboring the crystallites? Does this mechanical state allows the crystallites to evolve, and in particular to rotate?

The samples and the experimental setup of the study did not allow to increase and decrease B while keeping λ perfectly constant and vice-versa. However, we believe that a more precise experimental setup would lead to a similar conclusion: the history of loading may slightly influence the orientation of the crystallites, but not in a significant way. Moreover, more different loading paths could be performed. But the different paths already studied highlighted the same results, for this reason we do not expect new conclusions from additionnal loading paths. Finally, the material studied here is carbon black filled NR. Several studies have shown that fillers (Trabelsi *et al.*, 2003b; Poompradub *et al.*, 2005) and cross-link density (Trabelsi *et al.*, 2003a; Tosaka *et al.*, 2004b; Chenal *et al.*, 2007a; Tosaka, 2007) has an effect on the misorientation of the strain-induced crystallites in NR. However, this effect is very small compared to the effect of mechanical loading. Consequently, we believe that the same study than ours on a different NR - filled or not- would lead to the same conclusions.

5.5 Acknowledgment

The authors thank Dr D. Thiaudière, Dr C. Mocuta and Dr A. Zozulya from the DiffAbs beamline in Soleil synchrotron facility for their great help during the experiments and the Soleil staff for smoothly running the facility.

Quatrième partie

Fatigue uniaxiale

Dans cette quatrième partie, nous nous intéressons à la cristallisation sous contrainte du caoutchouc naturel en fatigue uniaxiale. Deux aspects de la fatigue sont étudiés. D'abord, au cours du premier chapitre, nous considérons un seul cycle de traction et mesurons l'effet de la vitesse de déformation sur la cristallisation. Ceci permet de comprendre l'évolution des cristallites lors d'un cycle à une vitesse proche de celle des essais de fatigue, c'est-à-dire équivalent à une fréquence d'1 Hz. Les deux chapitres suivants sont dédiés à l'évolution de la cristallisation sous contrainte avec le nombre de cycles pour différents niveaux de déformation : le deuxième chapitre s'intéresse à l'évolution des paramètres des cristallites, alors que le troisième chapitre est dédié à l'évolution du taux de cristallinité.

Effect of strain rate on strain-induced crystallization in carbon black-filled natural rubber

S. Beurrot-Borgarino, B. Huneau, E. Verron
Accepté dans Rubber Chemistry and Technology avec modifications mineures

L'effet de la vitesse de déformation sur la cristallisation sous contrainte du caoutchouc naturel chargé au noir de carbone pendant un cycle de traction uniaxiale est mesuré par diffraction des rayons X aux grands angles par rayonnement synchrotron. Les essais montrent que le nombre de cristallites par unité de volume n'est pas influencé par la vitesse de déformation mais que le volume des cristallites décroit lorsque la vitesse de déformation augmente ; la conséquence est un taux de cristallinité beaucoup plus faible. Les seuils de cristallisation et fusion des cristallites sont décalés vers des extensions plus grandes. De plus, la désorientation des cristallites et les paramètres de maille sont aussi légèrement influencés par la vitesse de déformation, même si leur évolution avec l'extension n'est pas qualitativement modifiée.

Characteristics of strain-induced crystallization in natural rubber during fatigue testing : in situ WAXD measurements using synchrotron radiation

S. Beurrot-Borgarino, B. Huneau, E. Verron, D. Thiaudière, C. Mocuta, A. Zozulya
Soumis à Rubber Chemistry and Technology

La cristallisation sous contrainte du caoutchouc naturel chargé au noir de carbone est mesurée par diffraction des rayons X synchrotrons aux grands angles pendant des essais de fatigue *in-situ*. Grâce à une méthode expérimentale originale, nous mesurons l'évolution du taux de cristallinité, des paramètres de maille et de la taille et de la désorientation des cristallites avec le nombre de cycles. On montre que lorsque l'extension minimale est plus petite que le seuil de fusion des cristallites, alors la taille des cristallites et le taux de cristallinité diminuent, alors qu'ils augmentent lorsque l'extension minimale est plus grande que le seuil de fusion. Dans les deux cas, la désorientation des cristallites décroit et les paramètres de maille sont constants.

Strain-induced crystallization of carbon black-filled natural rubber during

fatigue measured by in-situ synchrotron X-ray diffraction

S. Beurrot-Borgarino, B. Huneau, E. Verron, P. Rublon
Publié dans International Journal of Fatigue, 47 :2013, 1-7

Le caoutchouc naturel a d'excellentes propriétés en fatigue qui sont généralement expliquées par sa capacité à cristalliser sous contrainte. Cependant, la cristallisation sous contrainte du caoutchouc naturel en fatigue n'a jamais été étudiée. Nous réalisons des essais de fatigue *in-situ* originaux durant lesquels le taux de cristallinité et le nombre et le volume des cristallites sont mesurés par diffraction des rayons X synchrotron. Pour tous les niveaux de déformation, le nombre de cristallites est constant. L'évolution de leur volume dépend de l'extension minimale imposée à chaque cycle. Les résultats montrent que les chargements cycliques modifient la structure macromoléculaire du matériau, et en particulier de sa phase amorphe.

Chapitre 6

Effet de la vitesse de déformation sur la cristallisation sous contrainte lors d'un cycle de traction

6.1 Introduction

Natural rubber (NR) is widely used in industrial applications for its great mechanical properties, such as large tensile strength, long fatigue life (Cadwell *et al.*, 1940; André *et al.*, 1999; Mars et Fatemi, 2006) and slow crack propagation (Lake, 1995). Those properties are generally attributed to the ability of NR to crystallize under strain. Strain-induced crystallization (SIC) in NR has been discovered by Katz (1925) and investigated since in a large number of studies. But the majority of those studies focus on relaxation and very low strain rate (quasi-static) tensile tests, whereas engineering applications involve a very wide range of strain rates. Only two studies have investigated the effect of strain rate on SIC in rubbers. Miyamoto *et al.* (2003) have investigated the effect of strain rate over four decades (from 7.10^{-4} s^{-1} to 7 s^{-1}) on SIC in synthetic isoprene rubber (IR): they showed that the onset of crysallization is shifted toward higher stretch ratios when the strain rate is increased. Rault *et al.* (2006a) studied the effect of strain rate on SIC in NR, but only for very low strain rates (5.5×10^{-3} s^{-1} and 4×10^{-5} s^{-1}).

From a macroscopic point of view, it is well-known that the tensile strength of filled rubbers increases with increasing strain rate. Such experimental results have been reported since the 60s for example by Mason (1960) and Dannis (1962). At this scale, number of studies include results obtained for different polymers, and not especially for rubbers (Krempl et Khan, 2003; Amin *et al.*, 2006). For very high strain rates, several papers focus explicitly on rubber (Roland, 2006; Al-Quraishi et Hoo Fatt, 2007; Hoo Fatt et Ouyang, 2008), nevertheless none of them investigates the influence of SIC on the mechanical response.

Here we focus on the effect of strain rate on SIC in carbon black-filled NR during a uniaxial tensile test. Two strain rates are considered: a low strain rate of about 10^{-3} s^{-1} which corresponds to a cycle usually designated as quasi-static and a high strain rate of about 6.4 s^{-1} which is of the same order of magnitude as during a 1 Hz fatigue test. To measure SIC in real time, wide-angle X-ray diffraction (WAXD) measurements are performed; synchrotron radiation is used to achieve very short exposure time (1 s) which is necessary for high strain rate in-situ measurements.

6.2 Experimental procedure

6.2.1 Material and samples

The material used in this study is a carbon black-filled natural rubber, cross-linked with 1.2 phr (parts per hundred of rubber) of sulphur and CBS accelerator. It also contains ZnO (5 phr) and stearic acid (2 phr) and is filled with 50 phr of N330 carbon black. The stress-strain response of the material is given in Figure 6.1 for both low and high strain rate cycles. The samples are classical flat dumbbell specimen with a 10 mm gauge length

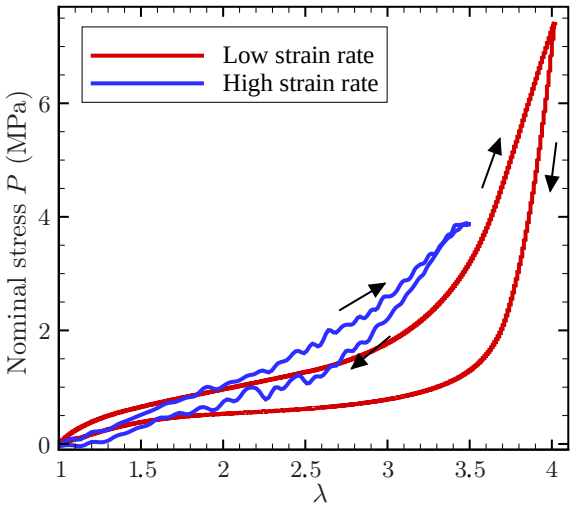

Figure 6.1: Evolution of the nominal stress P with λ during low and high strain rate cycles.

and a 2 mm *times* 4 mm section.

6.2.2 Synchrotron

The synchrotron measurements are carried out at the DiffAbs beamline in the French national synchrotron facility SOLEIL (proposal number 20100096). The wavelength used is 1.319 Å and the beam size is 0.3 mm in diameter at half-maximum. The 2D WAXD patterns are recorded by a MAR 345 CCD X-ray detector. The exposure time is 1 s (minimum time to record a workable scattering pattern) for the high strain rate cycle. For the low strain rate cycle, it is set to 2 s in order to enhance the accuracy of the measurements.

6.2.3 Mechanical loading conditions

The fatigue tests have been conducted with a homemade stretching machine, designed to keep the center of the specimen fixed during the fatigue tests.

In order to lower the residual elongation due to both Mullins effect and viscoelasticity, all the samples are pre-cycled just before testing (5 cycles) at a higher strain level than during the tests.

During the low strain rate cycle, the sample is elongated of 90 mm at 0.012 mm.s^{-1}; the total duration of the cycle is about 2 hours. It corresponds to the maximum stretch ratio $\lambda_{max} = 4.02$ and the mean stretch ratio rate $\dot{\lambda} = 1.07 \times 10^{-3}$ s^{-1}. A scattering pattern is recorded every 98 seconds. The stretch ratio at the center of the sample λ is measured continuously by optical method.

During the high strain rate cycle, the sample is elongated of 66.4 mm and the speed of the clamps varies between 33 mm.s^{-1} and 118 mm.s^{-1} in order to keep the stretch ratio rate constant at $\dot{\lambda}$=6.4 s^{-1}. The maximum stretch ratio achieved is λ_{max}=3.65. It corresponds to a cycle of about 4 seconds. The stretch ratio λ is not measured directly, but is determined thanks to the relationship between the displacement of the clamps and λ measured during the low strain rate cycle. As the exposure time is one second, the patterns cannot be recorded while the clamps are in motion, as during the low strain rate cycle. For this reason, the cycle is "paused" for pattern recording. In order not to accumulate relaxation effects during the several one-second pauses of the cycle, the high strain rate cycle results are reconstructed from several cyclic tests: high strain rate cycles are interrupted at different stretch ratios in order to record a pattern, only one measurement (and one pause) is performed per cycle. Furthermore, because of possible viscous effects on the material during repeated high strain rate cycles, a new sample is used for each measurement. In consequence, each WAXD measurement during the reconstructed high strain rate cycle represents one sample and one cyclic test; for this reason, the number of measurements is small compared to the number of measurements performed during the low strain rate cycle.

6.2.4 Scattering pattern analysis

In this study, we consider large angle scattering: the range of diffraction angles is $2\theta \in [8°, 26.7°]$. We used the (012) reflections of Cr_2O_3 powder placed on each side of a specimen to calibrate the diffraction angles 2θ (a=4.9590 Å and c=1.3596 Å). An air scattering pattern (without sample) is first collected and is used to correct the patterns. Moreover, the change in thickness of the sample under extension and the change of intensity of the incident photons are also considered. All these corrections are performed by following the well-established method of Ran *et al.* (2001). An example of corrected diffraction pattern is given in Figure 6.2.

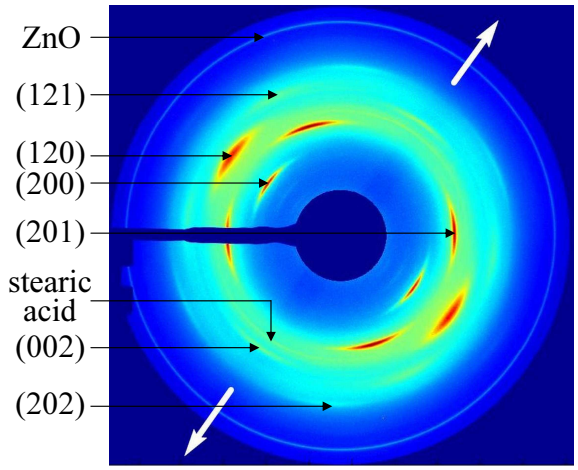

Figure 6.2: Example of diffraction pattern of crystallized NR in uniaxial tension. The white arrows show the tension direction. The Miller indices of the planes corresponding to the diffraction arcs are also indicated in the figure.

The intensity of photons diffracted by the isotropic phases in the material $I_{iso}(2\theta)$ is extracted from the diffraction patterns by considering the minimum intensity along the azimuthal angle β for each Bragg angle 2θ. Then, the intensity of photons diffracted by

the anisotropic phases $I_{\text{ani}}(2\theta, \beta)$ is calculated as the difference between the total intensity of photons diffracted $I_{\text{total}}(2\theta, \beta)$ and $I_{\text{iso}}(2\theta)$. The spectra extracted from $I_{\text{ani}}(2\theta, \beta)$ and $I_{\text{iso}}(2\theta)$ are classically fitted by series of Pearson functions (Toki *et al.*, 2000; Trabelsi *et al.*, 2003a; Rault *et al.*, 2006a; Chenal *et al.*, 2007b). Figures 6.3a and 6.3b present examples of fitting and deconvolution of a $(2\theta,I_{\text{iso}})$ spectrum and a $(2\theta,I_{\text{ani}})$ spectrum, respectively.

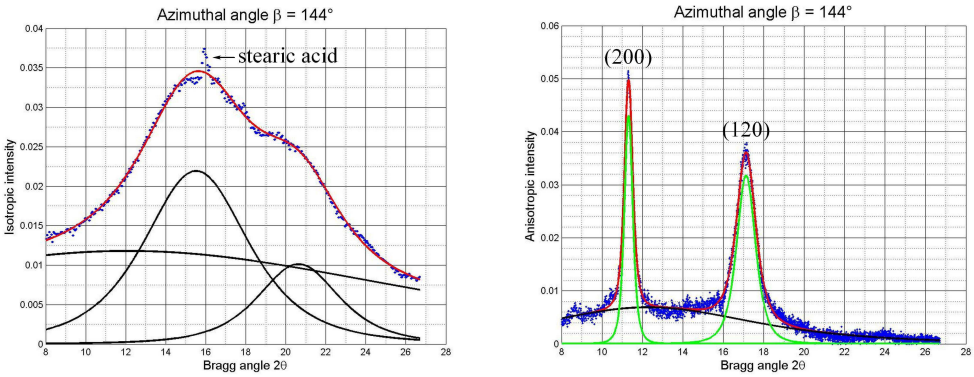

(a) (b)

Figure 6.3: Examples of deconvolution of (a) a spectrum $(2\theta,I_{\text{iso}})$ and (b) a spectrum $(2\theta,I_{\text{ani}})$ fitted by series of Pearson functions.

The index of crystallinity χ is calculated as follow:

$$\chi = \frac{\mathcal{I}_{\text{cryst}}}{\mathcal{I}_{\text{cryst}} + \mathcal{I}_{\text{amorph}}}, \tag{6.1}$$

where $\mathcal{I}_{\text{cryst}}$ is the integrated intensity of the (120) and (200) peaks (measured on one $(2\theta,I_{\text{ani}})$ spectrum at the azimuthal angle of highest intensity of the peaks) and $\mathcal{I}_{\text{amorph}}$ is the integrated intensity of the amorphous halo, considered equal to the intensity I_{iso} integrated on a $(2\theta,I_{\text{iso}})$ spectrum.

The mean crystallites size is deduced from the Scherrer formula (Guinier, 1963) as Trabelsi *et al.* (2003a,b, 2004), Tosaka *et al.* (2004b), Poompradub *et al.* (2005) and Chenal *et al.* (2007a):

$$l_{hkl} = \frac{K\lambda}{\text{FWHM}_{2\theta}\cos\theta}, \tag{6.2}$$

where l_{hkl} is the crystallites size in the direction normal to the (hkl) diffraction plane, K is a scalar which depends on the shape of the crystallites (here we adopt 0.78 as Trabelsi *et al.* (2003a)), λ is the radiation wavelength, θ is the Bragg angle and $\text{FWHM}_{2\theta}$ is the full width at half-maximum of the (hkl) peak in 2θ. A mean volume of the crystallites $\overline{V}_{\text{cryst}}$ is calculated from the crystallites size in three different directions:

$$\overline{V}_{\text{cryst}} = l_{200} \cdot l_{120} \cdot l_{201}. \tag{6.3}$$

As the shape of the crystallites in NR remains unknown, it is not possible to calculate the real volume of the crystallites. But assuming that this shape does not change with strain and strain rate (even if the size in the different directions changes), $\overline{V}_{\text{cryst}}$ is proportional to the real mean volume of the crystallites.

Assuming the incompressibility of the material, and that the volume crystallinity is equal to the mass crystallinity, we calculate an index of number of crystallites par unit

volume N_{cryst}:

$$N_{\text{cryst}} = \frac{\chi \cdot V_{\text{irradiated}}}{\overline{V}_{\text{cryst}}} = \frac{\chi}{\overline{V}_{\text{cryst}}} \frac{\pi R^2 h_0}{\sqrt{\lambda}}, \tag{6.4}$$

where $V_{\text{irradiated}}$ is the volume irradiated by the X-ray beam, R is the radius at half-maximum of the beam, h_0 is the thickness of the sample in the undeformed state and λ is the local stretch ratio of the sample. N_{cryst} is proportional to the number of crystallites per irradiated deformed unit volume.

The misorientation ψ_{hkl} (compared to the mean orientation) of the (hkl) diffraction planes of the crystallites is given by half the full width at half-maximum (FWHM_β) of the peaks, measured on the azimuthal profiles of the reflection.

Finally, the lattice parameters of the crystal cell of the polyisoprene are calculated considering an orthorhombic crystal system, as determined by Immirzi *et al.* (2005) and Rajkumar *et al.* (2006). On the scattering pattern, we identify 18 diffraction arcs that result from the diffraction due to 6 different planes (see Fig. 6.2). As only three lattice parameters (a, b and c) must be calculated, each of them is the average of two values measured from two different reflections.

6.3 Results

6.3.1 Index of crystallinity

Figure 6.4 shows the evolution of the crystallinity index χ with the stretch ratio λ during a low strain rate and a high strain rate cycle. The evolution of χ is quite similar for

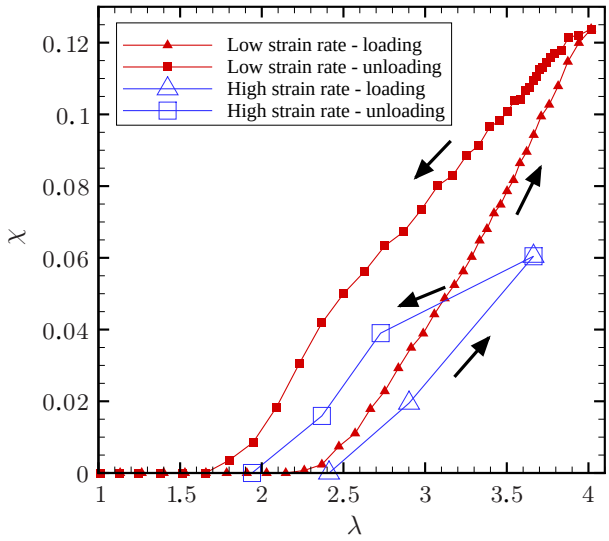

Figure 6.4: Evolution of the index of crystallinity χ with λ during a low (small filled symbols) and a high (large unfilled symbols) strain rate cycle. Triangular symbols: loading phase; square symbols: unloading phase.

both cycles. As expected (Tosaka, 2007), we observe the existence of two onsets: an onset of crystallization during the loading phase, referred to as λ_C in the following; and an onset of melting of the crystallites during the unloading phase, referred to as λ_M. Furthermore, the index of crystallinity is higher during the unloading phase than during the loading

phase for a given stretch ratio. But there are significant differences between the low strain rate and the high strain rate cycles:

- for a given stretch ratio, the index of crystallinity is lower of about 40 % during the high strain rate cycle than during the low strain rate cycle,
- λ_C and λ_M are higher for the high strain rate cycle. For the low strain rate cycle, λ_C=2.2 and λ_M=1.7. For the high strain rate cycle, it is not possible to determine precisely the values of the onsets as there are not enough measurements, but we observe that $2.4 < \lambda_C < 2.9$ and $1.9 < \lambda_M < 2.4$.

6.3.2 Size and volume of the crystallites

Figure 6.5 shows the evolution of the mean size of the crystallites during a low strain rate and a high strain rate cycle in the directions normal to the (120), (200) and (201) diffraction planes. The size calculated from the (202), (121) and (002) reflections are too

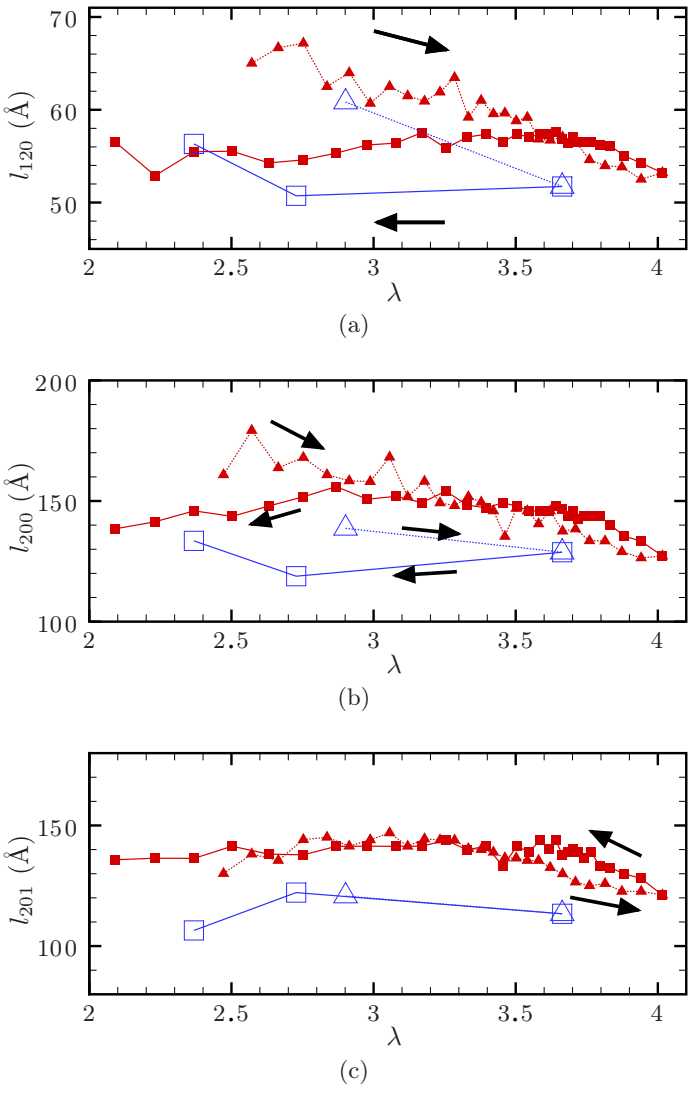

Figure 6.5: Evolution of the size of the crystallites in different directions during a low (small filled symbols) and a high (large unfilled symbols) strain rate cycle. Triangular symbols: loading phase; square symbols: unloading phase.

noisy to be conclusive and are not shown here. Fig. 6.5 shows that the crystallites are smaller of about 10% to 20% during a high strain rate cycle than during a low strain rate cycle. But the evolution of the size of the crystallites is similar during both cycles and for the three directions:

- during the loading phase, the size decreases with λ,
- during the unloading phase, for $\lambda < 3.65$, the size is smaller or the same as during the loading phase. Higher stretch ratios have not been tested for the high strain rate cycle.

As expected, this difference in size leads to a difference in volume as shown in Figure 6.6: the crystallites are about 30 % smaller during the high strain rate cycle than during the low strain rate cycle. The evolution of the volume with λ is the same for both cycles and is the same than the evolution of the size.

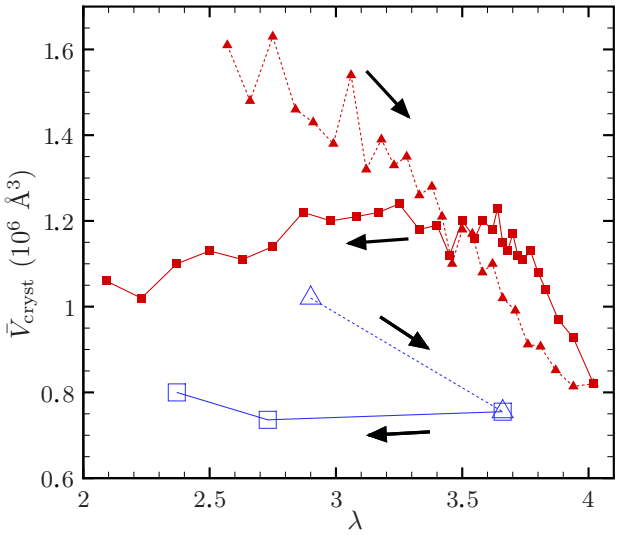

Figure 6.6: Evolution of the volume of the crystallites during a low (small filled symbols) and a high (large unfilled symbols) strain rate cycle. Triangular symbols: loading phase; square symbols: unloading phase.

6.3.3 Number of crystallites

Figure 6.7 shows the evolution of the index of number of crystallites per unit volume during a low and a high strain rate cycle. The number of crystallites increases with the stretch ratio for both loading and unloading phases. The onsets λ_C and λ_M are increased during the high strain rate cycle, as already observed in Fig. 6.4. But contrary to the index of crystallinity χ, the number of crystallites increases rapidly at the beginning of the high strain rate cycle, and is very close for both cycles during most of the loading phase. During the unloading phase, the number of crystallites is equal or lower during the high strain rate cycle than during the low strain rate cycle.

6.3.4 Orientation of the crystallites

Figure 6.8 shows the evolution of the misorientation compared to the mean orientation of the (120), (200), (201) and (002) diffraction planes of the crystallites during a low and a high strain rate cycle. The misoriention of the (202) and (121) planes are not shown here

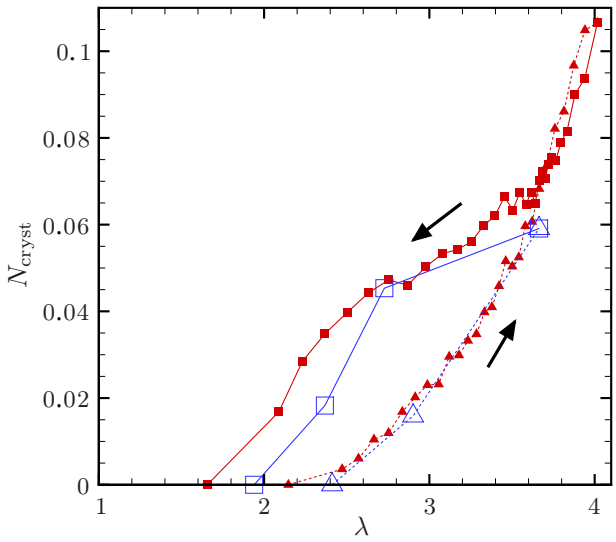

Figure 6.7: Evolution of the index of number of crystallites per unit volume during a low (small filled symbols) and a high (large unfilled symbols) strain rate cycle. Triangular symbols: loading phase; square symbols: unloading phase.

as the data are to noisy to be conclusive. The evolution of the misorientation of the planes are similar for both cycles: ψ_{201}, ψ_{200} and ψ_{002} increase with the stretch ratio, whereas ψ_{120} slightly decreases. And quantitatively, the misorientations are close for both strain rates: from about 8° to 13°. But we also observe differences between the low and high strain rate cycles:

- during the high strain rate cycle, the misorientation of the crystallites is significantly lower than during the low strain rate cycle, especially during the loading phase of about 8% to 30%, except the misorientation of the (120) planes which are more misoriented during the high strain rate cycle than during the low strain rate cycle,
- during the low strain rate cycle, the misorientation of all the diffraction planes is lower during the unloading phase than during the loading phase, except for very low stretch ratios. On the contrary, during the high strain rate cycle, ψ_{002} and ψ_{201} seem higher during the unloading phase, ψ_{120} lower and ψ_{200} the same as during the loading phase.

6.3.5 Lattice parameters

Figure 6.9 shows the evolution of the lattice parameters a, b and c during a low and a high strain rate cycle. The lattice parameters are very close during both cycles: a ranges from 12.65 Å to 12.78 Å, b varies between 9.12 Å and 9.22 Å and c ranges from 8.31 Å and 8.42 Å. During the low strain rate cycle, a and b decrease whereas c increases with λ. In other words, when NR is stretched, the unit cells of the crystallites are stretched in the direction of tension and retracted in the directions normal to the tension direction. During the loading phase (triangular symbols in Fig. 6.9), the unit cells are less elongated during the high strain rate cycle than during the low strain rate cycle: a and b are higher whereas c is smaller. The effect of the strain rate on lattice deformation during the unloading phase of a cycle (rectangular symbols in Fig. 6.9) is not clear: more accurate data would be necessary to conclude.

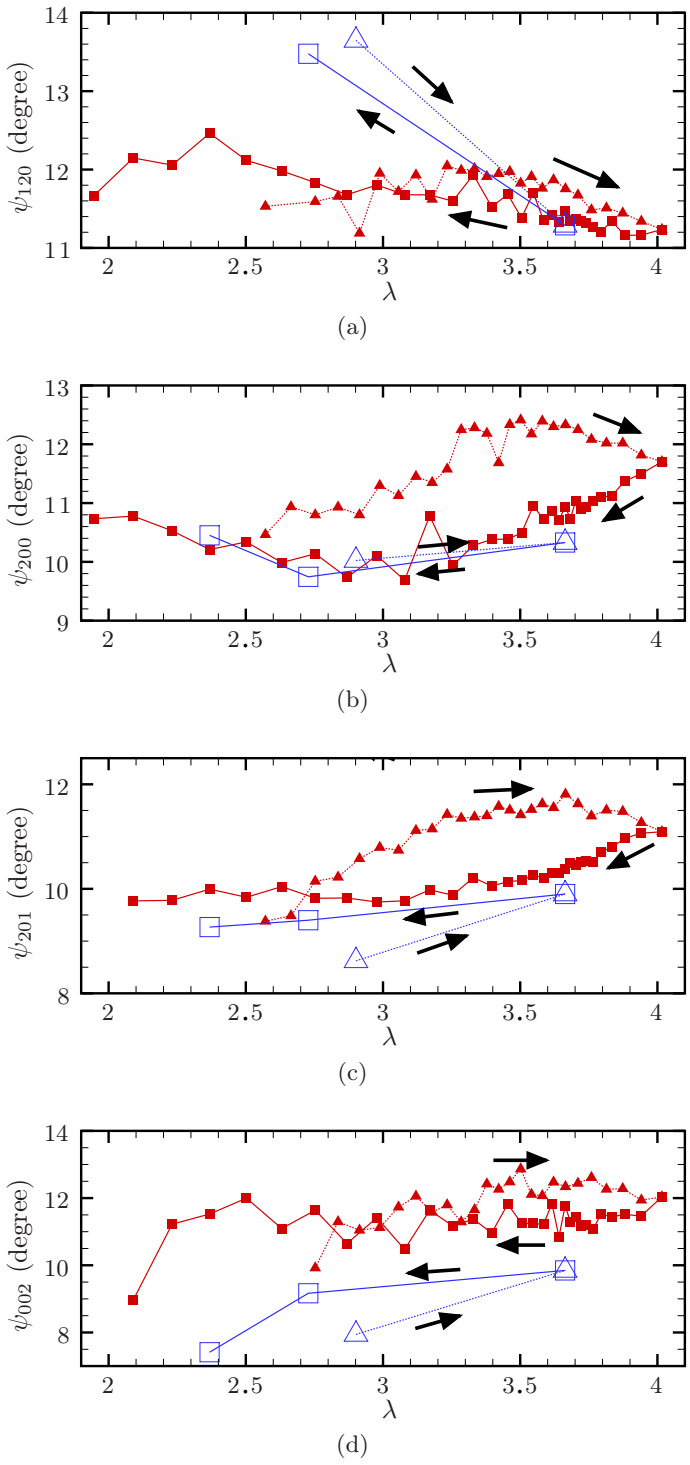

Figure 6.8: Evolution of the misorientation of the crystallites during a low (small filled symbols) and a high (large unfilled symbols) strain rate cycle. Triangular symbols: loading phase; square symbols: unloading phase.

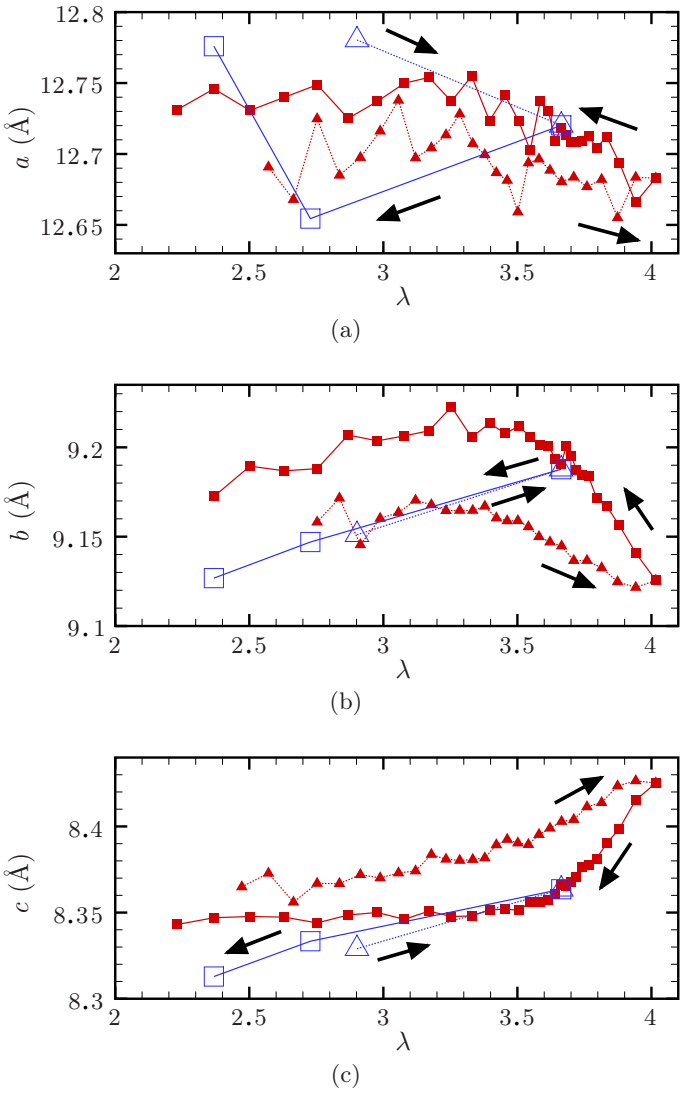

Figure 6.9: Evolution of the lattice parameters during a low (small filled symbols) and a high (large unfilled symbols) strain rate cycle. Triangular symbols: loading phase; square symbols: unloading phase.

6.4 Discussion

The number of measurements during the high strain rate cycle is very small: six measurements, including two while the material is 100 % amorphous. Therefore, when the difference between the two cycles is very significant (such as for χ and $\overline{V}_{\text{cryst}}$) or when the measurements exhibit negligeable noise (such as for χ and N_{cryst}), we consider that the number of measurements is relevant to discuss the effect of strain rate. Concerning the other characteristics, the differences between the two cycles must be discussed more carefully. Particularly, for l_{hkl} and ψ_{hkl}, only the caracteristics common to several diffraction planes are considered. The results specific to only one diffraction plane are not discussed here.

In addition, the results concerning the low strain rate cycle are the subject of a dedicated article to be published (Beurrot-Borgarino *et al.*, c). In this study, we focus on the effect of strain rate on SIC. In this way, the low strain rate cycle results are only discussed by comparison with the high strain rate cycle results, and not by comparison with other studies concerning low strain rate deformation.

6.4.1 Effect of strain rate on the mechanisms of crystallites nucleation and growth

The degree of crystallinity of a material is the ratio of the volume of the crystallized phase and the total volume of the material. Moreover, the volume of the crystallized phase varies only if *(i)* the number of crystallites varies and/or *(ii)* the volume of those crystallites varies. In the case of low and high strain rate cycles, Figs. 6.4, 6.6 and 6.7 clearly show that the evolution of χ during a cycle is due to the evolution of the number of crystallites. Indeed, the increase of χ with λ is due to the increase of N_{cryst}, which over-compensates the decrease of the volume of the crystallites $\overline{V}_{\text{cryst}}$. Furthermore, the hysteresis of χ is mainly explained by the hysteresis of N_{cryst}, and as well by the hysteresis of $\overline{V}_{\text{cryst}}$.

But eventhough the evolution of χ is qualitatively similar during low and high strain rate cycles, the strain rate has a strong quantitative effect on χ. During high strain rate cycles, χ is almost half smaller than during the low strain rate cycle for any given stretch ratio, and the onsets of crystallization λ_C and melting λ_M are higher. Those results are consistent with the results of Miyamoto *et al.* (2003) on synthetic polyisoprene rubber (IR), except for λ_M which was not influenced by the strain rate in their study. We observe that the effect of the strain rate on χ is mostly due to a difference in crystallites size and volume. Indeed, N_{cryst} is very close for both strain rates (Fig. 6.7), especially during the loading phases, whereas the volume is about 30 % smaller during high strain rate cycles (Fig. 6.6). It shows that strain rate has no effect on the number of nucleation sites of crystallites in the material. Furthermore, the lattice parameters are not much changed by the strain rate (Fig. 6.9), which means that the difference in $\overline{V}_{\text{cryst}}$ is not due to lattice deformation but to a difference in number of macromolecules per crystallites: $\overline{V}_{\text{cryst}}$ is smaller of about 30 % during high strain rate cycles than during low strain rate cycles.

Moreover, the dimensions of the crystallites do not change much during a cycle for both strain rates (Fig. 6.5), even at the beginning of crystallization for λ close to λ_C. It suggests that the number of macromolecules per crystallite is nearly constant from nucleation to melting. It means that strain rate may have an effect on the nucleation mechanism by decreasing the number of macromolecules involved in the nucleation of a crystallite. Also, during high strain rate cycles, λ_C is greater: the nucleation happens at higher stretch ratio. Both of those effects on the nucleation mechanism may be due to a rate of sollicitation high compared to the characteristic time of the macromolecules. Indeed, during a quasi-

static test, the rate of sollicitation is very small compared to the characteristic time of the macromolecules, which is the time necessary for the macromolecules to react to a sollicitation. When the strain rate is increased, the rate of sollicitation increases but the characteristic time of the macromolecules does not change. If the strain rate is high enough (here $\dot{\lambda} = 6.4\ s^{-1}$), the rate of sollicitation becomes high compared to the characteristic time of the chaines; it leads to two consequences:

- when the local stretch ratio necessary to nucleate a crystallite is achieved, the macromolecules need time to form this crystallite - it is the characteristic time. But once this characteristic time has passed and the crystallite is finally nucleated, the stretch ratio is already higher because the sollicitation rate is very high. As a consequence, the onset of crystallization λ_C appears higher during a high strain rate cycle than during a low strain rate cycle,
- when a crystallite nucleates, there are less macromolecular chains available to form the crystallite, i.e. less chains with the relevent elongation and position. It leads to smaller crystallites; and as the strain rate has no effect on the number of nucleation sites, the degree of crystallinity is lower.

Finally, the difference in crystallites size and volume between the two strain rates is quite constant with λ; the evolution of l_{hkl} and $\overline{V}_{\text{cryst}}$ during a cycle is qualitatively similar. It indicates that the crystallites growth mechanism during uniaxial tensile cycles may not be influenced by the strain rate. The difference in size and volume is the consequence of the influence of the strain rate on crystallites nucleation.

6.4.2 Effect of strain rate on the lattice parameters and the misorientation of the crystallites

As noted in the beginning of the Discussion section, the number of measurements during the high strain rate cycle is small and further investigations would be necessary to fully discuss the evolution of the misorientation of the crystallites and of the lattice parameters during the high strain rate cyle.

Nonetheless, we observe that strain rate has an identical effect on the misorientation of the crystallites and on the lattice parameters during the loading phase of a cycle. Indeed, if a parameter decreases with λ during a low strain rate cycle, then it is higher during high strain rate cycles than during low strain rate cycles; this is the case for ψ_{120}, a and b. Conversely, if a parameter increases during a low strain rate cycle, then it is lower during high strain rate cycles; this is the case for ψ_{200}, ψ_{201}, ψ_{002} and c.

As previously, this effect of strain rate may be due to the long characteristic time of the macromolecular chains compared to the sollicitation rate. Indeed during low strain rate cycles, during which the material is close to the equilibrium state, the sollicitation rate is very small and the stretch ratio does not have the time to evolve during the characteristic time of the macromolecules. On the contrary, during high strain rate cycles, the sollicitation rate is very high and the stretch ratio increases significantly during the characteristic time, i.e. while the macromolecules react to the sollicitation. As a consequence, the value of a parameter (lattice parameter or misorientation) during high strain rate cycles at a given λ corresponds to a lower λ during low strain rate cycles. It is to note that this reasoning is true only for the loading phase of the cycles; it does not explain the effect of strain rate on the crystallites misorientation and on the lattice parameters during the unloading phases.

Finally, it is not possible here to determine which characteristic time is involved: is it directly the characteristic time of the crystallized macromolecules, or is it the characteristic time of the surrounding amorphous macromolecules which constrain the crystallites and

monitor their orientation and lattice deformation ?

6.5 Conclusion

Qualitatively, strain rate has no effect on the evolution of SIC in NR during a cycle: the degree of crystallinity, the number of crystallites and their size and orientation evolve similarly during low and high strain rate cycles. But quantitatively, several differences can be highlighted between cycles at different strain rates.

To summarize, during high strain rate cycles, compared to low strain rate cycles:

- the thresholds of crystallization λ_C and melting λ_M are higher,
- after the onset of crystallization, the number of crystallites per unit volume is unchanged,
- the crystallites are smaller in all the directions,
- as a result, the crystallinity is lower,
- the orientation of the crystallites is also quiet similar. The misorientation ψ_{120} is greater and ψ_{200}, ψ_{201} and ψ_{002} are smaller,
- the lattice parameters are very close. The unit cell is slightly less stretched in the direction of tension during the loading phases (a and b are greater and c is smaller) and slightly more stretched during the unloading phase (a and b smaller and c greater).

It is to note that during the high strain rate cycle, the measurements have been performed during a one-second "pause", during which the material has relaxed and the crystallites have evolve to a state closer to the equilibrium state, i.e. closer to the state obtained during a low strain rate cycle (eventhough the material is not at the equilibrium state during this cycle). Therefore, the effect of strain rate on SIC is most probably higher than the one measured during this study. One way to obtain an accurate measurement of this effect would be to lower the exposure time to a fraction of second or to use a stroboscopic device in order to accumulate the weak signal over a large number of high strain rate cycles. This type of experiment has been previously proposed by Kawai (1975); but the repetition of a cycle - known as fatigue - also has a significant effect on the crystalline phase of NR as shown in Beurrot *et al.* (2011b).

Moreover, the effect of strain rate on the volume and number of crystallites shows that strain rate has no effect on the number of nucleation sites but has two effects on the crystallites nucleation mechanism: when the strain rate is increased *(i)* λ_C increases and *(ii)* the number of macromolecules per crystallite at nucleation decreases. Those effects may be due to a long characteristic time of the macromolecules compared to the sollicitation rate. As strain rate seems to have no effect on the crystallites growth mechanism, it leads to smaller crystallites and therefore lower crystallinity during cycles at high strain rate.

Finally, the effect of strain rate on the crystallites misorientation and lattice deformation may as well be due to a long characteristic time of the macromolecules, either in the crystallized phase or in the amorphous phase of the material. It is expressed by an onset in the evolution of the misorientation of the crystallites and of the lattice parameters during cycles at high strain rate.

6.6 Acknowledgment

The authors thank Dr D. Thiaudière, Dr C. Mocuta and Dr A. Zozulya from the DiffAbs beamline in Soleil synchrotron facility for their great help during the experiments and the Soleil staff for smoothly running the facility.

Chapitre 7

Caractéristiques de la cristallisation sous contrainte en fatigue

7.1 Introduction

Natural Rubber (NR, cis-1,4-polyisoprene) vulcanizates have the ability to crystallize under strain at room temperature. Strain-induced crystallization (SIC) of NR has been discovered by Katz (1925) with the help of X-ray diffraction. This technique has since permitted to obtain the crystallographic data of NR (Bunn, 1942; Nyburg, 1954), to exhibit the existence of stretch ratio thresholds of crystallization and melting of the crystallites (Toki *et al.*, 2000; Trabelsi *et al.*, 2002), to relate SIC to the mechanical hysteresis of the stress-strain response (Clark *et al.*, 1941; Toki *et al.*, 2000), and to put into light the effect of fillers such as carbon black (Lee et Donovan, 1987). For more details on the use of X-ray diffraction for SIC in NR, the reader can refer to the recent review of Huneau (2011).

The great majority of studies on SIC of NR focus on uniaxial quasi-static tensile tests and relaxation tests. But NR is often used in engineering applications for its great properties in fatigue such as long fatigue life, even at large strain (Cadwell *et al.*, 1940; André *et al.*, 1999; Saintier *et al.*, 2006b). The mechanical properties of NR in fatigue have been thoroughly studied (Mars et Fatemi, 2002; Legorju-jago et Bathias, 2002; Le Saux *et al.*, 2010); but studies on the evolution of SIC during fatigue testing of NR are very rare, though it is often accepted that its remarkable macroscopic fatigue properties are closely related to SIC. This lack of investigation is mainly due to the typical frequencies of fatigue tests (1 Hz or more) which are not compatible with the long time acquisition required by X-ray diffraction measurements (from a few seconds to an hour). Nevertheless, Kawai (1975) succeeded in measuring SIC during fatigue by using a stroboscopic technique to accumulate the weak intensity of the diffracted beam over a large number of cycles. He studied only one set of loading conditions for which both minimum and maximum stretch ratios in cycles are 3.5 and 4.5, respectively. More recently, Rouvière *et al.* (2007) measured the evolution of crystallinity along fatigue life for different uniaxial loading conditions by performing interrupted fatigue tests. However, their method requires an exposure time of 45 minutes for the acquisition of the X-ray diffractogram and therefore does not allow to separate SIC induced by fatigue from SIC induced by constant stretching. In both of these studies, only the degree of crystallinity of NR was measured, eventhough X-diffraction technique allows to measure more characteristics of the crystallized phase such as the size and orientation of the crystallites and the lattice parameters of the unit cells.

The aim of the present study is to measure the evolution of the different characteristics of the crystallized phase of NR during fatigue at different stretch ratios. For this purpose,

we developed an innovative experimental method which allows to measure SIC in real time during a fatigue test. With this machine, in-situ wide angle X-ray diffraction (WAXD) measurements are performed with a very short exposure time thanks to synchrotron radiation.

7.2 Experimental procedure

7.2.1 Instrumentation

The synchrotron measurements have been carried out at the DiffAbs beamline in the French national synchrotron facility SOLEIL (proposal number 20100096). The wavelength used is 1.319 Å and the beam size is 0.3 mm in diameter at half-maximum. The 2D WAXD patterns are recorded by a MAR 345 CCD X-ray detector. The exposure time is 1 s which is the minimum exposure time to record a workable scattering pattern. A PIN-diode is used in order to measure the transmitted photons.

The experiments have been conducted with the homemade stretching machine shown in Figure 7.1. It is composed of four electrical actuators, but only two opposite ones were

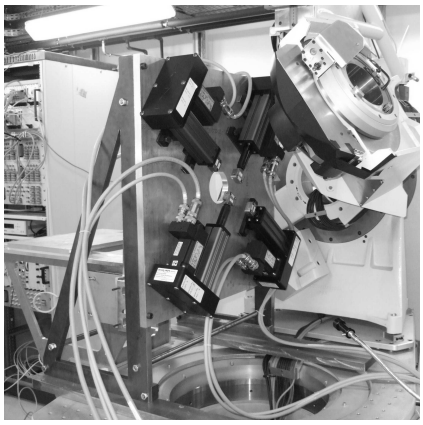

Figure 7.1: Fatigue testing machine in DiffAbs beamling in Soleil, France.

used in this study. Their movements are synchronized in order to keep the center of the specimen fixed during fatigue tests. Their loading capacity is ±500 N and their stroke is 75 mm each.

7.2.2 Material and samples

The material used in this study is a carbon black-filled natural rubber, cross-linked with 1.2 g of sulphur and 1.2 g of CBS accelerator for 100 g of rubber. It also contains 5 g of ZnO and 2 g of stearic acid and is filled with 50 g of N330 carbon black. The samples are classical flat dumbbell specimen with a 10 mm gauge length and a 2×4 mm^2 section.

A quasi-static test is conducted beforehand in order to determine *(i)* the relation between the local stretch ratio λ at the center of the sample and the displacements of the grips and *(ii)* the thresholds of crystallization λ_C and melting λ_M of the material at room temperature (similarly as Trabelsi *et al.* (2003a)). A five-cycle accommodation of the sample is first performed. During these experiments, the sample is elongated of 90 mm at the speed 0.012 mm.s^{-1}, the total duration of the cycle being about 2 hours. A scattering pattern is recorded during 2 seconds every 98 seconds and the local stretch ratio λ is measured continuously with a motion analysis system (Tema motion ®). Finally, this

experiment is a quasi-static test from $\lambda = 1$ to $\lambda = 4$ at $\dot{\lambda} = 1.1\,10^{-3}\ \mathrm{s}^{-1}$. Figure 7.2 shows the evolution of the index of crystallinity with λ; we obtain $\lambda_C = 2.36$ on the loading path and $\lambda_M = 1.80$ on the unloading path for the material studied here.

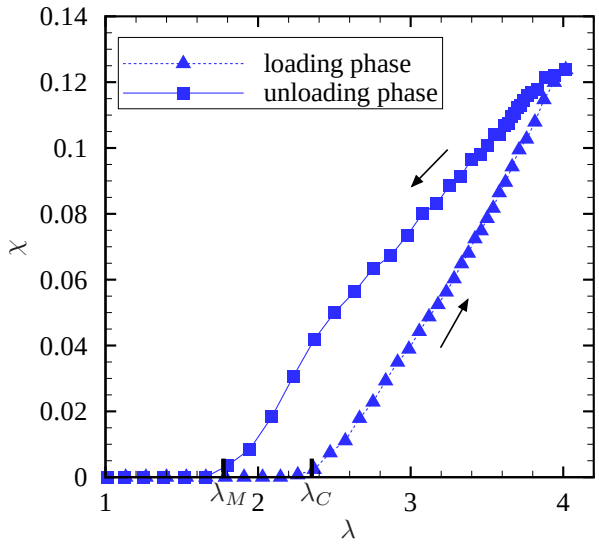

Figure 7.2: Evolution of the index of crystallinity during a quasi-static tensile test.

7.2.3 Procedures

In order to lower the residual elongation of the sample due to viscous and Mullins effects, all the samples are pre-cycled just before testing: 50 cycles at a higher strain level than during the tests.

The fatigue tests are conducted by prescribing constant displacements of the grips at each cycle. They are performed at conventional frequencies, i.e. around 1 Hz. As the minimum exposure time to record a diffraction pattern is 1 s (about the duration of a whole cycle), it is not possible to record diffraction patterns while the actuators are in motion. Therefore, to measure the evolution of SIC during fatigue testing, the tests are paused at maximum stretch ratio every 250 cycles to record a complete diffraction pattern. As the fatigue machine is triggered by the monitoring system of the X-ray beam, the duration of the pause is less than 1.5 s. The first scattering pattern is recorded at maximum strain of the first cycle of the test.

Four different fatigue tests have been performed. Table 7.1 presents the minimum and maximum displacements of the grips $d_{\min}$ and $d_{\max}$, the corresponding minimum and maximum stretch ratios $\lambda_{\min}$ and $\lambda_{\max}$ and the loading frequency f. To summarize the

Table 7.1: Fatigue loading conditions.

test No.	$d_{\min}$(mm)	$d_{\max}$(mm)	$\lambda_{\min}$	$\lambda_{\max}$	f(Hz)
1	0	20	1.00	2.90	2.5
2	4	33.2	1.44	3.66	0.8
3	9.3	33.2	1.98	3.66	1
4	25	45	3.18	4.02	1.5

fatigue tests, Figure 7.3 presents the loading conditions in terms of stretch ratios, and

compares them to the thresholds of crystallization λ_C and melting λ_M of the material measured during the quasi-static test.

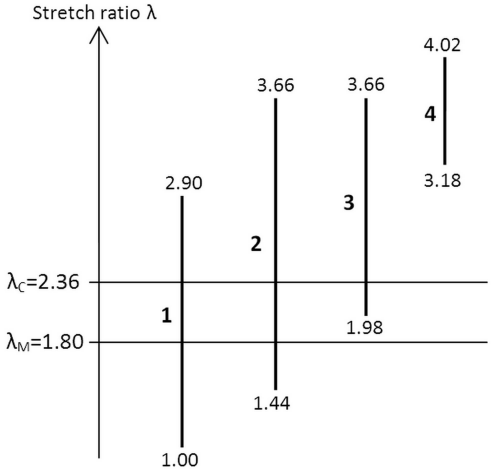

Figure 7.3: Minimum and maximum stretch ratios reached during fatigue tests compared to stretch ratio thresholds for crystallization λ_C and melting λ_M. Bold numbers stand for fatigue test numbers.

7.2.4 Scattering pattern analysis

In this study, we consider wide angle scattering: the range of diffraction angles is $2\theta \in [8°, 26.7°]$. We use the (012) reflections of Cr_2O_3 powder placed on each side of a specimen to calibrate the diffraction angles 2θ (the lattice parameters of Cr_2O_3 are $a = 4.9590$ Å and $c = 1.3596$ Å). Moreover, we follow the well-established correction method of Ran *et al.* (2001): an air scattering pattern (without sample) is first collected and is used to correct the patterns, and the change in thickness of the sample under extension and the change of intensity of the incident photons are also considered. An example of corrected diffraction pattern is given in Figure 7.4.

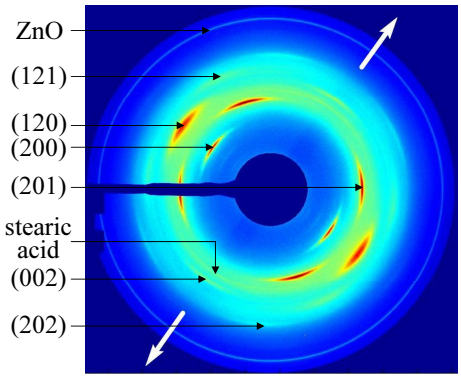

Figure 7.4: Example of diffraction pattern of crystallized NR in uniaxial tension. The white arrows show the tension direction. The Miller indices of the diffraction planes corresponding to the different reflections are indicated in the figure.

Once the corrections performed, the intensity of photons diffracted by the isotropic phases of the material $I_{\text{iso}}(2\theta)$ is extracted from the diffraction patterns by considering

the minimum intensity along the azimuthal angle β for each Bragg angle 2θ. Then, the intensity of photons diffracted by the anisotropic phase $I_{\text{ani}}(2\theta, \beta)$ is calculated as the difference between the total intensity of photons diffracted $I_{\text{total}}(2\theta, \beta)$ and $I_{\text{iso}}(2\theta)$. The spectra extracted from $I_{\text{ani}}(2\theta, \beta)$ and $I_{\text{iso}}(2\theta)$ are classically fitted by series of Pearson functions (Toki *et al.*, 2000; Trabelsi *et al.*, 2003a; Rault *et al.*, 2006a; Chenal *et al.*, 2007b). Different characteristics of the crystallized phase of NR are calculated from those quantities.

An index of crystallinity χ is calculated:

$$\chi = \frac{\mathcal{I}_{\text{cryst}}}{\mathcal{I}_{\text{cryst}} + \mathcal{I}_{\text{amorphous}}}, \tag{7.1}$$

where $\mathcal{I}_{\text{cryst}}$ is the integrated intensity of the (120) and (200) reflections measured on one spectrum (2θ, I_{ani}), and $\mathcal{I}_{\text{amorphous}}$ is the integrated intensity of the amorphous halo, assumed equal to the integrated intensity I_{iso}. The index χ is proportional to the degree of crystallinity of the material.

The size l_{hkl} of the crystallites in the direction normal to the (hkl) diffraction planes is deduced from the Scherrer formula (Guinier, 1963):

$$l_{hkl} = \frac{K\lambda}{\text{FWHM}_{2\theta} \cos\theta}, \tag{7.2}$$

in which K is a scalar which depends on the shape of the crystallites (here we adopt 0.78 as Trabelsi *et al.* (2003a)), λ is the radiation wavelength, θ is the Bragg angle and $\text{FWHM}_{2\theta}$ is the full width at half-maximum of the hkl reflection in 2θ. An index of the mean volume of the crystallites $\overline{V}_{\text{cryst}}$ is calculated from the crystallites size in three different directions:

$$\overline{V}_{\text{cryst}} = l_{200} \cdot l_{120} \cdot l_{201}. \tag{7.3}$$

The misorientation ψ_{hkl} of the (hkl) diffraction planes in the crystallites (compared to their mean orientation) is simply given by half the full width at half-maximum (FWHM_{β}) of the peaks, measured on the azimuthal profiles of the reflection.

Finally, the lattice parameters of the unit cell of the polyisoprene are calculated considering an orthorombic crystal system, as determined by Immirzi *et al.* (2005) and Rajkumar *et al.* (2006). On the scattering patterns, we identify 18 diffraction arcs which are due to 6 different diffraction planes (see Fig. 7.4). As only three lattice parameters (a, b and c) must be calculated, each of them is the average of two values measured from reflections due to two different diffraction planes.

7.3 Results and discussion

As mentioned above, the fatigue tests were performed by prescribing constant minimum and maximum displacements of the grips. As the material is cycled, Mullins and viscous effects reduce the strain level reached at a given displacement of each cycle. This phenomenon is reduced by the accommodation of the material before fatigue testing, but it cannot be completely suppressed. Thus, all the results here are obtained for constant minimum and maximum displacements which correspond to decreasing minimum and maximum strain levels. As shown in Fig. 7.3, fatigue tests No. 1 and 2 are performed with minimum stretch ratios lower than λ_M. Moreover, even if the initial minimum stretch ratio in fatigue test No. 3 is slightly higher than λ_M, it becomes lower after a few cycles only. So, for these three tests, the same phenomenon takes place during each cycle: all the

crystallites melt when the minimum displacement is reached, and new crystallites nucleate when the sample is stretched again. For fatigue test No. 4, the minimum stretch ratio achieved at each cycle decreases with the number of cycles as well, but it is always greatly larger than the threshold of melting λ_M (and then than λ_C). Therefore, in the material, some crystallites never melt while some others melt at each cyle at low stretch ratios.

7.3.1 Evolution of χ during fatigue tests

The evolution of the index of crystallinity χ measured at maximum deformation during fatigue tests is shown in Figure 7.5. As expected, the index of crystallinity depends on

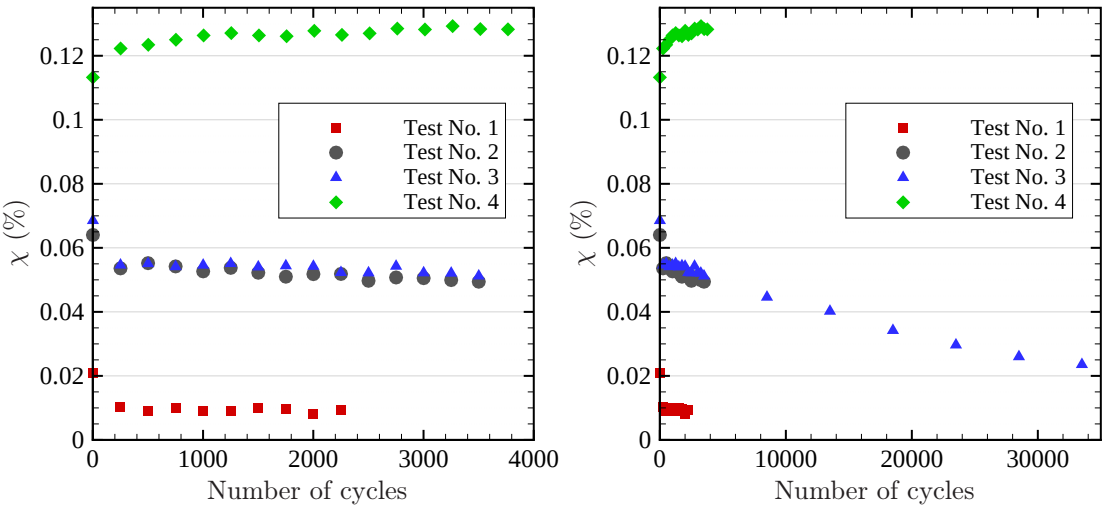

(a) During the first 4,000 cycles.

(b) During the first 35,000 cycles of test No. 3.

Figure 7.5: Evolution of the crystallinity index during fatigue tests.

the stretch ratio: the larger the strain, the higher the crystallinity. And the index of crystallinity is equal during fatigue tests No. 2 and 3, which are performed at the same λ_{max}.

During the three fatigue tests with the lowest minimum and maximum strain levels (tests No. 1, 2 and 3), i.e. tests during which all the crystallites melt at each cycle, the index of crystallinity decreases of about 15 % to 50 % during the first 250 cycles, and then continues to decrease at a lower but constant rate until the end of the tests. It is to note that the results shown in Fig. 7.5 (a) only correspond to the first 4000 cycles, but fatigue test No. 3 has been performed during 35,000 cycles as shown in Fig. 7.5 (b) and we observe that χ decreases at a constant rate during the whole test, down to about χ=2 % in comparison with χ=7 % at the beginning of the test.

During fatigue test No. 4, during which the minimum stretch ratio is higher than λ_C and λ_M, the evolution of the index of crystallinity is very different: χ increases with the number of cycles of about 13 % during the first 4000 cycles. This result is in agreement with those of Kawai (1975) obtained during a fatigue test with $\lambda_{min} = 3.5$ and $\lambda_{max} = 4.5$.

7.3.2 Size and volume of the crystallites

In the following, the data of fatigue test No. 1 are not shown as the degree of crystallinity during this test is too small to allow good measurements on the diffraction arcs in the scattering patterns.

Figures 7.6 and 7.7 show the evolution of the size of the crystallites during the first 4000 cycles of fatigue tests No. 2 and 3 and fatigue test No. 4, respectively. Only the

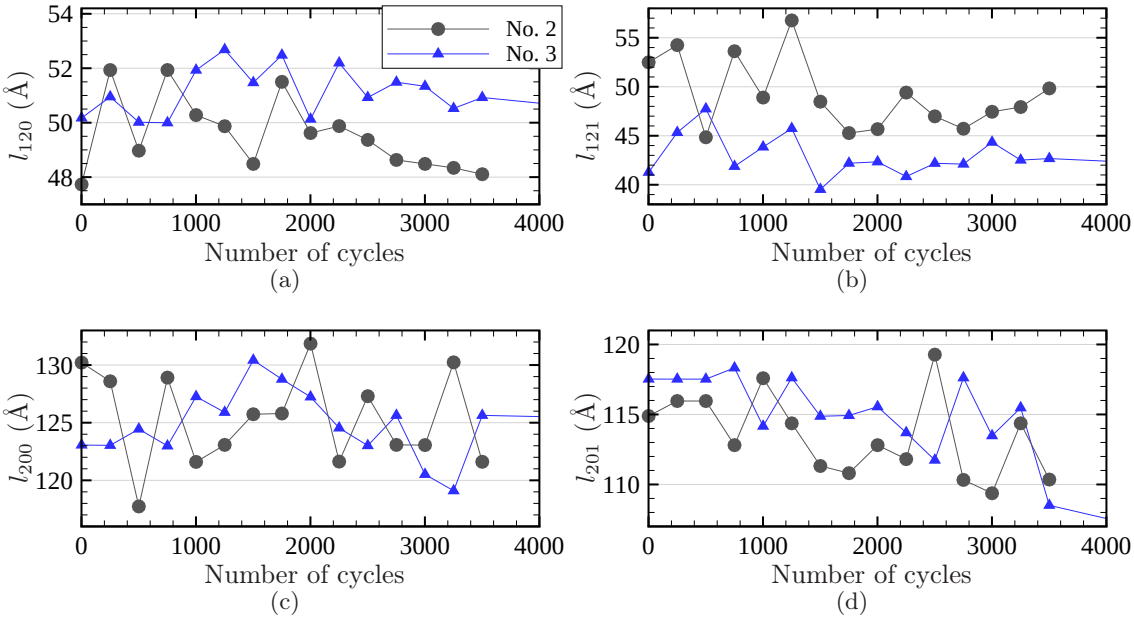

Figure 7.6: Evolution of the size of the crystallites during fatigue tests No. 2 and 3.

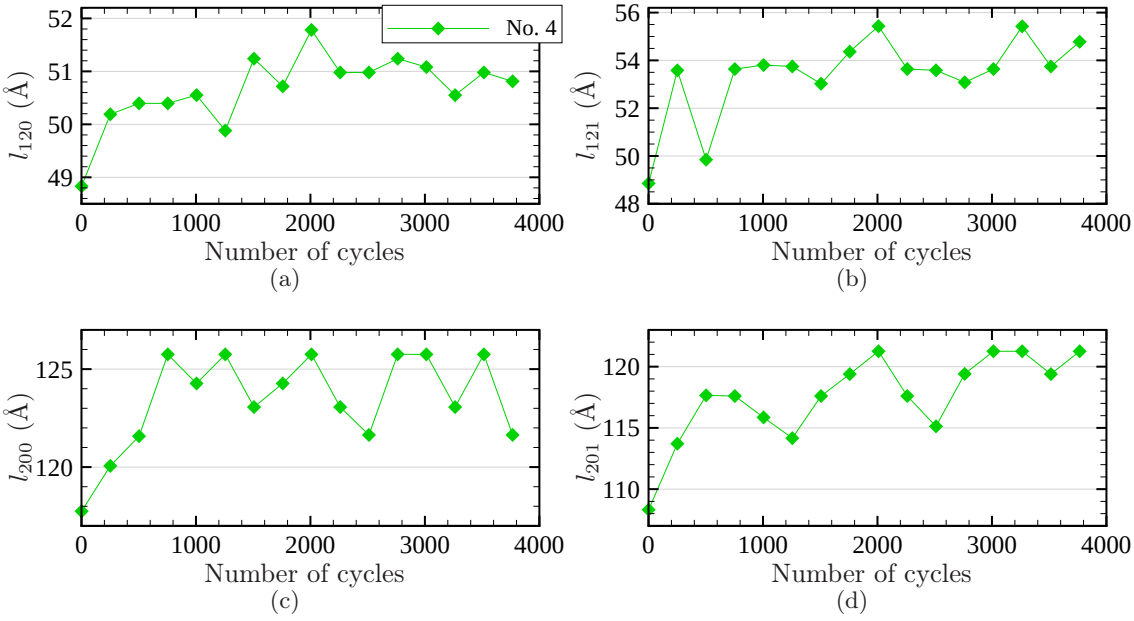

Figure 7.7: Evolution of the size of the crystallites during fatigue test No. 4.

size in the directions normal to the diffraction planes (120), (121), (200) and (201) are shown; the reflections (002) and (202) are too weak to be measured accurately. The size of the crystallites is very close for the three tests, eventhough λ_{max} varies: $l_{120} \approx 50$ Å, $l_{121} \approx 45$ Å, $l_{200} \approx 125$ Å and $l_{201} \approx 115$ Å. This result is consistent with the results of Trabelsi *et al.* (2003b) and Poompradub *et al.* (2005) for carbon black-filled NR. Moreover, the sizes measured here are very close to the sizes obtained during a high strain rate cycle

for the same material at about $\dot{\lambda} = 6.4\ s^{-1}$ (Beurrot-Borgarino *et al.*, a). During fatigue tests No. 2 and 3, the size of the crystallites slighlty decreases, of a few percent only during the first 4,000 cycles. On the contrary, during fatigue test No. 4, the size of the crystallites increases in the four directions of about 8 %. The rate of increase is higher at the beginning of the test during the first 250 cycles than during the rest of the test.

The evolution of the volume of the crystallites during the three fatigue tests is shown in Figure 7.8; Fig. 7.8 (a) and (b) show the evolution during the first 4,000 cycles and the first 13,500 cycles respectively of tests No. 2 and 3, Fig. 7.8 (c) shows the evolution during the first 4,000 cycles of test No. 4. Of course, the evolution of the volume is similar to the

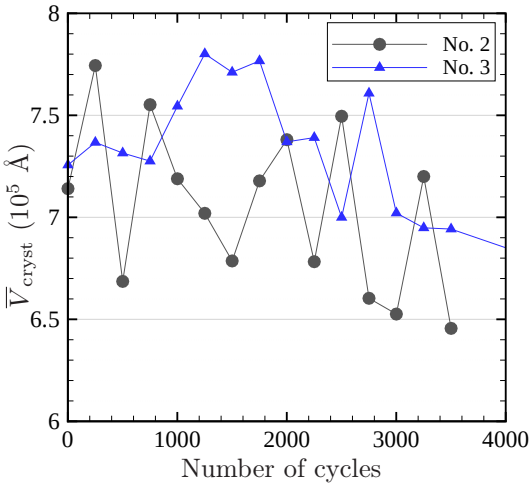

(a) During the first 4,000 cycles of fatigue tests No. 2 and 3.

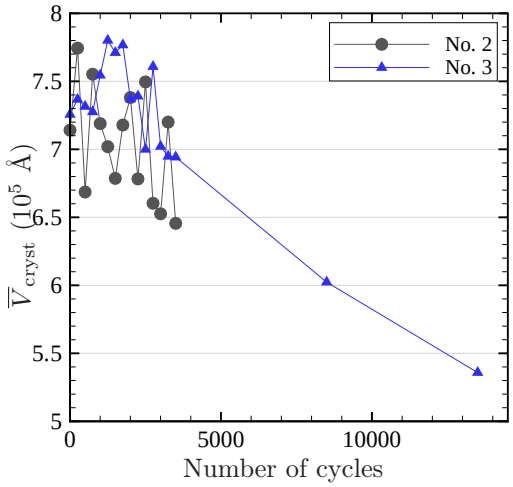

(b) During the 13,500 cycles of fatigue test No. 3.

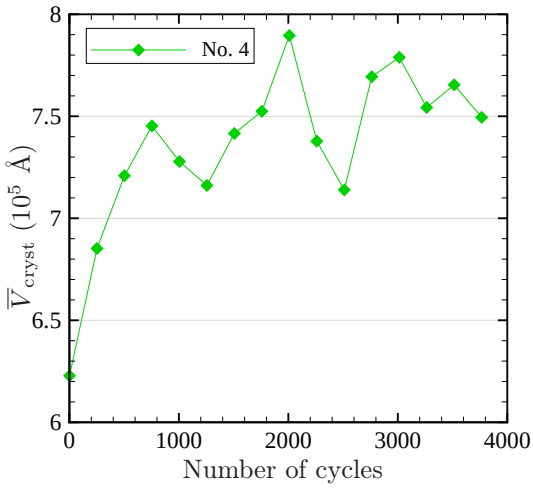

(c) During fatigue test No. 4.

Figure 7.8: Evolution of the volume of the crystallites during fatigue tests No. 2 to 4.

evolution of the dimensions of the crystallites:

– During tests No. 2 and 3, which are performed with λ_{min} lower than the threshold of melting λ_M, the volume of the crystallites decreases with the number of cycles. This decrease may explain the decrease of χ observed in Fig. 7.5, but its origin is unexplained yet. Most probably, this decrease is not due to the decrease of λ_{max} with the number of cycles during the fatigue tests; indeed during a quasi-static test the size of the crystallites decreases when the stretch ratio increases (Poompradub *et al.*,

2005). Furthermore, the decrease of the crystallites size is surprising considering that all the crystallites melt at each cycles during the fatigue tests. It means that the new crystallites nucleate with a smaller size than the previous ones.

– During test No. 4, which is performed with λ_{min} higher than the threshold of crystallization λ_C, the mean volume of the crystallites increases; it is consistent with the increase of χ observed in Fig. 7.5. As previously, the origin of this evolution is unknown. It might be due to the decrease of λ_{max} as $\overline{V}_{cryst}$ decreases with λ during a quasi-static tensile test (Poompradub *et al.*, 2005; Beurrot-Borgarino *et al.*, c)).

7.3.3 Misorientation of the crystallites

The evolution of the misorientation of the crystallites during fatigue tests is shown in Figure 7.9. Only the misorientation of the planes (200), (201), (120) and (002) are

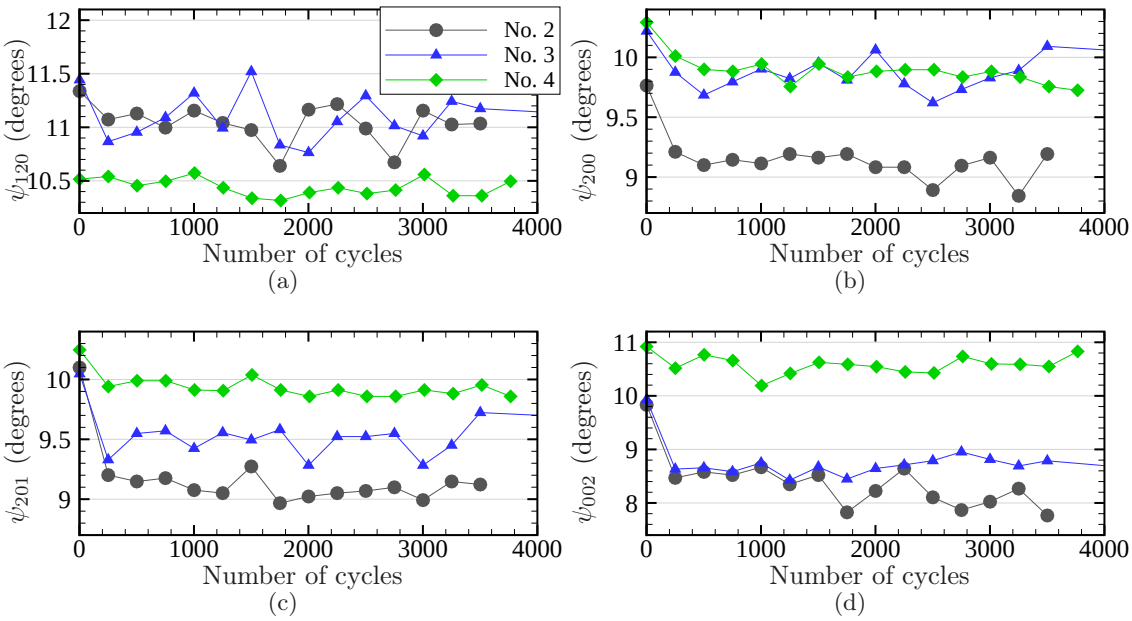

Figure 7.9: Evolution of the misorientation of the crystallites during the first 4000 cycles of the fatigue tests.

shown; the measurements of the other diffraction planes are too noisy to be conclusive. The misorientation of the crystallites ranges from 8° to 11.5° depending on the diffraction plane considered and the stretch ratio. These values are similar to those measured by Poompradub *et al.* (2005) and much smaller than those measured by Trabelsi *et al.* (2003b) during a quasi-static tensile test of a carbon black-filled NR. They are also very close to the misorientation obtained during a high strain rate cycle on the same material (Beurrot-Borgarino *et al.*, a).

For the three fatigue tests, the misorientation of the crystallites decreases of about 5 % to 15 % during the first 250 or 500 cycles, depending of the fatigue test and the diffraction plane considered; then during the rest of the fatigue tests the misorientation is constant or very slightly decreases, depending on the diffraction plane and the fatigue test considered. The decrease is smaller for the (120) diffraction planes than for the three other planes and it is smaller for fatigue test No. 4 than for the other tests. This decrease of ψ_{hkl} might be due to the decrease of λ_{max} with the number of cycles. Indeed, the evolution of the misorientation of the crystallites with the stretch ratio in carbon black-filled NR during

a quasi-static test is unclear yet: Poompradub *et al.* (2005) showed that ψ_{hkl} decreases with λ whereas Trabelsi *et al.* (2003b) showed that ψ_{hkl} increases. In a previous study, we performed a quasi-static tensile test on the same material and measured the evolution of the misorientation of the crystallites with λ (Beurrot-Borgarino *et al.*, c). The evolution of ψ_{200} and ψ_{120} during this cycle are shown in Figure 7.10 (a) and (b) respectively. We

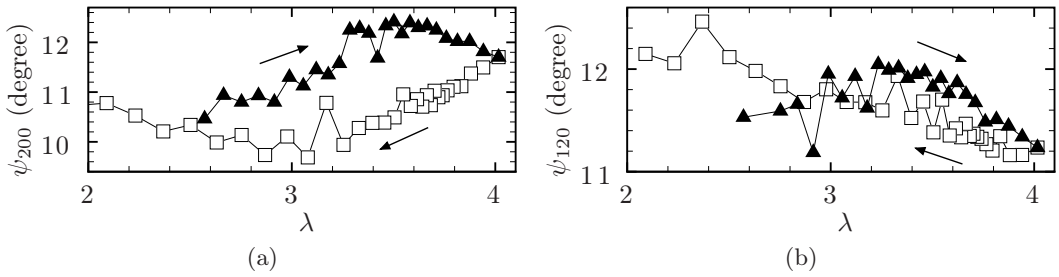

Figure 7.10: Evolution of the misorientation of the (200) and (120) diffraction planes of the crystallites (compared with their mean orientation) during a quasi-static tensile test in a carbon black-filled NR. Loading phase: filled triangles; unloading phase: unfilled squares.

observed that the misorientation of all the diffraction planes evolves similarly to ψ_{200}, expect ψ_{120}. Additionnal information on the experimental method and the results obtained are given in (Beurrot-Borgarino *et al.*, c). Fig. 7.10 shows that during the loading phase, the misorientation increases with λ for $\lambda < 3.6$ approximately and then decreases; during the unloading phase the misorientation first decreases and then slightly increases for $\lambda < 3.1$. The evolution of ψ_{120} is close, except it increases from the beginning of the unloading phase of the cycle, as shown in Fig. 7.10 (b). Indeed, if we consider that during a fatigue test ψ_{hkl} at λ_{max} follows the loading curves of Fig. 7.10 when λ_{max} decreases, it would explain the decrease of ψ_{200}, ψ_{201} and ψ_{002}. Furthermore, ψ_{120} should then increase and not decrease; it is not the case but however we observe that the decrease of ψ_{120} is smaller than for the other diffraction planes. Moreover, we also observe that during fatigue test No. 4, which is performed with the highest λ_{max}, ψ_{201}, ψ_{200} and ψ_{002} are higher and ψ_{120} is lower than during the other fatigue tests. This is consistent with the evolution of the misorientation of the crystallites with λ during the loading phase of a quasi-static cycle.

Surprisingly, for tests No. 2 and 3 which are performed with the same λ_{max}, ψ_{200} and ψ_{201} measured at λ_{max} also depend on λ_{min} (but ψ_{120} and ψ_{002} do not). During those fatigue tests, λ_{min} is smaller than λ_M, i.e. all the crystallites melt at each cycle. It means that the stretch ratio reached when the material is totally amorphous has an influence on the orientation of the crystallites nucleated subsequently.

7.3.4 Lattice parameters

Figure 7.11 shows the evolution of the lattice parameters a, b and c during the first 4000 cycles of fatigue tests; beyond 4000 cycles the crystallinity is too small to allow accurate measurements of the lattice parameters. The values of the lattice parameters are similar to those obtained by Poompradub *et al.* (2005) during a quasi-static tensile test on a carbon black-filled NR: 12.67 Å $< a <$ 12.80 Å, 9.14 Å $< b <$ 9.24 Å and 8.33 Å $< c <$ 8.41 Å. During the three fatigue tests, the lattice parameters seem constant. As expected, for test No. 4 which is performed at the highest λ_{max}, a and b are smaller and c is higher than for the other fatigue tests (Tosaka *et al.*, 2004b; Poompradub *et al.*, 2005; Tosaka, 2007), i.e. the unit cell is more elongated in the tension direction and more contracted in the

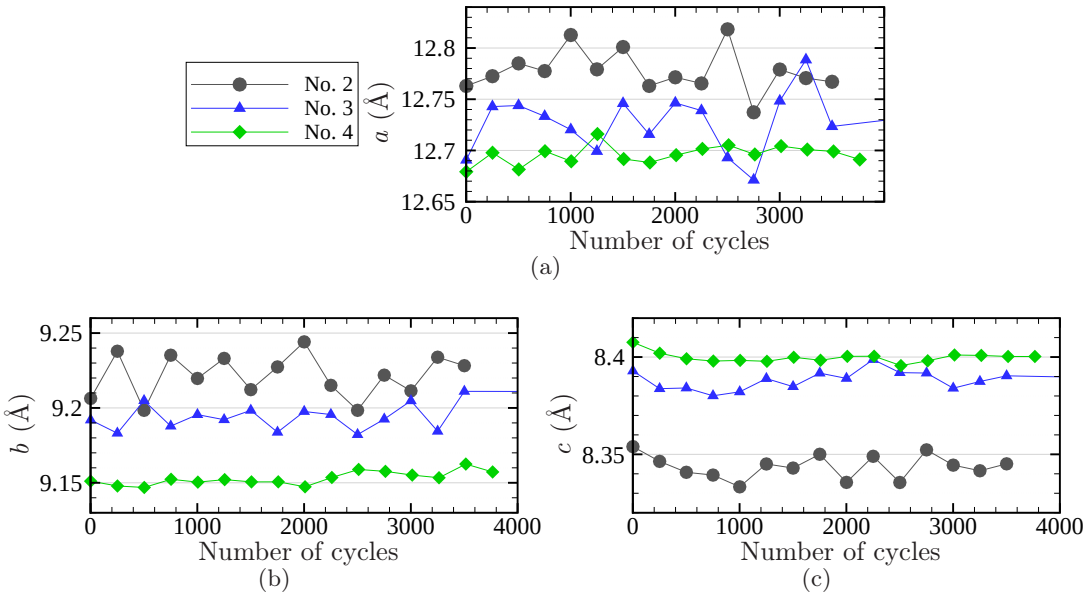

Figure 7.11: Evolution of the lattice parameters during fatigue tests.

transverse directions.

Moreover, the lattice parameters are also very different between tests No. 2 and 3 which are performed at the same $\lambda_{\max}$. During test No. 2, which is performed at the lowest $\lambda_{\min}$, a and b are higher and c is lower. This result is surprising considering that at each cycle during tests No. 2 and 3, all the crystallites melt at each cycle and new ones nucleate when the material reaches λ_C. It means that the material, which is complitely amorphous at $\lambda_{\min}$, is modified by the fatigue tests and then does not crystallize in the same way once λ reaches λ_C and then $\lambda_{\max}$. During fatigue testing, the lattice parameters seem to be constant or not to evolve much compared to the data noise. Nevertheless, it is probable that during the fatigue tests, the lattice parameters a and b slightly increase and the parameter c slightly decreases with the number of cycles as $\lambda_{\max}$ decreases during the tests. Indeed, during a quasi-static test, a and b decrease and c increases with λ (Poompradub *et al.*, 2005; Tosaka, 2007; Beurrot-Borgarino *et al.*, c).

7.4 Conclusion

To close this paper, we summarize the evolution of the different parameters of crystallization during fatigue tests, performed at constant minimum and maximum displacements of the grips at each cycle:

- the size of crystallites decrease when $\lambda_{\min} < \lambda_M$ whereas it increases when $\lambda_{\min} > \lambda_M$. Despite of this evolution, the size of the crystallites does not depend much on the values of $\lambda_{\min}$ and $\lambda_{\max}$,
- the crystallinity decreases with the number of cycles when $\lambda_{\min} < \lambda_M$, i.e. when all the crystallites melt at each cycle. When $\lambda_{\min} > \lambda_M$, i.e. when some of the crystallites never melt, the crystallinity increases with the number of cycles. Those changes may be due to the increase of $\overline{V}_{\text{cryst}}$. Moreover, the crystallinity depends on the value of $\lambda_{\max}$ and not of the value of $\lambda_{\min}$,
- the experimental data do not show any evolution of the lattice parameters with the number of cycles, eventhough it is probable that the parameters a and b slightly

increase and c slightly decreases. The values of a, b and c highly depend on both $\lambda_{\min}$ and $\lambda_{\max}$, even when all the crystallites melt at each cycle,

– For all the fatigue tests, the misorientation of the crystallites decreases during the first 250 or 500 cycles and is then constant or slightly decreases. This decrease is smaller when $\lambda_{\min} > \lambda_M$. Furthermore, the value of misorientation highly depend on both $\lambda_{\min}$ and $\lambda_{\max}$.

As all the parameters are measured at $\lambda_{\max}$ and as all of them (except the size of the crystallites) depend on the stretch ratio (as shown by the low strain rate cycle (Beurrot-Borgarino *et al.*, c)), it is not surprising to observe that they depend on the maximum stretch ratio achieved during the fatigue tests. On the contrary, the effect of $\lambda_{\min}$ (even when inferior to λ_M) on the lattice parameters and the orientation of the crystallites was unexpected. It shows that the loading conditions applied to the material when it is totally amorphous has a significant effect on the crystallites nucleating at a higher stretch ratio. Moreover, all the crystallites parameters, except the size and volume of the crytallites, depend on $\lambda_{\max}$; they can be classified into two groups: the lattice parameters and the orientation of the crystallites achieved at maximum stretch ratio also depend on $\lambda_{\min}$ but have the same evolution with the number of cycles whatever the value of $\lambda_{\min}$; whereas the size of the crystallites and the crystallinity do not depend on $\lambda_{\min}$, but their evolutions depend on it, more precisely it differs whether $\lambda_{\min}$ is smaller of larger than λ_M.

Chapitre 8

Evolution de la cristallisation sous contrainte en fatigue

8.1 Introduction

Natural Rubber (NR, cis-1,4-polyisoprene) vulcanizates have the ability to crystallize under strain at room temperature. Strain-induced crystallization (SIC) of NR has been discovered by Katz (1925) with the help of X-ray diffraction. This technique has since permitted to obtain the crystallographic data of NR (Bunn, 1942; Nyburg, 1954), to exhibit the existence of stretch ratio thresholds of crystallization and melting of the crystallites (Toki *et al.*, 2000; Trabelsi *et al.*, 2002), to relate SIC to the mechanical hysteresis of the stress-strain response (Clark *et al.*, 1941; Toki *et al.*, 2000), and to put into light the effect of fillers such as carbon black (Lee et Donovan, 1987). For more details on the use of X-ray diffraction for SIC in NR, the reader can refer to the recent review of Huneau (2011).

The great majority of the studies on SIC of NR focus on uniaxial quasi-static cycles and relaxation tests. But NR is often used in engineering applications for its great properties in fatigue such as long fatigue life, even at large strain (Cadwell *et al.*, 1940; André *et al.*, 1999; Saintier *et al.*, 2006b). The mechanical properties of NR have been thoroughly studied (Mars et Fatemi, 2002; Legorju-jago et Bathias, 2002; Le Saux *et al.*, 2010); but studies on the evolution of SIC during fatigue testing of NR are very rare, though it is often accepted that these remarkable features are closely related to SIC. This is mainly because the typical frequencies of fatigue tests (1 Hz or more) are not compatible with the long time acquisition required by X-ray diffraction measurements (from a few seconds to an hour). Nevertheless, Kawai (1975) succeeded in measuring SIC during fatigue by using a stroboscopic technique to accumulate the weak intensity of the diffracted beam over a large number of cycles. He studied only one set of loading conditions for which both minimum and maximum stretch ratios achieved are 3.5 and 4.5, respectively. In this case, he observed an increase in the degree of crystallinity with the number of cycles. Furthermore, Rouvière *et al.* (2007) recently measured the evolution of crystallinity along fatigue life for different uniaxial loading conditions by performing interrupted fatigue tests. Nevertheless, this method does not allow to separate SIC induced by fatigue from SIC induced by constant stretching during the 45-minute acquisition of the X-ray diffractogram.

The aim of the present study is to measure the evolution of the strain-induced crystallinity during fatigue of carbon black-filled NR and to determine the mechanisms that drive this evolution. For this purpose, we developed an innovative experimental method which allows to measure SIC in real time during a fatigue experiment. In-situ wide angle X-ray diffraction (WAXD) measurements are performed with a very short exposure time

achieved thanks to synchrotron radiation. Thanks to the results obtained, we highlight the key role of the melting stretch ratio and we propose two mechanisms of SIC in NR fatigue depending on loading conditions.

8.2 Experimental

8.2.1 Material and samples

The material used in this study is a carbon black-filled natural rubber, cross-linked with 1.2 phr (per hundred of rubber) of sulphur and CBS accelerator. It also contains ZnO (5 phr) and stearic acid (2 phr) and is filled with 50 phr of N330 carbon black. The samples are classical flat dumbbell specimen with a 10 mm gauge length and a 2 mm $\times$ 4 mm section.

8.2.2 Testing machine

Experiments have been conducted with the homemade stretching machine shown in Figure 8.1. It is composed of four electrical actuators, but only two opposite ones were

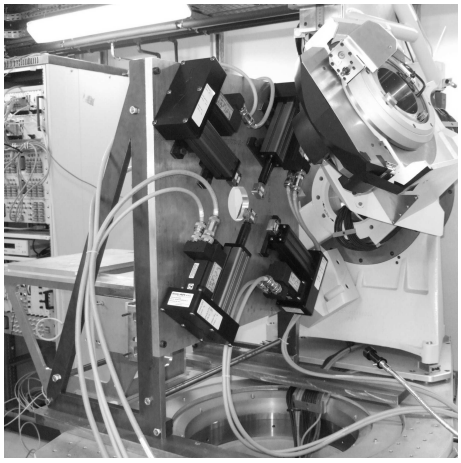

Figure 8.1: Uniaxial fatigue machine in DiffAbs beamline.

used in this study. Their movements are synchronized, in order to keep the center of the specimen fixed during the fatigue tests. Their loading capacity is $\pm$500 N and their stroke is 75 mm each.

8.2.3 Procedures

Accommodation

In order to lower the residual stretch ratio of the sample due to Mullins effect and viscoelasticity, all the samples are pre-cycled just before testing (5 cycles, and additional 50 cycles before fatigue tests) at a higher strain level than during the tests.

Preliminary quasi-static experiment

A quasi-static test is beforehand conducted to determine *(i)* the relation between the stretch ratio λ and the displacements of clamps which will be used in all other experiments, and *(ii)* the stretch ratio thresholds of crystallization λ_C and melting λ_M of the material at room temperature (similarly as Trabelsi *et al.* (2003a)). During these experiments, the

sample is elongated of 90 mm at the speed 0.012 mm.s^{-1}, the total duration of the cycle being about 2 hours. A scattering pattern is recorded every 98 seconds and the local stretch ratio λ at the center of the sample is measured continuously by optical means. Finally, this experiment is a quasi-static test from $\lambda = 1$ to $\lambda = 4$ at $\dot{\lambda} = 1.1\,10^{-3}$ s^{-1}, and it leads to $\lambda_C = 2.36$ on the loading path and $\lambda_M = 1.80$ on the unloading path.

Fatigue experiments

The fatigue tests are conducted by prescribing constant displacements of the clamps at each cycle. They are performed at conventional frequencies, i.e. around 1 Hz. As the minimum exposure time to record a diffraction pattern is 1 s (about the duration of a full cycle), it is not possible to record the diffraction patterns while the actuators are in motion. Therefore, to measure the evolution of SIC during fatigue testing, the tests are paused at maximum strain every 250 cycles to record a complete diffraction pattern. As the fatigue machine is triggered by the monitoring system of the X-ray beam, the duration of the pause is less than 1.5 s. The first scattering pattern is recorded during the first cycle of the test.

Four different fatigue tests have been performed. Table 8.1 presents the corresponding minimum and maximum displacements of the clamps $d_{\min}$ and $d_{\max}$, the corresponding minimum and maximum stretch ratios $\lambda_{\min}$ and $\lambda_{\max}$ and the loading frequency f. To

Table 8.1: Fatigue loading conditions.

test No.	$d_{\min}$(mm)	$d_{\max}$(mm)	$\lambda_{\min}$	$\lambda_{\max}$	f(Hz)
1	0	20	1.00	2.90	2.5
2	4	33.2	1.44	3.66	0.8
3	9.3	33.2	1.98	3.66	1
4	25	45	3.18	4.02	1.5

summarize the fatigue tests, Figure 8.2 presents the loading conditions in terms of stretch ratios, and compares them to the thresholds of crystallization λ_C and melting λ_M (measured during the preliminary experiment).

Relaxation experiments

The relaxation tests consist in quickly stretching a sample to a given stretch ratio and then maintaining the same stretch level. They last 28 min and scattering patterns are recorded every 2 min. Table 8.2 presents the stretch ratios at which the three relaxation experiments are conducted. The stretch rate $\dot{\lambda}$ of the loading path is between 5.6 and 6.0

Table 8.2: Relaxation loading conditions.

test No.	λ
5	2.41
6	2.90
7	3.66

for the three tests.

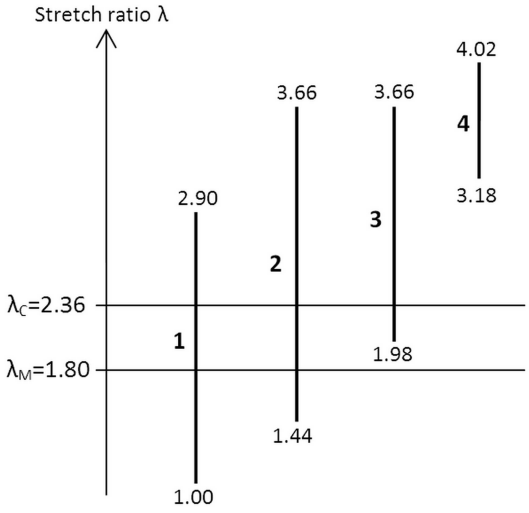

Figure 8.2: Minimum and maximum stretch ratios reached during fatigue tests and threshold stretch ratios for crystallization λ_C and melting λ_M. Bold numbers stand for the fatigue tests numbers.

8.2.4 Synchrotron

The synchrotron measurements have been carried out at the DiffAbs beamline in the French national synchrotron facility SOLEIL. The wavelength used is 1.319 Å and the beam size is 0.3 mm in diameter at half-maximum. The 2D WAXD patterns are recorded by a MAR 345 CCD X-ray detector. The exposure time is 1 s (minimum time to record a workable scattering pattern) for the fatigue and relaxation tests. For the low strain rate cycle test, it is set to 2 s in order to enhance the accuracy of the measurements. A PIN-diode beam stop was used in order to make an accurate correction of air scattering.

8.2.5 Scattering pattern analysis

In this study, we consider large angle scattering: the range of diffraction angles is $2\theta \in [8°, 26.7°]$. We used the (012) reflections of Cr_2O_3 powder placed on each side of a specimen to calibrate the diffraction angles 2θ (a=4.9590 Å and c=1.3596 Å). Moreover, we follow the well-established correction method of Ran *et al.* (2001): an air scattering pattern (without sample) was first collected and has been used to correct the patterns, and the change in thickness of the sample under extension and the change in intensity of the incident photons have also been considered. Once the corrections performed, the intensity of photons diffracted by the isotropic phases in the material $I_{\text{iso}}(2\theta)$ is extracted from the diffraction patterns by considering the minimum intensity along the azimuthal angle β for each Bragg angle 2θ. Then, the intensity of photons diffracted by the anisotropic material $I_{\text{ani}}(2\theta, \beta)$ is calculated as the difference between the total intensity of photons diffracted $I_{\text{total}}(2\theta, \beta)$ and $I_{\text{iso}}(2\theta)$. The spectra extracted from $I_{\text{ani}}(2\theta, \beta)$ and $I_{\text{iso}}(2\theta)$ are classically fitted by series of Pearson functions (Toki *et al.*, 2000; Trabelsi *et al.*, 2003a; Rault *et al.*, 2006a; Chenal *et al.*, 2007b). With these quantities, it is possible to calculate: an index of crystallinity, an index of the mean volume of crystallites, and an index of number of crystallites.

Crystallinity

The index of crystallinity χ is calculated as follow:

$$\chi = \frac{\mathcal{I}_{\text{cryst}}}{\mathcal{I}_{\text{cryst}} + \mathcal{I}_{\text{amorph}}} \tag{8.1}$$

where $\mathcal{I}_{\text{cryst}}$ is the integrated intensity of the (120) and (200) Bragg reflections of NR measured on one (I_{ani},2θ) spectrum and $\mathcal{I}_{\text{amorph}}$ is the integrated intensity of the amorphous halo at the same diffraction angle, assumed equal to the integrated intensity I_{iso}.

Mean volume of crystallites

An index of the mean volume of the crystallites $\overline{V}_{\text{cryst}}$ is calculated from the crystallites size in three different directions:

$$\overline{V}_{\text{cryst}} = l_{200} \cdot l_{120} \cdot l_{201} \tag{8.2}$$

where the mean crystallites size l_{hkl} is deduced from the Scherrer formula (Guinier, 1963):

$$l_{hkl} = \frac{K\lambda}{\text{FWHM}_{2\theta} \cos\theta} \tag{8.3}$$

in which l_{hkl} is the crystallites size in the direction normal to the hkl diffraction plane, K is a scalar which depends on the shape of the crystallites (here we adopt 0.78 as Trabelsi *et al.* (2003a)), λ is the radiation wavelength, θ is the Bragg angle and $\text{FWHM}_{2\theta}$ is the full width at half-maximum of the peak hkl in 2θ.

Number of crystallites

Assuming the incompressibility of the material and that the volume crystallinity is equal to the mass crystallinity, we calculate an index of number of crystallites per unit of undeformed volume N_{cryst}:

$$N_{\text{cryst}} = \frac{\chi}{\overline{V}_{\text{cryst}}} V_{\text{irradiated}}. = \frac{\chi}{\overline{V}_{\text{cryst}}} \frac{\pi R^2 t_0}{\sqrt{\lambda}} \tag{8.4}$$

where $V_{\text{irradiated}}$ is the volume irradiated by the X-ray beam, R is the radius at half-maximum of the beam, t_0 is the thickness of the sample in the undeformed state and λ is the stretch ratio.

8.3 Results and discussion

8.3.1 Evolution of crystallinity during fatigue tests

The evolution of the index of crystallinity (measured at maximum deformation) during fatigue tests for different strain levels is shown in Figure 8.3.

As expected, larger is the strain, higher is the crystallinity. During the three fatigue tests with the lowest minimum and maximum strain levels (tests No. 1, 2 and 3), the index of crystallinity decreases (of 15 % to 50 %) during the first 250 cycles, and then continues to decrease at a lower but constant rate until the end of the tests. During fatigue test No. 4, which minimum and maximum strain levels are much higher (see Fig. 8.2), the evolution of the index of crystallinity is very different: χ increases with the number of cycles (of about

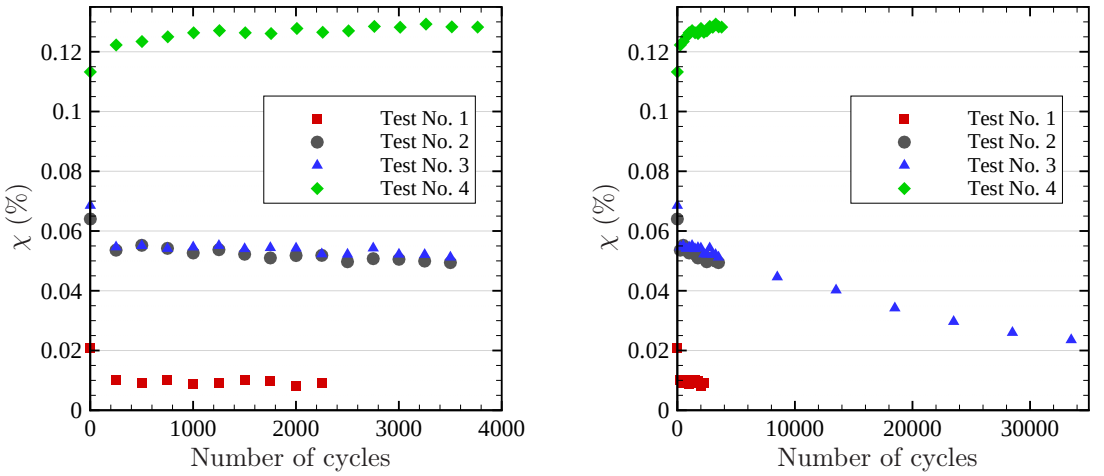

(a) During the first 4,000 cycles.

(b) During the first 35,000 cycles of test No. 3.

Figure 8.3: Evolution of the crystallinity index during fatigue tests.

13 % during the first 4000 cycles). This result is in agreement with those of Kawai (1975) obtained during a fatigue test at $\lambda_{min} = 3.5$ and $\lambda_{\max} = 4.5$. It is to note that the results shown in Fig. 8.3 (a) only correspond to the first 4000 cycles, but fatigue test No. 3 was performed during 35,000 cycles as shown in Fig. 8.3 (b) and we observe that χ decreases at a constant rate during the whole test, down to about χ=2 % in comparison with χ=7 % at the beginning of the test.

As mentioned above, the fatigue tests were performed by prescribing constant maximum and minimum displacements of the clamps. As the material is cycled, Mullins and viscous effects reduce the strain level reached at a given displacement of each cycle. This phenomenon is reduced by the accommodation of the material, but it cannot be completely suppressed. Thus, all results of the fatigue tests are obtained for a constant maximum displacement which corresponds to a decreasing maximum strain level. As shown in Fig. 8.2, fatigue tests No. 1 and 2 are performed with minimum stretch ratios lower than λ_M. Moreover, even if the initial minimum stretch ratio in the fatigue test No. 3 is slightly higher than λ_M, it becomes lower after a few cycles only. So, for these three tests, the same phenomenon takes place during each cycle: all the crystallites melt when the minimum displacement is reached, and new crystallites nucleate when the sample is stretched again; and χ decreases with the number of cycles. For fatigue test No. 4, the minimum stretch ratio reached at each cycle decreases with the number of cycles as well, but it is always greatly larger than the threshold of crystallization λ_C, and then than the threshold of melting λ_M.

Finally, three cases can be highlighted:

- The maximum stretch ratio in one cycle $\lambda_{\max}$ is lower than the threshold of crystallization λ_C: χ remains equal to 0,
- $\lambda_{\max}$ is higher than λ_C and the minimum stretch ratio in one cycle $\lambda_{\min}$ is lower than the threshold of melting λ_M: all crystallites melt at each cycle and the maximum crystallinity index decreases with the number of cycles. This is the case of tests No. 1, 2 and 3.
- $\lambda_{\max}$ is higher than λ_C and $\lambda_{\min}$ is higher than λ_M. During the cycles, some crystallites never melt: the maximum crystallinity index reached in each cycle increases with the number of cycles. This is the case of the test No. 4.

As the change in crystallinity can be induced by the change in the mean number of crystal-

lites and/or the change in the mean volume of crystallites, the two latter aforementioned cases will be analyzed in terms of these quantities.

8.3.2 $\lambda_{\max} > \lambda_C$ and $\lambda_{\min} < \lambda_M$: tests No. 2 and 3

In this section, only tests No. 2 and 3 are considered because the results for test No. 1 are too noisy to be analyzed, due to a very small degree of crystallinity. Similarly, only the first 14,000 cycles of test No. 3 are considered. The evolution of the mean volume of the crystallites and of the number of crystallites is shown in Figure 8.4 (a) and (b) respectively. It shows that the mean volume of crystallites decreases continuously with the

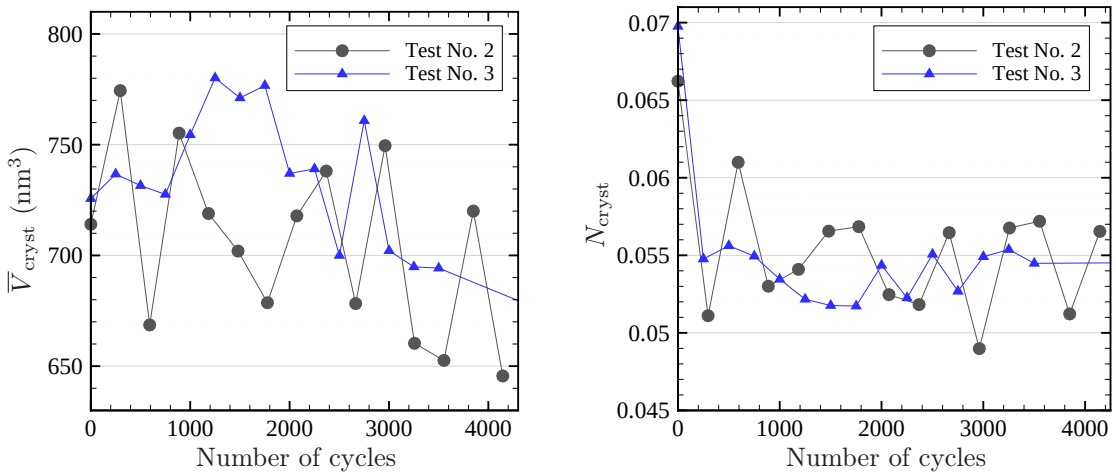

(a) Volume of the crystallites (b) Number of crystallites

Figure 8.4: Evolution of the crystallites during fatigue tests No. 2 and 3.

number of cycles. Their number decreases during the first 250 cycles, and is then constant. We observe the same evolution of both quantities for higher number of cycles as illustrated by the results for fatigue test No. 3 given in Figure 8.5. Thus, the decrease in crystallinity

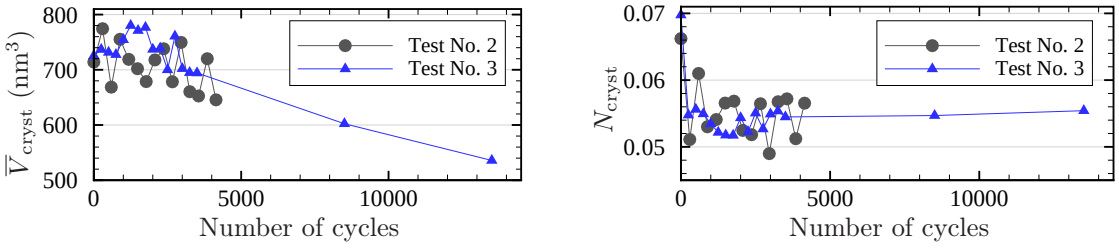

(a) Volume of the crystallites (b) Number of crystallites

Figure 8.5: Evolution of the crystallites during fatigue test No. 2 and the 14,000 first cycles of fatigue test No. 3.

shown in Fig. 8.3 is due to the simultaneous decrease in volume and number of crystallites at the beginning of the tests (250 cycles), and only to the decrease in size for further cycles. Recalling that all crystallites are melted at the end of each cycle, it means that at each cycle the newly nucleated crystallites are smaller than the ones nucleated and melted during the previous cycle. It is to note that the decrease of $\overline{V}_{\text{cryst}}$ with the number of cycles is not explained by the decrease of λ_{max}: indeed, during quasi-static tests, the lower the strain, the higher the size of the crystallites, as shown by Trabelsi *et al.* (2003a,b), Tosaka *et al.*

(2004b), Poompradub *et al.* (2005) and Tosaka (2007). Moreover, results are the same for tests No 2 and 3 which are performed at the same maximum stretch ratio $\lambda_{max} > \lambda_C$ but two different minimum stretch ratios $\lambda_{min} < \lambda_M$. Then, it proves that when the minimum stretch ratio is smaller than the threshold of melting, the value of this minimum stretch ratio does not influence how the material crystallizes at minimum deformation.

As a summary: *(i)* $\overline{V}_{cryst}$ and χ depend on the number of cycles, and *(ii)* N_{cryst}, $\overline{V}_{cryst}$ and χ at λ_{max} do not depend on λ_{min}. These observations can be interpreted in following way:

- The mechanical history, i.e. strain and stress, for strain smaller than λ_M has no effect on the material,
- The mechanical history for strain larger than λ_C modifies the material. Indeed, as the crystallites evolve in time for the same loading conditions, it means that the macromolecular structure of the material changes from one cycle to another.
- Our experiments show that the crystalline phase of NR is different from one cycle to another, eventhough the mechanical conditions are similar; it shows that the macromolecular structure of the material is modified along fatigue testing, including the amorphous phase of NR.

8.3.3 $\lambda_{max} > \lambda_C$ and $\lambda_{min} > \lambda_M$: test No. 4

During fatigue test No. 4, for which the stretch ratio always remains greater than λ_C, the crystallinity index increases with the number of cycles. Yet, it is well-established that crystallinity increases as well during relaxation experiments when the stretch ratio is higher than λ_C (Treloar, 1941; Komura *et al.*, 2008). One can wonder whether the increase of crystallinity during fatigue is related to its evolution during relaxation, and in which ways. On this purpose the relaxation experiments described in Section 8.2.3 are conducted. Figure 8.6 presents the evolution of the index of crystallinity in time for the fatigue test No. 4 and relaxation experiments. As expected, χ increases during relaxation

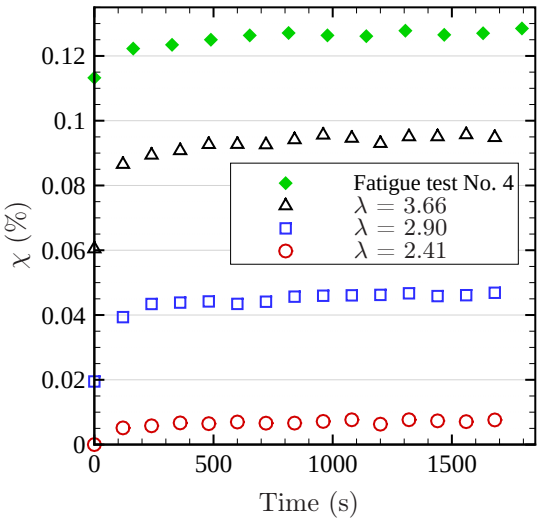

Figure 8.6: Evolution of the crystallinity index χ with time during fatigue test No. 4 and relaxation tests. The stretch ratios λ at which the relaxation tests are performed are given in the legend.

because the stretch ratio is maintained higher than the threshold of crystallization λ_C and the equilibrium state is very long to achieve.

Figure 8.7 presents the evolution of the volume of the crystallites and their number for both test No. 4 and two relaxation tests. Quantitatively, both volumes and numbers

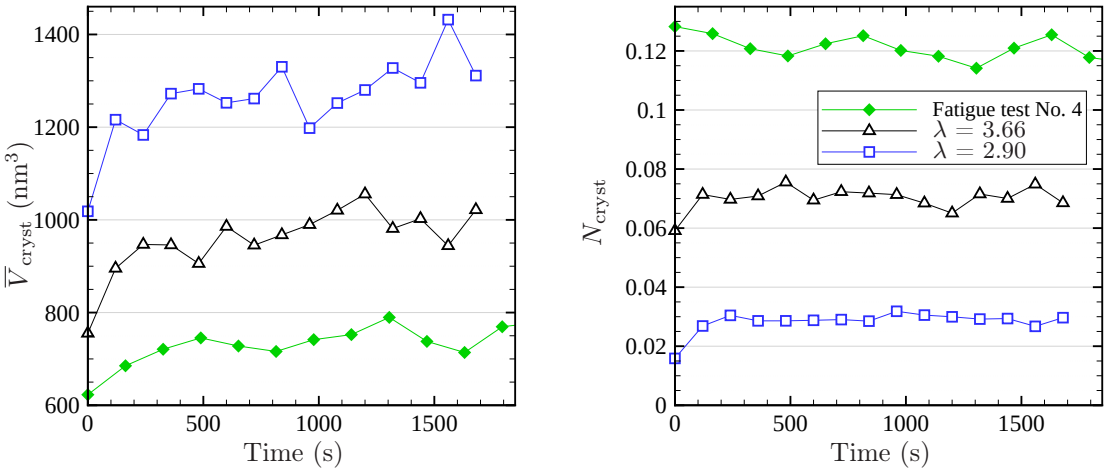

(a) Volume of crystallites (see (b) for legend).

(b) Number of crystallites.

Figure 8.7: Evolution of the crystallites during fatigue test No. 4 and relaxation tests. The stretch ratios λ at which the relaxation tests are performed are given in the legend.

highly differ from one test to another. These differences are due to the values of λ_{max} for each test: the higher the stretch ratio, the smaller and the more numerous the crystallites, as exhibited by Trabelsi *et al.* (2003b) and Poompradub *et al.* (2005).For all the tests, the volume increases in time, and this increase is higher during relaxation than during fatigue (about +20 % for fatigue test and +33 % for both relaxation tests). Moreover, the number of crystallites seems to be constant for the fatigue test whereas it slightly increases at the beginning of the relaxation tests then remains constant.

During the fatigue test No. 4, because the stretch ratio is always larger than λ_M we think that two families of crystallites coexist. At each cycle:

- some crystallites do not melt. They evolve during the whole fatigue test as crystallites in NR subjected to relaxation: their volume increases in time,
- the other crystallites disappear; new ones will nucleate during the next cycle. Those crystallites behave as during fatigue tests No. 2 and 3: their volume decreases from one cycle to another.

The sum of the number of crystallites of both families is constant. As shown in Figs 8.4 and 8.7 the increase in volume during relaxation is higher of more than one decade than the decrease in volume during fatigue tests No. 2 and 3. Assuming that the change in crystallites volume of each family follows the same trend as for relaxation and fatigue tests No. 2 and 3, respectively, the mean volume of crystallites increases during fatigue test No. 4 and then it explains the increase of crystallinity during this test. It must be noted that as in fatigue tests No. 2 and 3, the macromolecular structure of the material (including of the amorphous phase) is modified in time during test No. 4 and then some crystallites which did not melt during a large number of cycles may eventually melt because of the evolution of the mechanical state of the neighbouring macromolecules. Similarly, some crystallites may nucleate after a large number of cycles and not melt afterwards.

8.4 Conclusion

In this study, we developed an original experimental method to measure in real time the evolution of strain-induced crystallization of NR during fatigue by in-situ synchrotron WAXD. The main results are twofold. First, the number of crystallites per unit volume measured at maximum strain is constant during fatigue. Second, the minimum stretch ratio reached at each cycle $\lambda_{\min}$ as compared to the threshold of melting λ_M drives the evolution of the mean volume of crystallites and therefore of the degree of crystallinity: if $\lambda_{\min} < \lambda_M$ the mean volume and the crystallinity decrease with the number of cycles, whereas if $\lambda_{\min} > \lambda_M$ they increase.

To explain those results, we propose the crystallization scenario detailed in Section 8.3; a simplified scenario, which shows only the main phenomena occuring during fatigue, is summarized in Figure 8.8. We believe that this unexpected behaviour is due to a modification of the macromolecular structure of the material, and especially of its amorphous phase, induced by cyclic loading conditions. The origin of this modification is not clarified yet: does the strain-induced crystallization change the macromolecular structure of the amorphous phase? If yes, does it explain the great fatigue strength of crystallizable elastomers (Cadwell *et al.*, 1940; Lake, 1995; André *et al.*, 1999; Saintier *et al.*, 2010)?

8.5 Acknowledgment

The authors thank Dr D. Thiaudière, Dr C. Mocuta and Dr A. Zozulya from the DiffAbs beamline in Soleil synchrotron facility for their great help during the experiments.

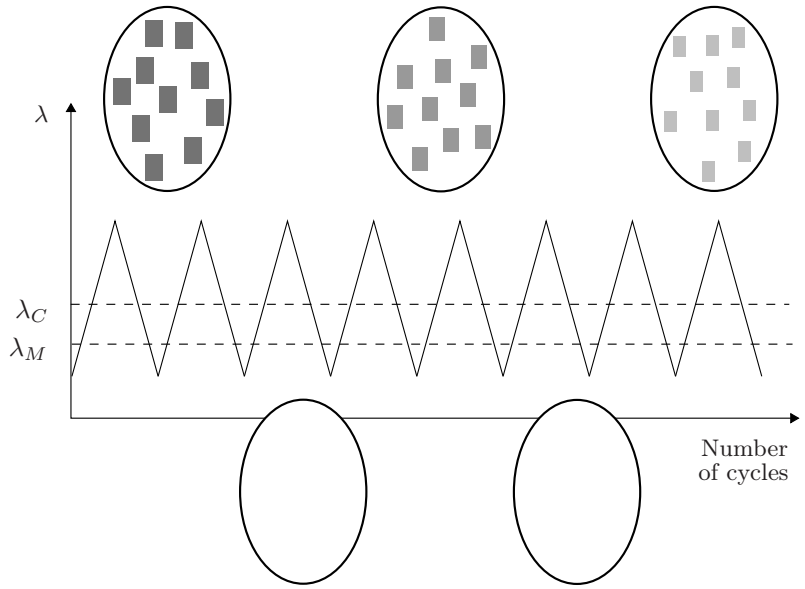

(a) $\lambda_{\min} < \lambda_M$

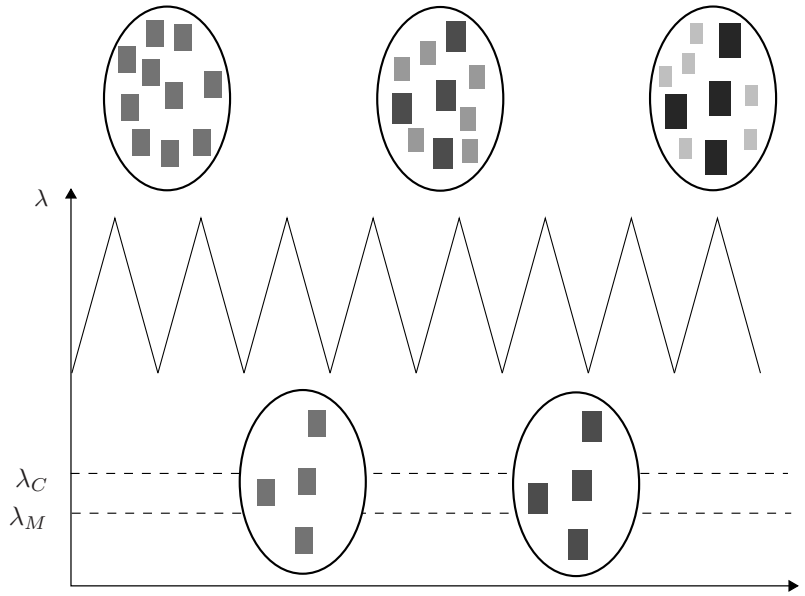

(b) $\lambda_{\min} > \lambda_M$

Figure 8.8: Scenario of crystallization under different fatigue loading conditions. The ovals stand for a unit volume of material. The ones at the top of the figures represent the material at maximum strain whereas the ones at the bottom represent the material at minimum strain. The grey rectangles stand for the crystallites and the larger the crystallite, the larger and darker the rectangle.

Conclusion générale

Le présent travail s'inscrit dans le cadre général de l'étude de la fatigue multiaxiale du caoutchouc naturel. Ce sujet a fait l'objet de nombreuses études ces dernières années, le plus souvent afin de mesurer et prédire la durée de vie de ce matériau très utilisé pour des pièces industrielles soumises à des sollicitations cycliques. L'objectif de cette thèse était de comprendre l'origine des excellentes propriétés en fatigue uniaxiale du caoutchouc naturel chargé au noir de carbone, c'est-à-dire la grande durée de vie et la faible vitesse de propagation des fissure de fatigue, et de comprendre leur lien avec le phénomène de cristallisation sous contrainte du caoutchouc naturel. Pour atteindre cet objectif, nous avons déterminé trois axes principaux d'étude : (*i*) la propagation des fissures de fatigue uniaxiale observée à l'échelle des fissures et micro-fissures, (*ii*) la déformation multiaxiale étudiée à l'échelle macromoléculaire, c'est-à-dire à l'échelle de la cristallisation sous contrainte, et enfin (*iii*) la cristallisation sous contrainte en fatigue uniaxiale.

Dans ce but, j'ai développé deux méthodes expérimentales originales. Tout d'abord, j'ai mis au point une méthode d'observation *in-situ* de la propagation des fissures de fatigue au microscope électronique à balayage. Ensuite, j'ai conçu une machine de fatigue multiaxiale originale qui a permis de réaliser des essais mécaniques innovants au synchrotron Soleil ; ces essais ont été suivis d'un travail minutieux d'analyse des clichés de diffraction.

A l'issue de cette étude, les contributions majeures de ces travaux quant à la compréhension des phénomènes mis en jeu dans le caoutchouc naturel en fatigue multiaxiale sont à mon avis les suivantes :

- Les essais de propagation des fissures de fatigue ont permis de corriger les résultats de Le Cam (2005) et de proposer un mécanisme dissipatif de propagation des fissures qui explique la faible vitesse de propagation observée pour ce matériau,
- Les essais de diffraction des rayons X ont montré que l'orientation des cristallites induites par la contrainte dépend très fortement de la multiaxialité de la déformation du matériau et que cette orientation évolue en même temps que la multiaxialité au cours d'un chemin de chargement complexe.
- Enfin, grâce aux essais de fatigue *in-situ* au synchrotron, j'ai montré que lors d'un essai de fatigue non relaxante, l'évolution de la phase cristalline, et en particulier le taux de cristallinité, dépend de la valeur de l'extension minimale par rapport à l'extension seuil de fusion des cristallites. Lorsque l'extension minimale est supérieure au seuil de fusion, alors le taux de cristallinité augmente avec le nombre de cycles, et lorsqu'elle est inférieure, les sollicitations cycliques modifient le matériau lorsqu'il est à l'état amorphe, ce qui influence les caractéristiques de sa phase cristalline.

Cependant, les travaux que j'ai effectués ne permettent pas de répondre pleinement à l'objectif initial de la thèse et d'établir totalement le lien existant entre la cristallisation sous contrainte du caoutchouc naturel et ses propriétés mécaniques. Ainsi, des travaux

ultérieurs seront nécessaires pour atteindre cet objectif. Par exemple, à court terme, il est possible de déterminer de manière formelle si les mécanismes de dissipation d'énergie observés à l'échelle mésoscopique lors de la propagation des fissures de fatigue sont liés à la cristallisation sous contrainte. Dans ce but, des essais similaires à ceux effectués lors de ma thèse peuvent être réalisés sur des élastomères non cristallisables, ou bien sur du caoutchouc naturel mais à une température supérieure à celle de la fusion des cristallites. A plus long terme, je pense que le travail qui a été mené ici doit conduire à développer un modèle de comportement du caoutchouc naturel prenant en compte la cristallisation sous contrainte. Notamment, la dualité entre le nombre et le volume des cristallites qui évoluent différemment en fonction des sollicitations mécaniques, ainsi que l'anisotropie induite par l'orientation des cristallites pour certaines déformations sont des caractéristiques démontrées ici et qui pourraient être avantageusement prises en compte dans un modèle de comportement.

Bibliographie

Al-Quraishi, A. A. et Hoo Fatt, M. S. (2007). Dynamic fracture of natural rubber. *Tire Science and Technology*, 35:252–275. 107

Albouy, P. A., Marchal, J. et Rault, J. (2005). Chain orientation in natural rubber, Part I : the inverse yielding effect. *The European Physical Journal E*, 17:247–259. 29, 60, 62

Alexander, L., Ohlberg, S. et Russel Taylor, G. (1995). X-ray diffraction studies of crystallization in elastomers. *Journal of Applied Physics*, 26:1068–1074. 30

Amin, A. F. M. S., Lion, A., Sekita, S. et Okui, Y. (2006). Nonlinear dependence of viscosity in modeling the rate-dependent response of natural and high damping rubbers in compression and shear : Experimental identification and numerical verification. *International Journal of Plasticity*, 22:1610–1657. 107

André, N., Cailletaud, G. et Piques, R. (1999). Haigh diagram for fatigue crack initiation prediction of natural rubber components. *Kautschuk und Gummi, Kunststoffe*, 52:120–123. 1, 107, 121, 133, 142

Andriyana, A. (2006). *Définition d'une nouvelle grandeur prédictive pour la durée de vie en fatigue des matériaux élastomères*. Thèse de doctorat, Ecole Centrale de Nantes et Université de Nantes. 1

Aït-Bachir, M. (2010). *Prédiction de l'initiation de fissures dans les élastomères par la mécanique configurationnelle*. Thèse de doctorat, Ecole Centrale de Nantes. 1

Beatty, J. R. (1964). Fatigue of rubber. *Rubber Chemistry and Technology*, 37(5):1341–1364. 37

Beurrot, S., Huneau, B. et Verron, E. (2011a). Strain-induced crystallization of natural rubber subjected to biaxial loading conditions as revealed by X-ray diffraction. *In* Jerrams, S. et Murphy, N., éditeurs : *Constitutive Models for Rubber VII*, pages 23–28. Taylor & Francis. 93, 97, 99

Beurrot, S., Huneau, B., Verron, E., Rublon, P., Thiaudière, D., Mocuta, C. et Zozulya, A. (2011b). In-situ synchrotron X-ray diffraction study of strain-induced crystallization of natural rubber during fatigue tests. *In* Jerrams, S. et Murphy, N., éditeurs : *Constitutive Models for Rubber VII*, pages 353–358. Taylor & Francis. 119

Beurrot-Borgarino, S., Huneau, B. et Verron, E. Effect of strain rate on strain-induced crystallization in carbon black-filled natural rubber. Submitted, a. 128, 129

Beurrot-Borgarino, S., Huneau, B. et Verron, E. Orientation of strain-induced crystallites in natural rubber subjected to multiaxial deformation. Submitted, b. 93, 97, 99

Beurrot-Borgarino, S., Huneau, B. et Verron, E. Strain-induced crystallization in unfilled and carbon black-filled natural rubber as revealed by x-ray diffraction. Submitted, c. 99, 117, 129, 130, 131, 132

Bunn, C. W. (1942). Molecular structure and rubber-like elasticity I. The crystal structures of beta gutta-percha, rubber and polychloroprene. *Proceedings of the Royal Society of London Series A-Mathematical and Physical Sciences*, 180(A980):40–66. 20, 63, 79, 84, 85, 121, 133

Cadwell, S. M., Merril, R. A., Sloman, C. M. et Yost, F. L. (1940). Dynamic fatigue life of rubber. *Industrial and Engineering Chemistry*, 12:19–23. 1, 107, 121, 133, 142

Chenal, J.-M., Chazeau, L., Guy, L., Bomal, Y. et Gauthier, C. (2007a). Molecular weight between physical entanglements in natural rubber : a critical parameter during strain-induced crystallization. *Polymer*, 48:1042–1046. 30, 57, 60, 63, 65, 68, 85, 102, 110

Chenal, J.-M., Gauthier, C., Chazeau, L., Guy, L. et Bomal, Y. (2007b). Parameters governing strain induced crystallization in filled natural rubber. *Polymer*, 48(23):6893–6901. 30, 57, 58, 81, 82, 85, 95, 97, 110, 125, 136

Clark, G., Kabler, M., Blaker, E. et Ball, J. M. (1940). Hysteresis in crystallization of stretched vulcanized rubber from X-ray data. Correlation with stress-strain behavior and resilience. *Industrial and Engineering Chemistry*, 32:1474–1477. 86

Clark, G. L., Le Tourneau, R. L. et Ball, J. M. (1941). Hysteresis in the crystallization of stretched vulcanized rubber II. X-ray studies of the effects of sulfur content and method of curing. *Rubber Chemistry And Technology*, 14:546–554. 79, 121, 133

Crepin, J., Bretheau, T., Caldemaison, D. et Ferrer, F. (2000). Low cycle fatigue behaviour of beta treated zirconium : Partial irreversibility of twinning and consequences for damage. *Acta Materialia*, 48:505–516. 49

Cyr, M., Husson, B. et Carles-Guibergues, A. (1998). Détermination, par diffraction des rayons X, de la teneur en phase amorphe de certains matériaux minéraux. *Journal de Physique IV*, 8, N°5:23–30. 30

Dannis, M. L. (1962). Stress–strain testing of rubbers at high rates of elongation. *Journal of Applied Polymer Science*, 6:283–296. 107

Demmerle, S. et Boehler, J. P. (1993). Optimal design of biaxial tensile cruciform specimens. *Journal of the Mechanics and Physics of Solids*, 41:143–181. 9, 12, 80, 94

Dumbleton, B. et Bowles, B. (1966). X-ray determination of crystallinity and orientation in poly(ethylene terephthalate). *Journal of Polymer Science Part A-2 : Polymer Physics*, 4, Issue 6:951–958. 30

Fukahori, Y. (2010). Mechanism of the self-reinforcement of cross-linked NR generated through the strain-induced crystallization. *Polymer*, 51:1621–1631. 72, 79

Guinier, A. (1963). *X-ray diffraction*. W. H. Freeman & Co. 14, 60, 82, 110, 125, 137

Guth, E. (1945). Theory of filler reinforcement. *Journal of Applied Physics*, 16:20–25. 81, 95

Hainsworth, S. V. (2007). An environmental scanning electron microscopy investigation of fatigue crack initiation and propagation in elastomers. *Polymer Testing*, 26:60–70. 37, 40, 49

Hamed, G. R. (1994). Molecular aspects of the fatigue and fracture of rubber. *Rubber Chemistry and Technology*, 67:529–536. 47, 50

Hannon, A. et Tiernan, P. (2008). A review of planar biaxial tensile test systems for sheet metal. *Journal of materials processing technology*, 198:1–13. 9, 12

Harwood, J. A. C. et Payne, A. R. (1966). Stress softening un natural rubber vulcanizates. 3. Carbon black-filled vulcanizates. *Journal of Applied Polymer Science*, 10:315. 81, 95

Helfenstein, J., Hollenstein, M. et Mazza, E. (2010). Investigation on the optimal specimen design for planar-biaxial materials testing of soft materials. *In* et al., H., éditeur : *Constitutive Models for Rubber VI*. Taylor & Francis Group, London. 9

Hoo Fatt, M. S. et Ouyang, X. (2008). Three-dimensional constitutive equations for styrene butadiene rubber at high strain rates. *Mechanics of Materials*, 40:1–16. 107

Huneau, B. (2011). Strain-induced crystallization of natural rubber : a review of X-ray diffraction investigations. *Rubber Chemistry And Technology*, 84:425–452. 57, 79, 93, 121, 133

Ikeda, Y., Kato, A., Shimanuki, J., Kohjiya, S., Tosaka, M., Poompradub, S., Toki, S. et Hsiao, B. S. (2007). Nano-structural elucidation in carbon black loaded NR vulcanizate by 3D-TEM and in situ WAXD measurements. *Rubber Chemistry and Technology*, 80:251–264. 29

Immirzi, A., Tedesco, C., Monaco, G. et Tonelli, A. E. (2005). Crystal structure and melting entropy of natural rubber. *Macromolecules*, 38:1223–1231. 20, 60, 63, 82, 85, 111, 125

Katz, J. R. (1925). Rontgen spectographic testings on expanded rubber and its possible relevance for the problem of the extension characteristics of this substance. *Naturwissenschaften*, 13:410–416. 79, 107, 121, 133

Kawai, H. (1975). Dynamic X-ray diffraction technique for measuring rheo-optical properties of crystalline polymeric materials. *Rheologica Acta*, 14:27–47. 119, 121, 126, 133, 138

Kohjiya, S., Tosaka, M., Furutani, M., Ikeda, Y., Toki, S. et Hsiao, B. S. (2007). Role of stearic acid in the strain-induced crystallization of crosslinked natural rubber and synthetic cis-1,4-polyisoprene. *Polymer*, 48(13):3801–3808. 29

Komura, M., Nakajima, K., Nishi, T., Ikehara, T. et Zhaobin, Q. (2008). Pulsed NMR studies on long-term crystallization behavior and melting process of natural rubber under elongation. *Rubber Chemistry And Technology*, 81(1):110–120. 140

Krempl, E. et Khan, F. (2003). Rate (time)-dependent deformation behavior : an overview of some properties of metals and solid polymers. *International Journal of Plasticity*, 19:1069–1095. 107

Kroon, M. (2010). A constitutive model for strain-crystallising rubber-like materials. *Mechanics of Materials*, 42:873–885. 79

Lake, G. J. (1995). Fatigue and fracture of elastomers. *Rubber Chemistry and Technology*, 68:435–460. 1, 35, 37, 50, 107, 142

Lake, G. J. et Lindley, P. B. (1965). Mechanical fatigue limit for rubber. *Journal of Applied Polymer Science*, 9:1233. 1, 35

Le Cam, J. B. (2005). *Endommagement en fatigue des élastomères*. Thèse de doctorat, Ecole Centrale de Nantes et Université de Nantes. 1, 145

Le Cam, J. B. (2010). A review of volume changes in rubbers : the effect of stretching. *Rubber Chemistry And Technology*, 83:247–269. 66

Le Cam, J. B., Huneau, B., Verron, E. et Gornet, L. (2004). Mechanism of fatigue crack growth in carbon black filled natural rubber. *Macromolecules*, 37:5011–5017. 37, 40, 49, 50

Le Saux, V., Marco, Y., Calloch, S., Doudard, C. et Charrier, P. (2010). Fast evaluation of the fatigue lifetime of rubber-like materials based on a heat build-up protocol and micro-tomography measurements. *International Journal of Fatigue*, 32(10):1582–1590. 121, 133

Lee, D. J. et Donovan, J. A. (1987). Microstructural changes in the crack tip region of carbon black-filled natural rubber. *Rubber Chemistry And Technology*, 60:910–923. 30, 121, 133

Legorju-jago, K. et Bathias, C. (2002). Fatigue initiation and propagation in natural and synthetic rubbers. *International Journal of Fatigue*, 24:85–92. 121, 133

Marchal, J. (2006). *Cristallisation des caoutchoucs chargés et non chargés sous contrainte : effet sur les chaînes amorphes*. Thèse de doctorat, Paris VI Orsay. 24, 29

Marckmann, G. et Verron, E. (2006). Comparison of hyperelastic models for rubberlike materials. *Rubber Chemistry And Technology*, 79:835–858. 79

Mark, J. E., Erman, B. et Eirinch, F. R., éditeurs (2005). *The Science and Technoloy of Rubber*. Elsevier Inc. 50

Mars, W. V. et Fatemi, A. (2002). A literature survey on fatigue analysis approaches for rubber. *International Journal of Fatigue*, 24:949–961. 1, 37, 121, 133

Mars, W. V. et Fatemi, A. (2005). Multiaxial fatigue of rubber. Part II : experimental observations and life predictions. *Fatigue & fracture of engineering materials & structures*, 28:523–538. 1

Mars, W. V. et Fatemi, A. (2006). Multiaxial stress effects on fatigue behaviour of filled natural rubber. *International Journal of Fatigue*, 28:521–529. 107

Mason, P. (1960). The strain dependence of rubber viscoelasticity, Part II. The influence of carbon black. *Journal of Applied Polymer Science*, 4:212–218. 107

Miyamoto, Y., Yamao, H. et Sekimoto, K. (2003). Crystallization and melting of polyisoprene rubber under uniaxial deformation. *Macromolecules*, 36(17):6462–6471. 29, 107, 117

Mullins, L. et Tobin, N. R. (1965). Stress softening in rubber vulcanizates. I. Use of a strain amplification factor to describe elastic behavior of filler-reinforced vulcanized rubber. *Journal of Applied Polymer Science*, 9(9):2993. 81, 95

Murakami, S., Senoo, K., Toki, S. et Kohjiya, S. (2002). Structural development of natural rubber during uniaxial stretching by in situ wide angle X-ray diffraction using a synchrotron radiation. *Polymer*, 43(7):2117–2120. 19, 29, 79

Nogales, A., Hsiao, B. S., Somani, R. H., Srinivas, S., Tsou, A. H., Balta-Calleja, F. J. et Ezquerra, T. A. (2001). Shear-induced crystallization of isotactic polypropylene with different molecular weight distributions : in situ small- and wide-angle X-ray scattering studies. *Polymer*, 42:5247 – 5256. 17

Nyburg, S. C. (1954). A statistical structure for crystalline rubber. *Acta Crystallographica*, 7(5):385–392. 79, 121, 133

Oono, R., Miyasaka, K. et Ishikawa, K. (1973). Crystalliization kinetics of biaxially stretched natural rubber. *Journal of Polymer Science*, 11:1477–1488. 79, 86, 93

Ostoja-Kuczynski, E. (2005). *Comportement en fatigue des elastomères : application aux structure antivibratoires pour l'automobile*. Thèse de doctorat, Ecole Centrale de Nantes et Université de Nantes. 1

Papadopoulos, I. C., Thomas, A. G. et Busfield, J. J. C. (2008). Rate transitions in the fatigue crack growth of elastomers. *Journal of Applied Polymer Science*, 109:1900–1910. 50

Poompradub, S., Tosaka, M., Kohjiya, S., Ikeda, Y., Toki, S. et Hsiao, B. S. (2004). Lattice deformation of strain-induced crystallites in carbon-filled natural rubber. *Chemistry Letters*, 33(3):220–221. 85

Poompradub, S., Tosaka, M., Kohjiya, S., Ikeda, Y., Toki, S., Sics, I. et Hsiao, B. S. (2005). Mechanism of strain-induced crystallization in filled and unfilled natural rubber vulcanizates. *Journal of Applied Physics*, 97(10):103529/1–103529/9. 29, 57, 60, 62, 63, 65, 66, 68, 85, 86, 102, 110, 127, 128, 129, 130, 131, 140, 141

Rajkumar, G., Squire, J. M. et Arnott, S. (2006). A new structure for crystalline natural rubber. *Macromolecules*, 39:7004–7014. 20, 60, 63, 82, 85, 111, 125

Ran, S., Fang, D., Zong, X., Hsiao, B. S., Chu, B. et Cunniff, P. F. (2001). Structural changes during deformation of kevlar fibers via on-line synchrotron SAXS/WAXD techniques. *Polymer*, 42(4):1601–1612. 15, 17, 58, 81, 97, 109, 124, 136, 155

Rault, J., Marchal, J., Judeinstein, P. et Albouy, P. A. (2006a). Chain orientation in natural rubber, Part II : 2H-NMR study. *The European Physical Journal E*, 21:243–261. 29, 58, 73, 81, 82, 107, 110, 125, 136

Rault, J., Marchal, J., Judeinstein, P. et Albouy, P. A. (2006b). Stress-induced crystallization and reinforcement in filled natural rubbers : 2H NMR study. *Macromolecules*, 39(24):8356–8368. 29, 95, 97

Rivlin, R. S. et Thomas, A. G. (1953). Rupture of rubber. I. characteristic energy for tearing. *Journal of Polymer Science*, X(3):291–318. 1

Roland, C. M. (2006). Mechanical behavior of rubber at high strain rates. *Rubber Chemistry And Technology*, 79:429–459. 107

Rouvière, J. Y., Bennani, A., Pachoutinsky, D., Besson, J. et Cantournet, S. (2007). Influence of mechanical and fatigue loading on crystallization of carbon black-filld natural rubber. *In* Eds. Taylor & Francis, P., éditeur : *Constitutive Models for Rubber V, Paris*, pages 323–326. 18, 24, 29, 121, 133

Sahores, J. (1973). New improvements in routine quantitative phase analysis by X-ray diffractometry. *Advances in X-Ray Analysis*, 16:187–196. 30

Saintier, N. (2000). *Prévision de la durée de vie du NR sous chargement multiaxial.* Thèse de doctorat, Ecole Nationale Supérieure des Mines de Paris. 18, 29

Saintier, N., Cailletaud, G. et Piques, R. (2006a). Crack initiation and propagation under multiaxial fatigue in a natural rubber. *International Journal of Fatigue*, 28:61–72. 1

Saintier, N., Cailletaud, G. et Piques, R. (2006b). Multiaxial fatigue life prediction for a natural rubber. *International Journal of Fatigue*, 28:530–539. 1, 121, 133

Saintier, N., Cailletaud, G. et Piques, R. (2010). Cyclic loadings and crystallization of natural rubber : An explanation of fatigue crack propagation reinforcement under a positive loading ratio. *Materials Science and Engineering A*, 528(3):1078–1086. 142

Takahashi, Y. et Kumano, T. (2004). Crystal structure of natural rubber. *Macromolecules*, 37:4860–4864. 20, 63, 85

Toki, S., Fujimaki, T. et Okuyama, M. (2000). Strain-induced crystallization of natural rubber as detected real-time by wide-angle X-ray diffraction technique. *Polymer*, 41: 5423–5429. 29, 58, 79, 82, 97, 110, 121, 125, 133, 136

Toki, S., Hsiao, B. S., Kohjiya, S., Tosaka, M., Tsou, A. H. et Dat-Ra, S. (2006). Synchrotron X-ray studies of vulcanized rubbers and thermoplastic elastomers. *Rubber Chemistry And Technology*, 79(3):460–488. 29

Toki, S., Minouchi, N., Sics, I., Hsiao, B. S. et Kohjiya, S. (2008). Synchrotron X-ray scattering. tensile strength and strain-induced crystallization in carbon black-filled natural rubber. *Kautschuk Gummi Kunststoffe*, 61(3):85–91. 85

Toki, S., Sics, I., Ran, S., Liu, L. et Hsiao, B. S. (2003). Molecular orientation and structural development in vulcanized polyisoprene rubbers during uniaxial deformation by in-situ synchrotron X-ray diffraction. *Polymer*, 44:6003–6011. 79

Toki, S., Sics, I., Ran, S., Liu, L. et Hsiao, B. S. (2004). Strain-induced molecular orientation and crystallization in natural and synthetic rubbers under uniaxial deformation by in-situ synchrotron X-ray study. *Rubber Chemistry and Technology*, 77:317–335. 29

Toki, S., Sics, I., Ran, S. F., Liu, L. Z., Hsiao, B. S., Murakami, S., Senoo, K. et Kohjiya, S. (2002). New insights into structural development in natural rubber during uniaxial deformation by in situ synchrotron X-ray diffraction. *Macromolecules*, 35(17):6578–6584. 19, 29, 79

Tosaka, M. (2007). Strain-induced crystallization of crosslinked natural rubber as revealed by X-ray diffraction using synchrotron radiation. *Polymer Journal*, 39:1207–1220. 62, 63, 65, 66, 68, 79, 99, 102, 111, 130, 131, 140

Tosaka, M. (2009). A route for the thermodynamic description of strain-induced crystallization in sulfur-cured natural rubber. *Macromolecules*, 42:6166–6174. 79, 81, 95

Tosaka, M., Kawakami, D., Senoo, K., Kohjiya, S., Ikeda, Y., Toki, S. et Hsiao, B. S. (2006). Crystallization and stress relaxation in highly stretched samples of natural rubber and its synthetic analogue. *Macromolecules*, 39:5100–5105. 29

Tosaka, M., Kohjiya, S., Murakami, S., Poompradub, S., Ikeda, Y., Toki, S., Sics, I. et Hsiao, B. S. (2004a). Effect of network-chain length on strain-induced crystallization of NR and IR vulcanizates. *Rubber Chemistry And Technology*, 77:711–723. 29

Tosaka, M., Murakami, S., Poompradub, S., Kohjiya, S., Ikeda, Y., Toki, S., Sics, I. et Hsiao, B. S. (2004b). Orientation and crystallization of natural rubber network as revealed by WAXD using synchrotron radiation. *Macromolecules*, 37:3299–3309. 57, 60, 62, 63, 66, 68, 71, 72, 85, 99, 102, 110, 130, 139

Trabelsi, S., Albouy, P. A. et Rault, J. (2002). Stress-induced crystallization around a crack tip in natural rubber. *Macromolecules*, 35(27):10054–10061. 30, 121, 133

Trabelsi, S., Albouy, P. A. et Rault, J. (2003a). Crystallization and melting processes in vulcanized stretched natural rubber. *Macromolecules*, 36(20):7624–7639. 30, 58, 60, 63, 65, 66, 68, 79, 82, 85, 97, 99, 102, 110, 122, 125, 134, 136, 137, 139

Trabelsi, S., Albouy, P. A. et Rault, J. (2003b). Effective local deformation in stretched filled rubber. *Macromolecules*, 36(24):9093–9099. 29, 30, 57, 60, 62, 63, 65, 66, 68, 72, 73, 85, 86, 102, 110, 127, 129, 130, 139, 141

Trabelsi, S., Albouy, P. A. et Rault, J. (2004). Stress-induced crystallization properties on natural and synthetic cis-polyisoprene. *Rubber Chemistry and Technology*, 77:303–316. 29, 30, 57, 60, 65, 110

Treloar, L. R. G. (1941). Crystallization phenomena in raw rubber. *Transactions of the Faraday Society*, 37(238):84–97. 140

Verron, E. et Andriyana, A. (2008). Definition of a new predictor for multiaxial fatigue crack nucleation in rubber. *Journal of the Mechanics and Physics of Solids*, 56:417–443. 1

Waldman, S. D. et Lee, J. M. (2005). Effect of sample geometry on the apparent biaxial mechanical behaviour of planar connective tissues. *Biomaterials*, 26:7504–7513. 9

White, J. R. et Thomas, E. L. (1984). Advances in SEM of polymers. *Rubber Chemistry and Technology*, 57:457–506. 50

Yu, Y., Wan, M., Wu, X.-D. et Zhou, X.-B. (2002). Design of a cruciform biaxial tensile specimen for limit strain analysis by FEM. *Journal of Materials Processing Technology*, 123:67–70. 9

Annexe A

Correction des clichés de diffraction

A.1 Correction du bruit expérimental et de la diffusion de l'air

Cette correction est fondée sur la méthode de Ran *et al.* (2001). On considère deux expériences : l'une sans éprouvette et l'autre avec une éprouvette étirée d'épaisseur d à l'état déformé. Les figures A.1 et A.2 présentent ces deux expériences. Les intensités mesurées par

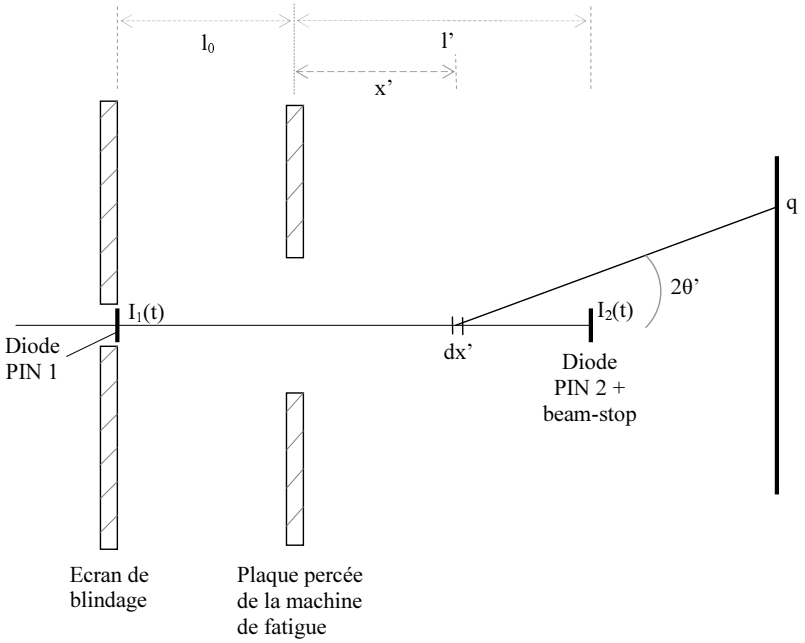

FIGURE A.1 – Expérience sans éprouvette.

les diodes PIN 1 et 2 et le détecteur sont notées I_1, I_2 et I_d respectivement ; les exposants SE et AE indiquent les expériences sans éprouvette et avec éprouvette respectivement.

A.1.1 Mesures sans éprouvette

On réalise un premier essai sans éprouvette, durant lequel l'intensité des photons est mesurée sur la diode PIN 2 et sur le détecteur pendant une période T_1. D'après la loi de Beer-Lambert, l'intensité I_2^{SE} mesurée par la diode PIN 2 intégrée sur la période T_1 est

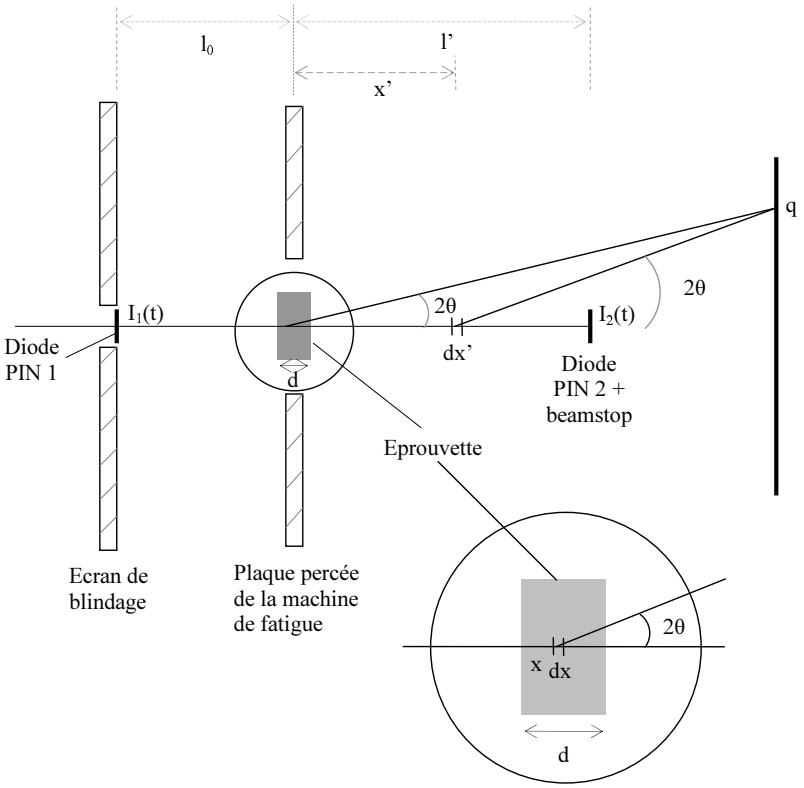

FIGURE A.2 – Expérience avec éprouvette.

l'intégrale de l'intensité de photons non absorbés par l'air entre les deux diodes PIN :

$$I_2^{\mathrm{SE}} = \eta_2 \int_0^{T_1} i_1(t) e^{-\mu_0(l_0+l')} \mathrm{d}t, \tag{A.1}$$

où η_2 est le coefficient de rendement de la diode PIN 2, $i_1(t)$ est l'intensité du flux de photons à l'emplacement de la diode PIN 1 et μ_0 est le coefficient d'absorption de l'air. Ici, on suppose que μ_0 est constant. L'équation peut également s'écrire :

$$I_2^{\mathrm{SE}} = \eta_2 \; e^{-\mu_0(l_0+l')} \; \mathbb{I}_{01}, \tag{A.2}$$

avec

$$\mathbb{I}_{01} = \int_0^{T_1} i_1(t) \mathrm{d}t = \frac{I_1^{\mathrm{SE}}}{\eta_1}, \tag{A.3}$$

où $\mathbb{I}_{01}$ est l'intensité incidente intégrée sur la période T_1 avant l'absorption par l'air et η_1 est le coefficient de rendement de la diode PIN 1.

L'intensité mesurée au point q du détecteur au cours du même essai est l'intensité transmise (non absorbée) par l'air entre la diode PIN 1 et le point x', puis diffusé au point x' avec un angle $2\theta'$, puis transmise (non absorbée) par l'air entre les points x' et q (x' étant situé entre l'emplacement de l'éprouvette et la diode PIN 2). On note que les photons diffusés entre la diode PIN 1 et l'emplacement de l'éprouvette ne sont pas considérés :

$$I_d^{\mathrm{SE}}(q) = \eta_d \int_0^{l'} \int_0^{T_1} i_1(t) e^{-\mu_0(l_0+x')} \mathrm{d}t \; S_a(q') \; e^{-\mu_0(l-x')/\cos 2\theta'} \mathrm{d}x', \tag{A.4}$$

où η_d est le coefficient de rendement du détecteur. On peut écrire cette fonction sous la forme :

$$I_d^{\mathrm{SE}}(q) = \eta_d \; \mathbb{I}_{01} \; \bar{S}_a(\bar{q}) \; e^{-\mu_0 l_0}, \tag{A.5}$$

avec

$$\bar{S}_a(\bar{q}) = \int_0^{l'} e^{-\mu_0 (l - x')/\cos 2\theta'} S_a(q') \mathrm{d}x'. \tag{A.6}$$

Le terme $\bar{S}_a(\bar{q})$ peut être vu comme un terme de diffusion moyenné.

Le ratio entre les deux intensités mesurées I_d^{SE} (par le détecteur) et I_2^{SE} (par la diode PIN 2) est :

$$\frac{I_d^{\mathrm{SE}}(q)}{I_2^{\mathrm{SE}}} = \frac{\eta_d}{\eta_2} \; \bar{S}_a(\bar{q}) \; e^{\mu_0 l'} \tag{A.7}$$

A.1.2 Mesures avec eprouvette

On réalise maintenant un deuxième essai avec une éprouvette sur une période de temps T_2. L'intensité mesurée par la diode PIN 2 est l'intégrale du flux de photons à l'emplacement de diode PIN 1 non absorbés par l'air entre la diode PIN 1 et l'éprouvette, par l'éprouvette puis par l'air entre l'éprouvette et la diode PIN 2 :

$$I_2^{\mathrm{AE}} = \eta_2 \int_0^{T_2} i_1(t) e^{-\mu_0 (l' + l_0)} e^{-\mu_m d} \mathrm{d}t, \tag{A.8}$$

où μ_m est le coefficient d'absorption du matériau de l'éprouvette. On peut également écrire la fonction sous la forme :

$$I_2^{\mathrm{SE}} = \eta_2 \; e^{-\mu_0 (l_0 + l') - \mu_m d} \; \mathbb{I}_{02} \tag{A.9}$$

$$\mathbb{I}_{02} = \int_0^{T_2} i_1(t) \mathrm{d}t, \tag{A.10}$$

où $i_1(t)$ est le flux de photons à l'emplacement de la diode PIN 1.

L'intensité mesurée en un point q du détecteur est la somme de l'intensité des photons diffractés par l'éprouvette et de l'intensité des photons diffusés par l'air entre l'éprouvette et la diode PIN 2 (comme précédemment, les photons diffusés entre la diode PIN 1 et l'éprouvette ne peuvent pas atteindre le détecteur). Les photons diffractés par l'éprouvette sont d'abord transmis (donc non absorbés) par l'air entre la diode PIN 1 et l'éprouvette, transmis par l'éprouvette jusqu'à un point x, puis diffractés au point x avec un angle 2θ et enfin transmis par la seconde partie de l'éprouvette puis par l'air entre l'éprouvette et le détecteur. Les photons diffusés par l'air sont d'abord transmis par l'éprouvette. Finalement, l'intensité mesurée par le détecteur est :

$$I_d^{\mathrm{AE}}(q) = \eta_d \int_0^d \int_0^{T_2} i_1(t) e^{-\mu_0 l_0 - \mu_m x} \mathrm{d}t \; S_S(q) \; e^{-\mu_c (d-x)/\cos 2\theta} e^{-\mu_0 l/\cos 2\theta} \mathrm{d}x + \eta_d \; e^{-\mu_0 l_0 - \mu_c d} \; \mathbb{I}_{02} \; \bar{S}_a(\bar{q}), \tag{A.11}$$

soit encore

$$I_d^{\mathrm{AE}}(q) = \eta_d \; \mathbb{I}_{02} \; e^{-\mu_0 (l/\cos 2\theta + l_0)} \; S_S(q) \; F(d, cos2\theta) + \eta_d \; e^{-\mu_0 l_0 - \mu_m d} \; \mathbb{I}_{02} \; \bar{S}_a(\bar{q}), \tag{A.12}$$

avec

$$F(d,\cos 2\theta) = \int_0^d e^{-\mu_m (x+(d-x)/\cos 2\theta)} \mathrm{d}x. \tag{A.13}$$

Le ratio entre les deux intensités mesurées I_d^{AE} (par le détecteur) et I_2^{AE} (par la diode PIN 2) est :

$$\frac{I_d^{\mathrm{AE}}(q)}{I_2^{\mathrm{AE}}} = \frac{\eta_d}{\eta_{p2}}\ S_S(q)\ F(d,\cos 2\theta)\ e^{-\mu_0 (l/\cos 2\theta - l') + \mu_c d} + \frac{I_d^{\mathrm{SE}}(q)}{I_2^{\mathrm{SE}}}. \tag{A.14}$$

A.1.3 Bilan

Finalement, la différence entre les équations (A.7) et (A.14) permet d'obtenir l'expression de la fonction de diffraction « corrigée » :

$$S_S(q) = \frac{\eta_{p2}}{\eta_d} \frac{e^{-\mu_0 (l' - l/\cos 2\theta) - \mu_c d}}{F(d,\cos 2\theta)} \left(\frac{I_d^{\mathrm{AE}}(q)}{I_2^{\mathrm{AE}}} - \frac{I_d^{\mathrm{SE}}(q)}{I_2^{\mathrm{SE}}} \right), \tag{A.15}$$

avec

$$F(d,\cos 2\theta) = \int_0^d e^{-\mu_c (x+(d-x)/\cos 2\theta)} \mathrm{d}x. \tag{A.16}$$

Aucune mesure ne sera effectuée au delà de l'angle de diffraction du premier anneau de ZnO, soit $2\theta = 27,1°$ et $\cos 2\theta = 0,89$. Ainsi, le terme intégral dans l'équation précédente peut être approché par :

$$\int_0^d \exp\left[-\mu_c \left(x + (d-x)/\cos 2\theta\right)\right] dx \approx \int_0^d \exp\left(-\mu_c d\right) dx = d \exp\left(-\mu_c d\right). \tag{A.17}$$

Finalement,

$$S_S(q) = \frac{\eta_2}{\eta_d} \frac{\exp\left[-\mu_0 \left(l' - l\right)\right]}{d} \left[\frac{I_d^{\mathrm{AE}}(q)}{I_2^{\mathrm{AE}}} - \frac{I_d^{\mathrm{SE}}(q)}{I_2^{\mathrm{SE}}} \right]. \tag{A.18}$$

En factorisant les termes constants, on obtient une fonction de diffusion $\mathcal{S}(q)$ corrigée de la diffusion de l'air :

$$\mathcal{S}(q) = S_S(q) \frac{\eta_d}{\eta_2} \exp\left[-\mu_0 \left(l - l'\right)\right] d_0 = \frac{d_0}{d} \left[\frac{I_d^{\mathrm{AE}}(q)}{I_2^{\mathrm{AE}}} - \frac{I_d^{\mathrm{SE}}(q)}{I_2^{\mathrm{SE}}} \right], \tag{A.19}$$

où d_0 est l'épaisseur de l'éprouvette dans l'état non déformé.

A.2 Calcul de l'épaisseur de l'éprouvette étirée

On considère à nouveau la loi de Beer-Lambert pour calculer la transmission de photons par l'air et l'éprouvette. Tout d'abord pour l'expérience sans éprouvette entre les deux diodes PIN :

$$\frac{I_2^{\mathrm{SE}}}{\eta_2} = \frac{I_1^{\mathrm{SE}}}{\eta_1} e^{-\mu_0 (l_0 + l')}. \tag{A.20}$$

Ensuite avec une éprouvette non étirée entre les deux diodes PIN d'épaisseur d_0 :

$$\frac{I_2^{\mathrm{NE}}}{\eta_{p2}} = \frac{I_1^{\mathrm{NE}}}{\eta_{p1}} e^{-\mu_0 l_0} e^{-\mu_m d_0} e^{-\mu_0 l'} = \frac{I_1^{\mathrm{NE}}}{\eta_{p1}} e^{-\mu_0 (l_0 + l') - \mu_m d_0}, \tag{A.21}$$

où l'exposant NE signifie « non étirée ». On obtient exactement la même expression pour l'éprouvette étirée en remplaçant NE et d_0, par E (pour « étirée ») et d :

$$\frac{I_2^{\mathrm{E}}}{\eta_2} = \frac{I_1^{\mathrm{E}}}{\eta_1} e^{-\mu_0(l_0+l')-\mu_m d}. \tag{A.22}$$

En combinant les équations (A.20) et (A.21), on obtient l'expression de μ_m :

$$\mu_m = \frac{1}{d_0} \ln\left(\frac{I_2^{\mathrm{SE}}/I_1^{\mathrm{SE}}}{I_2^{\mathrm{NE}}/I_1^{\mathrm{NE}}}\right). \tag{A.23}$$

Rq : on a bien $I_2^{\mathrm{SE}}/I_1^{\mathrm{SE}} > I_2^{\mathrm{NE}}/I_1^{\mathrm{NE}}$ et donc $\mu_m > 0$. Le rapport des équations (A.21) et (A.22) conduit à

$$\mu_m(d-d_0) = \ln\left(\frac{I_2^{\mathrm{NE}}/I_1^{\mathrm{NE}}}{I_2^{\mathrm{E}}/I_1^{\mathrm{E}}}\right) < 0. \tag{A.24}$$

En considérant ces deux dernières équations, il vient

$$\frac{d}{d_0} = \frac{\ln\left(\frac{I_2^{\mathrm{SE}}/I_1^{\mathrm{SE}}}{I_2^{\mathrm{E}}/I_1^{\mathrm{E}}}\right)}{\ln\left(\frac{I_2^{\mathrm{SE}}/I_1^{\mathrm{SE}}}{I_2^{\mathrm{NE}}/I_1^{\mathrm{NE}}}\right)}. \tag{A.25}$$

On vérifie bien $0 < d < d_0$ puisque $I_2^{\mathrm{SE}}/I_1^{\mathrm{SE}} > I_2^{\mathrm{E}}/I_1^{\mathrm{E}} > I_2^{\mathrm{NE}}/I_1^{\mathrm{NE}}$.

A.3 Bilan

Finalement, l'index que nous extrairons des données expérimentales est obtenu à partir des équations (A.19) et (A.25) :

$$\boxed{\mathcal{S}(q) = \frac{\ln\left(\frac{I_2^{\mathrm{SE}}/I_1^{\mathrm{SE}}}{I_2^{\mathrm{NE}}/I_1^{\mathrm{NE}}}\right)}{\ln\left(\frac{I_2^{\mathrm{SE}}/I_1^{\mathrm{SE}}}{I_2^{\mathrm{E}}/I_1^{\mathrm{E}}}\right)} \left(\frac{I_d^{\mathrm{AE}}(q)}{I_2^{\mathrm{AE}}} - \frac{I_d^{\mathrm{SE}}(q)}{I_2^{\mathrm{SE}}}\right)} \tag{A.26}$$

où I_1^{SE}, I_2^{SE} et $I_d^{\mathrm{SE}}(q)$ sont mesurées lors d'un même essai « de référence » sans éprouvette ; I_1^{NE} et I_2^{NE} sont mesurées lors d'un deuxième essai « de référence » avec une éprouvette non étirée ; et enfin I_1^{E}, I_2^{E}, I_2^{AE} et $I_d^{\mathrm{AE}}(q)$ sont les mesures prises durant l'essai que l'on cherche à dépouiller.

Résumé

Le caoutchouc naturel est connu pour ses excellentes propriétés mécaniques en fatigue multiaxiale et celles-ci sont généralement attribuées à sa faculté à cristalliser sous contrainte. Cependant, le lien entre la cristallisation sous contrainte et les propriétés mécaniques du caoutchouc naturel n'a jamais été établi. L'objectif de cette thèse est donc de comprendre l'origine des excellentes propriétés en fatigue multiaxiale du caoutchouc naturel chargé au noir de carbone, en considérant deux échelles d'étude fines, par opposition à l'échelle macroscopique généralement considérée. La première partie de la thèse est dédiée aux mécanismes de propagation des fissures de fatigue uniaxiale et de dissipation d'énergie à l'échelle des fissures et micro-fissures ; ces mécanismes sont déterminés grâce à des essais originaux de propagation *in-situ* observés au microscope électronique à balayage. Dans la deuxième partie de la thèse, la cristallisation sous contrainte est étudiée à l'échelle macromoléculaire, en déformation quasi-statique multiaxiale d'une part et en fatigue uniaxiale d'autre part, par des essais de diffraction des rayons X réalisés au synchrotron Soleil. Les différentes caractéristiques des cristallites, c'est-à-dire leur taille, orientation, nombre et paramètres de mailles sont mesurées lors des différents essais mécaniques. Il apparaît qu'en déformation multiaxiale, les cristallites sont de même taille et ont les même paramètres de maille que celles nucléées en déformation uniaxiale, mais leur orientation varie fortement avec la multiaxialité de la déformation et n'est pas influencée par le chemin de déformation. Enfin, on montre qu'en fatigue uniaxiale, les caractéristiques des cristallites évoluent avec le nombre de cycles, différemment en fonction des extensions minimales et maximales imposées à chaque cycle.

Mots-clés Caoutchouc naturel, cristallisation sous contrainte, fatigue, déformation multiaxiale, diffraction des rayons X, synchrotron

Strain-induced crystallization of natural rubber in fatigue and multiaxial deformation

Natural rubber is well-known for its excellent mechanical properties in multiaxial fatigue and those are generaly attributed to the ability of the material to crystallize when strained. However, the relationship between strain-induced crystallization and mechanical properties of natural rubber has never been established. The aim of this thesis is therefore to understand the origin of the great multiaxial fatigue properties of carbon black-filled natural rubber, by considering two small scales of study, as opposed to the macroscopic scale generally considered. The first part of this thesis is dedicated to uniaxial crack growth and energy dissipation mechanisms at the cracks and micro-cracks scale ; those mechanisms are determined thanks to original in-situ propagation tests observed with scanning electron microscope. In the second part of the thesis, strain-induced crystallization is studied at the macromolecular scale, in static multaxial deformation on the one hand and in uniaxial fatigue on the other hand, thanks to X-ray diffraction measurements performed at the Soleil synchrotron facility. The characteristics of crystallites, i.e. their size, orientation, number and lattice parameters, are measured during the different mechanical tests. We observe that in multiaxial deformation, the crystallites are similar in size and have the samei lattice parameters than those nucleated in uniaxial deformation, but their orientation strongly varies with the multiaxiality of the deformation and is not influenced by the loading path. Finally, we show that in uniaxial fatigue, the characteristics of the crystallites evolve with the number of cycles, differently depending on the minimum and maximium stretch ratios reached at each cycle.

Keywords Natural rubber (NR), strain-induced crystallization (SIC), fatigue, multiaxial deformation, wide-angle X-ray diffraction (WAXD), synchrotron

Discipline Sciences de l'ingénieur